université PARIS-SACLAY

NNT : 2019SACLS221

Thèse de doctorat

UNIVERSITÉ PARIS SUD

Comprendre le monde, construire l'avenir

# Fast luminosity monitoring and feedback using monocrystalline CVD diamond detectors at the SuperKEKB electron-positron collider in Japan

Thèse de doctorat de l'Université Paris-Saclay
préparée à l'Université Paris-Sud

Ecole doctorale n°576 Particules, Hadrons, Énergie, Noyau, Instrumentation, Imagerie, Cosmos et Simulation (PHENIICS)

École Doctorale PHENIICS Doctoral School

Spécialité de doctorat : physique des accélérateurs

Thèse présentée et soutenue à Orsay, le 05 Septembre 2019, par

**CHENGGUO PANG**

Composition du Jury :

| | |
|---|---|
| M. Fabien CAVALIER<br>Directeur de Recherche, LAL | Président |
| Mme Marica BIAGINI<br>Directrice de Recherche, INFN/Frascati | Rapporteur |
| Mme Isabelle RIPP-BAUDOT<br>Directrice de Recherche, IPHC | Rapporteur |
| M. Yukiyoshi OHNISHI<br>Professeur, KEK | Examinateur |
| Mme Cécile RIMBAULT<br>Chargée de Recherche, LAL | Examinatrice |
| M. Philip BAMBADE<br>Directeur de Recherche, LAL | Directeur de thèse |

Laboratoire de l'Accélérateur Linéaire n°LAL 19 – 011

# Monitorage rapide et asservissement de la luminosit de collisionneur électron-positron japonais SuperKEKB avec des capteurs diamant CVD monocristallins

## Résumé

Construit dans le laboratoire KEK de Tsukuba au Japon, SuperKEKB est le premier grand accélérateur mis en œuvre depuis le LHC. Bien que loin d'atteindre les hautes énergies de ce dernier, il sera le plus "lumineux" au monde. La nouvelle machine conçue et construite par une équipe de physiciens et d'ingénieurs japonais produira 40 fois plus de collisions par seconde que son prédécesseur KEKB.

Le principe de cette nouvelle machine est de faire se collisionner des électrons de 7 gigaélectronvolts (GeV) contre des positons (des antiélectrons) de 4 GeV. Électrons et positons circulent dans deux anneaux différents et se rencontrent au point d'interaction où se situera le détecteur Belle II. La luminosité sans précédent du collisionneur permettra d'étudier finement les propriétés de certaines particules comme les quarks b et c ou encore le lepton tau. Le Modèle standard sera ainsi mis à l'épreuve dans ses propriétés les plus subtiles comme la symétrie CP qui pourrait être la clé de la suprématie de la matière sur l'antimatière dans l'Univers.

Le collisionneur SuperKEKB, dédié à l'expérience Belle II, prévoit une très haute luminosité, inégalée à ce jour. Son objectif est de fournir une luminosité instantanée de $8 \times 10^{35}\ cm^{-2}s^{-1}$ en mettant en collision des faisceaux minuscules au point d'interaction (IP) sur la base du schéma "nano-beam",. Par conséquent, un excellent contrôle de l'orbite du faisceau à l'IP est nécessaire pour assurer un recouvrement géométrique optimal entre les deux faisceaux en collision, et ainsi maximiser la luminosité. Par ailleurs, des instruments efficaces pour diagnostiquer le comportement des faisceaux à l'IP ainsi que les interactions

potentielles entre paquets successifs le long du train sont également essentiels pendant le processus long et plutôt difficile d'ajustement des paramètres des faisceaux pour atteindre les valeurs nominales.

SuperKEKB, étant à la fine pointe des collisionneurs de particules de forte luminosité, en impliquant des faisceaux extrêmement minuscules à l'IP basés sur le «schéma à nano-faisceaux», nécessite un excellent contrôle de son orbite à l'IP pour assurer un chevauchement géométrique optimal des faisceaux en collision. et maximise ainsi la luminosité. En présence de vibrations mécaniques causées par le mouvement du sol, le décalage induit entre les deux faisceaux en collision à l'IP peut être important par rapport à la taille du faisceau, ce qui dégrade considérablement la luminosité. Même pour des décalages inférieurs à la taille du faisceau, la dégradation de la luminosité peut devenir importante en raison de la sensibilité supplémentaire due aux effets de projection du sablier et du faisceau. Pour maintenir une luminosité très élevée en présence de mouvement du sol, des systèmes de rétroaction en orbite de faisceau sont nécessaires. Cependant, le grand angle de croisement à l'IP dans le plan horizontal se traduit par de très faibles déviations faisceau-faisceau dans ce plan. Limitée par la résolution que les BPM peuvent atteindre à l'heure actuelle, la méthode de déviation faisceau-faisceau n'est pas viable pour stabiliser l'orbite du faisceau horizontal à l'IP. Par conséquent, un système de rétroaction en orbite à dithering a été adopté et testé, ce qui nécessite des signaux de luminosité précis et rapides en entrée.

De plus, étant le premier collisionneur au monde à fonctionner avec des faisceaux aussi minuscules à l'IP, il est prévisible que le réglage automatique de la SuperKEKB en fonction des paramètres nominaux du faisceau sera un processus long et assez difficile, ce qui imposera des exigences spécifiques au système. mesures de luminosité. Un premier exemple est la mesure de la taille du faisceau vertical à l'IP pendant la compression $\beta_y^*$, qui peut être déduite des changements de luminosité lors des balayages de décalage faisceau-faisceau vertical. Pour éviter l'influence de l'interaction faisceau-faisceau, qui pourrait conduire à une explosion du faisceau et confondre les résultats du pincement $\beta_y^*$, il faut le faire à très faible courant de régime ($\sim$ 0,1 mA / groupe à partir de la simulation dans le cas SuperKEKB), ce qui entraîne une très faible luminosité. Cela conduit à des exigences spécifiques sur la sensibilité de la surveillance de la luminosité. Le deuxième exemple concerne les interactions possibles entre les grappes le long du train, ce qui peut induire des variations de la taille de leur faisceau et de leur alignement relatif. De tels effets peuvent être étudiés en utilisant les signaux de luminosité paquet par paquet en association avec les paramètres machine pertinents (par exemple, courants de faisceau). Par conséquent, il est important de disposer d'un système fournissant les informations de luminosité paquet par paquet avec une précision

suffisante. Globalement, une surveillance rapide de la luminosité avec une très grande sensibilité est très importante en présence d'imperfections dynamiques, pour la rétroaction et l'optimisation.

Dans ce cadre, cette thèse présente le développement et l'implémentation d'un système de monitoring rapide de la luminosité de SuperKEKB basé sur des détecteurs en diamant sCVD qui fournit: (1) un signal de luminosité intégré toutes les 1 ms qui sera utilisé en tant qu'entrée pour l'asservissement de l'orbite du faisceau à l'IP, sa précision relative devant être meilleure que 1% lorsque la luminosité atteindra $10^{34}\ cm^{-2}s^{-1}$, (2), un signal de luminosité intégré toutes les 1 s, qui doit être sensible sur une grande dynamique de luminosité, et qui sera envoyé à la salle de contrôle de SuperKEKB comme observable pour permettre le réglage des paramètres des faisceaux en collision, et (3) des signaux de luminosité intégrés toutes les 1 s pour chaque paquet des trains, avec une précision relative suffisante pour surveiller les paramètres de chacun d'entre-eux individuellement.

Pour atteindre une précision relative aussi élevée et couvrir une gamme dynamique de luminosité élevée, le processus de diffusion Bhabha radiatif à très petit angle est utilisé, dont la section efficace d'interaction est très importante et relativement bien connue. Des détecteurs diamant sCVD, dont le signal est rapide et qui ont une bonne tolérance au rayonnement, sont utilisés pour détecter les particules chargées dans les gerbes électromagnétiques induites par l'interaction entre les particules Bhabha diffusées et perdues dans le tube à vide du faisceau, et dans les autres matériaux , en particulier un radiateur, à des emplacements choisis spécialement en aval de l'IP, dans les deux anneaux LER et HER.

Une simulation de bout en bout du système d'asservissement de l'orbite du faisceau à l'IP basé sur notre signal de luminosité rapide et précis a été réalisée, qui comprend: une estimation du signal du détecteur de diamant sCVD, basé sur des mesures de laboratoire à l'aide d'une source radioactive, la construction de séquences de signal représentatives de SuperKEKB comprenant les bruits de fond à un seul faisceau et les particules diffusées par le processus Bhabha, un traitement du signal de luminosité, et la simulation de l'asservissement de l'orbite. Il a été possible de vérifier la faisabilité de ce système pour maintenir la très haute luminosité de SuperKEKB en présence des mouvements du sol et déterminer la précision relative du signal de luminosité rapide qu'il est possible d'obtenir toutes les 1 ms. En outre, les dommages causés par le rayonnement au niveau des détecteurs diamant sCVD dans le LER ont également été estimés sur la base de la simulation FLUKA et de l'hypothèse NIEL.

Basé sur l'ADC et le FPGA, le système DAQ a été conçu par l'ingénieur électronicien de notre groupe à LAL pour fournir simultanément des signaux de luminosité relatifs train / groupe par paquets au détecteur de diamant sCVD d'une épaisseur de 140 $\mu m$ couplé à l'amplificateur de courant large bande. Dans ce cas, le déclenchement du signal n'était pas nécessaire et, après une synchronisation minutieuse, une surveillance continue pouvait être réalisée. De plus, un autre calcul de la luminosité du train intégré a également été mis en œuvre, basé sur la somme de tous les points de prélèvement supérieurs à un seuil prédéfini, ne nécessitant aucune synchronisation spécifique, était donc plus robuste à cet égard et pouvait également être utilisé pour les calculs. le détecteur de diamant sCVD d'une épaisseur de 500 $\mu m$ couplé à un amplificateur de charge rapide.

Un tube de faisceau sur mesure avec une fenêtre inclinée à 45 $^\circ$ a été construit et installé pour permettre des taux de signal très élevés dans le LER, et donc une excellente précision statistique pour notre surveillance rapide de la luminosité. Des simulations détaillées comprenant la génération de particules, le suivi optique et l'estimation du signal dans le détecteur de diamant ont été effectuées à la fois pour les signaux de luminosité issus de la diffusion de Bhabha à angle de fuite et pour les signaux de fond, provenant principalement de la diffusion de Bremsstrahlung et de Touschek. Les résultats ont été utilisés comme information de base pour la simulation du retour d'orbite en orbite. Cela nous a également permis de mieux comprendre à la fois la luminosité et les signaux de fond des expériences.

Pendant la phase 2 et phase 3 in 2019 de mise en service de SuperKEKB, ainsi qu'au début de la phase 3, notre moniteur de luminosité rapide basé sur des détecteurs en diamant sCVD a été installé et utilisé avec succès. Les processus de perte de faisceau, principalement ceux provenant des processus de Bremsstrahlung et de Touschek, ont été étudiés en détail et, par rapport à la simulation, un bon accord a été trouvé. Lors de la mise en service de la collision, des signaux de luminosité intégrés toutes les secondes étaient fournis en continu pour le réglage des paramètres des faisceaux à l'IP. Par exemple. les tailles de faisceau verticales ont été déterminées avec la technique de balayage du décalage vertical basée sur nos signaux de luminosité, tant pour la valeur moyenne sur tous les paquets que pour chaque paquet individuel, ce qui est très important et utile pour l'optimisation des collisions et pour le réglage de l'optique locale à l'IP. En outre, un signal de luminosité intégré toutes les 1 ms avec la précision relative attendue a également été fourni et utilisé comme entrée du système d'asservissement de l'orbite à l'IP, pour des premiers tests conduits avec succès avec des décalages de faisceau horizontaux introduits volontairement. Davantage de tests de ce système d'asservissement sont attendus pour assurer son bon fonctionnement en continu à l'avenir.

Sur la base de tous les résultats et de l'expérience obtenus lors de la précédente mise en service de SuperKEKB, nous avons également découvert quelques problèmes restants, que nous résumons ci-dessous, ainsi que des mesures d'atténuation possibles. Certaines des améliorations décrites et d'autres études seront nécessaires compte tenu de l'augmentation attendue de la luminosité et de l'évolution de la machine dans les années à venir.

En tant que premier collisionneur circulaire $e^+e^-$ avec une taille de faisceau à l'échelle du nanomètre et à la luminosité instantanée la plus élevée du monde jusqu'à présent, SuperKEKB pourrait fournir une expérience utile pour l'avenir luminosité $e^+e^-$ collisionneurs circulaires utilisant le "schéma à nano-faisceaux", tels que par exemple CEPC et FCCee à la frontière des hautes énergies, ou les usines à super charme Tau actuellement en discussion à l'intensité frontière. Sur la base des résultats et de l'expérience de notre projet, il faudra peut-être envisager certaines conséquences pour les futurs collisionneurs circulaires en ce qui concerne le contrôle rapide de la luminosité, en particulier pour la stabilisation de l'orbite du faisceau à la propriété intellectuelle, les interactions possibles entre les grappes et l'optique locale. accord à l'IP avec des balayages de décalage vertical basés sur des signaux de luminosité précis à très faible luminosité, pour éviter les effets d'interaction faisceau à faisceau. Ces trois applications dépendent principalement de la disponibilité de signaux de luminosité intégrés, rapides et détaillés. Par conséquent, pour les futurs collisionneurs circulaires à haute luminosité $e^+e^-$, il faudra certainement tenir compte des exigences de la surveillance rapide et précise de la luminosité, et les travaux effectués pour le SuperKEKB décrits dans cette thèse pourraient servir. comme exemple pour de tels futurs collisionneurs.

**Mots clés:** monitorage rapide de la luminosité, détecteur diamant sCVD, diffusion Bhabha radiative, système d'asservissement de l'orbite par modulation et détection synchrone, SuperKEKB

# Fast luminosity monitoring and feedback using monocrystalline CVD diamond detectors at the SuperKEKB electron-positron collider in Japan

## Abstract

SuperKEKB is at the foremost frontier of high luminosity $e^+e^-$ colliders, dedicated to the Belle-II experiment. It aims to provide an instantaneous luminosity of $8 \times 10^{35}\ cm^{-2}s^{-1}$ by involving extremely tiny beams colliding at the Interaction Point (IP) based on the "nano-beam scheme". Therefore, excellent control of its beam orbit at the IP is required to ensure the optimum geometrical overlap between the two colliding beams, and thereby maximize the luminosity. Besides, effective instrumentation to diagnose the behavior of the beam at the IP and possible beam interactions between bunches along the trains are also quite essential during the long and rather difficult process of machine tuning towards the nominal beam parameters.

In this context, this thesis presents the development and implementation of a fast luminosity monitoring system based on sCVD diamond detectors at SuperKEKB, which provides: (1), train integrated luminosity signals every 1 ms which will be used as input to the dithering orbit feedback system, its relative precision is expected to be better than 1% when luminosity reaches $10^{34}\ cm^{-2}s^{-1}$, (2), sensitive train integrated luminosity signals over a large luminosity dynamic range every 1 s which will be sent to the SuperKEKB control room as immediate observable for machine collision tuning, and (3) bunch integrated luminosity signals every 1 s with sufficient relative precision to monitor the collision performance for each single bunch.

To achieve such high relative precision and to cover a large luminosity dynamic range, the radiative Bhabha process at vanishing scattering angle will be measured, whose interaction cross-section is quite large and reasonably well known. The sCVD diamond detectors, which have fast signal formation and good radiation tolerance, are used to detect the charged

particles in the secondary showers induced by the interaction between the lost Bhabha scattered particles and the beam pipe and specific radiator materials, at carefully chosen locations downstream of the IP, in both the LER and HER.

A start-to-end simulation was performed for the dithering orbit feedback system using our fast and precise luminosity signal as input, based on: sCVD diamond detector signal estimation based on laboratory measurements with a radioactive source, signal sequence construction at SuperKEKB including single beam backgrounds and Bhabha scattered particles, luminosity signal procession, dithering orbit feedback simulation. It enabled verifying the feasibility of this system to maintain very high luminosity in the presence of ground motion, in particular it determined the needed precision for the provided luminosity signals. Besides, the radiation damage of the sCVD diamond detectors in the LER was also estimated based on a FLUKA simulation and applying the NIEL hypothesis.

During the Phase-2 and early Phase-3 commissioning periods of SuperKEKB, our fast luminosity monitor based on sCVD diamond detectors was installed and operated successfully. Single beam loss processes, mainly Bremsstrahlung and Touschek, were studied in detail and compared with the simulation, showing good agreement. During the collision commissioning, train and bunch integrated luminosity signals every 1 s were provided for machine tuning, and the vertical beam sizes could be determined with the vertical offset scan technique based on our luminosity signals, both the average and for the individual bunches, which is very important and useful for the collision and IP local optics tuning during the long and rather difficult process of SuperKEKB machine tuning towards the nominal beam parameters. Besides, a train integrated luminosity signal every 1 ms with the expected relative precision was also provided as input to the dithering orbit feedback system for its first successful tests with deliberately introduced horizontal beam-beam offsets. More tests of the dithering orbit feedback system are expected to establish its future continuous operation.

**Keywords:** fast luminosity monitoring, sCVD diamond detectors, radiative Bhabha scattering, dithering orbit feedback system, SuperKEKB

I would like to dedicate this thesis to my loving parents ...

# Acknowledgements

It is not a fair task to acknowledge all the people who made this PhD thesis possible with a few words. However, I will try to do my best to extend my great appreciation to everyone who helped me scientifically and emotionally throughout this study.

First and foremost, I would like to express my great appreciation to my supervisors, Philip BAMBADE and Cécile RIMBAULT, their consistent support and encouragement enabled me to complete my PhD from the very beginning. Their passion and dedication for work and rigorous attitude to research left a deep impression on me and inspired me a lot. I benefited enormously from the academic as well as the non-academic discussions with them and also learned a lot from their discussions with the others. In addition, I also thank them for the great opportunities to work and collaborate with the other local and international experts, which gave me a broader perspective and developed the ability to work in teams, especially in a completely different culture.

Many thanks to every person in our group for every single thing that they helped me in every manner. Thanks to S. DI CARLO, D. JEHANNO, V. KUBYTSKYI, Y. PEINAUD. I would like to thank D. EL KHECHEN and R. YANG for their great help and valuable advice at the very beginning of the thesis study. Many thanks as well to everyone of the DEPACC group, for all the physics and non-physics discussions with them during the lunch time and coffee break. Many thanks as well to all the people of the administrative service at LAL and Universié Paris-Sud for helping me in all the administrative issues.

My sincere appreciation should be addressed to our collaborators at KEK. Their hard-working, persistent and sincere efforts towards the research have certainly inspired me. Sincere thanks to Y. FUNAKOSHI, S. UEHARA, Y. OHNISHI, M. MASUZAWA, K. KANAZAWA, M. TOBIYAMA, and all the other KEK collaborators, for all the supports, advice, discussions on my work they gave me during the past three years. Thanks to A. FISHER and U. WIENANDS for their helpful advices and comments on the fast luminosity monitoring signal as the input to the dithering orbit feedback system. Meanwhile, a lot of thanks to the BEAST II collaborators for their useful comments and discussions and experience on single beam background signal analysis. In addition, I also would like to thank

J. URAKAWA, S. ARIMOTO and K. SHIMOMURA for all their kind help and support during my stay in KEK.

I would like to thank the Chinese Scholarship Council (CSC) for providing me the financial support and the great opportunity of my PhD study at Universié Paris-Sud. Part of this work has been supported financially by the H2020 European Commission RISE project E-JADE (contract No.645479) and the Toshiko Yuasa France Japan Particle Laboratory (TYL-FJPPL), project A_RD_08, so many thanks to them. As well many thanks to the Ecole doctorale PHENIICS for funding my study to the very nice course JUAS.

Finally and most importantly, big thanks to my beloved family members, my grandparents, my parents and my brother, I have been encouraged, sustained, inspired and tolerated by them.

Although it is impossible to mention all the people who helped me in the process of completing my doctoral thesis, but their kind support will be remembered throughout my life.

# Table of contents

# List of figures

# List of tables

# Chapter 1

# Introduction

In the history of humans exploring the laws of physics, especially in the sub-atomic domain (at distance scales of about $10^{-13}$ cm and smaller), as a major invention of the 20th century, particle accelerators have played a significant role. From the first linear accelerator built by Rolf Wideroe [1–4] in an 88 cm long glass tube in Aachen, Germany, in the 1920s to the gigantic 27 km circumference deep underground Large Hadron Collider (LHC) [5] at CERN in Geneva, particle accelerators have evolved remarkably and have had profound influence on our lives and on the way that how we are thinking and working.

As observed by the ATLAS and CMS experiments at CERN's LHC in July 2012 [6, 7], the confirmation of the predicted Higgs boson particle was an immense success for the Standard Model, which describes three of the four known fundamental forces in the universe (weak, strong and electromagnetic interactions), as well as classifying all the elementary particles, as shown in Figure 1.1. However, despite of the success of the Standard Model theory, several experimental observations are still waiting for an explanation, for instance the origin of the dark matter and matter-antimatter asymmetry and CP violation [8, 9] in the universe. Moreover, a clear explanation for the origin of the Higgs mechanism, and a detailed study of the characteristics of the discovered Higgs boson are not yet available. Furthermore precise investigations and searches for new physics expected beyond the Standard Model require both higher collision luminosity and energy.

## 1.1 High energy and high luminosity colliders

Nowadays, particle physics research with particle accelerator colliders follows two different, while complementary approaches. The high energy frontier approach is based on particle accelerators that are able to provide the highest possible energy to search for new particles or unknown processes at very high center of mass energies. For example, the LHC proton-

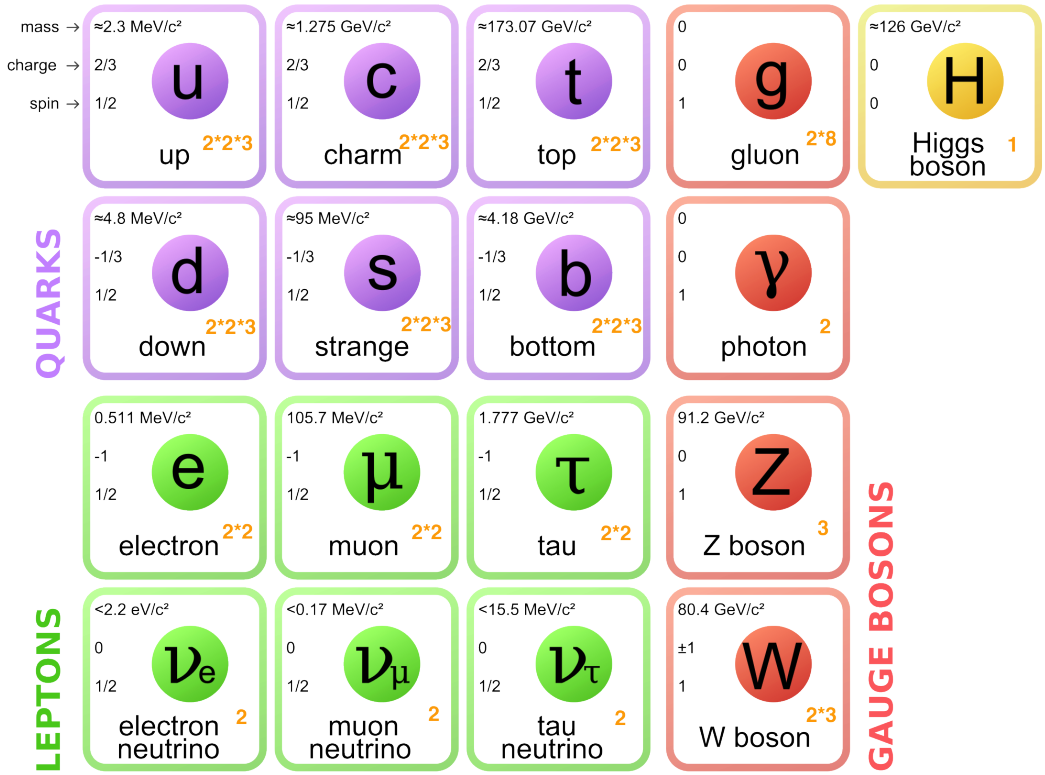


**Figure 1.1:** The elementary particles of the Standard Model.

proton collider where the Higgs boson was observed is now still operating at CERN, and several ambitious future colliders are being prepared or have been proposed including High Luminosity LHC (HL-LHC) [10], which aims at a peak luminosity up to $5\times10^{34}\ cm^{-2}s^{-1}$ and center of mass energy up 14 to TeV; Future Linear Collider such as Compact Linear Collider (CLIC) [11] is a future $e^+e^-$ linear collider project based in CERN, aiming at a nominal luminosity of $6\times10^{34}\ cm^{-2}s^{-1}$ and energy of 3 TeV, the International Linear Collider (ILC) [12, 13], another $e^+e^-$ linear collider, presently under consideration in Japan with a center of mass energy of 250 GeV, or the Circular Collider (FCC) (ee, hh) [14, 15] at CERN, with a 100 km tunnel to be constructed in the Geneva area, which aims at colliding $e^+e^-$ beams with an energy in the center of mass of up to 400 GeV, as well as the proton beams with a center of mass energy of 100 TeV, and finally the Circular Electron Positron Collider (CEPC) [16], which is another future circular $e^+e^-$ collider ring of 100 Km circumference planned in China, and which can be upgraded to a Superconducting Proton-Proton Collider (SPPC) at very high energies at a second stage.

Another approach is using a collider with much higher luminosity, but lower energy to study certain well known processes or particles in the Standard Model with very high precision, including searching for very rare decays, to investigate phenomena that are not

contemplated within the Standard Model, through effects they can induce on measurable physical observables at higher orders in the theory. The latter approach is followed by Belle II [17] experiment at the SuperKEKB accelerator [18]. SuperKEKB is an upgrade of the previously operating KEKB asymmetric electron-positron collider, which aims to reach a luminosity of $8\times10^{35}\ cm^{-2}s^{-1}$, about 40 times that of KEKB, by doubling the beam currents and colliding the extremely low emittance beams with a large crossing angle at the Interaction Point (IP), using a new collision geometry refereed to as the "nano-beam scheme", which enables focusing the beams to very small vertical sizes at the IP (see Section 2.2.1). In this project, one of the main priorities is dealing with rare events (e.g. processes with a very small cross-section) which may show departures from the Standard Model predictions, and it is clear that the luminosity determines the ultimate success in terms of physics reach.

Figure 1.2 shows the luminosity as the function of collision energy achieved or projected for past and future colliders, respectively. In general, high energies can be achieved by huge rings or long linear colliders (for lepton colliders), requiring for the latter accelerator technologies with the highest possible gradients. For future hadron colliders, the challenge is the development of very high field superconducting magnets. In general, high luminosity colliders also require small, in some cases very small, beam sizes at the IP and high beam currents.

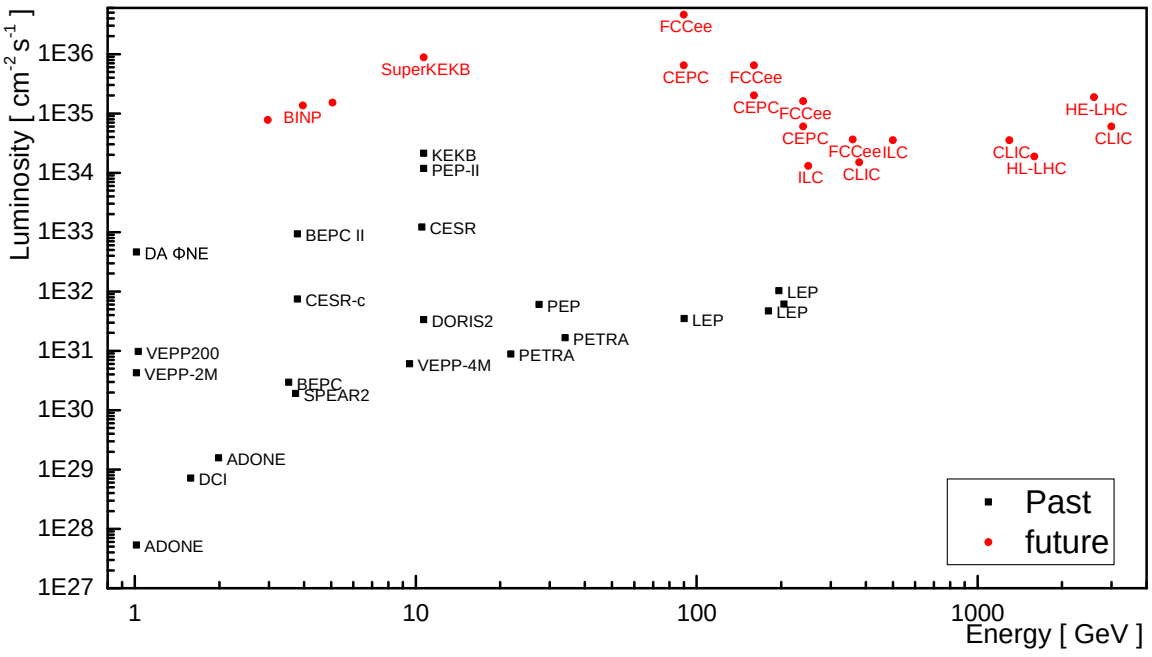


**Figure 1.2:** Luminosity as function of collision C.M.S energy for past and future particle colliders. Both CEPC and FCCee will be operated in Z, W, and Higgs modes.

## 1.2 Beam orbit feedback

Nowadays, with the development of the accelerator technology and the ever more demanding performances which are required, particle accelerators must be manipulated more and more precisely, one typical example is the accurate beam orbit control.

Beam orbit feedback systems are widely used in particle accelerators, such as synchrotron light source, e.g., the fast orbit feedback system at SLS [19–21], which is used to damp the orbit distortions mainly caused by ground and girder vibration. Another example is the beam orbit feedback system for the particle accelerator colliders to maintain an optimum collision condition, to maximize the luminosity in the presence of mechanical vibrations caused by ground motion and other effects, especially for those very high luminosity colliders with extremely small beam sizes at the IP, e.g., the beam orbit feedback system used at the IP at PEP-II, KEKB and SuperKEKB [22–24].

In principle, there are two possible methods used for the orbit feedback system for the particle colliders. One is based on the measurement of the beam orbits around the IP with Beam Position Monitors (BPMs), which has been successfully utilized for years at KEKB [23, 25]; The other is a straightforward method, since the luminosity is the ultimate goal of the collider machines, it uses directly the measurement of the luminosity as input (luminosity-driven-system). Several years of operational experience at PEP-II have proven that the luminosity-driven feedback system works excellently in a double ring collider [22, 26].

With the first method, we can know in which direction we should change the orbits when an orbit drift is detected, as long as the accuracy of the orbit measurements is precise enough, and we can in this way maintain an optimized geometrical overlap between the two colliding beams to achieve high integrated luminosity. However, the accuracy of the orbit measurements and the long-term stability of the orbit measurement system may limit its application. On the other hand, for the second method, when the luminosity degradation due to the orbits drift is observed, we cannot know in which direction we should change the beam orbits to recover the luminosity. In addition, there are also many other effects causing the luminosity change at relatively low frequencies, such as beam size and beam intensity vibrations, which will confuse us in determining the reason of the luminosity degradation. Therefore, the beam orbits need to be changed continuously in some manner (e.g. dithering with relatively high frequency at which the noise effects are negligible) so as to extract the beam orbit drifts and correct them to maximize the luminosity with this method. As a result, this intentional variations in the orbits are needed to continuously search for the optimum collision and that will necessarily result in some luminosity loss (e.g. 1%).

In future double-ring colliders or linear colliders, the possibility to incorporate both systems could be pursued, since the two systems are very complementary. For example, by

working one of the feedback systems and monitoring the input parameters for the other, one may be able to obtain information to improve the performance of both systems. In addition, in some situation, one of the two systems becomes preferable. For instance, at KEKB, the fast luminosity monitor had a problem of narrow acceptance and therefore the luminosity-driven feedback did not work well [23]. At PEP-II, the deflection driven feedback did not work well due to the reliability problem and was replaced by the luminosity driven system soon after the start of operation [27]. With such a unified system, one can switch the two feedback systems according to the situations.

## 1.3 Luminosity monitoring

In a particle collider, the luminosity quantifies the event rate for a physical process with unit cross-section, see Equation 1.1, with unit of $cm^{-2}s^{-1}$ or $b^{-1}s^{-1}$ [28]. Luminosity L is one of the most important parameters for a particle collider, this is especially true when rare events with very small production cross-sections $\sigma_p$ are studied.

$$\frac{dR}{dt} = L * \sigma_p \tag{1.1}$$

Today's particle colliders all employ the bunched beams. A basic expression of the luminosity is:

$$L = \frac{N_1 N_2 f n_b}{4\pi\sigma_x\sigma_y} R_L \tag{1.2}$$

where $N_1$ and $N_2$ correspond to the particle population for each collision bunch; $f$ is the collision frequency; $n_b$ is the number of bunches circulating in the ring and assumed to be the same for both beams; $\sigma_{x,y}$ correspond to the RMS of beam spot sizes in the horizontal and vertical planes at the IP, also assumed to be the same for both beams. $R_L$ is the luminosity reduction factor due to different kinds of effects, such as crossing angle, bunch length, beam-beam interaction and so on.

In $e^+e^-$ colliders, the rate of the well known Bhabha scattering process (see 1.3) [29] is often used as the main observable to measure the luminosity because of its large and well known cross-section. For example, the backward and forward end-caps of the Electromagnetic Crystal Calorimeter (ECL) in the Belle (KEKB) [30] and Belle II (SuperKEKB) experiments [31] measure the coincidence rates at relative large angles in the opposite sectors for Bhabha events to provide the absolute value of the luminosity after proper internal calibration.

$$e^+ + e^- \rightarrow e^+ + e^- + \gamma \tag{1.3}$$

In addition to the absolute luminosity measurements, which in general are slow and have relative low statistics, fast and precise relative luminosity measurements are also needed for machine optics tuning and luminosity optimization. As described in Section 1.2, orbit feedback systems are in general required to keep the high luminosity in most contemporary colliders in the presence of mechanical vibration caused by ground motion or other perturbations. Since modern colliders typically use tiny beam sizes at the IP to achieve a high luminosity, they become more sensitive to ground motion induced vibration of small magnitudes. Therefore, the fast and precise luminosity measurement signal is generally needed in the case of the luminosity-driven feedback system. The Bhabha scattering process at vanishing scattering angle, which has a large and reasonably well known cross-section of about 150 mbarn is for example used for this purpose at KEKB, PEP-II and SuperKEKB [22, 24, 32].

Apart from the train integrated luminosity monitoring, the bunch integrated luminosity signals, which accumulate the luminosity signals for each crossing bunch, are also very important to investigate the beam behavior along the bunch train, since the possible interactions between bunches can induce variations in their beam sizes and relative alignment thereby result in unexpected luminosity degradation.

At SuperKEKB, two different while complementary technologies are used for the fast luminosity measurements: LumiBelle2, which is based on sCVD diamond detectors from our group at LAL, CNRS, France, and ZDLM (Zero Degree Luminosity Monitor) from the group at KEK, Japan. The detectors of both projects are installed in both rings downstream of the IP at carefully selected positions and a relative precision of 1% at 1 kHz was specified for the train integrated luminosity signal to meet the requirement of the dithering feedback system, and about 1% relative precision for the 2500 bunch integrated luminosity signals at 1 Hz [33].

During the Phase-2 commissioning of SuperKEKB in 2018, the fast luminosity monitoring system based on diamond detectors was successfully developed and employed, and the dithering orbit feedback system was also successfully tested. With several months' operation experience in both single and colliding beam modes, good general performance and reliability were found. Besides, good quantitative and qualitative agreement between the experiments and simulations was observed. The experience gained in 2018 and early commissioning in 2019 gives us confidence that the fast luminosity monitoring and dithering orbit feedback systems can be used in the longer term for the operation of SuperKEKB.

My main contributions to this project are summarized as follow: I studied the characteristics of the signals from the diamond detectors coupled with amplifiers with the Sr-90 electron source in the clean room at LAL, which are quite important to develop the DAQ system. I

developed a new start-to-end simulation of the whole chain of the dithering orbit IP feedback system, including the physics process generation, particle tracking, signal generation in the diamond detectors, DAQ process, lock-in amplifier model, beam-beam offset generator based on measured ground motion data, and beam orbit control part. The radiation tolerance of diamond detector was estimated with FLUKA. I made significant contributions to the whole systems preparation, installation, online and offline data processing and archiving, and those luminosity data analyses with related machine parameters. I attended the dithering orbit IP feedback tests and analyzed the results with the simulation.

This thesis is organized in six chapters including the **Introduction** (**Chapter 1**):

**Chapter 2** gives a brief introduction to the SuperKEKB project, including its design, goals, operation phases, the Belle II detector and the BEAST II beam background evaluation.

**Chapter 3** describes the fast luminosity monitoring systems, including the motivations, dithering orbit feedback systems, characterization of the diamond detectors with radioactive source in the clean room at LAL, and the data acquisition system based on an ADC and FPGA.

**Chapter 4** describes the numerical simulation study for the preparation of the fast luminosity monitoring and dithering orbit feedback system, including detailed signal estimation in the sCVD diamond detectors based on modeling the Bhabha scattering generation at the IP, the optical transport in the beam line of the scattered particles down to their exit points and their subsequent interactions with the materials of the beam pipe and the diamond detector; The data acquisition system model based on MATLAB and the processing of the signal sequences are described, either. Background signals from single beam losses and the dithering orbit feedback are also studied in simulations.

**Chapter 5** describes the overall mechanical and electronic setup of the project during Phase-2, including the experimental set-up, data acquisition, and so on. The results of off-line data analysis on single beam losses and colliding beams are presented and compared with detailed simulations. Based on the vertical beam scans, vertical beam size determination at the IP is also described. Dithering orbit feedback tests based on our fast luminosity monitoring are finally described.

**Chapter 6** summarizes all the results and discusses the future prospects.

# Chapter 2

# The SuperKEKB collider and Belle II

KEKB, as a 3 km circumference asymmetric electron-positron collider, operated from 1998 to 2000 at KEK, reached the world record instantaneous luminosity of $2.11 \times 10^{34}\ cm^{-2}s^{-1}$ and the total integrated luminosity collected by the Belle detector was 1041 $fb^{-1}$[34]. The asymmetric beam energies were chosen to produce B-meson pairs at production threshold, with their center of mass moving with respect to the laboratory frame to facilitate, taking into account their finite lifetimes, detection of their decays in flight. The Belle experiment precisely analyzed the characteristics of pairs of B and anti-B-mesons and confirmed the effect of CP-violation, together with the Babar experiment at PEP-II, SLAC, as predicted by the theory of Makoto Kobayashi and Toshihide Maskawa [35–39]. However, the measured data is by far not sufficient to quantitatively explain the CP-violating asymmetry. In addition, the quantities of matter and anti-matter are believed equal at the beginning of the universe, while almost no anti-matter is presently discovered in nature. Therefore, a much deeper understanding of the related phenomena is required based on more detailed data. In this context, the KEKB collider and the Belle experiment were upgraded to deliver much higher luminosity and improve its detection capabilities, respectively.

## 2.1 Motivations and goals

The next generation B-factory will complement the exploration of new physics beyond the Standard Model currently being carried out at the energy frontier by the experiments at the LHC. While the LHC experiments provide a direct probe of the TeV mass scale, high-precision measurements of rare decays and CP-violation in heavy quarks and leptons provide a unique probe of new physics at these and even higher mass scales through the effects of new particles in higher order processes. In the past, measurements of processes involving

internal loops have given access to high mass scales before accelerators were available to directly probe these scales.

SuperKEKB [18], is an upgrade project at KEK to increase the instantaneous luminosity by about a factor of 40, up to $8 \times 10^{35}\ cm^{-2}s^{-1}$, which will make it as the highest luminosity particle accelerator collider that has ever existed. The peak luminosity of the particle accelerator colliders is shown as function of year of operation in Figure 2.1. The ambitious goal is to accumulate an integrated luminosity of 50 $ab^{-1}$ in about 10 years of operation, by the end of the next decade, which is about 50 times more data than what the previous Belle detector acquired.

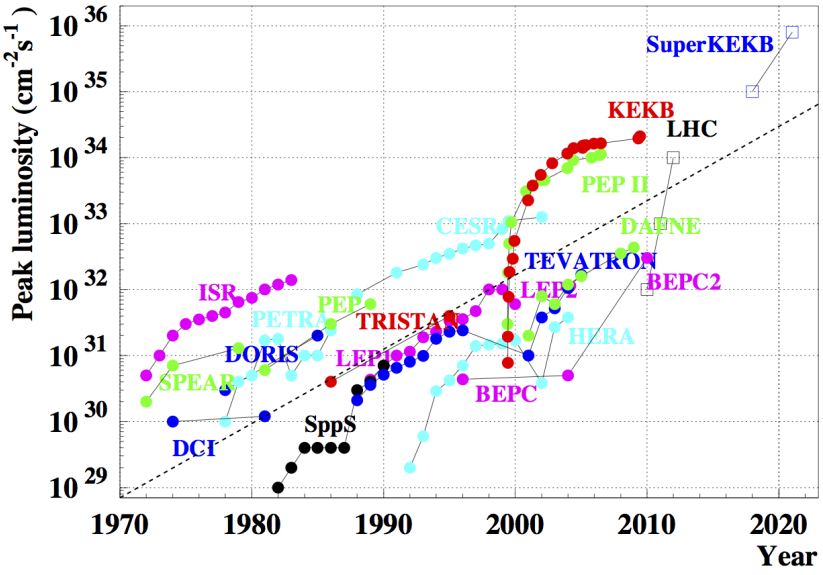


**Figure 2.1:** History of peak luminosity of particle accelerator colliders: SuperKEKB is designed to reach the highest luminosity of $8 \times 10^{35}\ cm^{-2}s^{-1}$ in the coming years.

## 2.2 SuperKEKB Accelerator

The upgraded SuperKEKB collider complex consists of a 4 GeV positron ring (the Low Energy Ring, LER), a 7.007 GeV electron ring (the High Energy Ring, HER), and an injector linear accelerator (Linac), including also a 1.1 GeV positron damping ring (DR), as shown in Figure 2.2.

The electrons are produced via the photoelectric effect in a pre-injector by a pulsed laser directed on a cold cathode target. They are accelerated by a linear accelerator (Linac) to 7 GeV and injected into the HER. Before the electrons are fully accelerated, some of them are used to generate positrons by irradiation of a Tungsten target located in the middle of the

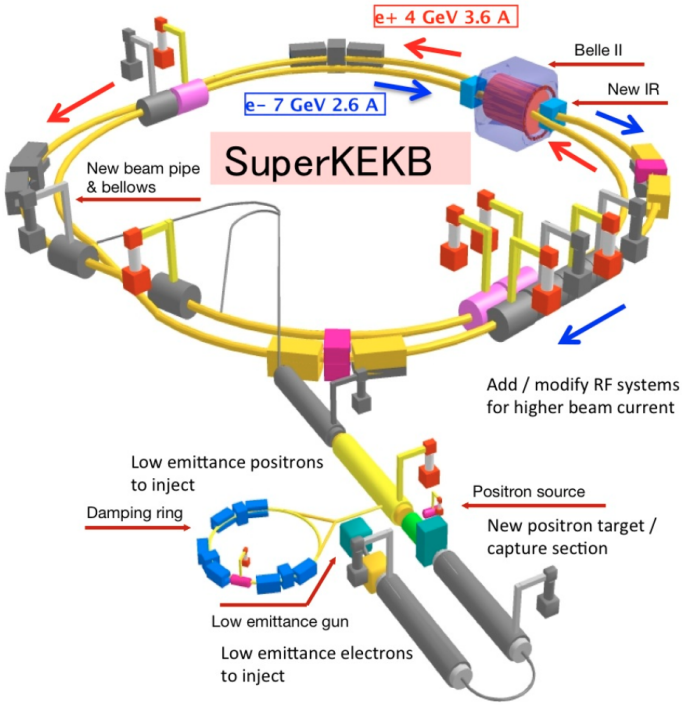


**Figure 2.2:** Schematic view of SuperKEKB. The electron and positron rings have four straight sections named Tsukuba, Oho, Fuji, and Nikko. The electron and positron beams collide at the IP in the Tsukuba straight section.

Linac. The spread of positions and momenta of the positrons produced in the electromagnetic showers in the Tungsten target and collected to generate a positron beam is very large. The DR is used to damp the corresponding emittance before re-injecting into the Linac to accelerate.

The two beams circulate in two separate rings, both with a circumference about 3.0 km, a 7 GeV electron beam in the HER and a 4 GeV positron beam in the LER. The center of mass energy is expressed as equation 2.1, where $E_{e^\pm}$ and $p_{e^\pm}$ are the energies and momenta of the positrons (+) and electrons (-) and the electron mass is neglected.

$$E_{cms} = \sqrt{s} = \sqrt{(E_{e^-} + E_{e^+})^2 - (p_{e^-} + p_{e^+})^2} \approx \sqrt{4E_{e^-}E_{e^+}} = 10.58 \quad GeV \tag{2.1}$$

### 2.2.1 SuperKEKB accelerator characteristics

Reaching a higher luminosity in a collider usually involves both increasing the beam currents and reducing the beam sizes at the IP. The most important effect which limits the luminosity of a particle collider is the so-called beam-beam interaction, which is the interaction of

each bunch with the electromagnetic field from the space-charge of the other bunch. The magnitude of the beam-beam interaction is usually quantified by the beam-beam strength parameters $\xi_{x,y}$:

$$\xi_{x,y\pm} = \frac{r_e}{2\pi\gamma_\pm} \frac{N_\mp \beta^*_{x,y}}{\sigma^*_{x,y}(\sigma^*_x + \sigma^*_y)} R_{\xi_{x,y}} \tag{2.2}$$

where $r_e$ and $\gamma_\pm$ are the classical electron radius and Lorenz factor, respectively; $N_\pm$ are the particle population for the colliding bunches; here, the suffix specifies the positron (+) or the electron (-). $\beta^*_{x,y}$ are the beta function and $\sigma^*_{x,y}$ are the beam sizes at the IP in horizontal and vertical planes, respectively; The reduction factor $R_{\xi_{x,y}}$ depends on the $\beta^*_{x,y}$, $\sigma_z$ and crossing angle. The beam-beam strength parameters correspond to the betatron tune shifts of the central particle of each beam due to the focusing force by the other beam, in each plane.

The luminosity L is generally expressed as Equation 2.3 by combining Equation 1.2 with the vertical beam-beam strength parameters $\xi_{y\pm}$ in Equation 2.2 and the stored beam current $I_\pm = N_\pm e f$:

$$L = \frac{\gamma_\pm}{2er_e}\left(1 + \frac{\sigma^*_y}{\sigma^*_x}\right)\left(\frac{I_\pm \xi_{y\pm}}{\beta^*_{y\pm}}\right)\left(\frac{R_L}{R_{\xi_y}}\right) \tag{2.3}$$

where parameter $e$ is the elementary electric charge of the electron. $I_\pm$ are the beam currents. For a round beam scheme, the luminosity gains a factor of 2 according to this equation. However, to focus the beam in both planes is very difficult for an extremely small $\beta^*$. Therefore, most of the $e^+e^-$ colliders adopt the flat beam scheme, where $\sigma^*_x \gg \sigma^*_y$. In this case, the luminosity is written as:

$$L = \frac{\gamma_\pm}{2er_e}\left(\frac{I_\pm \xi_{y\pm}}{\beta^*_{y\pm}}\right)\left(\frac{R_L}{R_{\xi_y}}\right) \tag{2.4}$$

According to Equation 2.4, in order to get a high luminosity, the beam current $I_\pm$ and beam-beam strength parameter $\xi_\pm$ should be increased and the vertical beta function $\beta^*_y$ should be squeezed.

In view of the requirements to achieve high luminosity described above, the "nano-beam scheme" was first originally proposed by Raimondi for the SuperB project [40] and later adopted for the SuperKEKB design strategy [18]. The "nano-beam scheme" mainly consists of: (1), A large crossing angle in terms of the Piwinski angle ($\theta_x \sigma_z / \sigma^*_x \gg 1$), where the $\theta_x$ is the half horizontal crossing angle. (2) A very small $\beta^*_y \ll \sigma_z$ and (3), very small horizontal and vertical emittances.

With the "flat nano-beam scheme" at SuperKEKB, beam bunches with sufficiently small beam size $\sigma^*_x$ collide at a large horizontal crossing angle, as shown in Figure 2.3, implying a

large Piwinski angle ($\Phi_{Piw} = \theta_x \sigma_z / \sigma_x^* \approx 20$). The longitudinal extent of the overlap between the two colliding beams is decreased by the Piwinski angle to $\sigma_x^*/\theta_x$, which is much shorter than the original bunch length $\sigma_z$. As the results, the $\beta_y^*$ can be decreased down to $\approx \sigma_z/\Phi_{Piw}$, while still avoiding the hourglass effect, which will lead to luminosity degradation due to lower beam density caused by the larger $\beta$ functions from the minima at the collision point. To achieve the large Piwinski angle $\Phi_{Piw}$, $\theta_x$ must be sufficient large and $\sigma_x$ sufficiently small, which means both very low horizontal emittance $\varepsilon_x$ and $\beta_x^*$ are required.

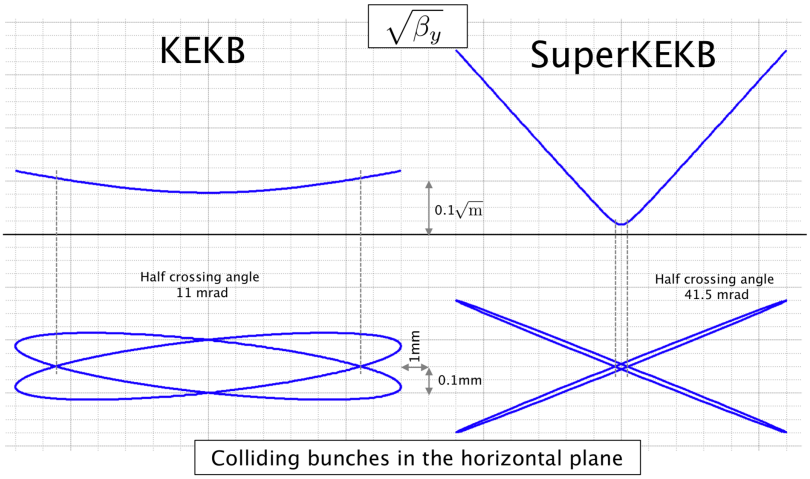


**Figure 2.3:** Schematic view of the nano-beam collision scheme [41].

On the other hand, due to the horizontal crossing angle, the effective beam size $\sigma_x^{eff}$ in the horizontal plane becomes $\sigma_z sin\phi_x$, which is much larger than the nominal horizontal beam size: $\sigma_x^*$, as shown in Figure 2.4. The horizontal beam size $\sigma_x^*$ should be replaced by the effective one: $\sigma_x^{eff}$ when calculating the horizontal beam-beam strength parameter $\xi_x$ (Equation 2.2) and luminosity (Equation 2.4). Therefore, the horizontal beam-beam strength parameter $\xi_x$ is very small compared to the head-on collision scheme, which is helpful for avoiding dynamic effects due to the beam-beam interaction in the horizontal plane.

As a conclusion, the "nano-beam scheme" is a way to reduce the $\beta_y^*$ significantly (much below the bunch length $\sigma_z$) while still allowing a lot of beam particles to be collided, and thereby increasing the luminosity with the same beam currents.

Table 2.1 shows the comparison of the key machine parameters between KEKB and SuperKEKB. As a summary of this comparison, the beam currents of SuperKEKB are increased by a factor of 2, the beam-beam strength parameters $\xi_y$ are almost the same as KEKB, and the vertical beta functions at the IP $\beta_y^*$ are decreased by a factor of 20. As the results, a luminosity 40 times higher than that of KEKB can be expected. Thanks to the final focus superconducting magnet system (details can be found in Section 2.2.2), low $\beta_{x,y}^*$ of 30

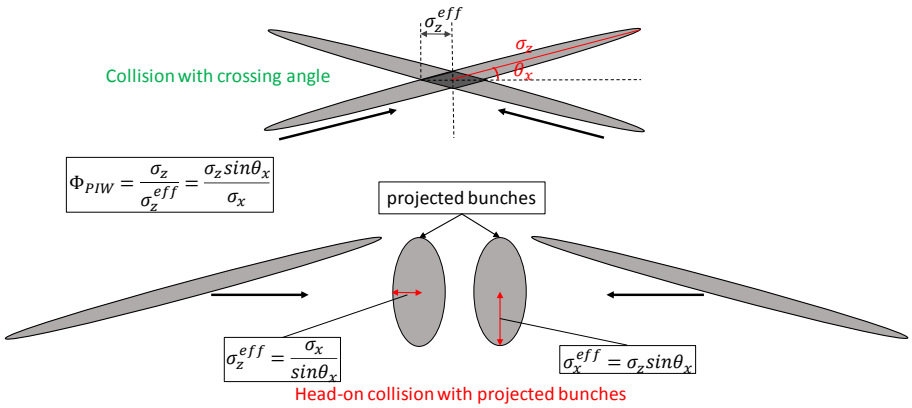


**Figure 2.4:** Illustration of SuperKEKB colliding beams with both a crossing angle and head-on collision using projected bunches.

| | | KEKB | | SuperKEKB | | |
|---|---|---|---|---|---|---|
| | | LER ($e^+$) | HER ($e^-$) | LER ($e^+$) | HER ($e^-$) | Units |
| Beam energy | $E$ | 3.5 | 8.0 | 4.0 | 7.007 | GeV |
| Circumference | $C$ | 3016.262 | | 3016.315 | | m |
| Half crossing angle | $\theta_x$ | 0(11$^{(*)}$) | | 41.5 | | mrad |
| Piwinski angle | $\phi_{piw}$ | 0 | 0 | 24.6 | 19.3 | rad |
| Horizontal emittance | $\varepsilon_x$ | 18 | 24 | 3.2(1.9) | 4.6(4.4) | nm |
| Vertical emittance | $\varepsilon_y$ | 150 | 150 | 8.64 | 12.9 | pm |
| Coupling | | 0.83 | 0.62 | 0.27 | 0.28 | % |
| Beta function at IP | $\beta_x^*/\beta_y^*$ | 1200/5.9 | 1200/5.9 | 32/0.27 | 25/0.30 | mm |
| Horizontal beam size | $\sigma_x^*$ | 147 | 170 | 10.1 | 10.7 | $\mu m$ |
| Vertical beam size | $\sigma_y^*$ | 940 | 940 | 48 | 62 | nm |
| Horizontal betatron tune | $\nu_x$ | 45.506 | 44.511 | 44.530 | 45.530 | |
| Vertical betatron tune | $\nu_y$ | 43.561 | 41.585 | 46.570 | 43.570 | |
| Momentum compaction | $\alpha_p$ | 3.3 | 3.4 | 3.20 | 4.55 | $10^{-4}$ |
| Energy spread | $\sigma_\varepsilon$ | 7.3 | 6.7 | 7.92(7.53) | 6.37(6.30) | $10^{-4}$ |
| Beam current | $I$ | 1.64 | 1.19 | 3.60 | 2.60 | A |
| Number of bunches | $n_b$ | 1584 | | 2500 | | |
| Particle/bunch | $N$ | 6.47 | 4.72 | 9.04 | 6.53 | $10^{10}$ |
| Energy loss | $U_0$ | 1.64 | 3.48 | 1.76 | 2.43 | MeV |
| Long. damping time | $\tau_z$ | 21.5 | 23.2 | 22.8 | 29.0 | msec |
| RF frequency | $f_{RF}$ | 508.9 | | 508.9 | | MHz |
| Total cavity voltage | $V_c$ | 8.0 | 13.0 | 9.4 | 15.0 | MV |
| Total beam power | $P_b$ | $\sim 3$ | $\sim 4$ | 8.3 | 7.5 | MW |
| Synchrotron tune | $\nu_s$ | -0.0246 | -0.0209 | -0.0245 | -0.0280 | |
| Bunch length | $\sigma_z$ | $\sim 7$ | $\sim 7$ | 6.0(4.7) | 5.0(4.9) | mm |
| beam-beam parameters | $\xi_x/\xi_y$ | 0.127/0.129 | 0.102/0.090 | 0.0028/0.088 | 0.0012/0.081 | |
| Luminosity | $L$ | $2.108 \times 10^{34}$ | | $8 \times 10^{35}$ | | $cm^{-2}s^{-1}$ |
| Integrated luminosity | $\int L$ | 1.041 | | 50 | | $ab^{-1}$ |

**Table 2.1:** Machine Parameters of KEKB and SuperKEKB. Values in parentheses for SuperKEKB denote parameters without intra-beam scattering. Note that the horizontal emittance increases by 30% owing to intra-beam scattering in the LER. The KEKB parameters are those achieved making use of the crab crossing, where the effective crossing angle was 0. (*) Before the crab crossing scheme, the luminosity of $1.76 \times 10^{34}$ $cm^{-2}s^{-1}$ was achieved at the half crossing angle of 11 mrad, where $\phi_{piw} \sim 1$.

mm and 300 $\mu m$ can be achieved in the horizontal and vertical planes at the IP, respectively. Taking into account the low emittances of 2∼5 nm (horizontal) and 9∼12 pm (vertical), flat beam bunches are formed with transverse beam sizes of $\sigma_x^*(\sigma_y^*) \approx 10\ \mu m\ (60\ nm)$ at IP.

### 2.2.2 Final focus superconducting magnet system

For this new collision scheme with extremely low $\beta_{x,y}^*$ at the IP, the optics of the interaction region has been changed with respect to KEKB. A new final focus system based on state-of-the-art superconductive magnet technology (QCS) is used to strongly squeeze the colliding beams in both horizontal and vertical planes at the IP. As shown in Figure 2.5 [42], the QCS consists of 8 main quadrupole magnets, 4 compensation solenoids, 35 corrector coils and 8 coils to cancel the leakage magnetic fields of QC1L(R)P. The main quadrupole magnets (QC1s for vertical plane and QC2s for horizontal plane), form a quadrupole doublet for each beam. Dedicated solenoids compensate the solenoid field of the Belle II detector so that $\int B_z ds = 0$ on each side of the IP. Field profiles of $B_z$ along the beam lines are carefully optimized to not increase the vertical emittance. All of the QCS magnets are accommodated in cryostats on the left and right sides of the IP.

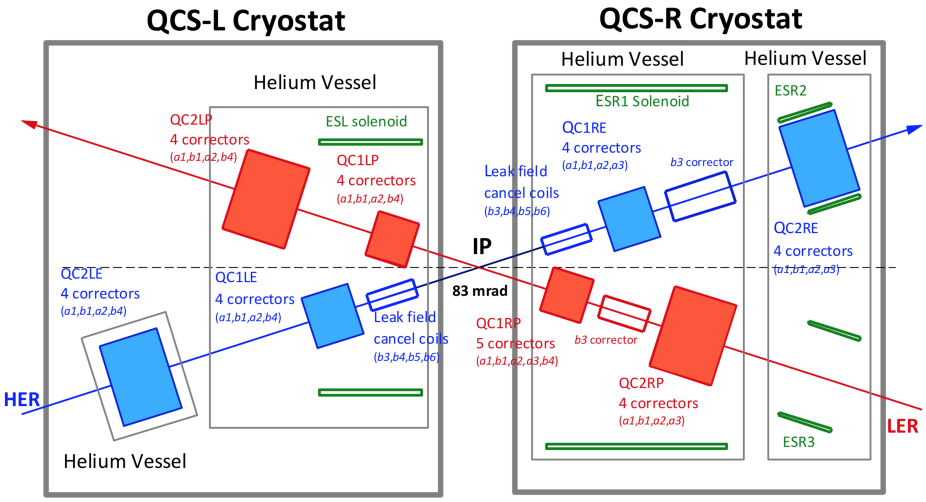


**Figure 2.5:** Schematic layout of the QCS system, which includes various corrector magnets, vertical and horizontal dipole (a1 and b1), skew quadruple (a2), skew and normal sextupole (a3 and b3), normal octupole, decapole and dodecapole (b4, b5 and b6) magnets [41].

### 2.2.3 Injection and damping ring

As a result of the very high beam currents (2.6 A for HER /3.6 A for LER) in SuperKEKB and the very small transverse emittances required by the "nano-beam scheme", the Touschek

lifetime in the LER becomes very short ($\approx$ 10 min). In order to maintain relatively stable beam currents for a stable collision luminosity, a bunch charge of about 4 nC needs to be continuously injected into both rings at a repetition frequency of 50 Hz. The injected beam parameters needed to meet the short beam lifetime and small dynamic apertures of both the HER and LER are summarized in Table 2.2. However, the generated positrons have a relatively large emittance and energy dispersion, much larger than the aperture of the LER. Therefore, a damping ring (DR) is needed to reduce the emittance before injecting the positron beam into the ring.

| Beam | Positron | Electron | |
|---|---|---|---|
| Beam energy | 4.0 | 7.007 | GeV |
| Normalized emittance $\gamma\varepsilon_x/\varepsilon_y$ | 100/15 | 40/20 | $\mu m$ |
| Energy spread | 0.16 | 0.07 | % |
| Bunch charge | 4 | 4 | nC |
| No. of bunches/pulse | 2 | 2 | |
| Repetition rate | 50 | | Hz |

**Table 2.2:** Beam parameters for the injection

As shown in Figure 2.6, the 600 m Linac is used simultaneously as injector to the Photon Factory (PF), the Photon Factory Advanced Ring (PF-AR) and the SuperKEKB rings, which involve also a positron damping ring. For the SuperKEKB rings, low-emittance, high-current electrons are generated by employing a photo-cathode RF gun, then the electron beams are accelerated to 7 GeV and ready for injection into the HER. High-current primary electrons for the positron production are generated with a thermionic gun, then the positrons are collected using a Flux Concentrator (FC), before getting damped to low emittance in the DR.

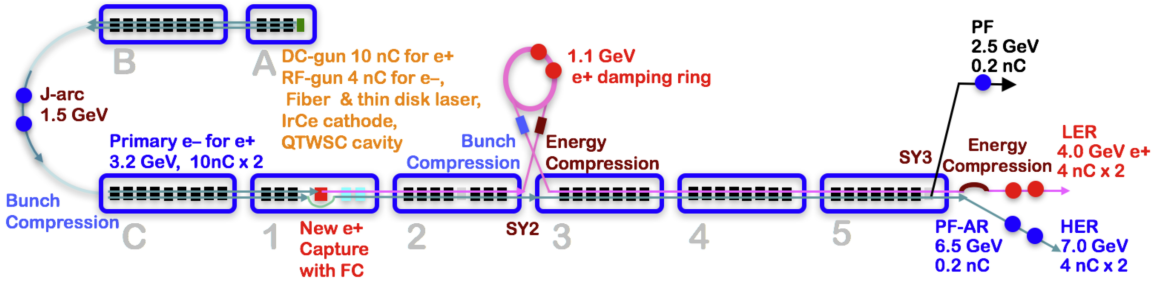


**Figure 2.6:** Overview of 600 m electron/positron injector Linac and damping ring [41].

The DR is a ring with circumference of about 135.5 m and a physical aperture of 34 mm. The positron beam with energy of 1.1 GeV is pulled out from the Linac and injected into the DR with emittance of 1400 nm through a transport line, the LTR (Linac to Ring), which

contains an Energy Compression System (ECS) to compress the energy spread from 1.67% to 0.5% to meet the requirement of the energy acceptance of the DR. A sufficiently short damping time, about 10 ms in the transverse plane, is achieved by using a "reverse-bend FODO" cell. After the damping, the physical transverse emittances at the exit of the DR are $\varepsilon_x = 41.4$ nm and $\varepsilon_y = 2.07$ nm and the energy spread is $5.5\times10^{-4}$. The damped positron beam exits the DR via the Ring To Linac (RTL) transfer line, coupled with the Bunch Compression System (BCS), which reduces the bunch length to 6.5 mm. After that, the 1.1 GeV positron beam are accelerated to 4 GeV and reach the LER injection point with horizontal emittance of 11.8 nm and vertical emittance of 0.86 nm.

### 2.2.4 The main rings and vacuum system

The main rings of SuperKEKB have a circumference of about 3016 meters. The two beams (electrons and positrons beams) are circulating in opposite directions with lifetimes of about a few minutes or hours in the different rings depending on different beam parameters and conditions. RF cavities are also employed to compensate the energy loss due to synchrotron radiation. In the upgrade of KEKB to SuperKEKB, the existing tunnel, infrastructure, and accelerator components for KEKB were reused wherever possible. In the SuperKEKB main rings, as shown in Figure 2.7, 93% of the beam pipes were renewed for the LER and 82% of the beam pipes are reused for the HER. To maintain the very small beam emittance and very low background noise in the Belle II detector, the vacuum system at SuperKEKB is expected to maintain an ultra-high vacuum ($\approx 10^{-7}$ Pa with beams) to reduce the interaction between beam particles with the residual gas molecules.

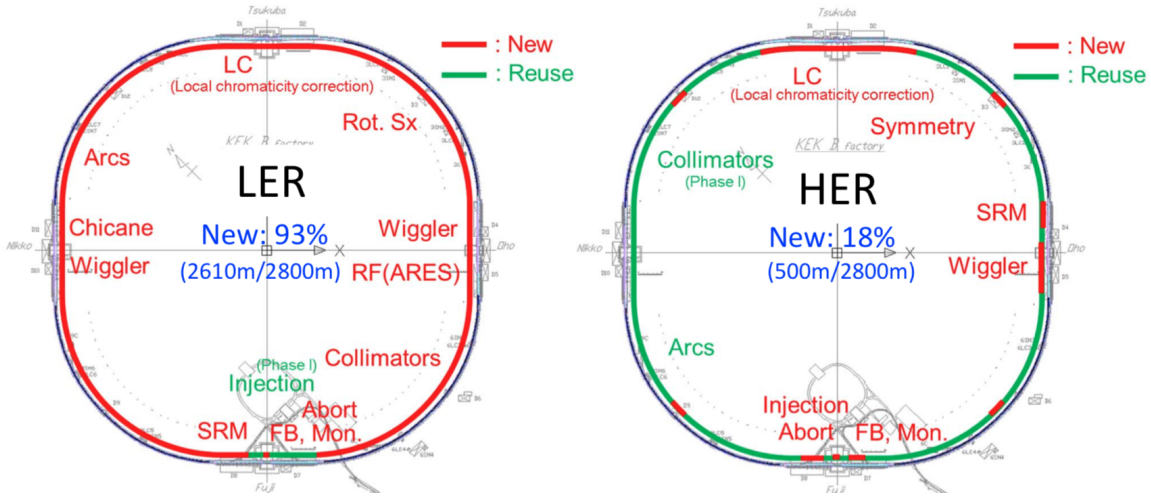


**Figure 2.7:** The main rings for LER and HER, about 93% of the beam pipes in length were renewed in the LER and about 18% in the HER [43].

In the LER, to mitigate the effects from the strong synchrotron radiation (SR) and induced electron clouds, due to the very high beam currents, and which may cause some instabilities for the beam, new beam pipes with antechambers (as shown in Figure 2.8) were installed. New flanges and bellows were also developed for those antechambers to mitigate impedance issues resulting from putting the Non Evaporable Getter (NEG) pumps, and SR masks in the antechambers; The energy of the electrons in the HER is decreased from 8 GeV in KEKB to 7 GeV in SuperKEKB, which reduces the synchrotron radiation power and makes the old copper beam pipes tolerable, allowing most of the old beam pipes from KEKB to be reused. In the wiggler section, which is used to make the damping time shorter, and where the SR power is stronger, the normal copper beam pipes were replaced by beam pipes with antechambers.

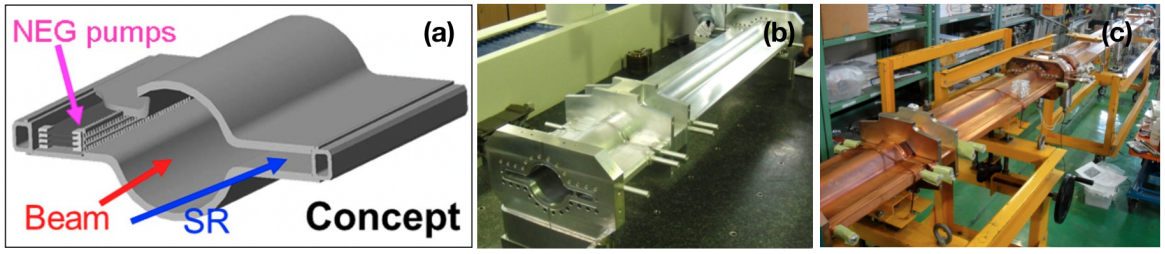


**Figure 2.8:** The concept of the antechamber on (a), prototype of aluminum-alloy beam pipe for the arc sections in LER (b), and copper antechamber beam pipes in HER (c).

### 2.2.5 SuperKEKB commissioning strategy

Upon approval of the upgrade from KEKB to SuperKEKB, a long period of construction started in 2010, lasting about 5.5 years. The communication between the accelerator and Belle II group led to the adoption of three phases for the commissioning [44, 45]. The phased commissioning was important to minimize the risk of Belle II detector radiation damage from insufficiently good conditions or accidents during the periods before establishing stable beam operation.

The overall schedule of the SuperKEKB/Belle II project is shown in Figure 2.9. The SuperKEKB beam commissioning started without Belle II detector and final-focus superconducting magnets (Phase-1) [46]. Phase-1 commissioning was single beam commissioning, with the purpose of conducting sufficient vacuum scrubbing, with a beam dose of up to several hundred A*hour, to sufficiently reduce the beam background, as well as other beam tuning such as beam injection and low emittance beam tuning needed before installing the QCS and Belle II detector [47, 48]. After the Phase-1 commissioning, Phase-2 commissioning was performed with the QCS and Belle II detector installed, except for the vertex

detector in the center. The beam collision tuning within the nano-beam collision scheme was performed with gradually squeezing of $\beta_y^*$. The Phase-3 commissioning was started after acceptable beam collision performance was achieved and sufficient understanding of the beam induced backgrounds in the Belle II detector was confirmed. The vertex chamber was installed and beam tuning is continuing aiming at the design luminosity, in parallel with physics data taking by the Belle II experiment, by both raising the beam currents and squeezing the vertical beam size at the IP.

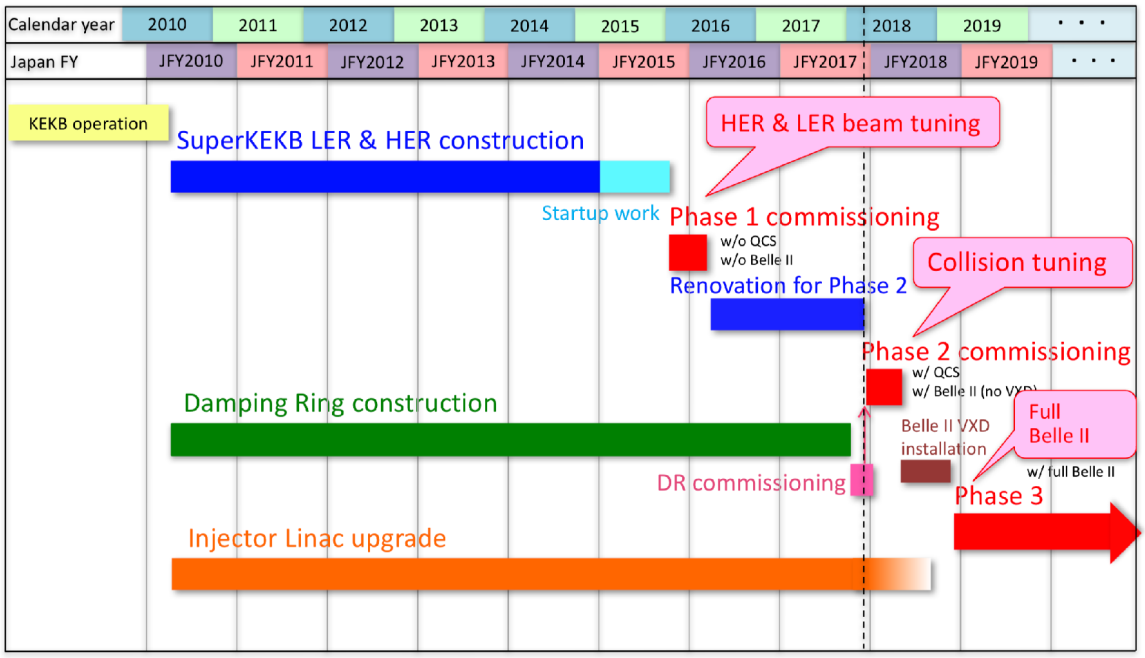


**Figure 2.9:** Overall schedule of the SuperKEKB/Belle II project [41].

### Phase-1 single beam commissioning

As already mentioned, SuperKEKB commissioning was started with Phase-1 commissioning which was single beam operation without insertion of superconducting final focus doublets and Belle II detector, and it was started on February 1st and finished at the end of June in 2016. Figure 2.10 shows the history of Phase-1 commissioning for SuperKEKB, the red, violet and cyan dots show the beam currents, averaged vacuum pressure and the beam lifetime, respectively [47]. During Phase-1 commissioning, the maximum beam currents reached were 1.01 A and 0.87 A for the LER and HER, respectively.

As some new beam pipes were installed both in the HER and LER, and to prepare the installation of the Belle II detector, vacuum scrubbing was essential. As shown in Figure 2.10, vacuum scrubbing proceeded smoothly. The averaged vacuum pressure was $4.7 \times 10^{-7}$

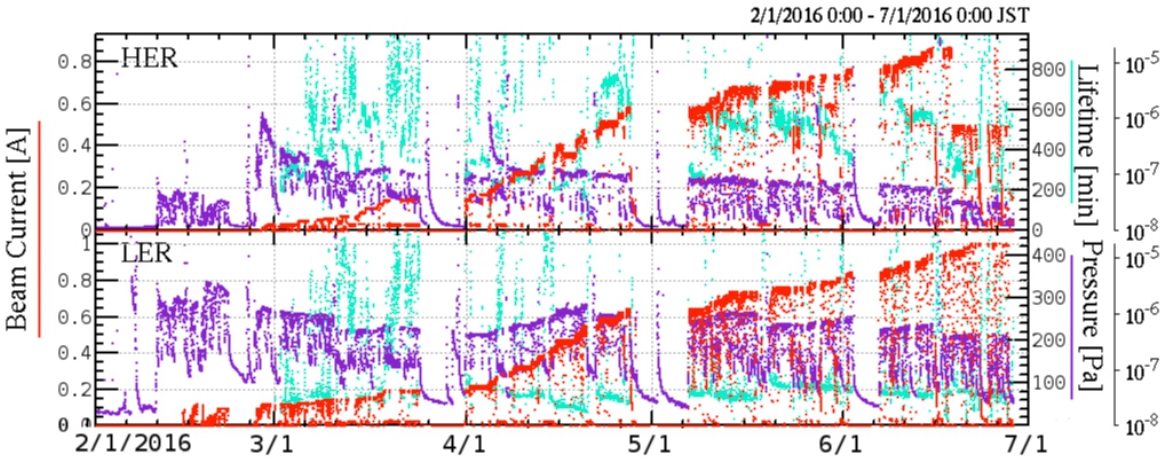


**Figure 2.10:** History of SuperKEKB commissioning in Phase-1 in 2016: beam currents in red, averaged vacuum pressure in violet and beam lifetime in cyan [47].

Pa with beam currents of 1.01 A for the LER and $5.7 \times 10^{-8}$ Pa with beam current of 0.87 A for the HER at the end of Phase-1 commissioning. The lifetimes of the stored beams were 60 min and 200 min for the LER and HER at that time. The main processes which determine the lifetime are the Touschek scattering process and the beam gas scattering including Bremsstrahlung and Coulomb scattering.

In the LER, a non-linear vacuum pressure rise against the beam current was observed. Aluminum bellows were expected of inducing this phenomenon, by multi-pactoring of the electrons. To overcome this effect, solenoid magnets were installed and the nonlinear vacuum pressure rise was much reduced for the filling pattern used for vacuum scrubbing with beam currents up to 1 A [49].

From the experience of KEKB operation, vertical beam size blow-up was expected in the LER due to the single-beam head-tail instability caused by the electron cloud effect [50, 51], and different countermeasures had to be taken as mitigation. During Phase-1 commissioning, the LER beam size blow-up was also observed when the beam current reached 500 mA and got worse with higher beam current [52]. Permanent magnets were installed to suppress the beam size blow-up, and this was shown to work well for a beam current up to 800 mA [53].

### Phase-2 beam collision commissioning

The Phase-2 commissioning started in March 2018 and continued for about 4 months. During Phase-2 commissioning, the superconducting final focus magnets and the main part of the Belle II detector were installed without the vertex detector [54]. This is because the vertex detector is very sensitive to the beam backgrounds, and it should be installed after sufficient beam collision tuning with the final focus magnets, and understanding of the beam

background rates, to make sure it can safely be installed. First beam collisions with actual first physics events were observed by the Belle II detector on the 26th of April 2018. The highest luminosity achieved was about $5.55 \times 10^{33}\ cm^{-2}s^{-1}$ during Phase-2 commissioning. The main experimental content of this thesis is from the Phase-2 commissioning, see Section 5.1.

**Phase-3 beam collision commissioning towards nominal luminosity**

The Phase-3 commissioning started with the full Belle II detector from March of 2019 and SuperKEKB is thereafter expected to continuously operate for about ten years with gradually squeezing of $\beta_y^*$ and increasing of beam currents toward the nominal luminosity: $8 \times 10^{35}\ cm^{-2}s^{-1}$ in parallel with the physics data taking by the Belle II experiment.

## 2.3 Belle II detector

Due to the much higher luminosity provided by the SuperKEKB collider, much higher collision rates are expected. And the higher beam currents and smaller beam sizes at SuperKEKB will also increase the beam induced backgrounds level (about 10∼20 times higher than KEKB). The Belle II detector (Figure 2.11) is being upgraded from the Belle detector, including a new Data Acquisition System redesigned with a network of optical fibers, faster trigger electronics, a new pixel detector providing better resolution for particle tracking and a new silicon vertex detector to cover a larger solid angle, an extended central tracking chamber, a time-of-propagation chamber and an aerogel ring-imaging Cherenkov detectors, more details can be found in [17].

The Belle II detector consists of 8 sub-detectors, the radii of which (measured from the beam line axis) are shown in Table 2.3 together with their angular acceptances. This section briefly describes each sub-detectors, starting with the innermost one:

**The Silicon Vertex detector** of Belle II consists of: pixel layers and double-sided strip layers:

The PiXel Detector (PXD) is wrapped around the beam pipe, it consists of two layers of pixels based on the DEPFET technology (DEPleted p-channel Field Effect Transistor). The inner cylinder has a radius of 1.4 cm and has eight segments, while the outer cylinder has a radius of 2.2 cm and has twelve segments.

The double-sided strip layers is mounted around the PXD. It consists of four layers containing strips of double sided silicon detectors (DSSD). The Lorentz boost of Belle II is smaller compared to Belle, which leads to less separation between the B decay vertices,

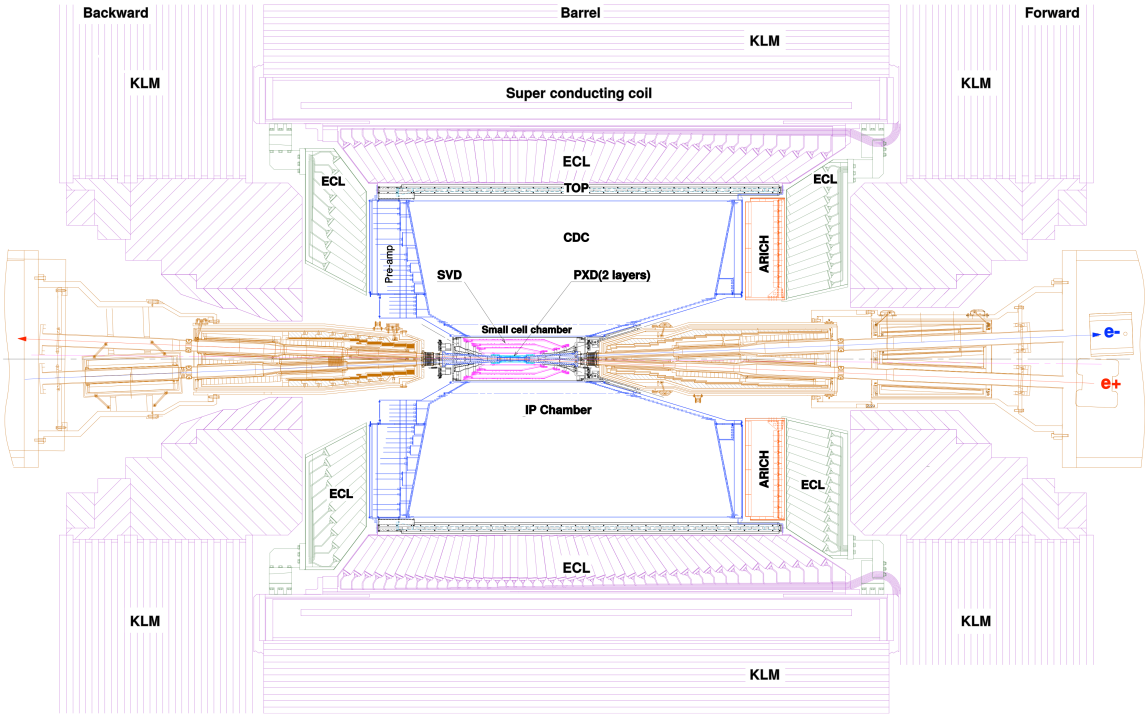


**Figure 2.11:** Cross section of the Belle II detector. The forward direction is on the right, and is the direction the electron beam travels. The whole detector is 5 m high, and symmetric in $\phi$ [17].

however, the beam pipe is smaller, which more than compensates and allows the Belle II SVD to have better performance compared to that of Belle.

**The Central Drift Chamber (CDC)** is the main device for charged particle tracking. It provides tracks and momentum measurements of charged particles, particle identification through energy loss within the gas volume, and efficient and reliable triggering for charged particles. Its smaller cell sizes compare to that of Belle gives it a better energy resolution.

**The Time of Propagation (TOP) sub-detector** is used for the particle identification in the barrel region of Belle II, especially to distinguish between kaons and pions. It consists of 16 modules which run parallel to the axis of Belle II. The TOP detectors measure the Cherenkov photons generated from charged tracks.

**The Aerogel Ring Imaging Cherenkov (ARICH) Detector** is used for the particle identification in the forward end-cap. It is located between the CDC and ECL end-cap.

**The Electromagnetic Calorimeter (ECL)** has several functions: high efficiency photon detection, precise photon energy and angular spectrum measurements, identification of electrons, trigger signaling, luminosity measurements. It consists of 8736 CsI(TI) crystals with typical dimension of $6 \times 6 \times 30\ cm^3$. It provides the absolute luminosity based on counting the coincident records in the front and back caps after some proper calibration.

| Sub-detector | Inner Radius (mm) | Outer Radius (mm) | $\theta_{min}$ (deg) | $\theta_{max}$ (deg) |
|---|---|---|---|---|
| PXD | 14 | 22 | 17 | 150 |
| SVD | 38 | 140 | 17 | 150 |
| CDC | 160 | 1130 | 17 | 150 |
| TOP | 1190 | 1243 | 32 | 128 |
| ARICH | 420 | 1140 | 13 | 34 |
| Forward ECL | 1378 | 420 | 12.3 | 32 |
| Barrel ECL | 1244 | 1617 | 32 | 130 |
| Backward ECL | 417 | 1392 | 130 | 155.1 |
| BKLM | 1952 | 2475 | 45 | 125 |
| EKLM | 1248 | 2475 | 20 | 145 |

**Table 2.3:** Belle II sub-detectors' inner and outer radii, measured from the forward direction. The detectors are approximately symmetric in $\phi$.

**The $K_L$-Muon detector (KLM)** detects the $K_L$ and muons. It is made of three components: two end-caps (EKLM) and a barrel (BKLM). It consists of thin planar detectors interleaved with the iron plates of the 1.5 T solenoid flux return yoke.

## 2.4 BEAST II

BEAST II (Beam Exorcism for A STable experiment project II) has the function of estimating and measuring the backgrounds generated in the Belle II detector by the circulating beams. In the presence of very high beam currents (twice those of KEKB) and much smaller beam sizes, and therefore very high luminosity (40 times higher than KEKB), the background levels are expected to increase a lot at the IP and thus in the Belle II detector. Such backgrounds may lead to some serious radiation damage for some sub-detectors of Belle II, which can affect their long term performance, and moreover lead to excessive occupancy potentially compromising their reconstruction and identification tasks.

BEAST II was started at the beginning of the Phase-1 commissioning of SuperKEKB, and continued during the Phase-2, aiming at validating the Monte Carlo simulation of the backgrounds by comparing with detailed measurements. It also provides important information on beam loss to SuperKEKB accelerator scientists, which was used during tuning. More details can be found in [55].

# Chapter 3

# Fast luminosity monitoring based on diamond detector

## 3.1 Motivations and specifications

As already explained in Chapter 2, to achieve the very high luminosity up to $8 \times 10^{35}\ cm^{-2}s^{-1}$ (40 times higher that of KEKB), SuperKEKB adopted the "nano-beam scheme" to collide the highly focused ultra-low emittance beam bunches every 4 ns. A particle collider with such small beam sizes at the IP requires excellent control over the two colliding beams to ensure an optimum geometrical overlap between them and thereby maximize the luminosity. In the presence of mechanical vibrations caused by the ground motion, the induced offset between the two beams at the IP can be large compared to the beam size, thereby significantly degrading the luminosity. Even for offsets smaller than the beam size, the luminosity degradation can become large due to additional sensitivity through the hourglass and beam-beam blow-up effects [56]. Figure 3.1 shows simulated results of luminosity changes with respect to the horizontal beam-beam offset based on the nominal beam parameters of SuperKEKB [57]. To maintain a very high luminosity in the presence of the ground motion, beam orbit feedback systems are needed. At SuperKEKB, due to the large crossing angle at the IP in the horizontal plane resulting in weak beam-beam deflection in that plane (details will be described in Section 3.1.1), a dithering orbit feedback system was adopted which uses the precise fast luminosity signal as input.

In addition, as the first collider with such tiny beam sizes at the IP, it is foreseeable that the machine tuning of SuperKEKB towards the nominal beam parameters will be a long and rather difficult process, which will put specific requirements on the luminosity measurements. One first example is the measurement of the vertical beam size at the IP during $\beta_y^*$ squeezing,

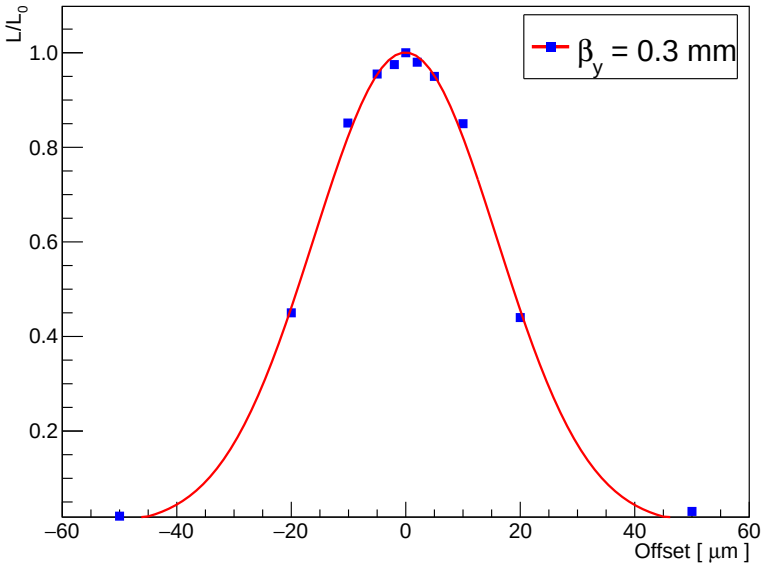


**Figure 3.1:** Simulated luminosity degradation with respect to the horizontal beam offset based on SuperKEKB nominal beam parameters.

which can be obtained based on recording the luminosity changes during a vertical beam-beam offset scan. To avoid beam blow-up from the beam-beam interaction, which could confuse the result of the $\beta_y^*$ squeezing, it must be done at very low bunch current ($\sim$0.1 mA/bunch in the SuperKEKB case), and that places specific requirements on the sensitivity of the luminosity monitoring. A second example is the possible interactions between bunches along the train, which can induce variations in their beam sizes and relative alignment. Such effects can be studied using bunch-by-bunch luminosity signals in association with relevant machine parameters (e.g. beam bunch currents). For this reason, it is essential to have a system which can also provide the bunch-by-bunch luminosity information with sufficient relative precision.

### 3.1.1 Orbit feedback methods and techniques

There are two methods for the IP orbit feedback system at SuperKEKB. One is beam-beam deflection driven method, based on the measurement of the beam orbit with Beam Position Monitors (BPM) upstream and downstream of the IP, to reconstruct the angular deflection as expressed to first order in Equation 3.1, where $\Delta x^{'}$ and $\Delta y^{'}$ are the deflection angles, $\Delta x$ and $\Delta y$ are the offsets between the beams, $\beta_{x,y}^*$ and $\xi_{x,y}$ are the beta functions and beam-beam parameters, and $\sigma_{x,y}^*$ are the effective horizontal ($\sigma_x^* = \sigma_z sin\phi_c$) and vertical beam sizes at the IP, respectively. With this method, we can know in which direction and how much we should change the orbits when an offset between the beams is detected, if the accuracy of the orbit

measurement (BPM) is precise enough, the optimum collision condition can be maintained with almost no luminosity loss. Using Equation 3.1, the beam-beam angular deflection in the horizontal and vertical planes can be estimated. Table 3.1 shows the beam-beam deflection resulting from offsets of 10% of the beam size in the corresponding direction. Taking into account the distance from the IP to the IP BPM of about 0.5 m, the offsets to be measured in the horizontal and vertical planes are about 0.14 $\mu m$ and 2.5 $\mu m$, respectively. For the vertical orbit feedback system, this method was adopted, since the offset is sizable, the requirement on BPM resolutions being about 1 $\mu m$ at repetition frequency of 1 kHz, see [58]. However, due to the large crossing angle between the two colliding beams, the beam-beam deflection in the horizontal plane is too weak and the limited resolution of the BPM makes it too hard to measure such a small beam deflection, thus the method based on deflection of beams cannot be used for horizontal beam orbit feedback. Some other techniques need to be developed for the beam orbit feedback in the horizontal plane.

$$\begin{aligned} \Delta x^{'} &= \frac{dx}{ds} = -\frac{2\pi}{\beta_x^*}\xi_x \Delta x = -\frac{Nr_e}{\gamma\sigma_x^*(\sigma_x^* + \sigma_y)}\Delta x \\ \Delta y^{'} &= \frac{dy}{ds} = -\frac{2\pi}{\beta_y^*}\xi_y \Delta y = -\frac{Nr_e}{\gamma\sigma_y(\sigma_x^* + \sigma_y)}\Delta y \end{aligned} \tag{3.1}$$

| | $I_{beam}$ [A] | $\beta_x^*$ [mm] | $\beta_y^*$ [mm] | $\xi_x^*$ | $\xi_y^*$ | $\Delta x^{'}$ [$\mu rad$] | $\Delta y^{'}$ [$\mu rad$] |
|---|---|---|---|---|---|---|---|
| LER | 3.6 | 32 | 0.27 | 0.0028 | 0.088 | 0.56 | 9.83 |
| HER | 2.6 | 25 | 0.30 | 0.0012 | 0.081 | 0.31 | 10.01 |

**Table 3.1:** The beam-beam deflection calculation with $\Delta x = 0.1\sigma_x$ and $\Delta y = 0.1\sigma_y$ in the horizontal and vertical planes for the nominal case at SuperKEKB. The deflection angles above are the full difference corresponding to the positive and negative deflections.

Another method is the luminosity driven system which is based on the measurement of the luminosity, which is a straightforward method in the sense that the luminosity is the ultimate goal of the B-meson factory. Several years of operational experience with this kind of method at PEP-II have proven that the luminosity driven feedback system works excellently at a double ring collider [22, 23, 26]. At SuperKEKB, this method is used for the horizontal beam orbit feedback, more details will be described in section 3.2.

## 3.2 Dithering orbit feedback system

Based on the measurement of the luminosity, we can know how much the offset between the two beams is, but we cannot easily know its sign, because the luminosity is a symmetrical

function of the offset. This makes it difficult to know how to correct the beam orbit to recover the luminosity. In addition, many other effects may also cause luminosity changes at relatively low frequency, such as beam size and beam intensity changes. In order to solve this problem, the beam orbit needs to be changed continuously in some manner so as to know the offset sign. For this reason, the dithering orbit feedback method used for beam orbit stabilization in the horizontal plane at PEP-II was adopted at SuperKEKB. The algorithm and the characteristics of the dithering orbit feedback system are described in detail below.

### 3.2.1 Algorithm for dithering orbit feedback

The principle of the dithering orbit feedback is that one beam is dithered sinusoidally in the horizontal plane with an amplitude of $\tilde{x}$ around an initial horizontal offset $x_0$ between the two beams, such that the luminosity varies according to

$$L(x) = L_0 exp\left(-\frac{x^2}{2\Sigma_x^2}\right) \tag{3.2}$$

where

$$x = x_0 + \tilde{x}\sin(2\pi ft), \;\; \Sigma_x^2 = \sigma_{x^+}^{*2} + \sigma_{x^-}^{*2} \tag{3.3}$$

Here, the parameters $f$ and $\sigma_{x^\pm}^*$ represent the dithering frequency and the effective horizontal beam sizes in the LER and HER at the IP, respectively. The effective horizontal beam size is expressed as $\sigma_{z^\pm}^* sin\theta_x$, as explained in 2.2.1. $\sigma_{z^\pm}^*$ is the bunch length and $\theta_x$ the half crossing angle of the two beams at the IP.

Then if we introduce Equation 3.3 into Equation 3.2 and expand it for the case of a dithering amplitude that is small compared to $\Sigma_x$ and an offset $x_0$ that is smaller or comparable to $\Sigma_x$, we obtain

$$L(x) = L_0\left(1 - \frac{x_0\tilde{x}}{\Sigma_x^2} sin(2\pi ft) - \frac{\tilde{x}^2}{2\Sigma_x^2} sin^2(2\pi ft)\right) exp\left(-\frac{x_0^2}{2\Sigma_x^2}\right) \tag{3.4}$$

When one of the beams is dithered around the zero-offset point, where the luminosity reaches the maximum, the luminosity drops on either side of the maximum, and leads to a modulation of the luminosity at the frequency of $2f$. When there is an offset $x_0$ between the two beams that is larger than the dithering amplitude, this modulation of the luminosity is instead at the base frequency $f$, as shown in Figure 3.2.

To maintain the luminosity at the peak over time, the magnitude of the fundamental dithering frequency $f$ should be minimized and that at the double dithering frequency $2f$ should be maximized in the frequency domain of the fast luminosity signals. Figure 3.3 shows the normalized luminosity signals at 1 kHz both in time and frequency domains for

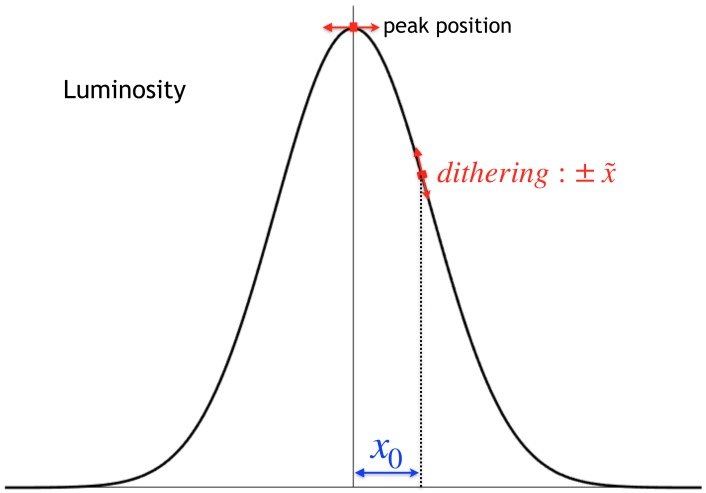


**Figure 3.2:** Luminosity dependence on the offset between the two beams at the IP: when sinusoidally dithering one of the beams with an amplitude $\tilde{x}$, the luminosity oscillates on both sides of the maximum when the offset is zero, and on one side only when the offset $x_0$ is larger than the dithering amplitude $\tilde{x}$.

zero-offset ((a) and (b)) and non-zero offset ($x_0 > \tilde{x}$) ((c) and (d)) cases when one of the beams is dithered with a dithering amplitude of $\tilde{x}$ at a frequency of 79 Hz. When the two beams are perfectly aligned and one of them is dithered around the peak luminosity position: only the double frequency $2f$ is observed in the frequency domain of the fast luminosity signals, and when there is an offset ($x_0 > \tilde{x}$) between the two colliding beams, mainly the fundamental frequency can be observed.

The peak at the fundamental frequency appears much more clearly as soon as there is an offset between the two colliding beams than the one at twice the fundamental frequency when the offset is minimized, as shown in Figure 3.4. For this reason, minimizing the magnitude of the peak at the fundamental frequency is the best choice to maximize the luminosity. The magnitude of the peak at the fundamental frequency is almost proportional to the offset between the two beams (when it is not exceeding the beam size), and reaches a minimum when beams overlap perfectly. The control algorithm can therefore use the Newton method that searches for a zero to calculate the needed corrections every second, based on the derivatives of the Fourier component at the fundamental dithering frequency with respect to the successive corrective moves. The sign ambiguity resulting from the evenness of the luminosity dependence with offset in Equation 3.2 is resolved by comparing the phase of the magnet current modulation used to dither the beam orbit with that of the resulting luminosity modulation [59]. Finally, twelve steering magnets dedicated to the IP orbit feedback are used to create a local bump at the IP in the orbit of the other beam, to compensate at least partially the offset between the two beams and recover the luminosity.

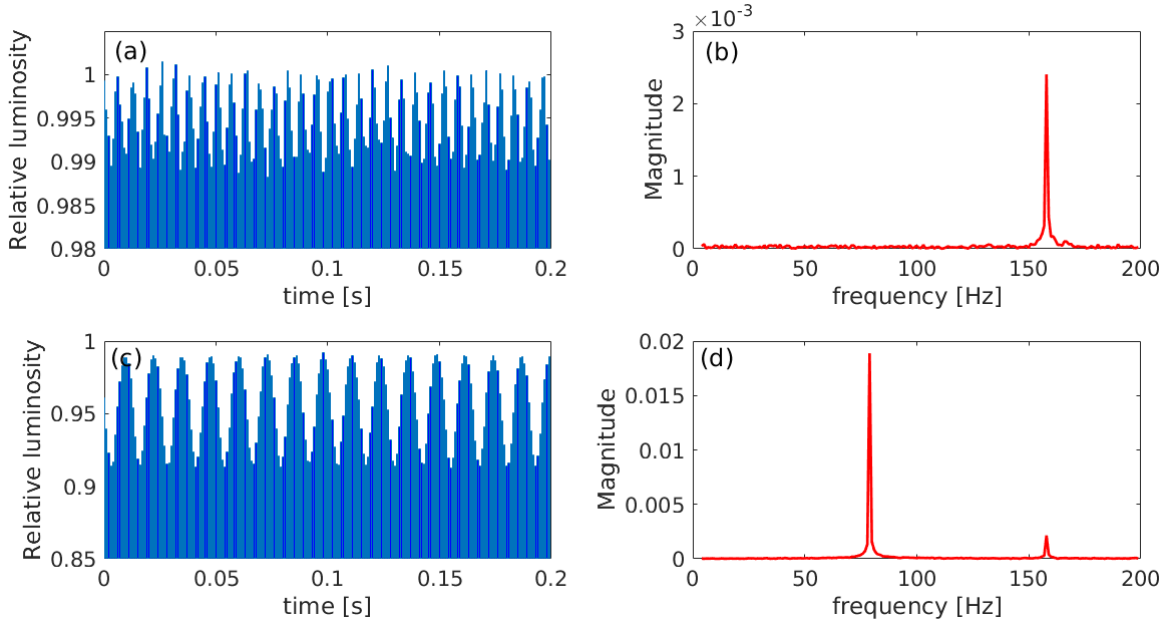


**Figure 3.3:** Normalized luminosity signals at 1 kHz when one beam is dithered with $0.1\sigma_x$ at 79 Hz both in time and frequency domains. (a) and (b) correspond to the zero-offset case ($x_0 = 0$), for which the luminosity is maximized, and the peak at twice the dithering frequency is observed; (c) and (d) correspond to the non-zero offset case ($x_0 > \tilde{x}$), for which the peak at the fundamental frequency dominates.

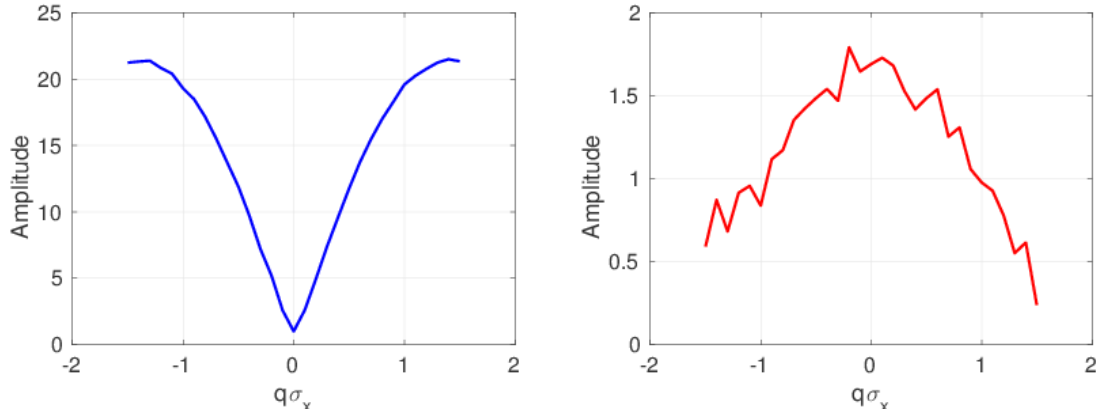


**Figure 3.4:** Magnitude of peaks at the fundamental (left) and twice the fundamental (right) frequency as a function of the offset between the two beams in the case of a dithering amplitude of 0.1 $\sigma_x$ and a relative precision of the fast luminosity signals of 1% per ms.

### 3.2.2 Dithering orbit feedback system at SuperKEKB

As already mentioned, dithering orbit feedback using a fast luminosity signal as input was adopted for the SuperKEKB IP orbit stabilization in the horizontal plane. Figure 3.5 shows a

conceptual diagram of the system implemented for SuperKEKB. It mainly consists of twelve dithering coils installed in the LER, two fast luminosity monitors (LumiBelle2 and ZDLM), a lock-in amplifier with two input channels, a Programmable Logic Controller (PLC) feedback process control system and twelve steering magnets installed in the HER for beam orbit correction.

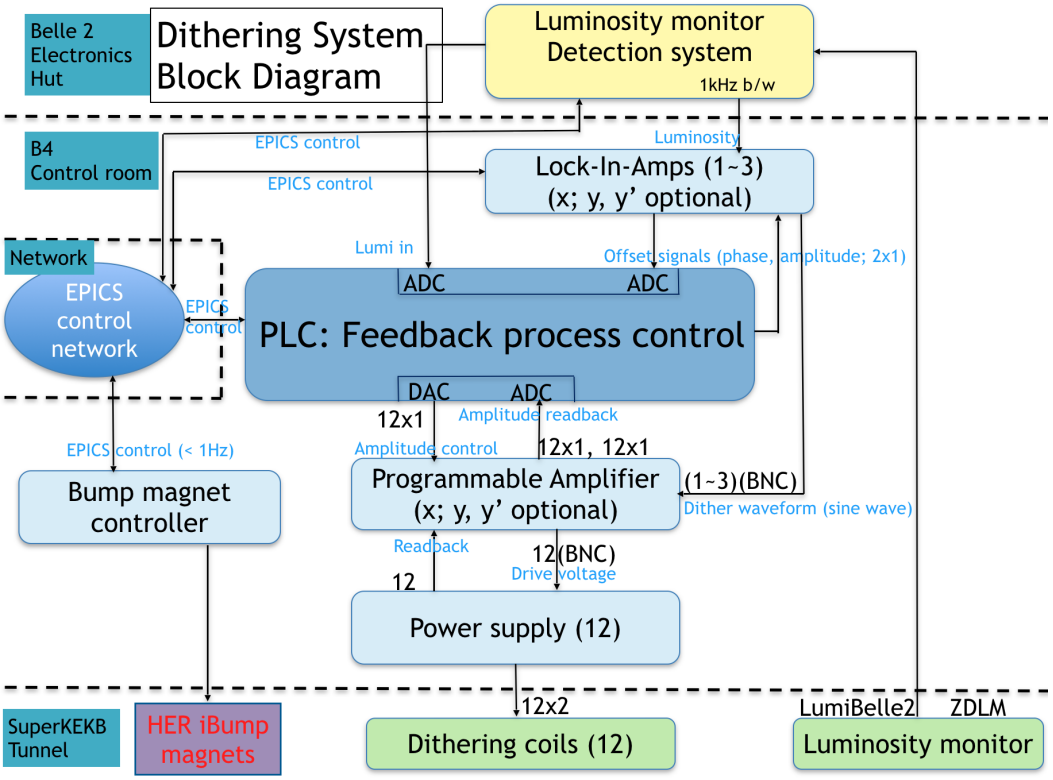


**Figure 3.5:** Block diagram of dithering orbit feedback system at SuperKEKB.

The twelve dithering coils are air-core magnet coils used to wiggle the LER beams horizontally at the collision point by a small distance sinusoidally at a frequency of 79 Hz, see Figure 3.6. They are mounted around the vacuum chamber (symmetric coils on the normal cylindrical beam pipe and asymmetric coils on antechamber beam pipe ) near the IP and will be able to vary the beam coordinates at the IP independently in position and angle in both directions while keeping the orbit change localized and correcting for the induced coupling effects. The dithering coils are for this reason divided into two parts: one dithers the LER beam at 79 Hz in the horizontal plane and the other gives a vertical kick to correct the x-y coupling caused by the misalignment of the horizontal dithering [24, 60].

Fast enough luminosity measurements are needed as input to the dithering orbit feedback system for luminosity optimization in the presence of mechanical vibrations caused by the ground motion, beam orbit slow drifts or other effects. Two different but complementary

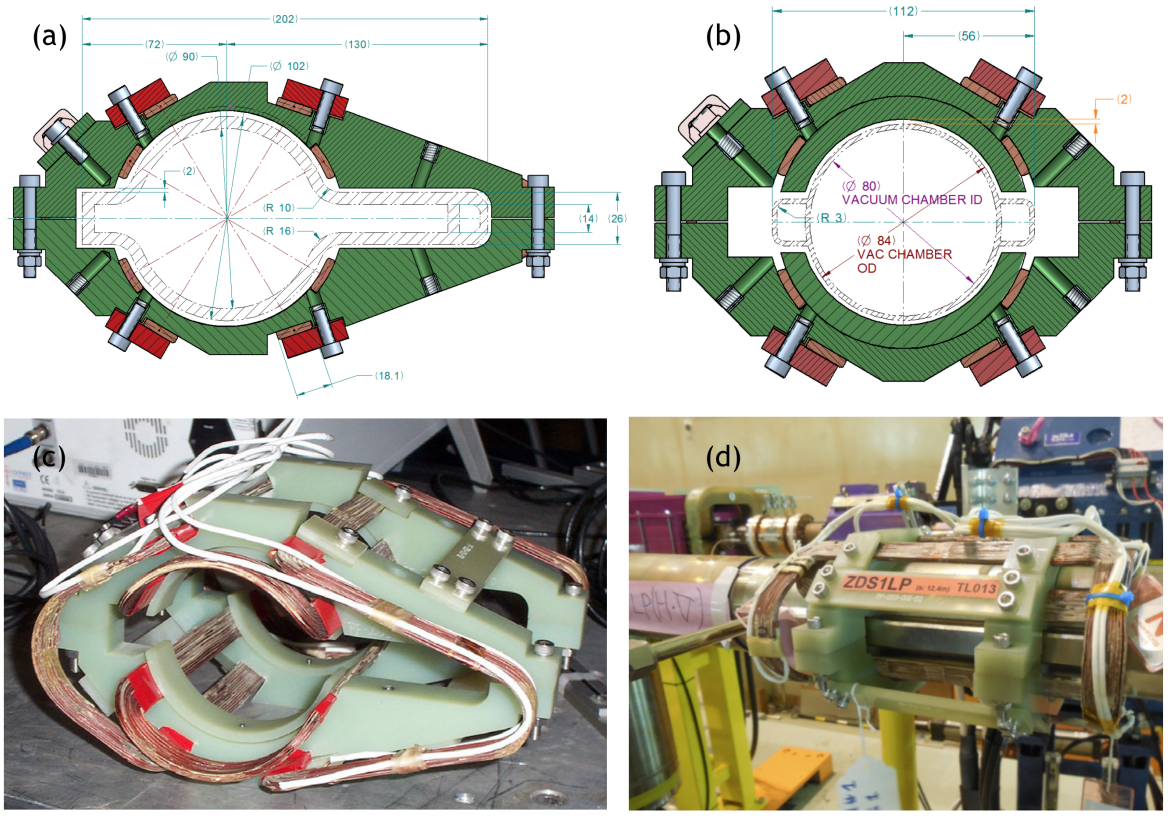


**Figure 3.6:** Example of dithering coils: (a) schematic of asymmetric dithering coil; (b) schematic of normal symmetric dithering coil; (c) asymmetric dithering coil for antechamber beam pipe (d) normal symmetric dithering coil installed in LER.

techniques were developed: one is called LumiBelle2 from LAL, based on sCVD diamond detectors and another is the ZDLM from KEK, based on Chenrenkov and Scintillator detectors, see Figure 3.7 [61, 62]. Both LumiBelle2 and ZDLM are placed at the same positions just outside of the beam pipe in both the HER and LER rings, and they are measuring the scattered Bhabha events at vanishing scattering angles to provide fast luminosity signals. A relative precision of $10^{-2}$ in 1 ms when integrating all 2500 bunches, over a luminosity range from $10^{34}\ cm^{-2}s^{-1}$ to $8 \times 10^{35}\ cm^{-2}s^{-1}$, with less than 1% contamination from non-luminosity scaling effects, was specified [59]. Meanwhile, relative luminosity signals for each single bunch crossing are also very important: when 2500 bunches circulate in each ring, variations in the bunch transverse positions and beam sizes are in principle possible, through a variety of effects, and should be monitored, just like the beam bunch currents.

An analog lock-in amplifier (bought from AMETEK Advanced Measurement Technology) is used to provide a dithering sine wave reference to the dither coil magnet power supply control system and extract the Fourier components of the luminosity signals at the dithering frequency and twice of its value [60]. By inputting the fast luminosity signals

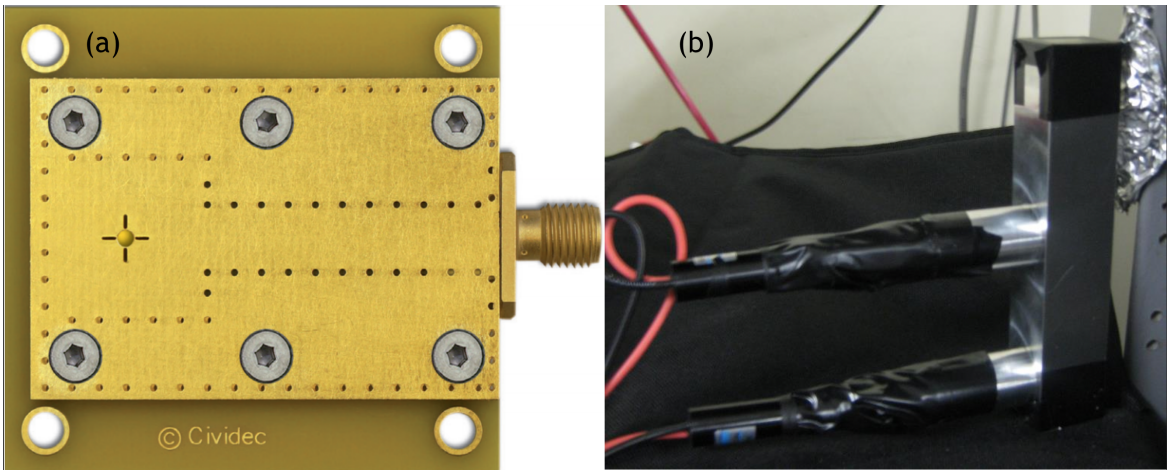


**Figure 3.7:** sCVD diamond detector (a) for LumiBelle2 and Scintillator and Cherenkov detectors (b) for ZDLM.

provided by LumiBelle2/ZDLM, it can output the magnitude of the fast luminosity signals at the fundamental dithering frequency in the frequency domain, as well as the phase which contains the information on the sign of the beam offset with respect to the optimum alignment. This phase is obtained by mixing the induced fast luminosity signal wave with the generated input dithering reference sine wave.

In addition, a beam orbit feedback process control system through a PLC was also developed. Once the offset between the two colliding beams is detected, based on the information provided by the lock-in amplifier (magnitude and phase), the corresponding needed corrective moves will be determined, and finally the twelve steering magnets installed in the HER are sent an instruction to make the required localized move at the IP to compensate for the offset between the two colliding beams and recover the optimum overlap between the two colliding beams, thereby maintaining an optimum luminosity.

## 3.3 Luminosity monitoring with diamond detector

LumiBelle2, one of the luminosity monitoring system, was developed based on a sCVD (single-crystal Chemical Vapor Deposition) diamond detector. It aims to provide the train integrated luminosity signals at 1 kHz with relative precision of $\sim 1\%$, used as input to the dithering orbit feedback system to stabilize the horizontal beam orbit in the presence of the mechanical vibrations caused by ground motion and beam orbit slow drifts, the train integrated luminosity signals at 1 Hz which will be sent to the SuperKEKB control room via the EPICS network as basic luminosity observable for the machine collision tuning, and the bunch integrated luminosity signals at 1 Hz with relative precision of $\sim 1\%$ for each bunch,

to study possible imperfect bunch alignment and effects from interactions between bunches along the bunch train [62–64].

The sCVD diamond detector, as a wide band gap semiconductor, with well known characteristics such as good radiation resistance, low dark current, fast response time and high carrier mobility, has drawn much attention recently in the field of ionization radiation detection for UV, gamma rays, electrons, neutrons, protons and heavy ions [65–70]. In our project, the diamond detectors are installed just outside of the beam pipe downstream of the IP in both rings, at locations which where have been carefully studied for fast luminosity monitoring with enough rates from the radiative Bhabha scattering events at vanishing scattering angles [64]. This process has a large cross-section (about 150 mbarn), which allows a high relative precision for measuring fast luminosity signals. As mentioned in Section 3.2.2, the relative precision mainly comes from the statistical fluctuation of detected Bhabha events, which are distributed according to a Poisson distribution:

$$\begin{aligned} N &= L \times \sigma \times \tau \times f \\ \nu &= \frac{1}{\sqrt{N}} \end{aligned} \tag{3.5}$$

where N is the number of detected Bhabha particles in the time duration of $\tau$, $\sigma$ is Bhabha scattering cross-section, $f$ is the detection efficiency, and $\nu$ is the relative precision.

The precision is required to be better than 1% in 1 ms when the luminosity is higher than $10^{34}\ cm^{-2}s^{-1}$ and up to the nominal luminosity of $8 \times 10^{35}\ cm^{-2}s^{-1}$. The required minimum detection efficiency for such a high precision to be achieved at the luminosity of $10^{34}\ cm^{-2}s^{-1}$ is $6 \times 10^{-3}$, see Table 3.2. For the final nominal luminosity of $8 \times 10^{35}\ cm^{-2}s^{-1}$, the relative precision should be improved by a factor of about 9 since the luminosity will be increased by a factor of 80, in case the same set-up is used. On the other hand, the position of the diamond detector to be installed relative to the beam pipe could be changed to reduce the Bhabha event detection efficiency and maintain the relative precision near 1% for the 1 kHz train integrated luminosity signals. Moreover, the same 1% relative precision can be achieved at 1 Hz for the train integrated luminosity signal with a luminosity about three orders of magnitude lower. The relative precision for bunch integrated luminosity signals at 1 Hz will then also be about 1.6% for 2500 bunches per train. Detailed results based on simulation can be found in Section 4.1.

To cover such a large range of detection efficiencies for the train-integrated luminosity signal, and provide the bunch-by-bunch integrated luminosity signal, two different types of sCVD diamond detectors ( $4 \times 4\ mm^2$ with different thickness: 140 and 500 $\mu m$) coupled with two different amplifiers (fast charge amplifier: C6, and broadband current amplifier: C2),

| Luminosity $[cm^{-2}s^{-1}]$ | $N_{Bhabha}$ @ IP $[ms^{-1}]$ | $\tau$ [ms] | $\nu$ in 1 ms | $f$ |
|---|---|---|---|---|
| $10^{34}$ | $1.5 \times 10^{6}$ | | | $6 \times 10^{-3}$ |
| $10^{35}$ | $1.5 \times 10^{7}$ | 1 | $10^{-2}$ | $6 \times 10^{-4}$ |
| $8 \times 10^{35}$ | $1.2 \times 10^{8}$ | | | $8.33 \times 10^{-5}$ |

**Table 3.2:** Requirements for the Bhabha event detection efficiency to obtain a relative precision better than 1% in 1 ms for the luminosity range from $10^{34}$ $cm^{-2}s^{-1}$ up to the nominal value of $8 \times 10^{35}$ $cm^{-2}s^{-1}$.

all bought from CIVIDEC [71], were used as the front-ends of the LumiBelle2 luminosity monitoring system. In addition, a Tungsten radiator coupled with a custom made 45° window shape beam pipe with a depression of 15 mm was mounted in the LER to boost the yield of charged secondary particles in the shower generated by the Bhabha positrons, thereby increasing the detection efficiency of the diamond detector. This part will be described in detail in Section 4.1 in Chapter 4.

### 3.3.1 CVD diamond detector

Diamond crystallizes in a face centered cubic lattice structure formed by carbon atoms (as shown in Figure 3.8 left plot ) in a covalent network lattice ($sp^3$-bonds) [1] [72, 73]. The discovery of diamond synthesis by "Chemical Vapor Deposition" (CVD) technology (see Figure 3.8 right plot) in the early 1980s opened a large range of new applications for the diamond, and was commonly used to produce diamond material. In the CVD process, a

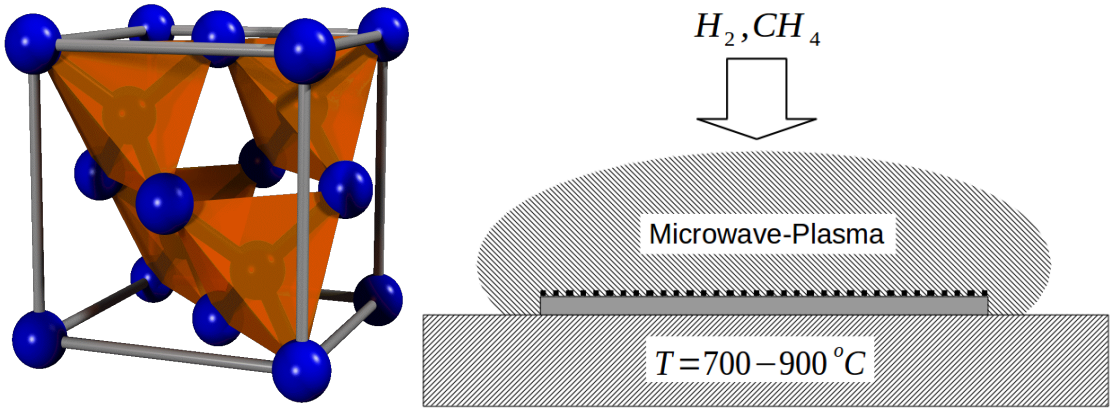


**Figure 3.8:** Face-centered cubic lattice structure of diamond (left) and CVD diamond growth scheme (right).

[1] A mixed hybridization state formed by one s-orbital and three p-orbital, namely $p_x$, $p_y$ and $p_z$. Diamond consists purely of $sp^3$ hybridized bonds.

mixture of hydrogen and methane gas is breathed into the microwave plasma, then ionized so that the carbon based radicals settle down on a substrate, commonly silicon or molybdenum. Typical deposition conditions are: 1% methane in hydrogen as source gas with deposition temperature of 700-1000 $^{\circ}C$ under gas pressures of 30-300 Torr [74].

CVD diamond has a number of properties that make it an attractive material for high-energy physics detector applications, as shown in Table 3.3, comparing with Silicon, another popular material. Its large band gap (5.5 eV) and large displacement energy (42 eV/atom) make it a kind of material that should be inherently radiation tolerant with very low leakage currents. Its small dielectric constant $\varepsilon_r$ (5.7) results in low detector capacitance and thereby, low-noise performance of the associated front-end electronics. Its large thermal conductivity, about 4-5 times that of copper at room temperature, makes it a material suitable for making devices that can be operated without cooling. Its large carrier saturation velocity (220 $\mu m/ns$) and mobility, combined with a large breakdown field ($10^7$ $V/cm$), enables very fast signal response.

| Property | Diamond | Silicon |
|---|---|---|
| Band gap [eV] | 5.47 | 1.12 |
| Breakdown Field [V/cm] | $10^7$ | $3 \times 10^5$ |
| Displacement energy [eV] | 43 | 13-20 |
| Electron mobility $[cm^2/Vs]$ | 1800 | 1450 |
| Hole mobility $[cm^2/Vs]$ | 1200 | 450 |
| Saturation velocity [cm/s] | $2.2 \times 10^7$ | $0.8 \times 10^7$ |
| Effective atomic number $Z_{eff}$ | 6 | 14 |
| Dielectric constant $\varepsilon_r$ | 5.7 | 11.9 |
| e-h creation energy [eV] | 11.6-16 | 3.62 |
| Minority carrier lifetime [s] | $10^{-9}$ | $2.5 \times 10^{-3}$ |
| Wigner energy [eV] | 43 | 13-20 |
| Radiation length [cm] | 12.2 | 9.36 |
| Resistivity $\rho_c$ $[\Omega/cm]$ | $>10^{12}$ | $2.3 \times 10^5$ |
| Mass density $\rho$ $[g\ cm^{-3}]$ | 3.53 | 2.33 |
| Thermal conductivity $k$ $[W\ cm^{-1}K^{-1}]$ | 21.9 | 1.5 |

**Table 3.3:** Comparison of properties between diamond and silicon relevant for dosimetric application.

CVD diamonds are divided into two groups based on the substrate: single-crystalline CVD (sCVD) and poly-crystalline CVD (pCVD) diamonds. Compared to the pCVD diamond, sCVD diamonds have a defect density that is significantly reduced, because the pCVD diamond contains many grain boundaries which act as charge trapping centers for free charge carriers. Therefore, the lifetime of the electron-hole pairs in pCVD is much shorter than

in sCVD. As a consequence, the charge collection distance (CCD) and Charge Collection Efficiency (CCE) for the pCVD decrease significantly compared to the sCVD diamonds, for the same bias voltage. In order to obtain a high detection efficiency, although pCVD diamond can be produced in larger sizes, considering the many advantages of sCVD diamond, we chose the sCVD diamond as the detector for our project of fast luminosity monitoring.

### Energy deposition of electrons in diamond detector

Low energy electrons deposit energy in matter mainly by ionization (collision) while high energy electrons (> 10 MeV) lose energy mainly due to the Bremsstrahlung (radiation) process [75]. A Minimum Ionizing Particle (MIP) is a particle whose mean energy loss rate through matter is close to the minimum, and in practice, all particles with energies higher than their MIP energy are regarded as approximately MIPs in the solid state detectors. For electrons, the MIP energy is around 1.6 MeV [76]. To understand the distribution of the deposited energy in the diamond detector by MIPs as well as calibrating the simulation method based on Geant4, the deposited energy by electrons with energy of 1.6 MeV in diamond detectors with thicknesses of 140 $\mu m$ and 500 $\mu m$ was simulated with the standard Monte-Carlo simulation tool Geant4 [77]. The simulated results are shown in Figure 3.9, and are well fitted by a Landau distribution, which is generally used to describe the deposited energy spectrum in thin layers of material.

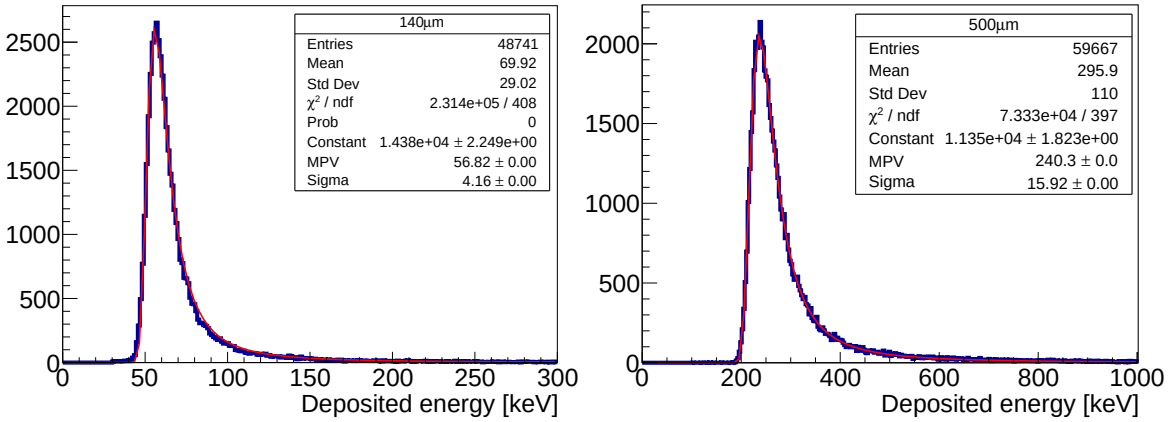


**Figure 3.9:** Landau distribution of deposited energy in the diamond detector (left: with thickness of 140 $\mu m$; right: with thickness of 500 $\mu m$) by 1.6 MeV electrons, based on simulation by Geant4.

As shown in Figure 3.9, the Most Probable Value (MPV) (Mean energy loss) fitted from the Landau distribution gives a deposited energy of 56.8 (69.9) keV for the 140 $\mu m$ diamond detector and 240.3 (295.9) keV for the 500 $\mu m$ diamond detector. As a comparison, the mean energy loss values calculated from the Bethe-Bloch formula [76] (see Figure A.1) are

72.7 keV and 289.3 keV for diamond detectors with thicknesses of 140 $\mu m$ and 500 $\mu m$, respectively. This relatively good agreement gives confidence that the simulation model based on Geant4 is reliable for further simulation studies of the signal response of the diamond detector. In addition, since the e-h creation energy is about 13 eV for the diamond detectors, the MPV of the generated charge will be about 0.7 fC for 140 $\mu m$ and 3.0 fC for 500 $\mu m$ diamond detectors.

### Charge collection process

The Shockley-Ramo theorem [78, 79] explains the mechanism of the signal generation in semiconductor detectors: the instantaneous electric current induced by a charge carrier is proportional to the charge $q$, instantaneous velocity $v$ of the particle, and the component of the electric field $E_v$ in the direction of the particle's moving:

$$i = E_v q v \tag{3.6}$$

The mechanism for charged particle detection by a diamond detector is illustrated in Figure 3.10. The charged particles, such as $e^-$, $e^+$, $\alpha$, etc... incident into the diamond detector will release energy due to ionization processes, then produce the electrons ($e^-$) and holes (h) as charge carrier pairs. The e-h charge carrier pairs are collected by applying an external electric field in which the charge carriers drift in opposite directions according to their different polarities. The electric field is usually generated by an external bias voltage $V$ of a few hundred volts, depending on the thickness of the diamond detector, to achieve for instance: 1 $V/\mu m$. The current induced by the e-h charge carriers movement on the electrodes, as described by the Shockley-Ramo theorem, is amplified by an amplifier and read out by an external system, with careful impedance matching. Once the charge carriers have arrived at the electrodes, the signal pulse ends.

During the charge collection process, the e-h charge carriers may get trapped or re-combined due to different kinds of defects inside the diamond. One important quantity characterizing the quality of a diamond sensor is the Charge Collection Efficiency (CCE), defined as:

$$CCE = \frac{Q_{coll}}{Q_{gene}} \tag{3.7}$$

where $Q_{gene}$ is the amount of charge (e-h pairs) generated in the diamond by the ionizing particle and $Q_{coll}$ is the charge collected by the readout electronics. For high quality sCVD diamond detectors, the CCE reaches 100% for electrical fields higher than 0.2 $V/\mu m$. In the

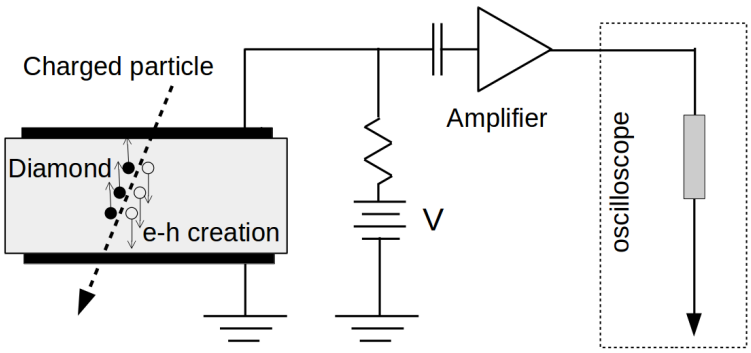


**Figure 3.10:** Schematic view of the diamond detector: the charge carriers (electron-hole pairs) generated by the incident charged particle are collected by applying an external electric field via the bias voltage V. The AC component of the signal is then amplified and read out by external system, such as an oscilloscope.

meantime, the pCVD diamond can typically only reach a CCE of $\sim 50\%$ with an electrical field of $1\ V/\mu m$.

Neglecting the border effects, the sum of the mean free paths $\lambda_k$ for electrons and holes gives the overall average distance that electrons and holes drift apart in an electric field, this value has been defined as the Charge Collection Distance (CCD): $d_c$.

$$CCD = CCE \times d = \sum_{k=e,h} \lambda_k \left[ 1 - \frac{\lambda_k}{d} \left( 1 - e^{-\frac{d}{\lambda_k}} \right) \right] \tag{3.8}$$

For sCVD diamond, thanks to its high purity, the CCE can be almost 100%, thus the CCD ($d_c$) can sometimes be equal to or even larger than the thickness of the diamond $d$, in this case the thickness of the diamond is used as the CCD in practice. The CCD ($d_c$) is also used to investigate radiation tolerance by checking the performance after some irradiation. In addition, the CCE and CCD are strongly dependent on the lifetime and drift velocity of the charge carriers before trapping. The electrical field has therefore to be taken into consideration when investigating the quality of a diamond.

### 3.3.2 sCVD diamond detector characterization with radioactive source

Some standard tests were performed to characterize the diamond detectors coupled with different pre-amplifiers in a specially equipped clean room at LAL. The Strontium-90 $\beta$ isotope radiation source is generally used to study the Landau distribution of MIPs. It undergoes a $\beta$ decay, with a half lifetime of 28.8 years and a decay energy of 0.546 MeV, into an electron, an anti-neutrino and the yttrium isotope Y-90, which is not stable, and therefore also undergoes a $\beta$ decay with a half lifetime of 64 hours and a decay energy of 2.28 MeV,

into an electron, an anti-neutrino and the zirconium (Zr-90), which is stable, see Equation 3.9. As the results, the electrons emitted by the Sr-90 $\beta$ source have energies from 0 to 2.28 MeV through these two processes. The radioactivity of the Sr-90 source used for our measurement was 37 MBq. Signal pulse shape characteristics were studied with an oscilloscope.

$$^{90}Sr \xrightarrow[\beta,28.8y]{<0.55MeV} {}^{90}Y \xrightarrow[\beta,64h]{<2.28MeV} {}^{90}Zr \tag{3.9}$$

The output signal is determined by several aspects: the initial space distribution of the induced charge carriers, the thickness of the diamond detector, the electric field and the resulting drift velocities of the charge carriers, and the type of amplifiers.

The sCVD diamond detectors with thicknesses of 140 $\mu m$ and 500 $\mu m$ coupled with either a fast charge amplifier C6 or a broadband current amplifier C2, were tested applying a bias voltage of 0.8 $V/\mu m$. The fast charge amplifier C6 is a dedicated charge amplifier with high gain (4 $mV/fC$) and low noise (Equivalent Noise Charge (ENC): 1000 $e^-$) for high speed applications. The output signal is a roughly Gaussian pulse shape with FWHM of about 14 ns. It is optimized for high speed single MIP particle detection and for fast spectroscopic applications in combination with diamond detectors. The broadband current amplifier C2 is a relatively low-noise amplifier (ENC$\approx$10000 electrons) with an analog bandwidth of 2 GHz and a gain of 40 dB, which enables us to preserve the timing characteristics of the instantaneous current signals.

### Tests with fast charge amplifier

To study the energy distribution of MIP electrons in the diamond detector, the fast charge amplifier (see Figure 3.11) was used to pre-process the signal. It integrates the current signal from the diamond detector and outputs a Gaussian shape signal with an amplitude proportional to the energy deposited in the diamond detector. An oscilloscope was used to record the segmented signals for offline analysis with MATLAB and ROOT.

Since the motivation is to investigate the Landau distribution of the MIP electrons in the diamond detector, the multiple trigger method was used to select the real signal from MIPs rather than other electrons with lower energies emitted by the Sr-90 source. As shown in Figure 3.12, the MIP electrons, after collimation by an Aluminum collimator with a diameter of 4 mm, will penetrate the diamond detector just 1 cm below it at a close to 90 degree angle and generate a signal, then go through the scintillator 1 cm below the diamond detector. The surface of the scintillator is $3 \times 3$ $cm^2$, which is relatively large compared to the diamond detector ($0.4 \times 0.4$ $cm^2$). Therefore, we can assume that the electrons which generate signals both in the diamond detector and scintillator can be regarded as MIPs. If we


**Figure 3.11:** Diamond detector and fast charge amplifier bought from CIVIDEC [71].

use the signal from the scintillator as the trigger, by studying the corresponding signal in the diamond detector, we can obtain the Landau distribution and do some further investigations, comparing for instance to the simulation of the deposited energy.

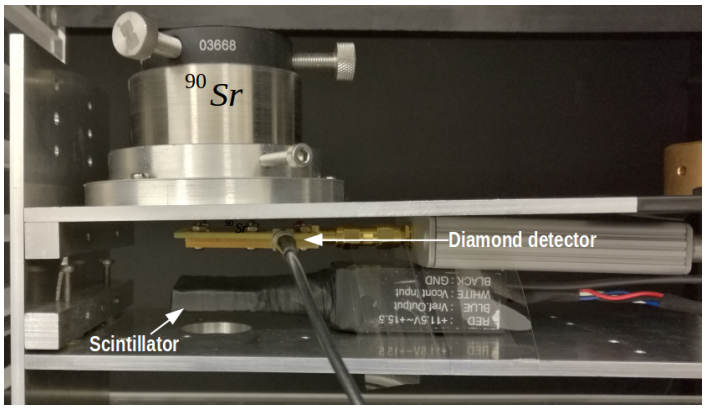


**Figure 3.12:** Measurement set-up for MIP electron detection with an external trigger from a scintillator.

In the multiple trigger mode, a time window of 5 ns is used taking into account the delay of the signals in the scintillator due to differences in cable lengths connecting the scintillator and diamond detector to the oscilloscope, as well as the different distances from the Sr-90 source to the diamond detector and scintillator. Figure 3.13 shows an example waveform of the coincident signals from the diamond detector and scintillator. The signal from the diamond detector is shown in pink and that from the scintillator in blue.

During the experiment, about 4000 coincident signals from the diamond detector were recorded for both types of diamond detector with different thicknesses (140 $\mu m$ and 500 $\mu m$). The histograms of the signal amplitudes are shown in Figure 3.14, they are consistent with a Landau distribution in both cases. The fitted results show that the MPVs of the

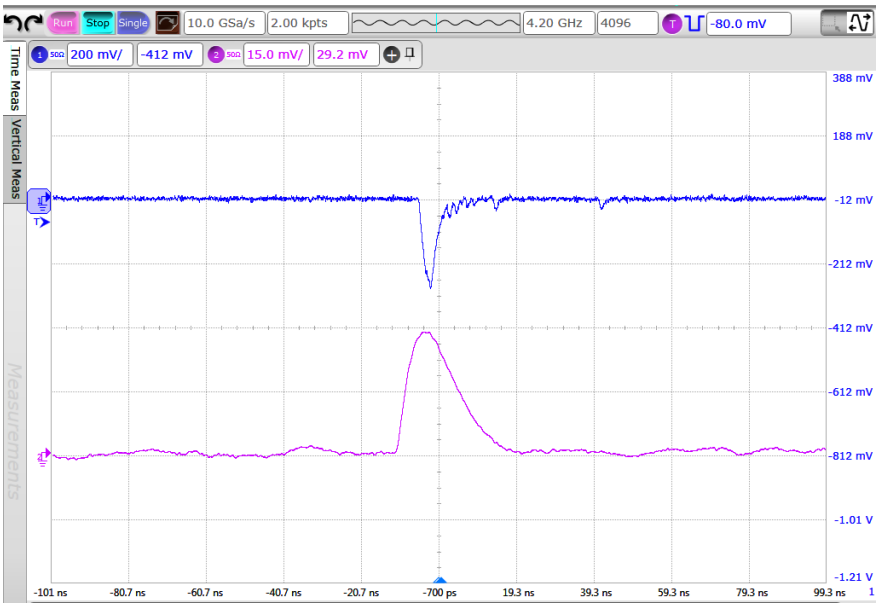


**Figure 3.13:** Screen shot from the oscilloscope showing the signals from the diamond detector coupled with a fast charge amplifier (pink) and from the scintillator used for triggering (blue).

signal amplitudes are 2.88 mV and 11.89 mV for 140 $\mu m$ and 500 $\mu m$ sCVD diamond detectors, respectively. The gain of the fast charge amplifier is 4 mV/fC, which means that the corresponding integrated charges generated in the diamond detector were 0.72 fC and 2.97 fC. These results are consistent with the previously calculated values (0.70 fC for 140 $\mu m$ and 2.96 fC for 500 $\mu m$ diamond detectors) for MIPs. The 3% difference could be explained by the fact that the energy and incident direction of the electrons may be slightly different between the experiment and simulation. This reasonably good agreement gives us confidence when developing the more complicated simulation that will be described to study the diamond detector's performance during fast luminosity monitoring.

### Tests with broadband current amplifier

As mentioned before, beams collide every 4 ns in the nominal case at SuperKEKB. In order to preserve the timing characteristics, a broadband current amplifier (C2) was proposed to amplify the current signals from the diamond detector, especially for the one with a thickness of 140 $\mu m$, see Figure 3.15.

More than 90000 signals from the diamond detector with thickness 140 $\mu m$ coupled with a C2 broadband current amplifier tested with the Sr-90 electron source were recorded by the oscilloscope in self-trigger mode. The Constant Fraction Discrimination (CFD) method was used to study the timing performance (rise time and full duration) of the signals, using a fraction of 5%.

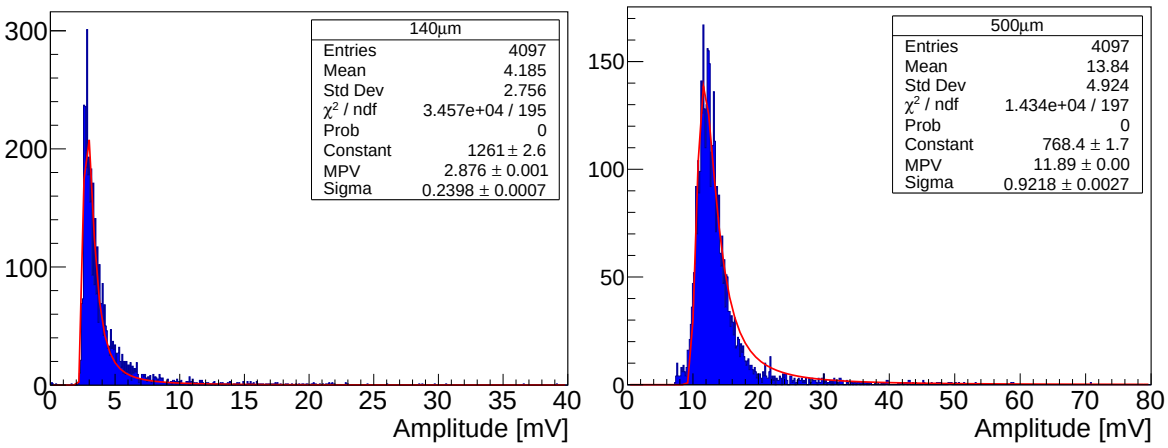


**Figure 3.14:** Histograms of the signal amplitudes fitted by Landau distributions: 140 $\mu m$ sCVD diamond detector on the left and 500 $\mu m$ sCVD diamond detector on the right.

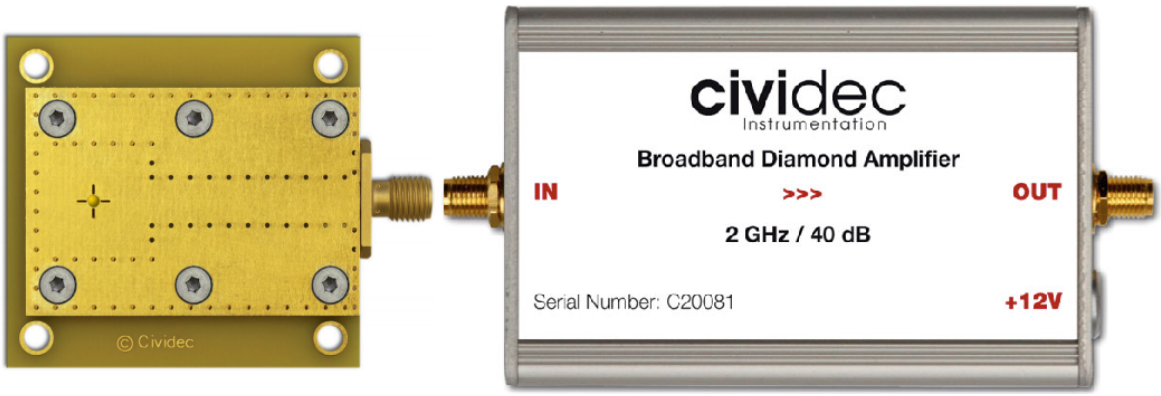


**Figure 3.15:** Diamond detector and 40 dB broadband current amplifier bought from CIVIDEC [71].

The results in Figure 3.16 show that the rise time peaks at 0.88 ns and that the full duration of most signals (more than 98%) are within 4 ns. The fixed rise time and narrow enough full duration guarantee that the maximum signal amplitudes can be sampled without any significant overlapping between subsequent pulses along the signal sequence during luminosity monitoring. The small impact from these partially overlapping pulses is at present neglected, but could in principle be taken into account as a correction.

The current amplifier directly amplifies the instantaneous current signal from the diamond detector rather than integrating the current to get the corresponding. The relationship between the signal amplitudes and charge generated in the detector should therefore be clear. After recording the data with the oscilloscope, the charge in the diamond detector was obtained by integrating the pulse area. Figure 3.17 shows the maximum amplitude of the signals as a function of the charge generated in the diamond detector. The good observed linearity makes

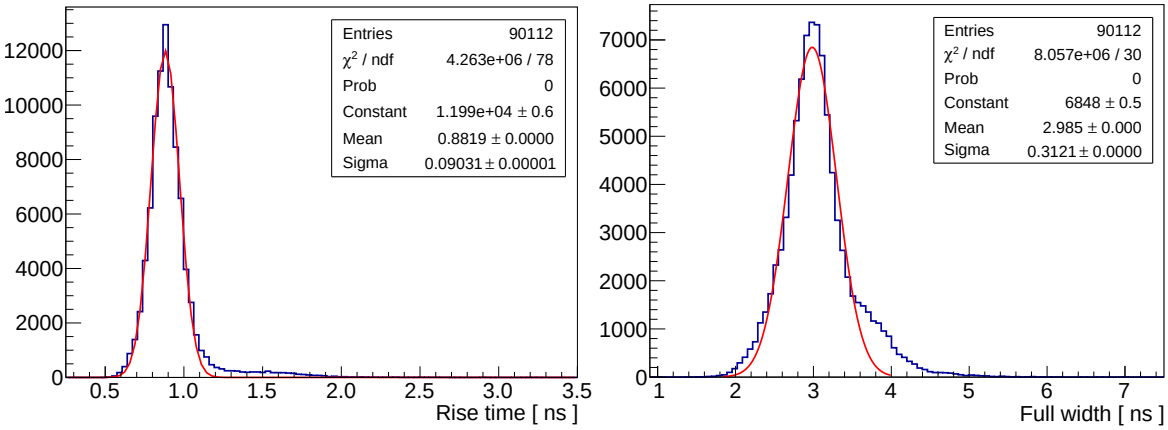


**Figure 3.16:** Distribution of rise time (left) and full duration (right) of signals from a 140 $\mu m$ diamond detector coupled with a broadband current amplifier tested with the Sr-90 electron source.

it possible to sum signal amplitudes turn by turn to evaluate the integrated relative Bhabha scattering rates separately from each bunch crossing [80].

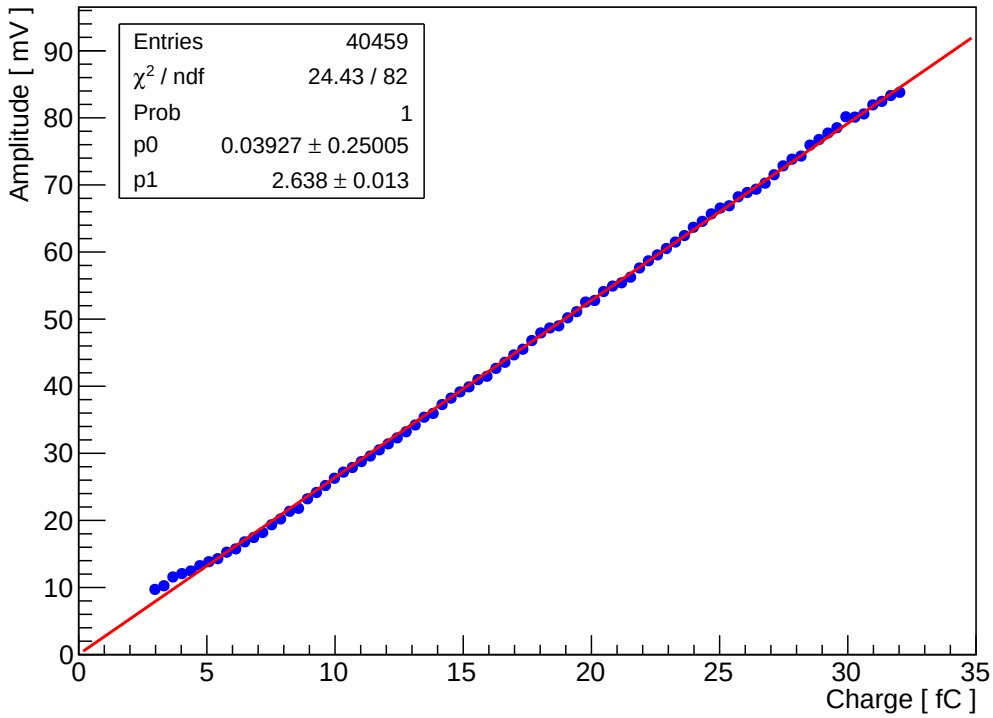


**Figure 3.17:** Relationship between signal amplitude and charge generated in the diamond detector with thickness 140 $\mu m$ coupled with a broadband current amplifier.

Based on the test results with the Sr-90 electron source, we found that the characteristics of linear relationship between the amplitude and charge, almost fixed rise time and narrow full duration of the signals for the diamond detector with thickness of 140 $\mu m$ coupled with

the broadband current amplifier make this set-up a very good candidate as the front-end of the fast luminosity monitoring system at SuperKEKB.

### 3.3.3 Data acquisition system for the fast luminosity monitoring

Based on the characteristics of the signals from sCVD diamond detectors and timing of the bunches along the trains at SuperKEKB, a data acquisition (DAQ) system based on an ADC and FPGA was developed by our group electronics engineer [81].

Figure 3.18 shows the DAQ functional diagram for the fast luminosity monitoring system based on the sCVD diamond detectors. Four signals are sent to a 10 bit AC-coupled ADC board (FMC126, 4DSP), requiring a 2 GHz clock to sample at 1 GHz (twice the RF clock at SuperKEKB: $f_{RF} \approx 508.9\,MHz$). This 2 GHz clock, generated by the PLL, is synchronized to the incoming LVDS 127 MHz ($f_{RF}/4$). Eventually, the samples are synchronized to the 508.9 MHz accelerator RF clock with a Phase shifter, with input range of 0-10 V, corresponding to about 4 ns (2 buckets) shift in the timing, see Figure A.2. The four ADC digital outputs are sent to a VERTEX-7 FPGA board (VC707, Xilinx), containing two independent and parallel

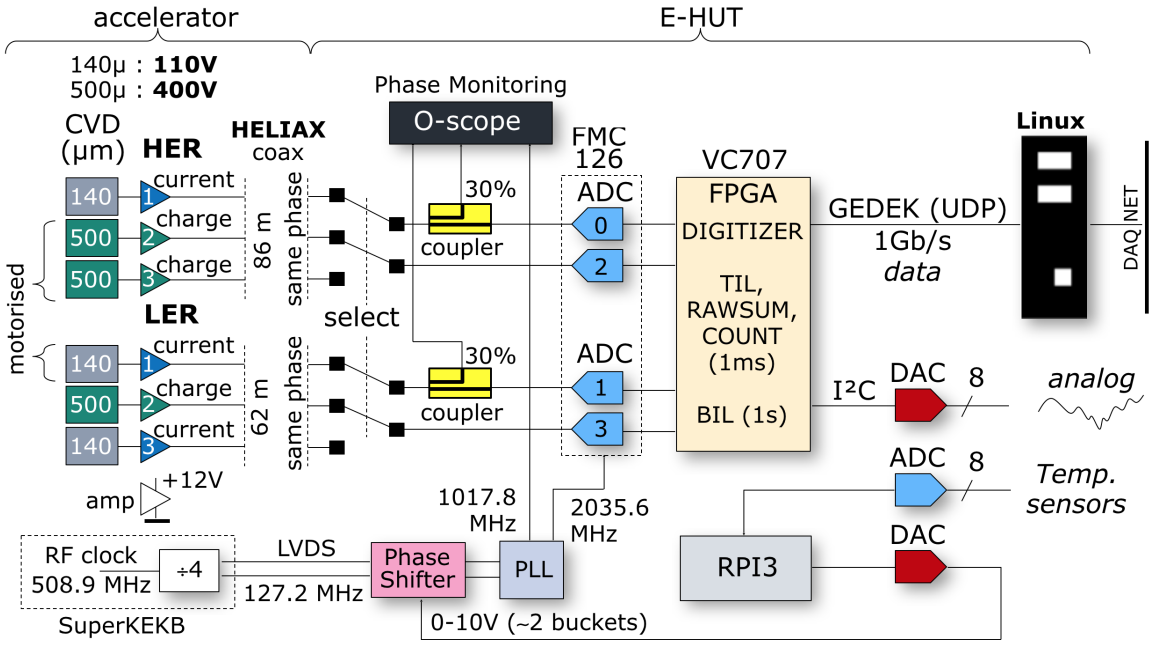


**Figure 3.18:** DAQ functional diagram for the luminosity monitoring system based on sCVD diamond detector (courtesy of D. Jehanno).

processes using the same signal samples: (1), Digitization path, allowing one full round trip sample set (10240) and used for slow monitoring; and (2), Luminosity path, clocked at 127 MHz, calculating the Train Integrated Luminosity (TIL) signals, Count (signal rates),

RAWSUM which directly sum the samples over 1 ms, and Bunch Integrated Luminosity (BIL) signals (Maximum: 5120 buckets) integrated over 1 s, in real time, for the four input channels simultaneously. Besides, the DAQ also contains a 16-bit DAC, providing 8 analog outputs with 1 kHz bandwidth, which can be configured independently to convert any TIL, Count, and RAWSUM values to analog signal, from any input channel.

The DAQ was initially designed to handle a maximum rate of one bunch every 2 ns, corresponding to train patterns with all or almost all buckets filled at SuperKEKB. It makes use of two principles: (1) the luminosity is proportional to the rate of Bhabha scattering events, which is partly detected by the sCVD diamond detector, (2) there is a stable common phase between the signals from sCVD diamond detectors and the RF clock, allowing to sample the maximum amplitudes of the signals. Because the ADC is AC-coupled, the mean value of the signal sequence is always centered at 0 V, which requires to measure the baseline near each signal pulse to get the real signal amplitude. This explains that we sample the signal sequence at twice the RF frequency. Figure 3.19, illustrates the DAQ processing of signals

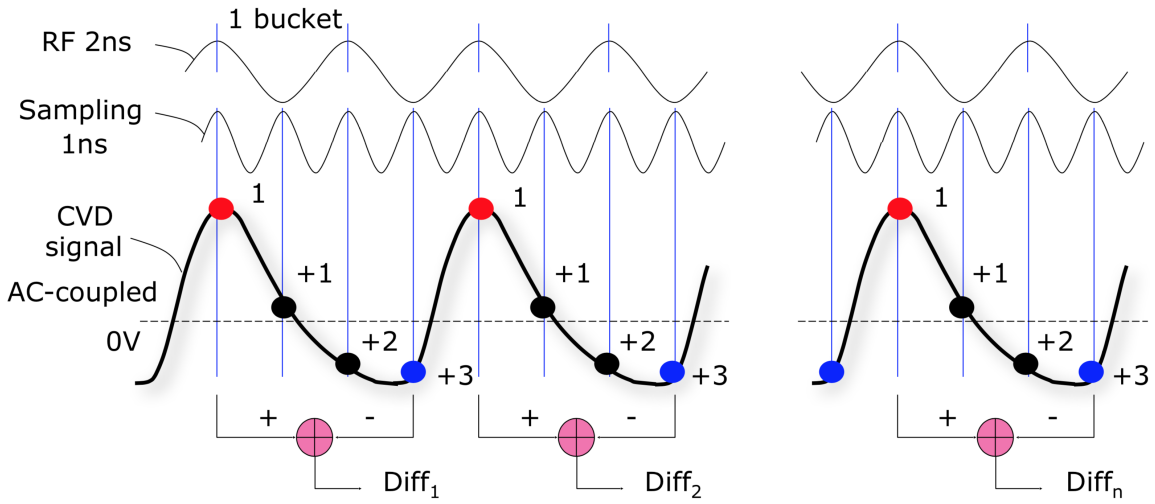


**Figure 3.19:** Illustration of DAQ processing of signals from a diamond detector with thickness of 140 $\mu m$ coupled with a broadband current amplifier C2 for the 4 ns bunch spacing case (nominal fill pattern at SuperKEKB) (courtesy of D. Jehanno).

from a sCVD diamond detector with thickness of 140 $\mu m$ coupled with a broadband current amplifier C2 for the 4 ns bunch spacing case, corresponding to the nominal fill pattern with very high luminosity at SuperKEKB. The calculations for the TIL, Count and RAWSUM at

1 kHz are shown below:

$$\begin{aligned} TIL &= \sum_{0}^{1\ ms} Diff_i, \quad if\ Diff_i > Threshold_1 \\ Count &= Count + 1, \quad if\ Diff_i > Threshold_1 \\ RAWSUM &= \sum_{0}^{1\ ms} (Sample_i - Threshold_2), \quad if\ Sample_i - Threshold_2 > 0 \end{aligned} \tag{3.10}$$

After careful synchronization to the RF clock with the phase shifter, the first sample (red) is positioned on the peak of the signals, the fourth sample (blue) will get the baseline thanks to the narrow enough signal pulse width from the sCVD diamond detector with thickness of 140 $\mu m$ coupled with a broadband current amplifier C2, and the two-bucket spacing fill pattern of SuperKEKB bunch trains. The difference between the first and fourth sample provides the real signal amplitude for the first bunch, and similarly for the subsequent bunches along the train. The luminosity process integrates over 1 ms the sum of all the differences ($Diff_n$) between the samples above a defined threshold ($Threshold_1$) to provide the TIL value. The sample process provides 5120 sums each 1 s corresponding to the BIL value for each bucket, see Equation 3.11, where $j$ and $n$ are the order of buckets and turns, respectively. The Count value for TIL gives the total number of pulses during the corresponding periods, and therefore the ratio TIL/Count provides an estimate of the average signal pulse amplitude. The RAWSUM value calculates the sum of all samples above a defined threshold ($Threshold_2$) and is intended for some channels which use the fast charge amplifier C6 with a 14 ns FWHM, and that cannot be handled easily in terms of TIL and BIL calculation. All the real-time data are uploaded to a Linux machine through a GEDEK protocol (ALSE) over a UDP link at 1 GB/s.

$$BIL[j] = \sum_{0}^{1\ s} Diff_{n,j}, \quad if\ Diff_{n,j} > Threshold_1 \tag{3.11}$$

# Chapter 4

# Simulation study for the preparation of fast luminosity monitoring and orbit feedback

A start-to-end simulation was done to understand and check the performance of the fast luminosity monitoring system for SuperKEKB based on sCVD diamond detectors. Bhabha scattering event generation at the IP was simulated based on Guinea-Pig++[82–84]. Particle losses from single beam processes and tracking of the scattered particles to the position of the sCVD diamond detectors were performed based on the Strategic Accelerator Design (SAD) software [85–87]. The sCVD diamond detector's signal was simulated based on Geant4 [77, 88]. The results will also be used to compare with the experimental data. Simulated signal sequences of the diamond detector were moreover used to simulate the DAQ signal process. Due to the very high luminosity and high relative precision of the fast luminosity signal, the potential radiation damage was also estimated based on simulation with FLUKA [89, 90] and previous experimental data. Finally, a full simulation based on above for the fast luminosity signals at 1 kHz was used as input to a model of the dithering feedback system to assess the performance of the dithering beam orbit feedback based on luminosity monitoring, taking into account a measured ground motion spectrum.

## 4.1 Bhabha detection efficiency study

The motivation is to monitor the luminosity of the SuperKEKB collider based on the Bhabha scattering process at vanishing scattering angle (see Figure 4.1). One of the most important parameters is the Bhabha scattering event detection efficiency of the monitor. Bhabha

scattering is one of the main sources of particle loss at high luminosity $e^+e^-$ colliders, such as SuperKEKB, CEPC, and FCCee.

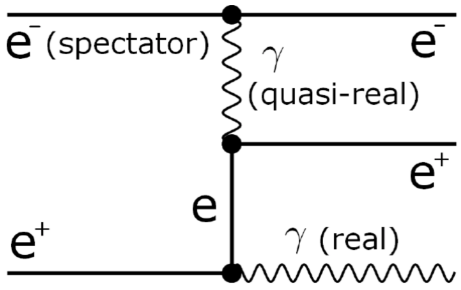


**Figure 4.1:** Radiative Bhabha scattering process at vanishing photon scattering angle.

The initial state electrons and positrons scatter through the exchange of a quasi-real photon with a very low energy and angle. The virtual photon interacts with a particle of the other beam and loses energy by emitting a real photon. The particle, which emitted the quasi-real virtual photon, referred to as the spectator, keeps its momentum and stays in the beam. However, the scattered particle loses part of its energy in the emission of the real photon and will be deflected more than the nominal energy beam particles by the bending magnets downstream of the IP. For this reason, it will at some point, depending on the magnitude of the energy loss, hit the vacuum chamber at some location downstream. Meanwhile, the emitted real photon will travel in a straight line along its scattering direction until it encounters an obstacle (accelerator component, such as beam vacuum pipe), interact with the obstacle's material and also get lost. The sCVD diamond detectors mounted just outside the vacuum pipe measure the charged particles in the secondary showers induced by the interaction between the lost Bhabha scattering particles with the encountered materials, to provide the luminosity information.

Following a careful study [64] taking into account the actual space available to install the sCVD diamond detectors on both sides of the IP, two locations were selected to place our diamond detectors, in the LER and HER, 10 and 30 meters downstream of the IP, for positron and photon detection, respectively. The criterion for the choice was detecting enough events from the radiative Bhabha process to keep a very high sensitivity, and thereby high relative precision for the fast luminosity signals, to provide an effective and powerful tool for optical tuning with extremely low beam currents.

### 4.1.1 Bhabha scattering simulation with Guinea-Pig++

Guinea-Pig++ is the C++ version of Guinea-pig, which is commonly used to simulate the beam-beam effects at the IP of high energy $e^+e^-$ linear colliders [82]. It is used by a

large part of the linear collider community since it provides high level modeling for the electromagnetic related quantum phenomena which occur during the $e^+e^-$ collision. It is able to predict the luminosity of the collision in the presence of the pinch and disruption effects resulting from the very dense charge distributions. It provides the beam particle distributions after interaction as well as secondary particles produced in the collisions and which can constitute backgrounds (Beamstrahlung, pair production, hadrons, Compton scattering...) and luminosity spectra, for which the purely analytical treatments do not exist.

For the Bhabha scattering process simulation, the information on the beam parameters at the IP, including the beam energies, intensities, $\beta$ functions, emittance and length of bunches should be provided. It is worth to mention that the code was initially prepared for the simulation of head-on collisions, which is not the case of SuperKEKB with its large crossing angle ($2\theta_c$=83 mrad). In the simulation, the intensities of electrons and positrons within the overlap region were used instead of the total intensities of the beams, and the effective bunch length: $\sigma_{z,eff} = \frac{\sigma_x}{sin(\theta_c)}$, where $\theta_c$ is half of the crossing angle (as shown in Figure 2.4). The output files contain energies and angular information of the incident beams, Bhabha scattered particles (positrons and electrons) and the emitted Bhabha photons.

The energy spectrum of the scattered Bhabha particles are shown in Figure 4.2 (Bhabha positrons and emitted photons along the positron beam on left, Bhabha electrons and emitted photons along the electrons beam on right). The energy of the scattered particles extends from very low energy to the beam energy, and the emitted photons are distributed in the same energy range, with values corresponding to the lost energies of the radiating charged particles. These simulated Bhabha scattered particles are used as the input source for the tracking in the SAD simulation.

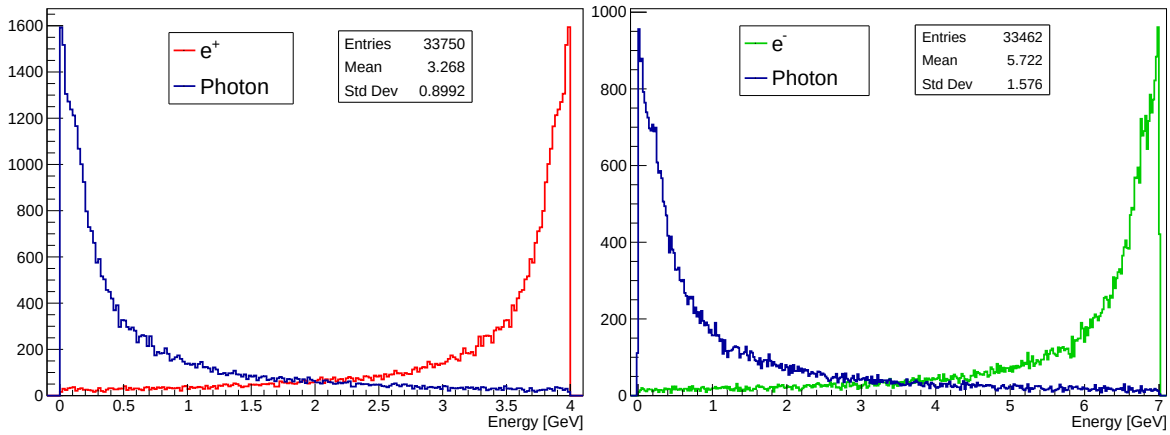


**Figure 4.2:** The energy distribution of Bhabha scattered particles along the positron (left) and electrons (right) beams.

### 4.1.2 Particle tracking

Once the scattered Bhabha particles have been generated at the IP (Bhabha positrons in LER and Bhabha photons in HER), the Bhabha positrons are tracked to the location of the diamond detector mounted downstream of the IP in the LER, based on the optics lattice [91] corresponding to each sub-phase of the SuperKEKB commissioning, using the SAD simulation. In HER, since the photons travel in a straight line and are not affected by the electromagnetic field, the central position of the photon loss is found through ray-tracing in the full 3D geometry.

#### 4.1.2.1 Case of Low Energy Ring

For the LER, the Bhabha scattered positrons are measured by the diamond detectors. It is well known that when a bunch of charged particles passes through a uniform magnetic field, the lower the energy, the smaller the bending radius, correspondingly, after passing through a magnet with a certain magnetic field, the deflection angle is larger for lower energy particles, while the higher energy particles will be bent less. Figure 4.3 shows the trajectory of the positron beam with different energies in a uniform magnetic field. We can assume the red one as corresponding to the trajectory of positrons with nominal energy (4 GeV), thus the Bhabha scattered positrons with less energy correspond to the lower part. The scattered positrons are still inside the beam at the IP and separated from the beam particles after the bending magnets then lost on the vacuum beam pipes.

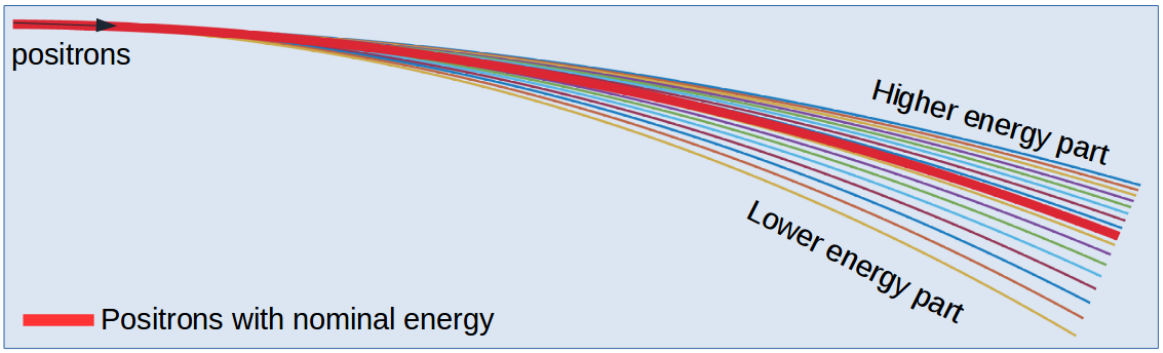


**Figure 4.3:** Trajectories of the positrons with different energies in a uniform magnetic field.

The energy of the Bhabha positrons is the dominating parameter determining the position where it will be lost downstream of the IP, and the effect from the scattering angle in the transverse plane is really small. Therefore, the Bhabha positron trajectories are almost the same for different collision optics, where only the $\beta_{x,y}$ functions are changed locally near the IP, and the dispersion function from the bending magnets remains unchanged. Figure

4.4 shows the $\beta_{x,y}$ and dispersion functions $\pm$27 meters from the IP (at 1416 m) for the Phase 3 optics in the LER. There are three dipole magnets between the IP and the location of the diamond detectors in the drift after the quadrupole QKBLP. The physical aperture of the vacuum pipe is 40 mm in radius from about 4 m downstream of IP, thus the tracked particles with transverse distances larger than 40 mm from the beam before the QKBLP can be regarded as lost and can be ignored, while the surviving positrons, with horizontal distances within 40 mm, may be detected by the diamond detectors.

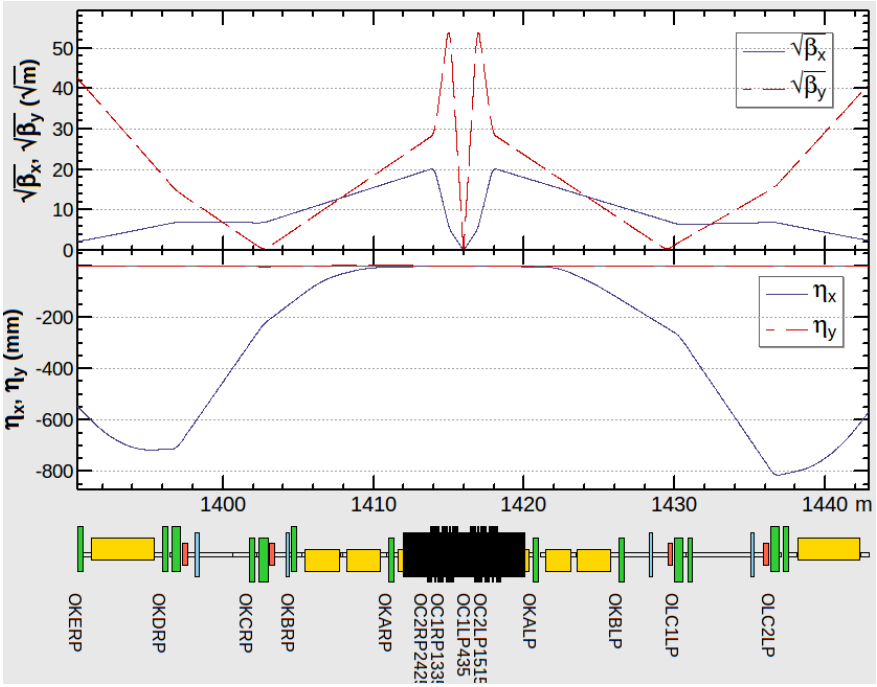


**Figure 4.4:** The $\beta_{x,y}$ and dispersion functions over $\pm$27 meters from the IP (1416 m) for Phase 3 optics in LER.

From the results during the Phase-1 commissioning [64], the diamond detector mounted just outside of the normal cylindrical beam pipe was not sufficient to measure enough Bhabha events, even though it was installed where the Bhabha positrons are most lost. A new vacuum beam pipe with a 45° inclined window and a depression of 15 mm (see Figure 4.5) was proposed to replace the regular cylindrical vacuum pipe (10 meters downstream of the IP in the LER, just after the QKBLP quadrupole) where we would mount our diamond detectors. The thickness of the flat plate is the same as the other copper vacuum pipe: 6 mm. In this way, Bhabha positrons with a horizontal distance from the nominal trajectory of the beam between 19 and 40 mm, will be lost on the inserted window.

Bhabha positrons were generated with Guinea-Pig++ as input to a SAD code based on the LER lattice, then tracked to the position just after the quadrupole magnet QKBLP. Figure

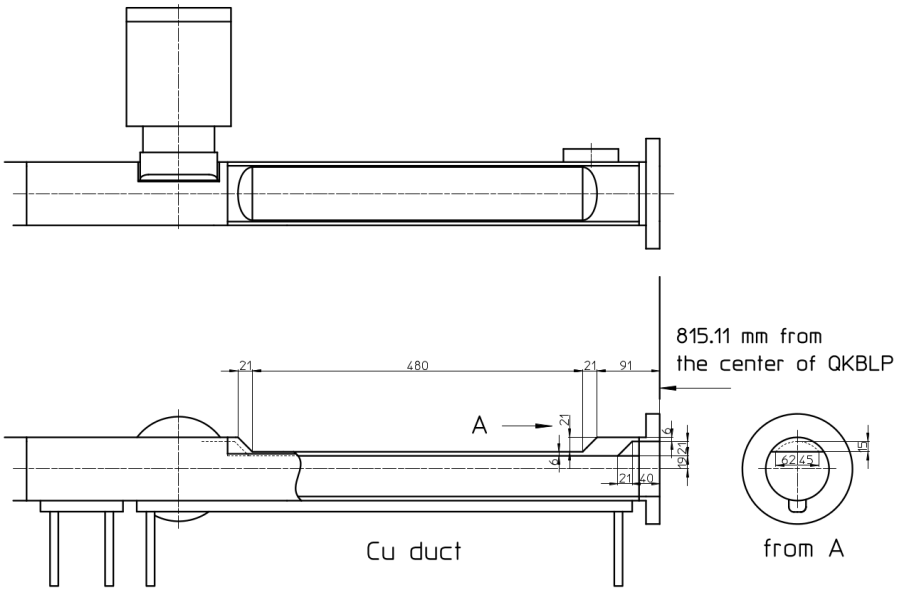


**Figure 4.5:** New designed beam pipe with a 45° window and depression of 15 mm.

4.6 shows the energy spectrum of the Bhabha positrons at the IP (blue), and the red region in the left corresponds to the part lost on the inserted window. The particles lost on the window have energies between 3.1 and 3.4 GeV and correspond to a fraction of 4.75% to the total Bhabha events generated at the IP. Our diamond detectors were installed just after the 45° degree window coupled with a carefully designed Tungsten radiator (details can be found in Section 4.1.3).

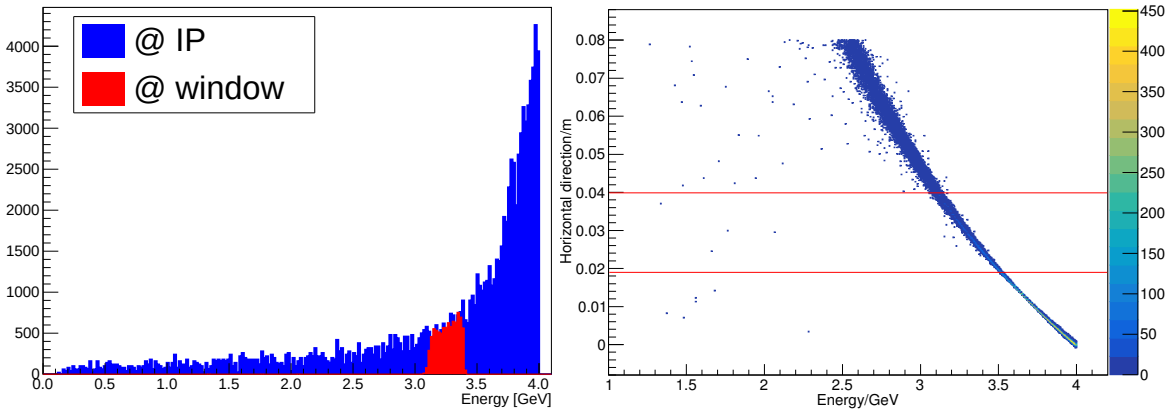


**Figure 4.6:** Energy spectrum of Bhabha positrons at the IP (blue) and the part incident on the window beam pipe (red) on the left, and the distribution of horizontal positions as a function of energy of the Bhabha positrons at the window shape beam pipe location on the right: the part between two red lines corresponds to the window of the vacuum pipe.

SAD was only used to track the Bhabha positrons from the IP to the window shape beam pipe based on the accelerator optics, without considering the geometry and materials. A standalone Geant4 model which includes the three-dimensional geometry and materials of the beam pipe, Tungsten radiator and detector was built up to estimate the signals in the diamond detectors precisely, and this will be described in Section 4.1.3.

#### 4.1.2.2 Case of High Energy Ring

In the HER, electrons with an energy of 7 GeV are circulating. Similar to the LER, diamond detectors were installed as a cross-check and back-up for LER, as well as for extending the dynamic range of the luminosity monitoring with the specified relative precision. Previous study [64] showed that it is not easy to find a suitable place to measure the Bhabha electrons like in the LER to provide luminosity information, because of the second to fourth dipole magnets (vertical bends), and the sextupoles used to correct chromaticity of the final focusing system, which make the Bhabha electron distribution in the E-x plane very complicated and erratic.

Since the photon is electrically neutral, it travels in a straight line and is not affected by the electromagnetic fields. In the HER, the Bhabha photons have an energy range which starts from very low energy up to the beam energy (7 GeV) with a very narrow transverse angular distribution for the nominal optics, as shown in Figure 4.7. Those emitted photons travel in the straight lines according to their angular distribution until they are lost on the vacuum beam pipe.

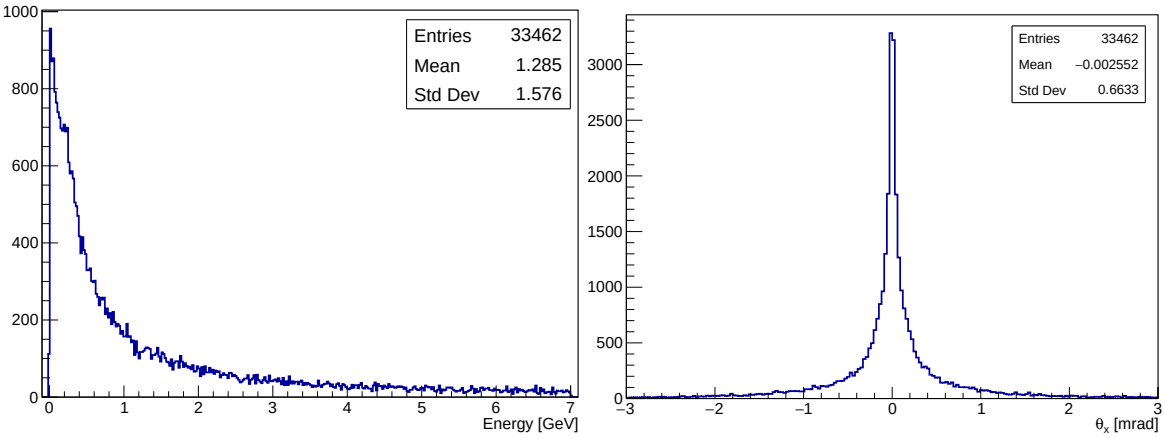


**Figure 4.7:** The energy spectrum and horizontal angular distribution of the Bhabha photons in the HER.

Figure 4.8 shows a schematic of the Bhabha photons' transportation in the HER based on extracting the coordinates of the beam orbit and vacuum pipe [92]. Here the complicated

geometry of the inner vacuum region from the IP to 35 m downstream was carefully considered, based on detailed information provided by the KEK vacuum group. The red line shows the trajectory of the Bhabha photons emitted at the IP along the nominal electron trajectory. Such photons hit on the ante-chamber edge about 29 m downstream of the IP with an angle of about 5.5 mrad. Due to the angular distribution of the beam at the IP, the photons are in reality emitted within a cone of a fraction of a mrad around the red line, which, projected on the surface of the vacuum pipe 29 meters from the IP, results in an extended distribution of photon exit points before and after.

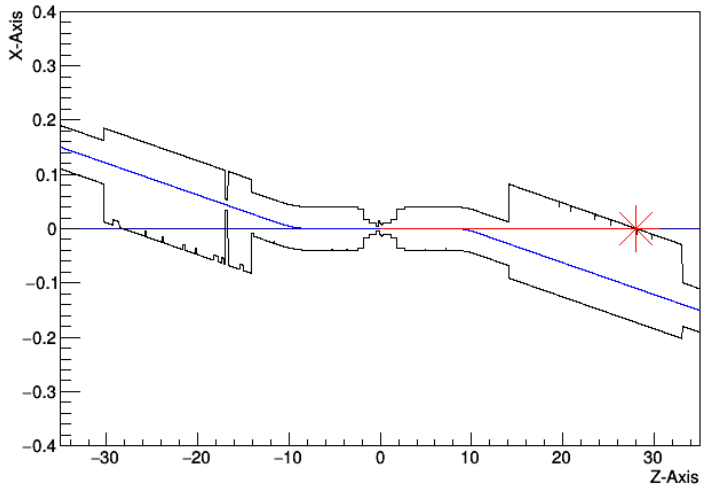


**Figure 4.8:** Schematic of Bhabha photon trajectory in the HER (courtesy of S. Di Carlo) [92].

While the geometry of the region from the IP to 35 m downstream doesn't change for different commissioning phases, the angular distribution of the Bhabha photons does according to the different beam parameters at the IP for different optics in sub-phases. Figure 4.9 shows the Bhabha photon exit point distribution for Phase-2.2 (left) and Phase-3 (right) optics [92]. It is obvious that the photon exit point distribution changes from Phase to Phase,in the process of the $\beta^*$ squeezing at the IP, while there is always a peak at the position of 28 m. Unfortunately, this point is inside of the sextupole SLYTRE. The closest free space for installation of the diamond detector and ZDLM scintillator and Cherenkov detector is the exit point of this sextupole or just after.

During Phase-2, the diamond detectors and ZDLM scintillator and Cherenkov detectors could be installed in the drift $\approx$ 30 meters downstream of the IP, where a small fraction of the photons exit. However, it is still not sufficient to measure enough Bhabha events to provide good enough precision even for the nominal luminosity. In Phase-3, a new position was chosen (see Figure 4.10), which corresponds to the tail of the photon exit point peak at 28 meters (the new installation is shown in Figure A.6).

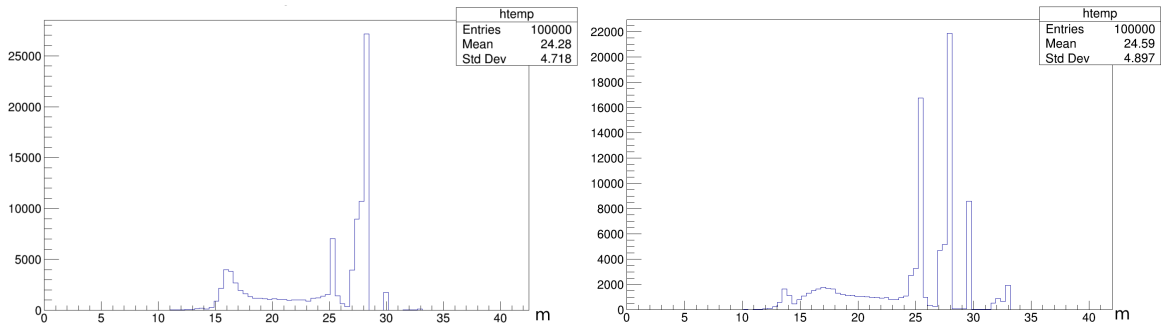


**Figure 4.9:** Loss position distribution of the Bhabha photons in the HER for the Phase 2.2 optics on the left and Phase 3 optics on the right (courtesy of S. Di Carlo) [92].

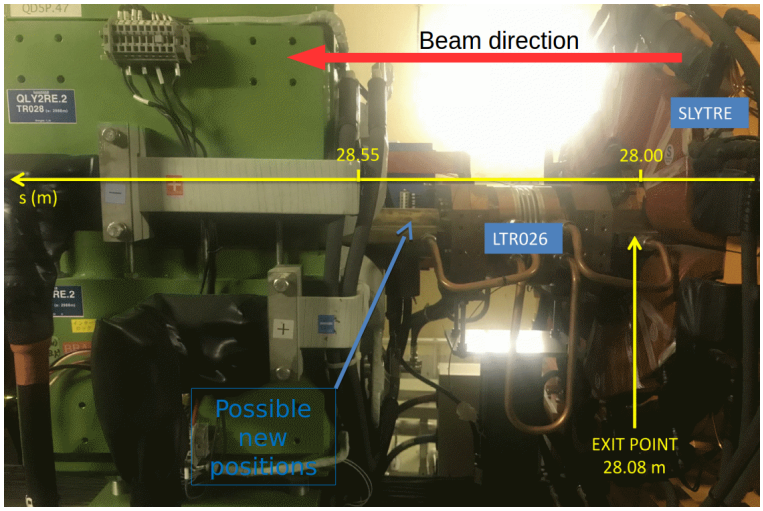


**Figure 4.10:** New location to install the detectors in HER for Phase-3.

### 4.1.3 Estimation of signal in the sCVD diamond detector

After tracking the scattered particles to the location where the diamond detectors are installed, the Geant4 Monte-Carlo simulation was used to study the signals they induce, taking into account their energy and exiting angles, and the geometry and material of the vacuum pipe.

In the LER, as mentioned before, a Tungsten radiator was placed after the 45° window shaped beam pipe to maximize the number of secondary particles incident on the diamond detector from the showering. The shape of the Tungsten radiator was also studied, both a parallelogram shape to ensure the same thickness for Bhabha positrons along the transverse direction and a trapezoid shape facilitating the installation of the diamond detector, details can be found in the Appendix A: Figure A.7 and A.8. The trapezoid shape Tungsten radiator was chosen, see Figure 4.11.

The optimum thickness of the Tungsten radiator was also studied to maximize the number of the charged secondary particles from the showers traversing the diamond detectors installed

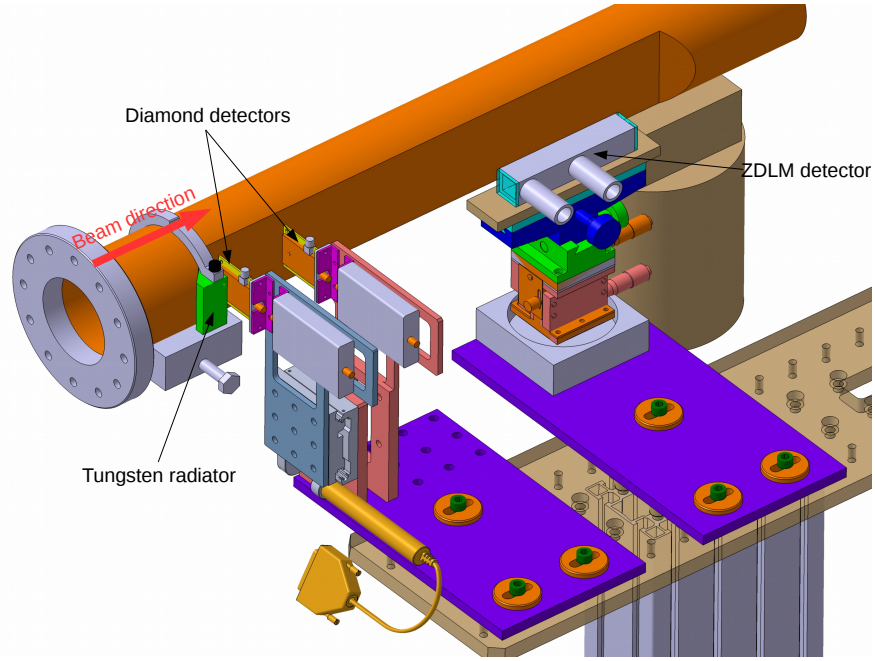


**Figure 4.11:** Set-up of diamond detectors in the LER.

behind perpendicular to the vacuum pipe. As shown in Figure 4.12, limited by the size of the PCB board of the diamond detector, the minimum distance between the center of the diamond detector and surface of the vacuum pipe is 12 mm which corresponds to the distance between the diamond center and the PCB board bottom edge.

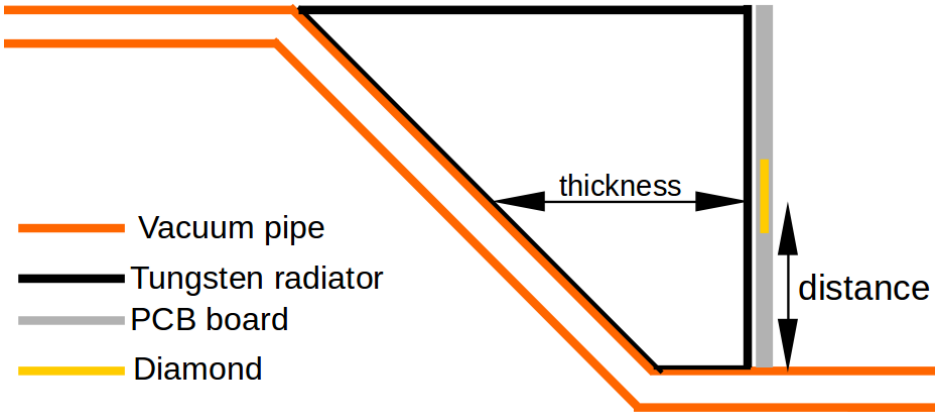


**Figure 4.12:** Geometry scheme of simulation study on diamond detector signal.

With this configuration, the thickness of the Tungsten radiator was studied. The average number of charged secondary particles as a function of the effective thickness of the Tungsten radiator is shown in Figure 4.13, where the thickness is given in units of Radiation Length (RL). For Tungsten, 1 RL=0.35 cm. It is clear that when the thickness of the Tungsten

radiator is set as 4×RL, the diamond detector receives the maximum number of charged secondary particles.

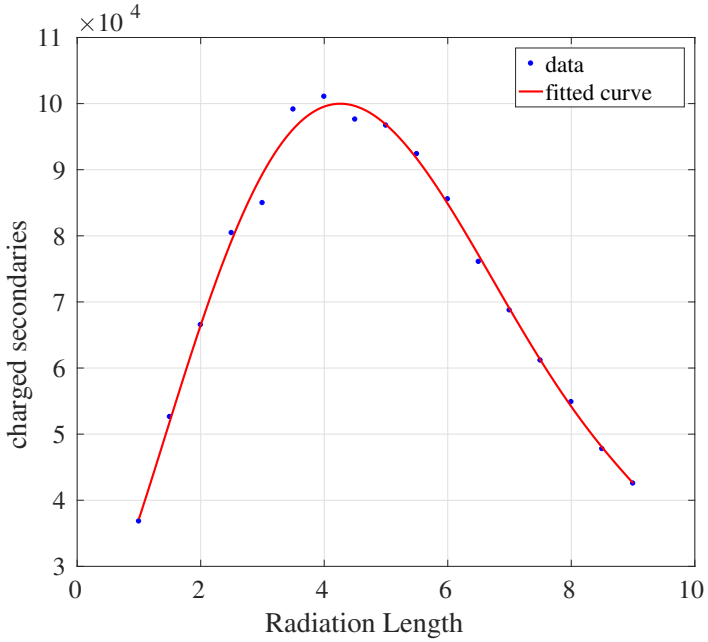


**Figure 4.13:** Number of charged particles across the diamond detector as a function of the effective thickness of the Tungsten radiator.

The output of the tracking with the SAD simulation after the quadrupole QKBLP was used as input to the three-dimensional Geant4 model, as shown in Figure 4.14, including the 45° window shaped copper vacuum pipe, and the trapezoid shaped Tungsten radiator. The Bhabha positrons go first through the Copper vacuum pipe then the Tungsten radiator, generating a set of charged secondary particles by interacting with the vacuum pipe and radiator materials. The diamond detector was placed just behind the Tungsten radiator and as close as possible to the surface of the vacuum pipe, see Figure 4.12. The energy deposited in the diamond detector was counted both per charged secondary particle and per Bhabha positron, as well as the number of detected charge particles per Bhabha positron as a function of a threshold.

Figure 4.15 shows the histogram of the deposited energy in the diamond detector for each charged secondary particle, left for the diamond detector with thickness of 140 $\mu m$ and right for the 500 $\mu m$ one. Peaks from the MIPs can be clearly observed, around 60 keV for 140 $\mu m$ and 250 keV for 500 $\mu m$ cases. The lower deposited energy part corresponds to particles with very low energy which lose all their energy inside the diamond detector, also the particles near an edge of the diamond detector. Because of the angles of the charged secondary particles incident onto the diamond detector, the trajectory length of the MIPs

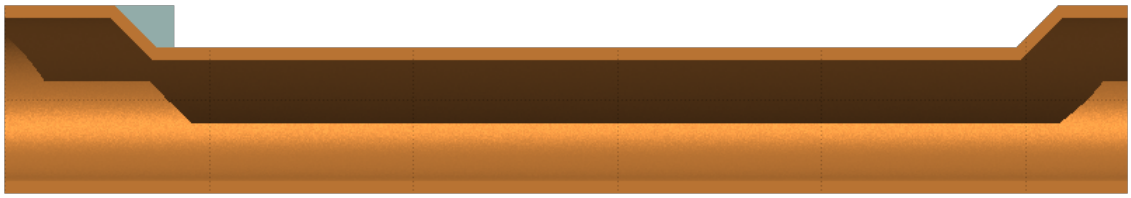

**Figure 4.14:** Geant4 model of the 45° window shaped beam pipe coupled with a Tungsten radiator with effective thickness of $4 \times RL$ installed after the quadrupole QKBLP in LER.

inside will be longer than the thickness of the diamond detector, and the peak position of the deposited energy could be slightly larger compared to the simulated results described in Section 3.3.1.

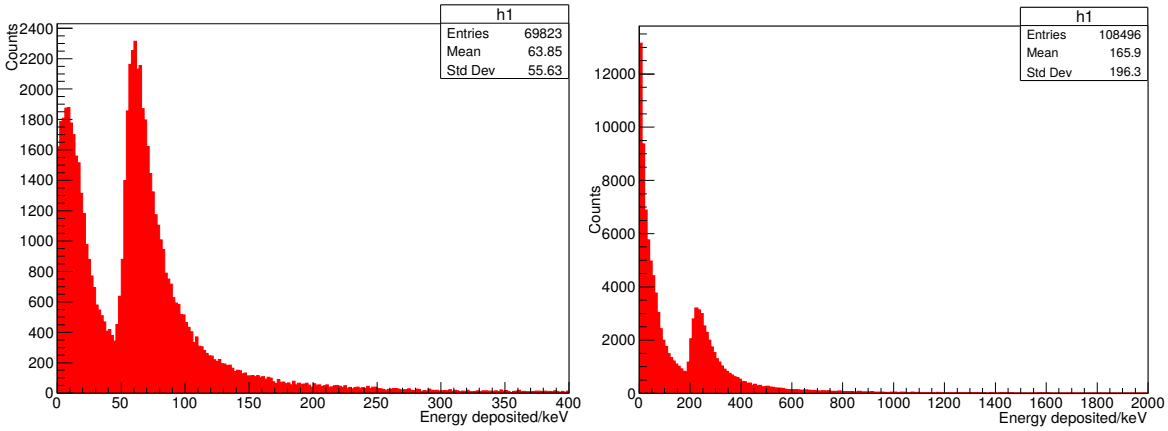


**Figure 4.15:** Histogram of the deposited energy in the diamond detector for each charged secondary: left for 140 $\mu m$, right for 500 $\mu m$.

To verify the explanation above, the initial energy of those charged secondary particles was also studied. Figure 4.16 gives the distribution of the energy deposited in the diamond detector as a function of the initial energy of the charged secondary particles for the diamond detector with thickness of 140 $\mu m$ on left and 500 $\mu m$ on right. It is obvious that the high energy charged secondaries deposit almost the same energy inside the diamond detector for both types of the diamond detectors, consistent with the Bethe-Bloch theory.

However, because of the presence of the Tungsten radiator, more than one charged particle induced by each Bhabha positron can go through the diamond detector, all depositing their energy inside the detector simultaneously. The energy deposited for each Bhabha positron is therefore used instead of the energy for each charged secondary particle to estimate the signal. Figure 4.17 shows the histogram of the deposited energy and number of charged secondary particles for each Bhabha positron lost on the 45° window and depositing energy in the diamond detector. For the detector with thickness of 140 $\mu m$ (left in Figure 4.17), the

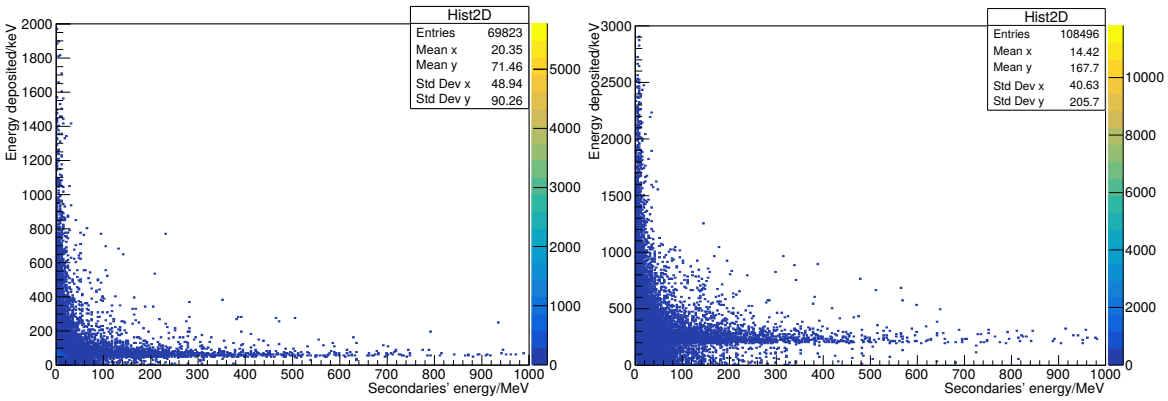


**Figure 4.16:** Distribution of energy deposited in the diamond detector as a function of the initial energy of charged secondaries: left for 140 $\mu m$, right for 500 $\mu m$.

average energy deposited in the diamond detector is about 516 keV, and the average number of charged secondary particles across the detector is 12.75, for each Bhabha positron. For the 500 $\mu m$ thick diamond, the average energy and number of charged particles are 1.745 MeV and 15.4, respectively. In comparison, only about 2 charged particles go through the diamond with the regular cylindrical vacuum pipe without 45° window and radiator. Similar work was also done for the HER ante-chamber vacuum pipe to estimate the signal in the diamond detectors [93].

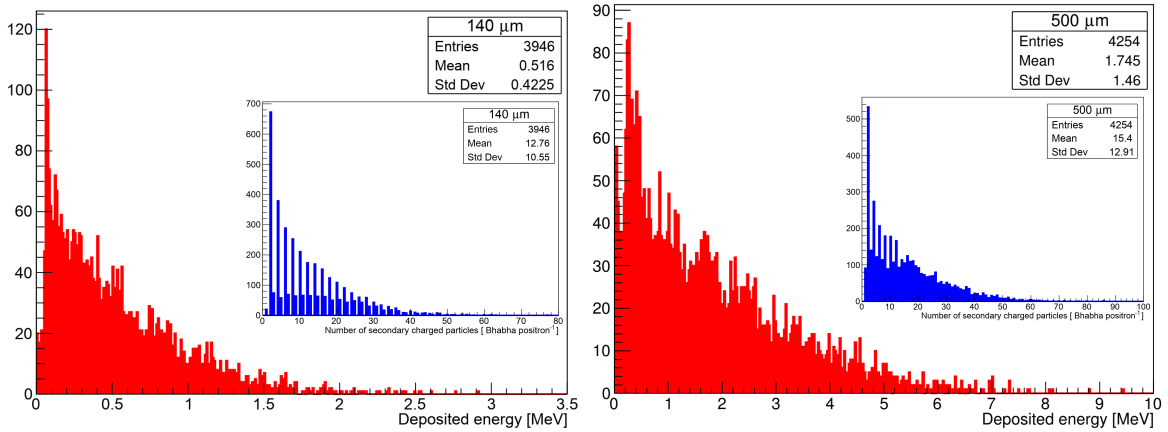


**Figure 4.17:** Histogram of deposited energy and number of secondary electrons for the diamond detector with thickness of 140 $\mu m$ on the left and 500 $\mu m$ on the right.

### 4.1.4 Detection efficiency estimation

After performing all the above simulation, we could estimate the detection efficiency of the diamond detector coupled with the amplifier, taking into account its noise. The C6,

fast charge amplifier has an ENC of about 1000 electrons (RMS), which corresponds to a deposited energy of about 13 keV (in the sCVD diamond, 13 eV is needed to produce an electron-hole pair); The C2, the broadband current amplifier has about 10 times larger noise than the C6, which means the RMS noise in deposited energy in the diamond detector is about 130 keV. To separate the effective signal from the noise, a threshold corresponding to $4 \times RMS$ of the noise will be set for the different types of amplifier. The detection efficiency for different combinations of detectors and amplifiers mounted at the optimum position in the HER and LER were calculated, as well as the corresponding relative precision that can be achieved for different luminosities. The results are shown in Table 4.1. When calculating the relative precision, only the statistical error is considered, based on the formula in Equation 3.5.

| | detection efficiency [%] | | relative precision @ 1 kHz [%] | |
|---|---|---|---|---|
| Detector type | LER | HER | Phase-2 [LER/HER] | Phase-3 [LER/HER] |
| 500 $\mu m$ + C6 | 2.76 | 0.00136 | 0.695/31.3 | 0.078/3.51 |
| 140 $\mu m$ + C2 | 1.17 | 0.00012 | 1.067/NA | 0.119/11.8 |

**Table 4.1:** Simulated detection efficiency of different detectors coupled with different amplifiers mounted at the optimum location as well as the relative precision that can be achieved in Phase-2 and Phase-3. The luminosity used to calculate the relative precision for Phase-2 is $1 \times 10^{34}\ cm^{-2}s^{-1}$ and $8 \times 10^{35}\ cm^{-2}s^{-1}$ for Phase-3.

Thanks to the 45° window shaped beam pipe coupled with a Tungsten radiator, the detection efficiency in the LER was improved by factor of 100 compared to the regular cylindrical vacuum pipe, for both types detectors, and now it is sufficient to provide precise enough (1%) fast luminosity signals at 1 kHz once the luminosity reaches $1 \times 10^{34}\ cm^{-2}s^{-1}$. In addition, it also meets the requirement for the very low beam current commissioning for optical tuning ($6 \times 10^{-3}$). However, the HER has lower detection efficiency (about 1000 times lower) due to detecting the Bhabha photons and because of the complex ante-chamber vacuum pipe. The Bhabha photons are distributed in a long region while many Bhabha positrons are lost on the window in the LER. However, this difference will be reduced with a new set-up on the HER side for Phase-3. More generally, it is helpful to cover a large luminosity dynamic range.

Given the characteristics of the output signals and DAQ system, as mentioned in Section 3.3.3, the diamond detector with thickness of 140 $\mu m$ coupled with the broadband current amplifier is used to preserve the timing characteristics, and mounted as close as possible to the Tungsten radiator. The detector with thickness of 500 $\mu m$ is mounted a little bit further while a lower noise amplifier (fast charge amplifier C6) is used to increase the signal detection

efficiency. In addition, a remotely controlled motor can be used to move the diamond detector in the horizontal direction in the range of 0-25 mm to give the possibility to change the detection efficiency according to requirements in different situations. In the longitudinal direction, the distance between the detector and the Tungsten radiator can also if needed be modified manually to adjust the detection efficiency. The detection efficiency reduction normalized to the optimum case (see Table 4.1) is shown in Figure 4.18.

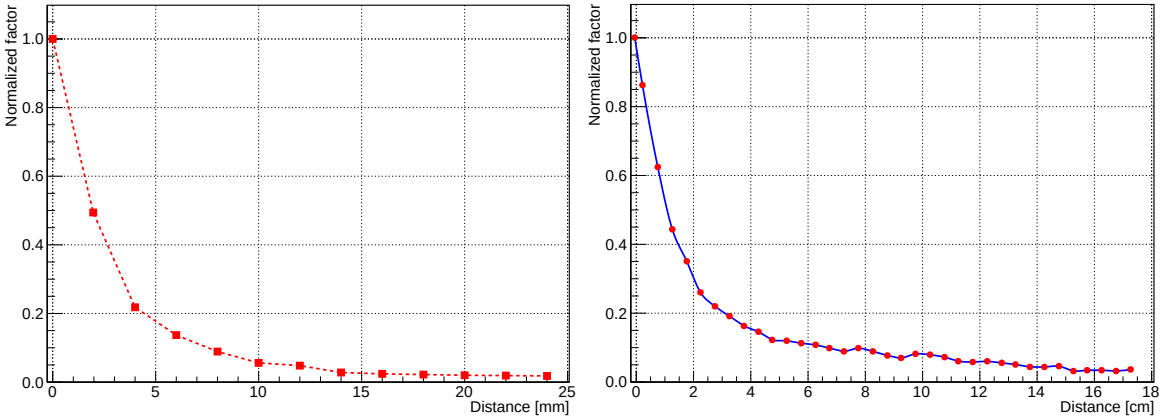


**Figure 4.18:** The reduction factor of the detection efficiency normalized to the optimum when moving the diamond installed on the LER: horizontally on the left and longitudinally on the right.

With the help of the remotely controlled motor, the sensitivity of the diamond detector mounted at the optimum location can be reduced by a factor of 20 when it is moved 25 mm away horizontally. While in the longitudinal direction, due to the forward distribution of the charged secondary particles in the showers, it losses 90% of its sensitivity when the detector is 8 cm away. The flexibility in the adjustment of the detection sensitivity allows us to maintain a large luminosity dynamic range while guaranteeing a certain relative accuracy, and to mitigate the detector's radiation damage during operation at the highest luminosity (this will be described in Section 4.4).

## 4.2 Simulation of DAQ signal processing

After determining the detection efficiency through the simulation study described in Section 4.1.3, a numerical simulation of the DAQ signal processing was done in MATLAB [94] to verify the reliability and to check the relative precision of the fast luminosity signals [63].

### 4.2.1 Signal sequence construction

Before simulating the DAQ signal processing, we need to build signal sequences that can represent the real signals at SuperKEKB, with realistic signal shapes, amplitudes and timing characteristics.

Since most of the secondary electrons induced by the interaction between Bhabha positrons and vacuum pipe materials are MIPs, the signals of the diamond detector tested with the MIP electrons emitted by a Sr-90 source can be used as a signal bank to construct the signal sequences. The time series of the signals should follow the collision timing characteristic from the fill pattern of the bunch train. Figure 4.19 shows the steps used to build our signal sequences.

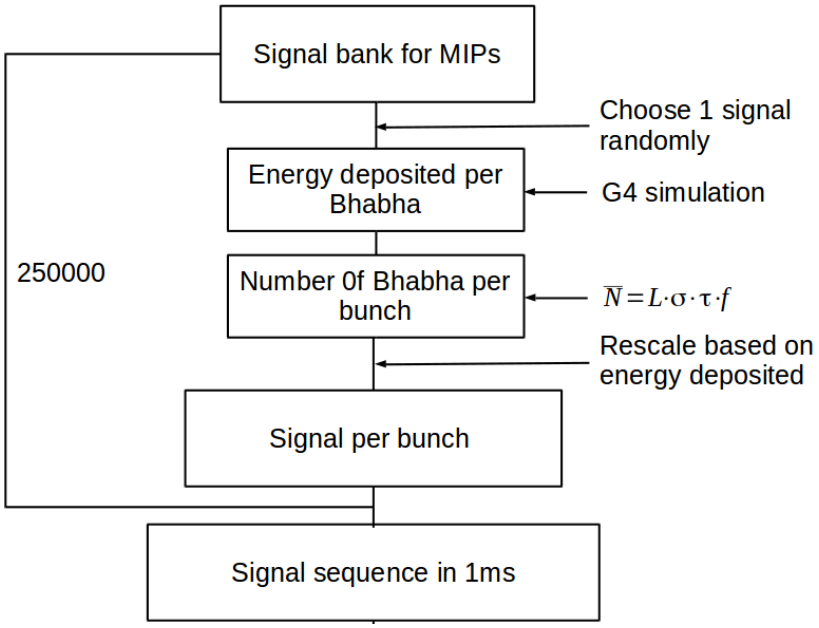


**Figure 4.19:** Schematic illustrating the signal sequence reconstruction used for the DAQ signal processing simulation to evaluate the fast luminosity signals.

The signal bank consists of 5000 diamond detector signals for MIP electrons collected with an oscilloscope at a sampling frequency of 10 GHz when irradiated with a Sr-90 source. For each bunch, according to the fill pattern, for example, the 2 bucket fill pattern with bunches every 4 ns, the expected number of Bhabha positrons to be detected by the diamond detector can be calculated based on the luminosity, the Bhabha scattering cross-section, and the detection efficiency. This number is then used as the mean of the Poisson distribution from which to generate the number of detected Bhabha positrons $\hat{N}$ for this bunch. After that, the total energy deposition for $\hat{N}$ events will be selected randomly from the energy distribution simulated with Geant4 (see 4.17) and used to rescale the shape of a randomly

selected signal from the signal bank for assignment to this bunch. For those bunches that have no signal, sequences from a Gaussian distribution with RMS corresponding to the amplifier's noise will be filled. After looping for 250000 times, a signal sequence lasting 1 ms is built with a time resolution of 0.1 ns, corresponding to the 10 GHz sampling frequency of the oscilloscope.

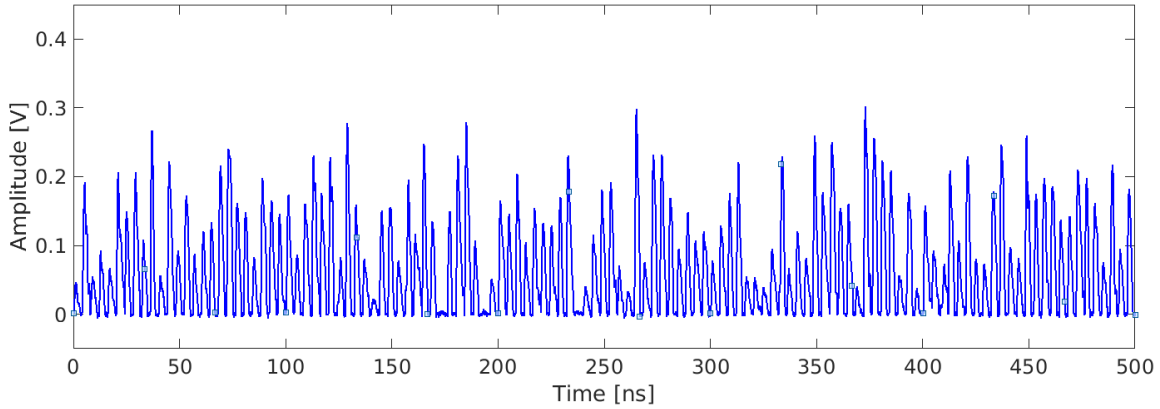


**Figure 4.20:** Example of signal sequence for the diamond detector with thickness of 140 $\mu m$ coupled with the C2 broadband current amplifier in the nominal luminosity case.

Figure 4.20 shows an example of the signal sequence for the diamond detector with thickness of 140 $\mu m$ coupled with the broadband current amplifier C2 in the nominal luminosity case with the 2-bucket fill pattern. For the most sensitive position, the mean number of Bhabha positrons to be detected is about 2.5 for each bunch, therefore, we can expect one signal almost every bunch. As a comparison, Figure 4.21 shows an example for the same detector with lower luminosity: $1 \times 10^{34}\ cm^{-2}s^{-1}$. The pulses are much less frequent in this case, and have an average separation of about 70 ns.

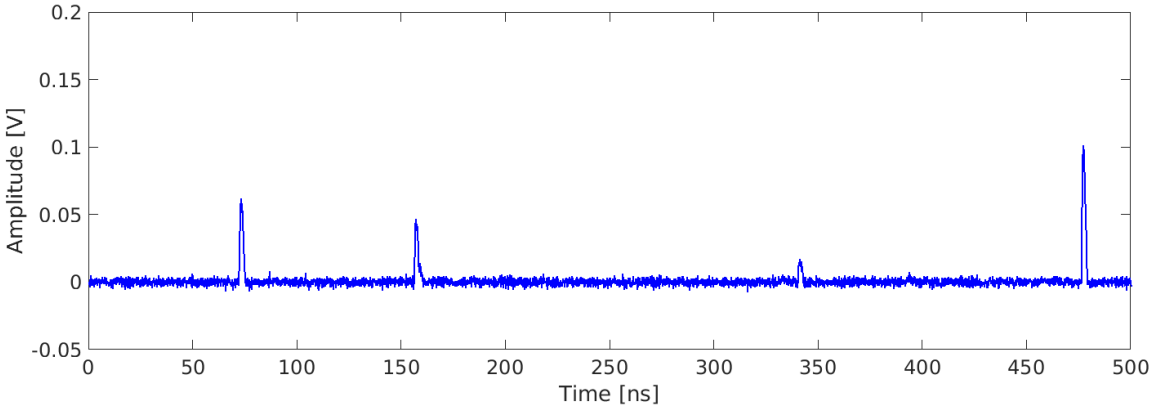


**Figure 4.21:** Example of signal sequence for the diamond detector with thickness of 140 $\mu m$ coupled with the C2 broadband current amplifier for Phase-2 target luminosity case: $1 \times 10^{34}\ cm^{-2}s^{-1}$.

### 4.2.2 DAQ signal processing simulation

Once signal sequences are constructed based on SuperKEKB machine collision characteristics, they are used as input to the DAQ model described in Section 3.3.3. Firstly, the baseline of the signal sequence will be shifted to keep the sum of all channels equal to zero, since the ADC is AC-coupled with a 65 kHz lower cutoff. Then the ADC will sample the signal sequence at 1 GHz with an optimized phase to obtain the signal amplitude for each signal. Figure 4.22 shows an example of sampling the constructed signal sequence for the 2-bucket fill pattern at the nominal luminosity of SuperKEKB (only the first 100 ns of the sequence are shown). The red dots correspond to the sampling points after the Phase adjustment. As can be clearly seen, the first of every four samples is always positioned at (or very close to) the peak amplitude of the signal, and the fourth sample gives an estimate of the baseline. This is based on the fact that the signal rise times are narrowly distributed around 0.9 ns and the full duration for most of the signals are within 4 ns, thus the overlap between two subsequent signals can be ignored for the diamond detector with thickness of 140 $\mu m$ coupled with the broadband current amplifier C2. Therefore, the real signal amplitude can be obtained by

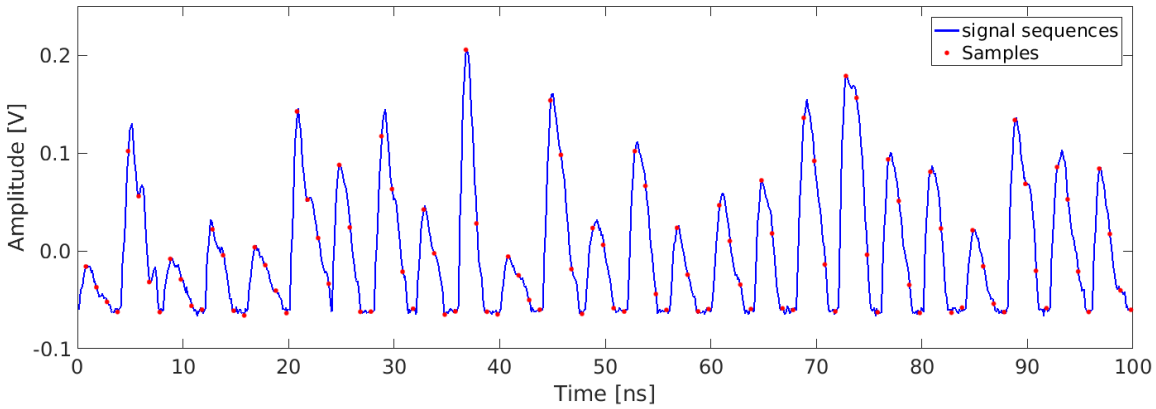


**Figure 4.22:** Example of sampling of constructed signal sequences for the expected fill pattern at the nominal luminosity of SuperKEKB after phase adjustment to get the maximum amplitude for each signal (the first 100 ns of the 1 ms sequence are shown).

getting the difference between the first and the fourth samples, which is used to evaluate the luminosity because the amplitude is proportional to the number of detected Bhabha positrons by the diamond detector. This amplitude is compared to the pre-defined threshold to select effective signals. The integrated luminosity signals, over all bunch crossings or for each bunch crossing, are obtained by summing the effective signals above the pre-defined threshold, according to Equation 3.10 and 3.11. The threshold is usually set to 4 times the amplifier's RMS noise, but it can also be modified based on the needs for different situations. TIL is the train integrated luminosity signal which directly accumulates the effective signal amplitudes

of the diamond detector. BIL, the bunch integrated luminosity signals, are separate sums of the signal amplitudes for each bunch in a certain period, typically 1 s. Train integrated luminosity signals were simulated for different luminosities, as well as the relative precision of the train integrated luminosity signals at 1 kHz.

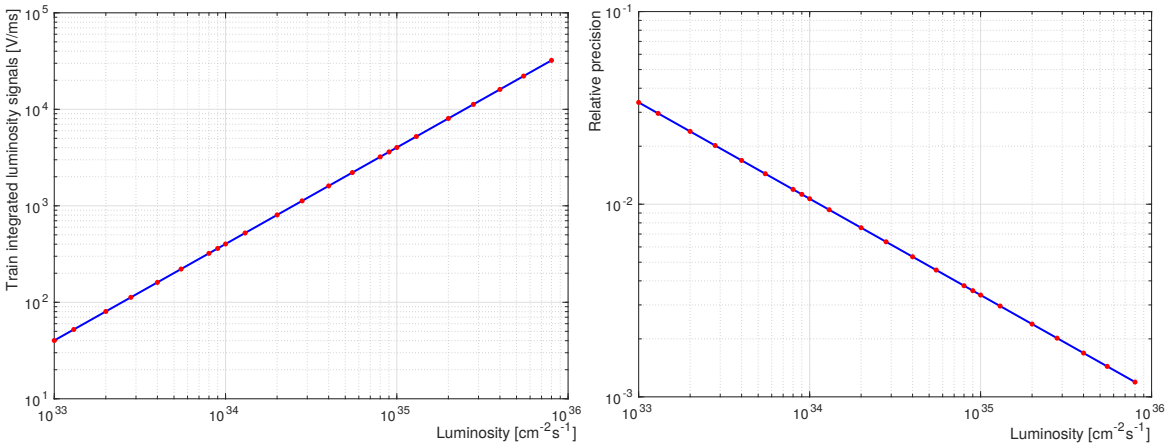


**Figure 4.23:** Example of simulated train integrated luminosity signal (left) and relative precision (right) at 1 kHz as a function of actual luminosity.

Figure 4.23 shows an example of the simulated train integrated luminosity signals from a diamond detector with thickness 140 $\mu m$ coupled with the C2 broadband current amplifier mounted at the optimum position in the LER to study how it correlates with the actual luminosity used as input to the simulation. Besides, the relative precision of the train integrated luminosity signals at 1 kHz was also estimated as a function of the luminosity. Good linearity is found between the train integrated luminosity signals and the actual luminosity. The relative precision will be better than 1% when the luminosity exceeds $10^{34}$ $cm^{-2}s^{-1}$, where the statistical error, energy distribution for each Bhabha, threshold to avoid the influence of amplifier's noise and potential imperfect peak sampling were all considered in the calculation. This simulation is a realistic representation of the actual operation of the diamond detector based luminosity monitor at SuperKEKB. It will be used as input to simulate the dithering orbit feedback system, which will be described in Section 4.5.

## 4.3 Background signal from single beam loss

In a machine like SuperKEKB, with very high beam currents (3.6 A in LER and 2.6 A in HER) and very small beam sizes, single beam losses, not only determine the beam lifetime, but are also some of the main sources of backgrounds in the Belle II detector. The main

single beam loss including the backgrounds to be considered are from synchrotron radiation, beam-gas scattering and Touschek scattering [55, 95–97]. The BEAST II project aims to measure and investigate the background signals in the Belle II detector at the IP, to verify that the background levels are safe for the Belle II detector. However, outside of the IP region, single beam losses are distributed all over the rings. Those lost particles interact with the beam pipe and the nearby materials, causing showers with charged secondary particles. Single beam losses affecting our luminosity monitors are also quite important to estimate the signal-to-noise ratio of our measurement.

### 4.3.1 Single beam loss processes

The fast luminosity monitors mounted downstream of the IP provide the luminosity information by measuring the radiative Bhabha scattering events at vanishing scattering angle. The particles lost from beam-gas Bremsstrahlung and Touschek scattering are the major background sources to be considered.

#### 4.3.1.1 Beam-gas scattering

The beam-gas scattering process is an interaction between a beam particle and a residual gas molecule. The rate of this interaction can be reduced by providing sufficient pumping to maintain a very good vacuum condition and by careful construction and preparation of the vacuum pipe to minimize the photon desorption of gas molecules. There are two principally different effects: single Coulomb scattering, which changes the direction of the beam particle, and Bremsstrahlung scattering, which reduce the energy of the beam particles [98–100]. Our experience in Phase-1 showed that the Bremsstrahlung scattering process dominates the single beam background signals caused by beam-gas scattering with a percentage more than 99% [64]. This can be easily explained by the fact that the momentum only changes direction from the Coulomb scattering while the energy dominates the scattered particle detection, similar to the Bhabha scattering positron detection.

In the case of the beam-gas Bremsstrahlung scattering, the electron or the positron emits a photon when it is deflected by the electromagnetic field of the nucleus or the electrons within the residual gas atom and leaves the atom in an unexcited state, and thus loses energy. It will then get lost either through the transverse aperture limit (dynamic or physical) or directly through the energy acceptance.

As shown in Figure 4.24, the Bremsstrahlung scattering process is a kind of deceleration of the beam particles. The spectral characteristics of the scattered beam particles (emitted photons) are very similar to the radiative Bhabha scattering process, while the difference is

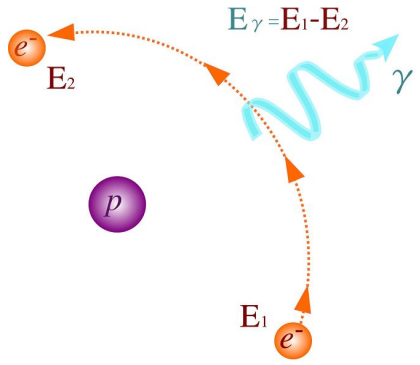


**Figure 4.24:** Bremsstrahlung scattering process of an electron in the field of the proton.

that the Bremsstrahlung scattering process occurs everywhere along the ring, whereas the radiative Bhabha scattering process only happens at the IP.

The differential cross-section for the energy loss from the beam-gas Bremsstrahlung scattering in the field of the nucleus of the residual gas can be expressed as Equation 4.1 [101, 102]:

$$\left(\frac{d\sigma}{d\varepsilon}\right)_N = \alpha\frac{4Z^2r_0^2}{\varepsilon}\left\{\left[\frac{4}{3}\left(1-\frac{\varepsilon}{E}\right)+\frac{\varepsilon^2}{E^2}\right]\left[183-\frac{2}{3}lnZ\right]+\left[\frac{1}{9}\left(1-\frac{\varepsilon}{E}\right)\right]\right\} \tag{4.1}$$

where $\alpha$ is the fine structure constant:1/137, $Z$ is the atomic number of the nucleus, $r_0$ is the classical electron radius, $E$ is the beam energy and $\varepsilon$ the energy of the emitted photons, the numerical constants inside the brackets correspond to the screening of the nucleus by the atomic electrons.

The differential cross-section for Bremsstrahlung scattering in the field of a bound electron of a residual gas atom is shown in Equation 4.2:

$$\left(\frac{d\sigma}{d\varepsilon}\right)_{e^-} = \alpha\frac{4Zr_0^2}{\varepsilon}\left\{\left[\frac{4}{3}\left(1-\frac{\varepsilon}{E}\right)+\frac{\varepsilon^2}{E^2}\right]\left[1194-\frac{2}{3}lnZ\right]+\left[\frac{1}{9}\left(1-\frac{\varepsilon}{E}\right)\right]\right\} \tag{4.2}$$

The total differential cross-section is given by the sum of these two independent processes, and the total cross section can be obtained by integrating from $\varepsilon_m$, the lowest energy loss which leads to particle loss, to the beam energy: E.

$$\begin{gathered}\sigma_B = \int_{\varepsilon_m}^{E}\left(\frac{d\sigma}{d\varepsilon}\right)d\varepsilon \simeq 4\alpha r_0^2\left\{\frac{4}{3}F\left[ln\frac{E}{\varepsilon_m}-\frac{5}{8}\right]+\frac{1}{9}Z(Z+1)\left[ln\frac{E}{\varepsilon_m}-1\right]\right\}, \\ where\ \varepsilon_m \ll E,\ F = Z^2 ln\left(\frac{183}{Z^{1/3}}\right)+Zln\left(\frac{1194}{Z^{2/3}}\right)\end{gathered} \tag{4.3}$$

For most of the practical cases, the contribution from the electrons is negligible. The beam loss rate caused by Bremsstrahlung scattering is proportional to the populations of the beam particles and residual gas, thus to the beam currents and residual gas pressure in the vacuum pipe. According to Equation 4.3, the Bremsstrahlung scattering cross section has a strong dependence on the atomic number of the residual gas species, but a weak dependence on the maximum energy acceptance which goes as $-ln(\varepsilon_m/E)$.

#### 4.3.1.2 Touschek scattering

The Touschek effect is an elastic scattering between electrons (positrons) within the bunch. Different from the intra-beam scattering, which is a multiple scattering process that leads to diffusion in all three directions and changes the beam dimensions, the Touschek effect is a single scattering process causing immediate loss of the colliding particles [103, 104]. The Touschek effect is one of the limiting mechanisms in low to moderate energy storage rings. It was first discovered and explained by Bruno Touschek after observations of the beam lifetime in the small storage ring ADA [105–107].

The Touschek scattering occurs in all planes but the energy transfers involved from the longitudinal plane to the transverse are insufficient to generate a betatron oscillation capable of leading to particle loss. If we consider the Touschek scattering of the two particles in the Center of Mass System (CMS), as shown in Figure 4.25, the betatron motion is purely in the transverse plane and a collision can transfer some of the momentum into the longitudinal direction, and the particles will either gain or loose some momentum after boosting to the laboratory system with the Lorentz factor $\gamma$. This momentum variation can cause beam loss if it exceeds the momentum acceptance of the ring.

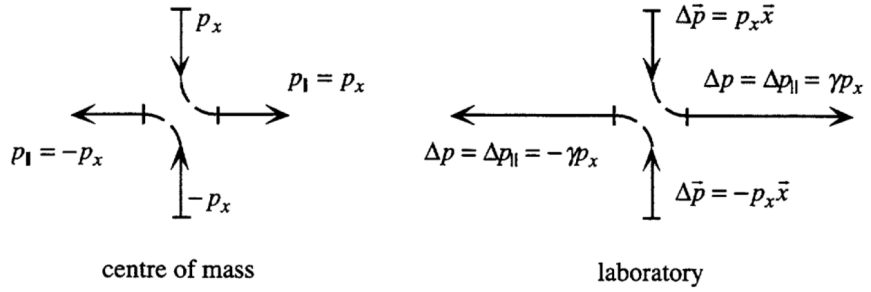


**Figure 4.25:** A typical example of Touschek scattering process in CMS and laboratory systems.

For a particle at a position in the ring where the betatron amplitude is $\sigma_x$ and the horizontal beta function is $\beta_x$, the maximum divergence is

$$\sigma_{x'} = \frac{\sigma_x}{\beta_x} = \sqrt{\frac{\varepsilon_x}{\beta_x}} = \frac{p_x}{p} \tag{4.4}$$

where $\varepsilon_x$ is the horizontal emittance.

Figure 4.26 shows the geometry of the Touschek scattering process in the CMS. We make the assumption that the motion in the transverse plane is non-relativistic in the CMS frame. The momentum transferred into the longitudinal direction in the laboratory system is $\gamma p_x cos\chi$, reaching a maximum when $\chi$ is 0. The scattered particle will be lost if this

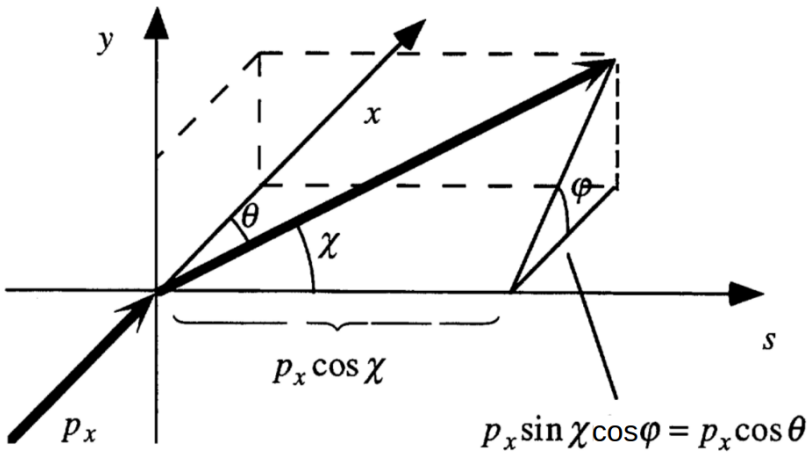


**Figure 4.26:** The geometry of Touschek scattering process in CMS frame.

exceeds the RF acceptance $\Delta p_{rf}$: $|cos\chi| \geq \Delta p_{rf}/\gamma p_x = \mu$. The differential cross section for Coulomb scattering of two particles with equal but opposite momenta in the non-relativistic approximation is given by Moller formula

$$\frac{d\sigma}{d\Omega} = \frac{4r_0^2c^4}{v^4}\left[\frac{4}{sin^4\theta} - \frac{3}{sin^2\theta}\right] \tag{4.5}$$

where $v$ is the relative velocity of the two colliding particles in the CMS frame, the $r_0$ is the classical electron radius and $\theta$ is the scattering angle. The total cross-section for Touschek scattering can be obtained as shown in Equation 4.6:

$$\begin{aligned}
\sigma_T &= \int_{|cos\chi|>\mu} \left(\frac{d\sigma}{d\Omega}\right) d\Omega \\
&= \frac{4r_0^2c^4}{v^4} \int_0^{cos^{-1}\mu} sin\chi d\chi \int_{-\pi}^{\pi} d\varphi \left[\frac{4}{\left(1-sin^2\chi cos^2\varphi\right)^2} - \frac{3}{\left(1-sin^2\chi cos^2\varphi\right)}\right] \\
&= \frac{8\pi r_0^2c^4}{v^4}\left[\frac{1}{\mu^2} - 1 + \mu^2\right],
\end{aligned} \tag{4.6}$$

For the loss rate caused by Touschek scattering, the number of collisions per unit time needs to be calculated. The loss rate from the Touschek scattering process is proportional to the square of the beam current, and based on the assumption that the particle distributions in the three planes are Gaussian, it is also proportional to the inverses of each beam size.

### 4.3.2 Simulation of backgrounds caused by single beam losses

A simulation code was developed based on SAD and Geant4 to estimate the single beam losses caused by beam-gas and Touschek scattering. It consists of two main parts: one is producing the scattered particles, tracking them to the concerned region, and then outputting the tracking results [108]. The other is estimating the signals in the diamond detector by using the tracking results as input to the Geant4 simulation. Here the simulation in the LER will be described and discussed in detail. Similar work was also performed for the HER and the results will be reported [92].

For the LER, some modifications were performed to adjust the physical aperture to take into account the insertion of the 45° window shaped beam pipe. Since in the SAD program, scattering events are generated at the beginning of each accelerator component, to increase the resolution in scattering positions, some elements had to be sliced [64]. Figure 4.27 shows the $\beta_{x,y}$ and dispersion functions in the IP region ($\pm$ 30 m) for Phase-3 with sliced accelerator components (dipole magnets and drifts). This adopted slicing enables us to increase the scattering position resolution while preserving the optics. The same simulations were repeated also for the other sub-phase optics. The results for Phase-2.2 will be described in detail below, and a conclusion for all sub-phases will be summarized in the end.

#### 4.3.2.1 Beam-gas scattering simulation for Phase-2.2

According to the cross-section described in Section 4.3.1.1, the total loss rate over the entire ring can be obtained once the beam current and vacuum pressure are specified. The scattered particles are tracked from each scattering point (each sliced element) to QKBLP, the quadrupole before the installed window shaped beam pipe, weighted by the fraction of length of the corresponding element (where the scattering occurred) to the total circumference of the ring.

The simulation was performed with a bunch current of 1 mA and an uniform vacuum pressure of 1 nTorr. Different ratios of vertical to horizontal emittance were used in the simulation to represent the residual x-y coupling, for the different sub-phases of the commissioning, according to the machine parameters, taking into account the progress of $\beta_y$ squeezing at the IP. Moreover, for the Bremsstrahlung scattering process, the loss rate does not only depend

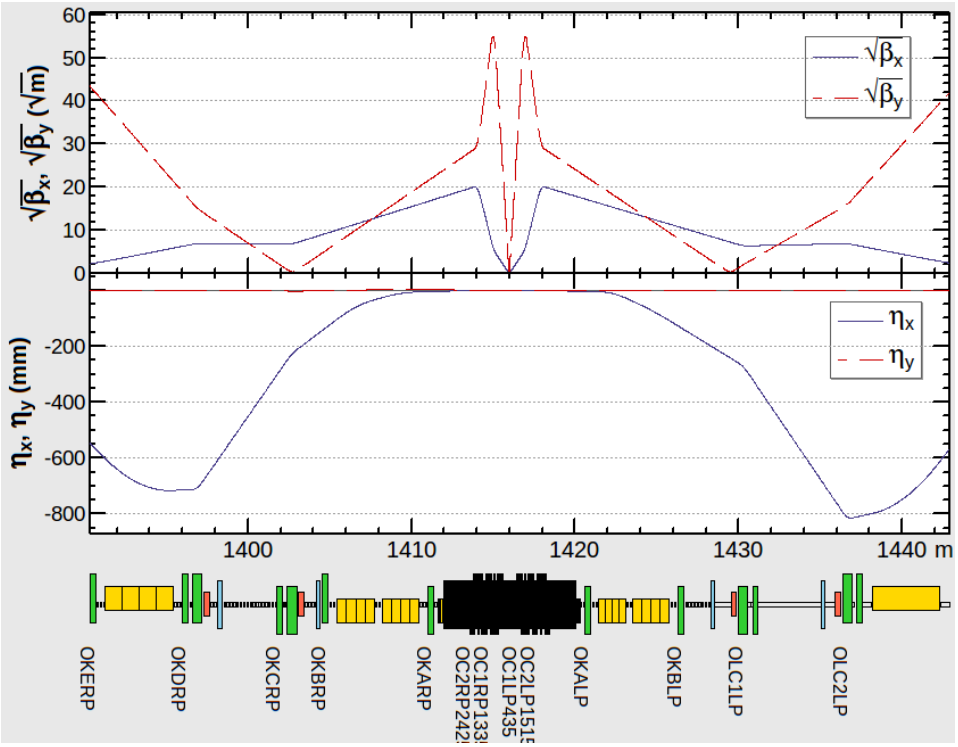


**Figure 4.27:** $\beta_{x,y}$ and dispersion functions for Phase-3 with sliced accelerator components (dipoles and drifts) in the IP region.

on the beam intensity but is also proportional to the vacuum pressure. A simulated vacuum profile [109] (see Figure A.9) was used to re-weight the simulated scattering events, in order to properly take into account the effect of the large vacuum bump which results from the much smaller beam pipe around the IP. It is worth mentioning that only the distribution of the vacuum profile was used, not its absolute value, with a rescaling to match the real vacuum pressure measured at the nearest vacuum sensor. After rescaling according to the real beam current and vacuum pressure, the simulation results can be compared with the experiment results.

Figure 4.28 shows the distribution of energy as a function of scattering position for the Bremsstrahlung positrons that are lost on the 45° window in the LER. The left plot corresponds to a uniform vacuum pressure (1 nTorr everywhere), and the right plot is after re-weighting by the simulated vacuum profile and rescaling by the effective atomic number of the residual gas [109]. It is quite clear that the Bremsstrahlung positrons lost on the window are mainly scattered near the IP ($\pm$1 m) after taking into account the vacuum profile. Positrons with lower energies ($<$2 GeV) mostly arise from scattering downstream of the IP, close to the window, which is consistent with expectations for charged particles deflected in magnetic fields as explained in Chapter 3.

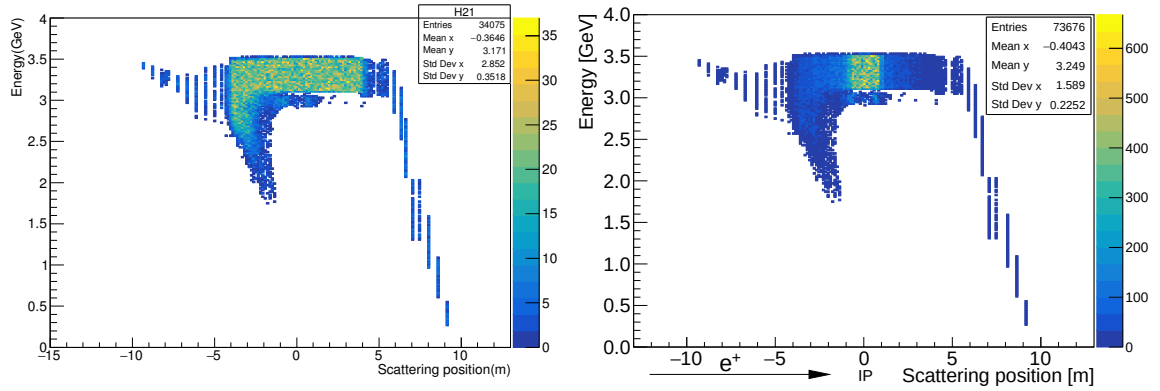


**Figure 4.28:** The energy of the Bremsstrahlung scattered positrons lost on the window as a function of their scattering position before (left) and after (right) being re-weighted by the vacuum profile, for the LER.

Figure 4.29 shows the energy distribution of Bremsstrahlung positrons lost on the window as a function of their horizontal incident angle, on left, and their energy spectrum, on right Even though the horizontal incident angle to the window are distributed in a range from 5 to 10 mrad, in the presence of the Tungsten radiator, the emitted charged secondary particles are almost the same. Therefore, our diamond detector installed just behind the Tungsten radiator is not sensitive to that angular distribution. The energies of the Bremsstrahlung positrons are mainly from 3 to 3.5 GeV, which is similar to the case of Bhabha positrons (3 to 3.4 GeV).

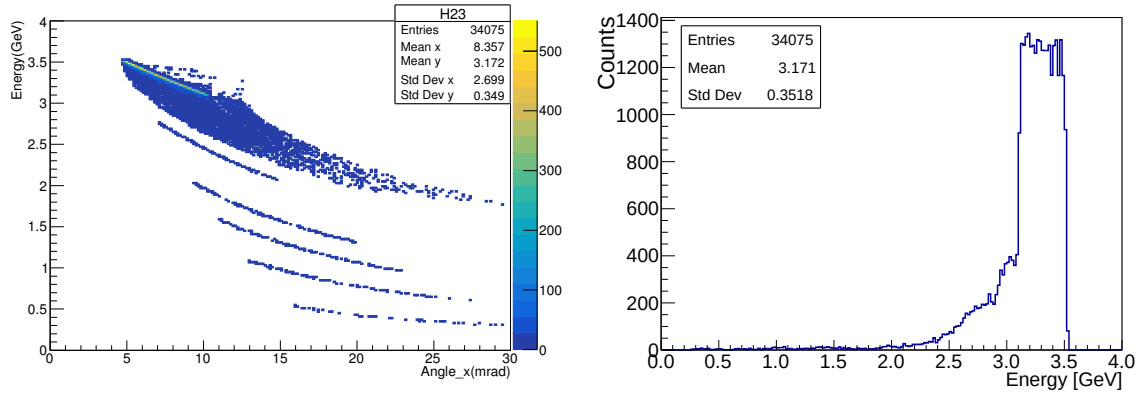


**Figure 4.29:** The energy of the Bremsstrahlung scattered positrons lost on the window as a function of their horizontal incident angle on the left and the energy spectrum for those Bremsstrahlung positrons on the right, in the LER.

Finally, the Geant4 model used to simulate the Bhabha positron detection efficiency was used again to estimate the signals induced by the Bremsstrahlung positrons. The fraction of Bremsstrahlung scattered positrons which will induce signals in the diamond detector with

thickness 140 $\mu m$ coupled with a C2 broadband current amplifier installed at the optimum location is 18% of the total lost particles on the window from Bremsstrahlung. The calculated loss rate for one bunch beam with a current of 1 mA can be used to estimate the loss rate from the Bremsstrahlung process in any configuration by rescaling with the total beam current and taking into account the vacuum pressure.

#### 4.3.2.2 Touschek scattering simulation for Phase-2.2

For the Touschek scattering process, as shown in Figure 4.25, one of the scattered particles gains energy and the other loses energy. Similar to the Bremsstrahlung scattering simulation, particle loss from Touschek process was also simulated with a bunch current of 1 mA/bunch for Phase-2.2.

Figure 4.30 shows the distribution of the energy of Touschek scattered positrons lost on the window as a function of their scattering position, on left, and their energy spectrum, on right. Similar to the Bremsstrahlung process, positrons lost on the window from the Touschek process are also mainly scattered around the IP ($\pm$1 m). However, the reason is different from the case of the Bremsstrahlung scattering, where the larger vacuum pressure near the IP was the dominating factor, here the extremely small beam size at the IP is the reason why the scattering position of Touschek positrons lost on window are mainly distributed near the IP region. In addition, the energy for those positrons needed to be between 3 and 3.5 GeV, similar to the case of the Bremsstrahlung and radiative Bhabha scattering processes, and that can more easily be achieved near the IP where the angular divergence of the beam is largest.

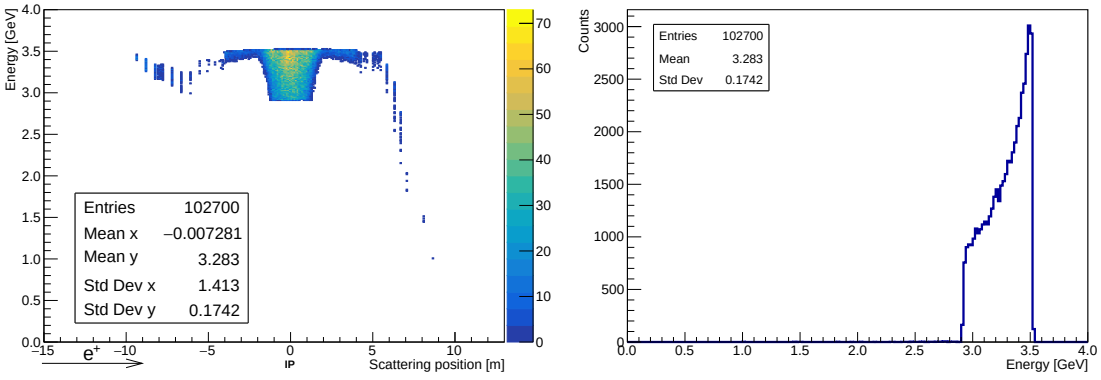


**Figure 4.30:** The energy of Touschek scattered positrons lost on the window as a function of their scattering position on the left and their energy spectrum on the right for the LER.

According to the simulation results from Geant4, the fraction of detected positrons by the diamond detector to the total lost positrons from Touschek positrons is the same as

for the Bremsstrahlung process. The total loss rate from the Touschek process for any beam configuration can be obtained by rescaling with the square of the bunch current and multiplying by the number of bunches in the train.

#### 4.3.2.3 Single beam loss rates for different phases of the SuperKEKB commissioning

After having simulated and tracked Bremsstrahlung and Touschek positrons to the QKBLP quadrupole in the LER and studied the induced signals in the diamond detector with thickness 140 $\mu m$ coupled with a C2 broadband current amplifier mounted at the optimum location, the detected loss rates can be calculated for a specified condition (1 single bunch with bunch current of 1 mA and an average vacuum pressure of 1 nTorr), and summarized in Table 4.2.

| $I_b$=1 mA/bunch, $P_{aver}$=1 nTorr | | | | |
|---|---|---|---|---|
| | Phase-2.0 | Phase-2.2 | Phase-2.3 | Phase-3 |
| Coupling factor | 0.1 | 0.05 | 0.014 | 0.0027 |
| Bremsstrahlung [$bunch^{-1}s^{-1}$] | 115.4 | 114.6 | 115.3 | 113.5 |
| Touschek [$bunch^{-1}s^{-1}$] | 20.2 | 26.3 | 41.4 | 87.6 |

**Table 4.2:** The detected single beam loss rates from Bremsstrahlung and Touschek processes by the diamond detector (140 $\mu m$ + C2) at the optimum location in the LER for different sub-phases of the SuperKEKB commissioning. The coupling factor is the assumed ratio of vertical to horizontal emittance, representing the residual cross-plane coupling following minimization by beam tuning.

After getting the loss rates for a single bunch with the specific conditions for each Phase, they can be rescaled to estimate the total background signals in the diamond detectors induced by single beam losses for any machine configuration. For example, for the diamond detector with thickness of 140 $\mu m$ installed at the optimum position in the LER, the total background rate caused by single beam losses is expected to be $8.6 \times 10^5/s$ in the nominal case of SuperKEKB (detailed machine parameters can be found in Table 2.1). In the mean time, the total number of Bhabha events detected by the same diamond detector is expected to be about $1.2 \times 10^9/s$, which implies a Signal-Noise-Ratio (SNR) larger than 1000.

## 4.4 Radiation damage estimation of the diamond detector

As already described, the extremely high luminosity and the requirement by the dithering feedback system of a high accuracy will lead the luminosity monitor based on the diamond detectors installed in the LER to continuously work in a harsh radiation environment. The diamond detector might be partly damaged in such a high radiation situation thus reducing the

detection efficiency. Therefore, it is important to understand the situation that the diamond will experience for different luminosity levels and find out the optimum balance between high relative precision of the fast luminosity signals and the detector's survival.

The radiation tolerance of diamond detectors has been studied extensively by the RD42 collaboration since 1995 [110–114]. In general, ionizing particles dominate the signal generation in the diamond detectors and the energy that they deposit is not sufficient to damage the diamond lattice thus not important in terms of radiation damage. Rather, radiation damage is determined by the so-called Non-Ionizing Energy Loss (NIEL) involving elastic scattering by the diamond lattice [115], which will cause the atoms displacement from its site if the NIEL is larger than the lattice binding energy, and thereby destroy the diamond lattice and induce the diamond detector radiation damage. The total radiation damage with respect to the type and energy of the primary particle can be calculated based on the NIEL model.

## Non-Ionizing Energy Loss (NIEL)

The NIEL hypothesis expresses the specific stopping power of the material, S = dE/dx as the sum of the energy transfer from ionization $S_i$ (energy to electrons) and a non-ionizing part $S_n$ (energy to nuclei) [116]. To calculate the fraction of $S_n$ in the total stopping power $S = S_i + S_n$, the Lindhard partition function $\xi(T)$, which depends on the kinetic energy of the primary particle, is used.

$$\begin{aligned} S = S_n + S_i = \frac{dE_n}{dx} + \frac{dE_i}{dx} \\ \xi(T) = \frac{S_n}{S} \end{aligned} \tag{4.7}$$

The NIEL is usually expressed as the stopping power in units of $keV * cm^2/g$ or NIEL cross-section for each atom in units of $MeV * mb$. The conversion between these two units is shown below:

$$\sigma_{NIEL}[MeVmb] = \frac{NIEL[GeV] * u[g/mole]}{d[cm] * \rho[g/cm^3] * N_A[mol^{-1}]} * 1000[\frac{MeV}{GeV}] \times 10^{27}[mb/cm^2] \tag{4.8}$$

where $u$ is the molar mass, $N_A$ is the Avogadro constant, $d$ is the thickness of the detector and $\rho$ is the density of the detector material.

Based on the Thomas-Fermi model, the partition function $\xi(T)$ is calculated in the Lindhard screened potential scattering theory [117]. Different from the silicon community in which the equivalent fluence is converted to 1 MeV neutrons for comparison, since most of the experimental irradiation data is available for 24 GeV protons in the diamond community,

the radiation damage for a particular particle is therefore normalized to 24 GeV proton equivalents. Figure 4.31 [118] shows a comparison of the calculated radiation damage in diamond caused by different types of particles with different kinetic energies using the NIEL model.

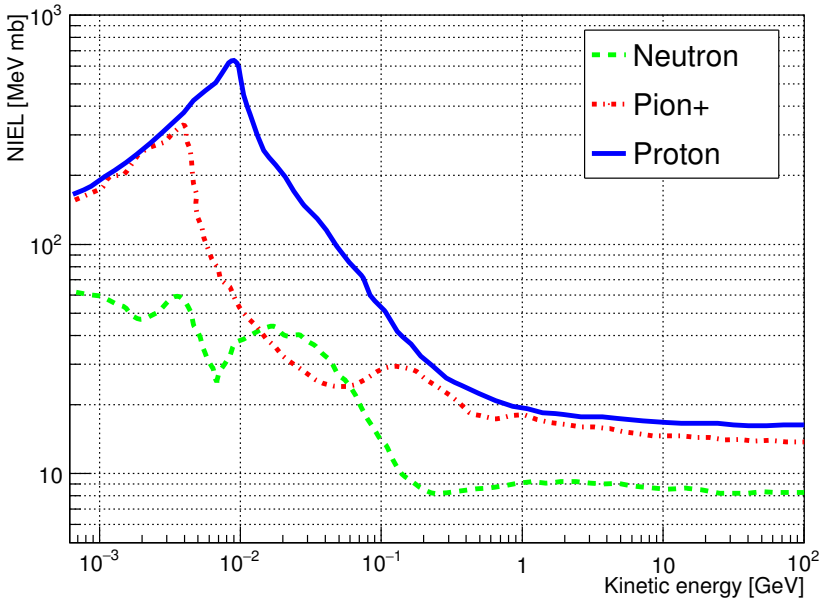


**Figure 4.31:** Radiation damage calculated for diamond with the NIEL model for different particle types and kinetic energies [118].

From the Figure 4.31, the NIEL cross-section is 16.59 MeV*mb for protons with energy of 24 GeV in the diamond detector, which corresponds to an average deposited energy of 40.89 eV in the diamond detector [$0.4 \times 0.4\ cm^2$, with thickness $0.014\ cm$] caused by the non-ionizing energy loss.

### 4.4.1 Signal degradation due to radiation damage

As far as the direct performance of the detector after radiation damage is concerned, the degradation of the magnitude of signals as a function of the cumulative radiation is often used as an important indicator. For example, the RD42 collaboration had performed several irradiation studies to analyze the degradation with accumulated radiation dose of the charge collection distance (CCD) of diamond detectors [111, 119–121]. A model was built to describe the reduction of the CCD of the diamond detector as a function of the radiation damage based on these studies. The charge collection efficiency of the diamond detector is determined by the mean free path length $\lambda$ of the charge carriers: $e^- - hole$ pairs. For a diamond detector with a mean free path length larger than its thickness $d$, the charge

collection efficiency is 100% thus the CCD equals the thickness $d$, which is the case for standard sCVD diamond. However, for pCVD diamond detector, the CCD is reduced due to the impurities at grain boundaries.

The standard model to describe the radiation damage is based on the assumption that the number of defects $N$ increases linearly with respect to the radiation damage:

$$N(\Phi) = N_0 + k_N \times \Phi \tag{4.9}$$

where $\Phi$ is the fluence of the particles causing radiation damage, $k_N$ is the damage constant defining the proportionality, and $N_0$ corresponds to the initial number of defects for the un-irradiated diamond detectors.

Since the lifetime $\tau$ of the charge carrier is inversely proportional to the number of defects $N$ in the lattice, and the mean free path length $\lambda$=$\tau \times v_{drift}$, $v_{drift}$ is the drift velocity of charge carrier and it stays constant for a constant electric field, we can re-write the Equation 4.9 as below:

$$\frac{1}{\lambda(\Phi)} = \frac{1}{\lambda_0} + k \times \Phi \tag{4.10}$$

The radiation damage expressed in Equation 4.10 is the commonly used parameterization in the diamond community. However, the mean free path length $\lambda$ can not be measured directly, so it was typically converted into the equivalent in CCD:

$$\frac{1}{CCD(\Phi)} = \frac{1}{CCD_0} + k \times \Phi \tag{4.11}$$

The CCD of a diamond detector which has been subjected to radiation damage is well characterized by the radiation constant $k$, resulting from the particle type and kinetic energy. Besides, the radiation damage mechanism for the pCVD and sCVD diamond detectors are the same except that the sCVD diamond detector has larger initial charge collection distance $CCD_0$ [122, 123]. Figure 4.32 [116] shows the CCD degradation of the both pCVD and sCVD diamond detectors after irradiated by 24 GeV protons, fitted with Equation 4.11. The radiation constant of $k = 6.5 \times 10^{-19}\ cm^2 \mu m^{-1}$ was obtained from the fitted parameters [124–126]. In those studies, the CCD of the diamond detector was measured regularly for different irradiation fluences. This standard model describes as well the CCD reduction of sCVD diamond detector with the same $k$ factor after considering the difference of the initial CCD value: $CCD_0$, which is much larger for the sCVD than pCVD diamond detectors.

After getting such a model to well agree with the experimental results on CCD reduction (see Figure 4.32), we can express the CCD reduction as a function of the NIEL, based on the NIEL cross-section shown in Figure 4.31 for the diamond detector with thickness of

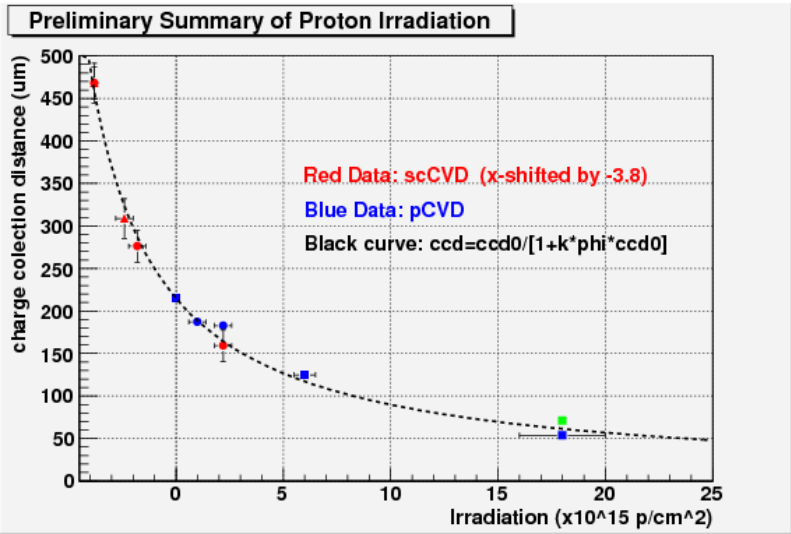


**Figure 4.32:** The charge collection distance degradation as a function of the irradiated fluence of 24 GeV protons from the RD42 collaboration [116].

140 $\mu m$ ($0.4 \times 0.4\ cm^2$). The results is shown in Figure 4.33, including the CCD value and normalized CCD to the $CCD_0$, as a function of the deposited energy in terms of NIEL.

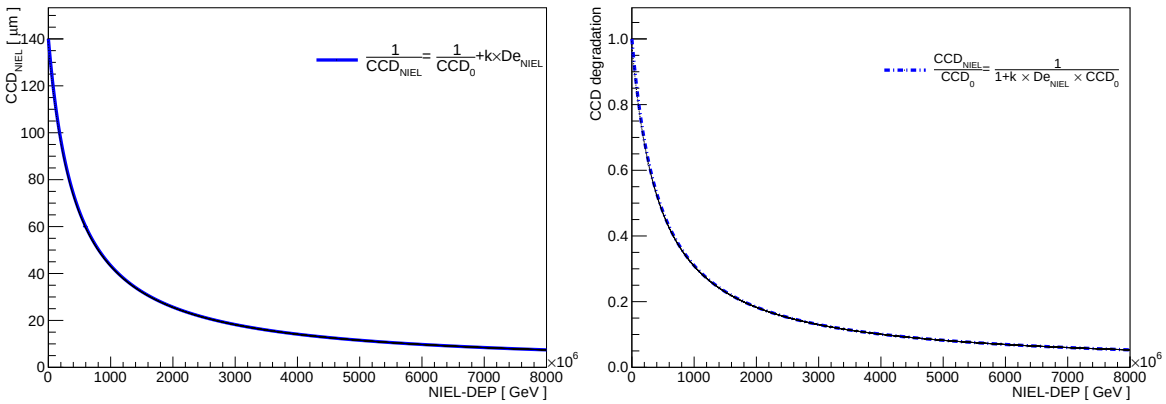


**Figure 4.33:** The CCD (on the left) and a normalized CCD degradation (on the right) of the sCVD diamond detector with thickness of 140 $\mu m$ as a function of the NIEL deposited in the detector.

For the sCVD diamond detector with thickness of 140 $\mu m$, its initial CCD is the same as its thickness. The CCD decreases by a factor of 2 after receiving deposited energy in terms of NIEL of about $4.5 \times 10^8$ GeV, and stay above 10% of $CCD_0$ for deposited energy in terms of NIEL up to $4 \times 10^9$ GeV. Based on the hypothesis that the lattice defects are caused by the NIEL, and are proportional to the total deposited energy from NIEL, then we could transform this CCD degradation in terms of deposited NIEL based on the fluence of particles, once we know their NIEL cross-section.

### 4.4.2 NIEL in diamond detector simulation in LER

To estimate the radiation damage of the diamond detector in the LER at SuperKEKB, the NIEL deposited in the diamonds was simulated with the Monte-Carlo code FLUKA [89], which has been widely used for the simulation study of atoms displacement (DPA) and NIEL when estimating the radiation damage of the materials [116, 127, 128]. The FLUKA model was built in the same way as the Geant4 model which was used to estimate the Bhabha positron induced signal detection efficiency described in Section 4.1.3 (see Figure 4.14). To enable the neutron production through the evaporation of excited nuclear resonances, the "SDUM" argument for the FLUKA "PHYSICS" control card was set to the value "EVAPORAT"; The new FLUKA model of evaporation without heavy fragmentation was implemented through the "PHYSICS" card. To provide the maximum precision, the "PRECISIO" for the "DEFAULTS" card was also set.

By using the "USRBIN" card, the deposited energy in terms of the NIEL can be obtained in unit of $GeV/cm^3$ normalized to 1 primary particle. Bhabha positrons lost on the window (red part in Figure 4.6: left) are used as input to the FLUKA simulation of the 45° window, with their momentum and position information. Two diamond detectors with thickness of 140 $\mu m$ were put at two typical locations that correspond to the relative precision of 0.1%(A) and 1%(B) for the train integrated luminosity signals at 1 kHz in the nominal luminosity ($8 \times 10^{35}\ cm^{-2}s^{-1}$) case at SuperKEKB (described in Section 4.1), as shown in Figure 4.34.

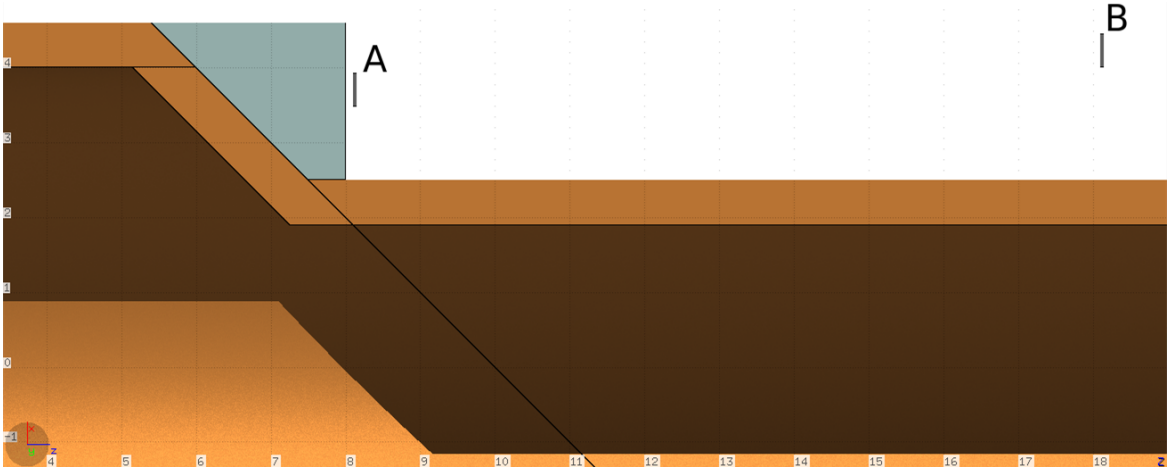


**Figure 4.34:** FLUKA model of the window shaped beam pipe in the LER to simulate the deposited energy in terms of the NIEL in the diamond detectors located at two typical locations that ensure a relative precision of 0.1%(A) and 1%(B) for the train integrated luminosity signal at 1 kHz with the nominal luminosity of SuperKEKB.

$10^6$ Bhabha positrons were used for the simulation, the NIEL was expressed as $GeV/cm^{-3}$ normalized to 1 Bhabha positron. The simulated 2-D distribution of the NIEL is shown in

Figure 4.35, the hottest regions are the Tungsten radiator and copper beam pipe regions, the two hot rectangle areas after the Tungsten radiator correspond to the diamond detectors. Their received obviously higher NIEL than the surrounding air region.

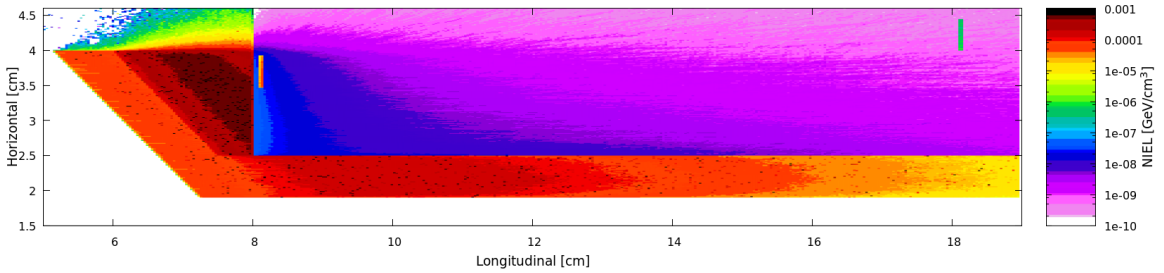


**Figure 4.35:** The NIEL distribution in the LER 45° window shaped beam pipe region including two diamond detectors at two typical locations (see text).

According to the simulation, the deposited energy from NIEL is $5.06 \times 10^{-5}\ GeV/cm^3$ for the diamond detector at the most sensitive location (A in Figure 4.34), corresponding to a deposited energy of $1.77 \times 10^{-7}\ GeV/e^+$ in terms of the NIEL in the diamond detector with thickness of 140 $\mu m$ ($0.4 \times 0.4\ cm^2$). In the mean time, the same detector located 10 cm further down longitudinally and 0.6 mm further out horizontally, at position B, with detection efficiency reduced by a factor of 100, will receive a deposited energy of about $1.89 \times 10^{-9}\ GeV/e^+$ in terms of the NIEL.

Since the deposited energy from NIEL was obtained with respect to each Bhabha positron lost on the window, considering the CCD degradation as a function of deposited energy from NIEL (as shown in Figure 4.33), the CCD degradation as a function of the number of positrons lost on the window can be obtained reliably based on the NIEL scaling hypothesis. The rescaled results are shown in Figure 4.36. From the result, the CCD decreases by a factor of 2 for the 0.1% luminosity signal relative precision case after $2.53 \times 10^{15}$ Bhabha positrons lost on the window; for the 1% luminosity signal relative precision case, the number of lost Bhabha positrons is $2.39 \times 10^{17}$ for the same CCD degradation. If we consider the nominal luminosity case of SuperKEKB, the loss rate of Bhabha positrons on the window is about $5.5 \times 10^9/s$ in LER, which means the CCD of the diamond detector located at the most sensitive position (A) will decrease by a factor of 2 after $4.6 \times 10^5$ s ($\approx$ 5.3 days) for full luminosity operation with maintaining the relative precision at 0.1% for the train integrated luminosity signal at 1 kHz. On the other hand, if we accept a relative precision of 1% for the train integrated luminosity at 1 kHz, which corresponds to the same diamond detector installed at position B, for which the detection efficiency is about 100 times lower, the CCD will decrease by a factor 2 after $4.35 \times 10^7$ s ($\approx$ 502 days) full luminosity operation.

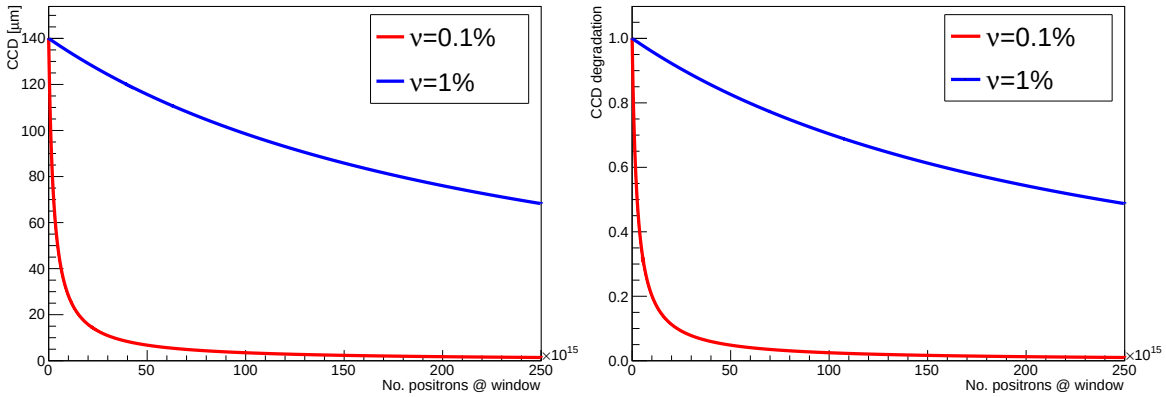


**Figure 4.36:** The CCD (on the left) and normalized CCD degradation (on the right) of the sCVD diamond detector with thickness of 140 $\mu m$ as a function of the number of the Bhabha positrons lost on the 45° window in the LER.

From the point view of the diamond detector's radiation damage, it is quite clear that the relative precision of the train integrated luminosity signal should be maintained as low as possible to ensure a long lifetime for the detector. Based on the NIEL scaling hypothesis, a relative precision of 1% makes it possible that the diamond detector works well for more than 500 days, which is quite acceptable. On the other hand, it should be checked if the relative precision of 1% is sufficient for the dithering orbit feedback system, which will be described in Section 4.5.

In addition, all the results for the radiation damage of diamond detector were obtained from simulation based on FLUKA, even though the simulation model including the geometry, material and the physics process was carefully treated, while its reliability is not so clear for many reasons, e.g. the NIEL hypothesis, the complicate radiation component, FLUKA disagreement to the measurement and so on. Therefore, the performance of the diamond detector should be monitored in the future with respect to the different integrated luminosities.

## 4.5 Horizontal dithering orbit feedback simulation

Since we can simulate realistic signal sequences for the diamond detectors at the speed required for the luminosity monitor at SuperKEKB, including the signal processing by the DAQ, to provide the simulated train integrated luminosity signals, we now aim to combine it with the ground motion characteristics and estimation of the luminosity degradation as a function of the beam-beam offset, to provide a start-to-end model of the horizontal dithering orbit feedback system. This will enable to check the effectiveness of the luminosity driven feedback system and for the measured ground motion spectrum.

Figure 4.37 shows the simulation diagram of the horizontal dithering orbit feedback system to maintain the very high luminosity in the presence of the mechanical vibration caused by ground motion. As already mentioned in Section 3.2, the LER beam is dithered sinusoidally at 79 Hz with a small amplitude $\Delta x$, typically of $0.1\sigma_x$. The measured ground

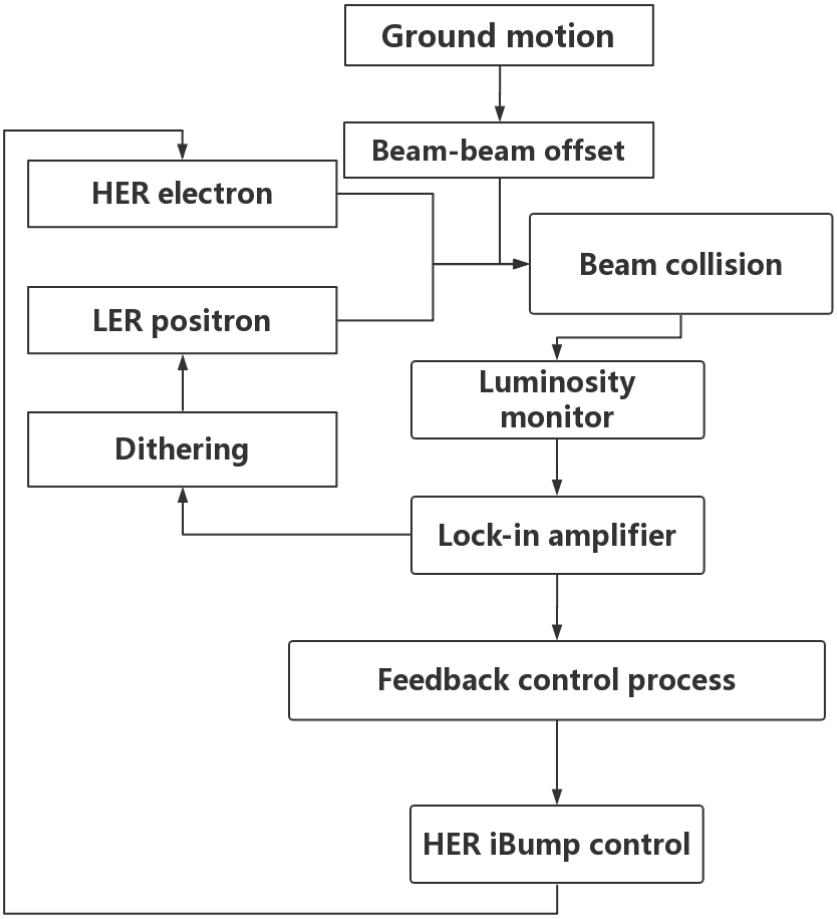


**Figure 4.37:** Flow-chart of the start-to-end simulation for the dithering orbit feedback system to maintain very high luminosity in the presence of mechanical vibration caused by ground motion.

motion data at SuperKEKB is used to represent the offset $x_0$ between the two colliding beams as a function of time. The train integrated luminosity at 1 kHz is then provided based on the signal sequence construction and processing described in Section 4.2, according to the instantaneous luminosity in the presence of the beam-beam offset. Then the 1 kHz train integrated luminosity signals are fed to the lock-in amplifier providing the dithering driven signal to the dithering magnet system, the lock-in amplifier processes the fast luminosity signal and outputs a signal that is proportional to the offset in a certain range. This signal is then processed by the feedback control part to calculate a correction kick signal sent to the

HER iBump control part in order to kick the HER beam and thereby cancel or at least reduce the offset between the two colliding beams.

### 4.5.1 Preparatory work

To perform such a full simulation of the dithering orbit feedback system at SuperKEKB, there are three key elements that are needed: (1) representative ground motion data that can be used as beam-beam offset information in the time domain; (2) a calculation of the luminosity degradation as a function of the beam-beam offset for the SuperKEKB case; (3) A proper model of the lock-in amplifier that extracts the beam-beam offset information from the luminosity signals.

#### Ground motion data

The vibration of the SuperKEKB tunnel floor and of some of the relevant magnets has been measured and reported [56, 129, 130]. One typical measurement is on the final focus quadrupole magnet: QC1RE. The measured PSD (Power Spectrum Density) and integrated amplitude spectrum are shown in Figure 4.38.

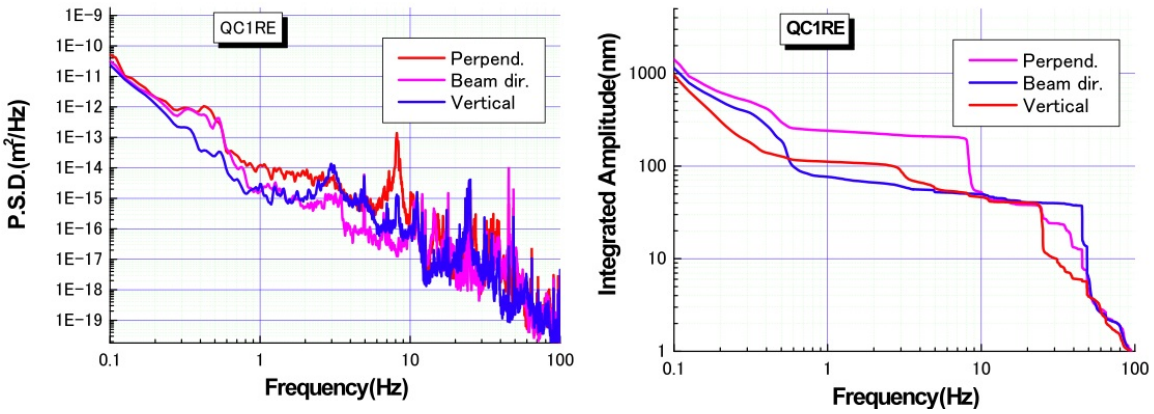


**Figure 4.38:** PSD (on the left) and integrated amplitude (on the right) of the QC1RE magnet vibration: the horizontal direction (labeled Perpend.) is shown in red on the left plot and in pink on the right plot.

The range of the measured data is only from 0.1 to 100 Hz. The RMS amplitude of the vibration in the perpendicular (horizontal) direction is about 0.3 $\mu m$ at 1 Hz and 1.2 $\mu m$ at 0.1 Hz. Using the PSD spectrum of the vibration induced by ground motion, examples of vibration data in the time domain can be obtained by applying an inverse Fast Fourier Transform (iFFT) with a random phase, see Figure 4.39. This vibration data in time domain is generated at 1 kHz to be consistent with the frequency of the fast luminosity signals. The

length the vibration data can be adjusted by changing the frequency resolution of the PSD with some data insertion methods (e.g. linear interpolation method). The obtained vibration data at 1 kHz will be used to represent the beam-beam offsets to check the performance of the dithering orbit feedback system.

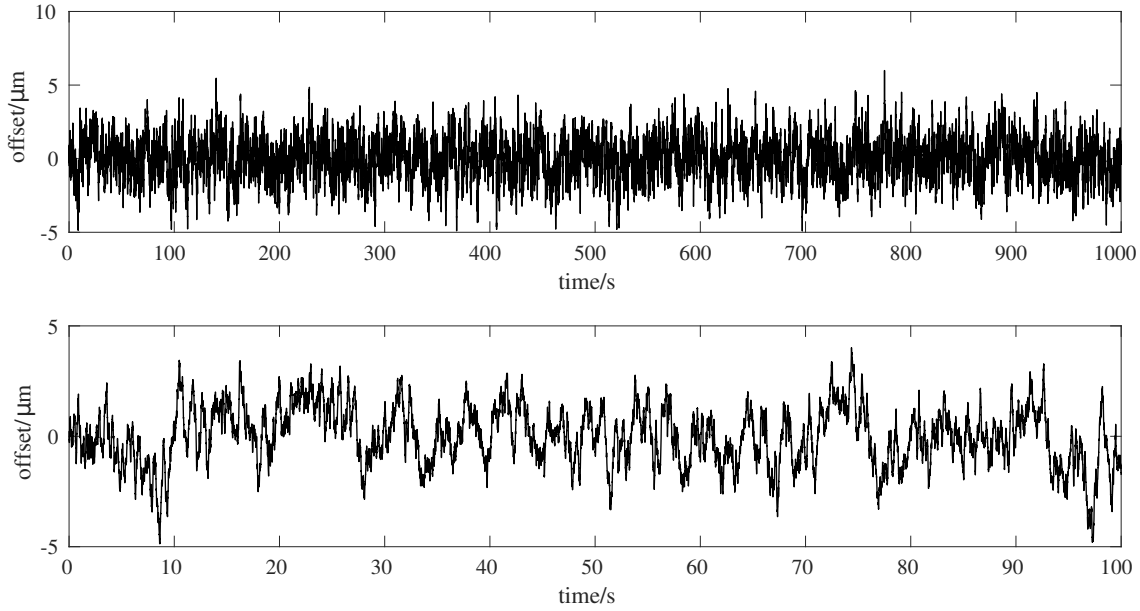


**Figure 4.39:** Example of ground motion induced vibration in the time domain obtained from the measured PSD spectrum (Figure 4.38) by application of iFFT.

### Luminosity degradation calculation

As it already has been introduced in Section 3.2, the luminosity degradation follows in the first approximation a Gaussian distribution as a function of the beam-beam offset resulting from the convolution of the two Gaussian distributed beams. However, in the horizontal plane, the calculation of the luminosity loss due to a beam-beam offset must in addition take into account the large crossing angle and extremely small vertical $\beta_y^*$ function at the IP, smaller than the actual bunch length, which are specified as part of the "nano beam collision scheme" [42], as well as the beam blow-up effects at high luminosity from non-linear beam-beam effects. Detailed simulations have been done with different vertical $\beta_y^*$ at the IP by KEK colleagues (see Figure 4.40) [57]. It is clear that due to the hourglass, beam blow-up and other effects, the luminosity degradation due to a horizontal beam-beam offset at the IP becomes important for the nominal $\beta_y^*$ value. As a comparison, the luminosity degradation for a pure head-on collision with the nominal beam parameters as a function of beam-beam offset was also calculated. The sensitivity is in that case slightly stronger than the real SuperKEKB

case with its nano-beam scheme, with a difference within 5% for beam-beam offsets not exceeding the beam size ($\sim 10\ \mu m$) . To simplify the simulation, the luminosity degradation factor due to horizontal beam-beam offsets for head-on collision mode is used here as a conservative and reasonable approximation for the realistic dependence in the case of the nominal luminosity operation.

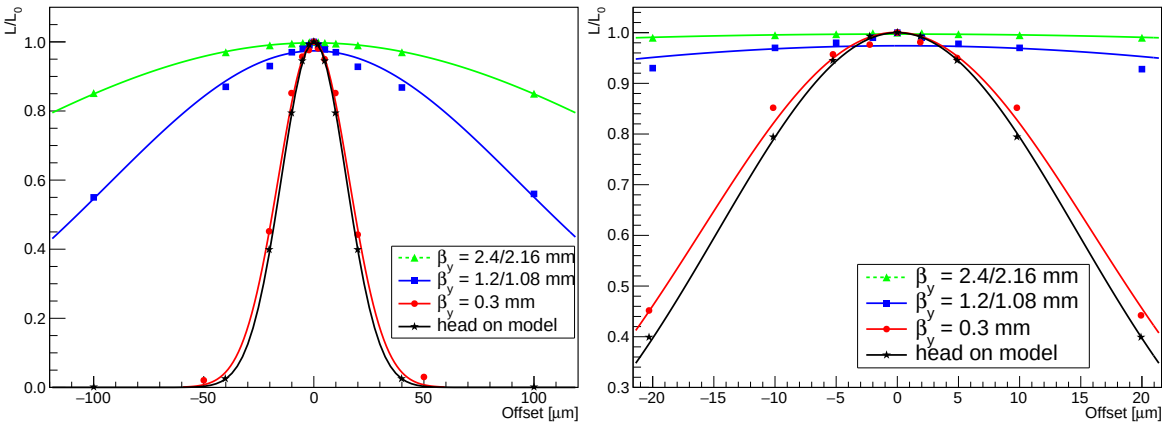


**Figure 4.40:** Luminosity degradation as a function of beam-beam offset simulated with different $\beta_y$ at the IP for the nano-beam collision geometry, and for the head-on model (with $\beta_y^*$ = 0.3 mm).

The instantaneous luminosity due to a horizontal beam-beam offset and when sinusoidal dithering is applied can be expressed as shown in Equation 4.12 for the case of a head-on collision:

$$L = L_0 exp\left[-\frac{[x_0 + \Delta x sin(2\pi f t)]^2}{2\Sigma_x^2}\right], \quad \Sigma_x^2 = \sigma_{x+}^2 + \sigma_{x-}^2 \tag{4.12}$$

where $L_0$ is the peak luminosity without horizontal beam-beam offset, $x_0$ is the offset between the two beams, $\Delta x$ is the dithering amplitude, $f$ is the dithering frequency (79 Hz) and $\sigma_{x\pm}$ correspond to the horizontal beam sizes of both beams.

Figure 4.41 shows the luminosity loss as a function of dithering amplitude and beam-beam offset normalized to the horizontal beam size. It is clear that the smallest possible dithering amplitude capable of creating a detectable luminosity change is preferable because it results in the smallest luminosity loss when there is no beam-beam offset between the two beams. For example, when the LER beam is dithered at 79 Hz with an amplitude of $0.1\sigma_x$ at SuperKEKB, the luminosity loss caused by dithering is about 0.12% for a perfect alignment of the two colliding beams. In the following simulation, the LER beam is dithered at 79 Hz sinusoidally with an amplitude of $0.1\sigma_x$.

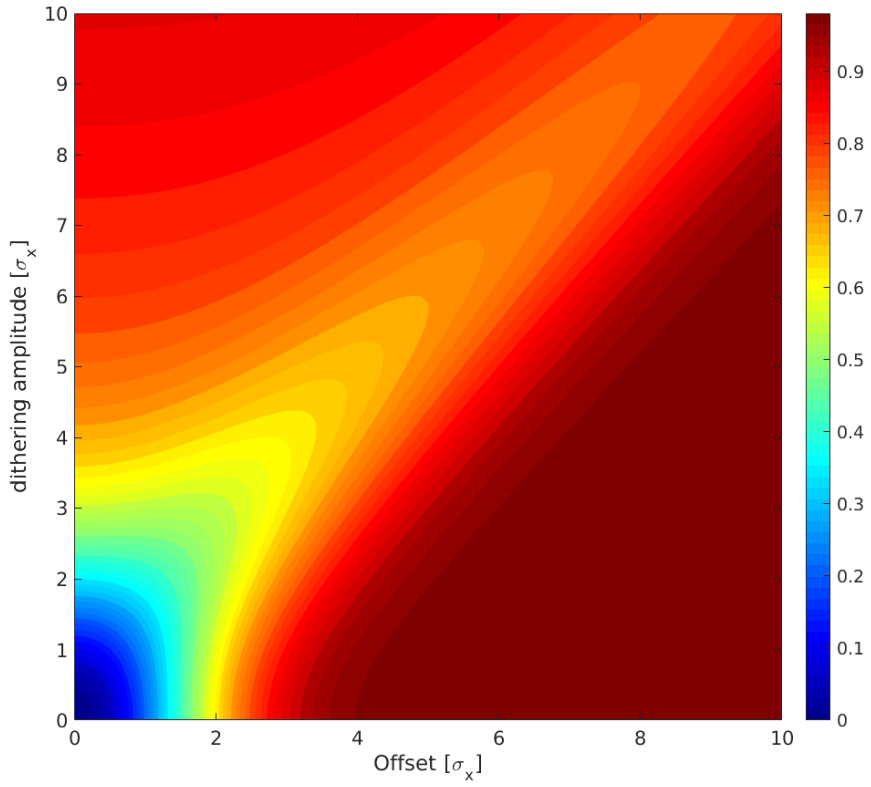


**Figure 4.41:** Luminosity loss map for different dithering amplitudes and offsets normalized to the horizontal beam size.

### Lock-in amplifier model

At SuperKEKB, an analog lock-in amplifier bought from Ametek Advanced Measurement Technology is used to extract the fast Fourier component of the fast luminosity signals at the dithering frequency (79 Hz), at a rate corresponding to the frequency of the applied orbit correction (1 Hz) [60]. Here, a two-step lock-in amplifier model is built to process the simulated luminosity signals, as shown in Equation 4.13: $R$ is the magnitude, $V_i$ is the luminosity signal amplitude, $f$ is the dithering frequency. The output of the lock-in amplifier $R$ is roughly proportional to the beam-beam offset for values not exceeding the horizontal beam size, and reaches a minimum when beams overlap perfectly.

$$\begin{aligned} R &= \sqrt{X^2 + Y^2} \\ X &= \sum V_i \times cos(2\pi f t) \\ Y &= \sum V_i \times sin(2\pi f t) \end{aligned} \tag{4.13}$$

The control algorithm of the dithering orbit feedback system then uses the Newton method to calculate the needed corrections $X_n$ every second, based on the slopes obtained

for the variation of the Fourier component at the dithering frequency with respect to the successive corrective moves. The sign ambiguity resulting from the evenness of the luminosity dependence with offset in Equation 4.12 is resolved by comparing the phase of the magnet driven current modulation used to dither the LER beam orbit with that of the resulting luminosity modulation.

$$\Delta b_n = K_p X_n + K_I \int_{k=1}^{n} a_I^{n-k} X_k \tag{4.14}$$

The iBump at the IP reduces the offset by moving the HER beam to a new position $b_n$. The proportional and integral parts of the standard PID (Proportional Integral Derivative) controller are used to calculate the correction moves $\Delta b_n$ to be implemented, as shown in Equation 4.14. $K_p$ and $K_I$ correspond to proportional and integral gains which are assigned values between 0 and 1. In addition, the integral correction is based on an exponentially weighted sum of past offsets. The weighting parameter $a_I$ is given a value slightly less than 1 so that old offsets are gradually forgotten (typically $0.9<a_I<1$). The integral corrections fix the steady-state residual error in a purely proportional control, as errors accumulate despite the proportional correction, the integral pushes harder toward the center. The tuning should begin with a small gain $K_I$ to avoid large overshoot.

### 4.5.2 Verification of feedback simulation

To investigate the performance of the horizontal dithering orbit feedback system, several horizontal offsets ($0.5\sigma_x$, $-\sigma_x$, and $1.5\sigma_x$) were introduced deliberately to test the ability of recovering and later maintaining the luminosity at a stable level, based on simulated fast luminosity measurements at 1 kHz with relative precision of 1%. The result is shown in Figure 4.42. The luminosity is plotted in blue (with and without feedback), the simulated fast luminosity signals at 1 kHz and the output signals of the lock-in amplifier, representing the magnitude of the fast Fourier component at the dithering frequency, are plotted in green and the offsets between the two beams in red (without feedback) and pink (with feedback). It is clear that the feedback system can correct these introduced horizontal beam-beam offsets and thus recover the luminosity by minimizing the output of the lock-in amplifier, without overshooting, and then maintain the luminosity at a quite stable level, by steering the HER beam toward the LER beam and thereby achieving optimum overlap between the two colliding beams.

A sine wave with a fixed frequency of 0.1 Hz and an amplitude of $2 \times \sigma_x$ was used as beam-beam offset to study the influence of the correction frequency on the performance of

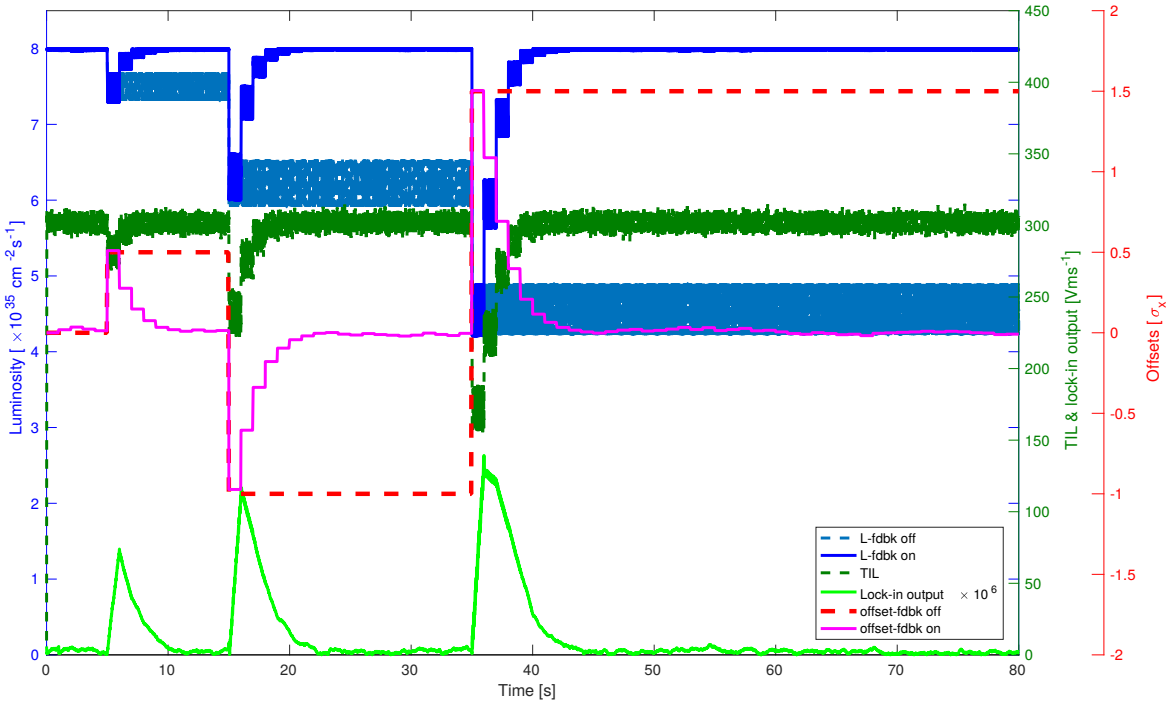


**Figure 4.42:** Simulated performance of feedback algorithm with several successive offsets. The luminosity is plotted in blue (with and without feedback), the simulated fast luminosity signal TIL in dark green, the magnitude of Fourier component at 79 Hz of the simulated fast luminosity signals in light green, and the offset between the two beams in red (without feedback) and pink (with feedback).

the feedback system, the result is shown on the left plot of Figure 4.43. It is obvious that correcting at high enough frequency is important. However, limited by the damping and phase delay induced on the magnetic field by the vacuum beam pipe, also the speed of the PLC control system at SuperKEKB [60], the maximum correction frequency is 1 Hz, thus the following simulations are based on a 1 Hz correction frequency. A sine wave with different frequencies and an amplitude of $2 \times \sigma_x$ was then also used to test the performance of the dithering feedback system with such a correction frequency of 1 Hz, see the plot on the right of Figure 4.43. It is clear that for correction frequency of 1 Hz, the feedback system can recover the luminosity to better than 98% if the frequency of the sine wave is about 30 times lower than the correction frequency. For higher frequencies than the correction frequency, the feedback system does not work anymore.

The dithering orbit feedback system works very well to mitigate the luminosity degradation caused by beam-beam offsets at low frequency ($f_{gm} \leq f_{correction}/30$) and to maintain the luminosity when there is significant vibration with higher frequencies. In the horizontal direction, the ground motion induced vibration is not serious at all at 0.1 Hz (see Figure 4.38) compared to the beam size, therefore corrections at a rate of 1 Hz should in principle be

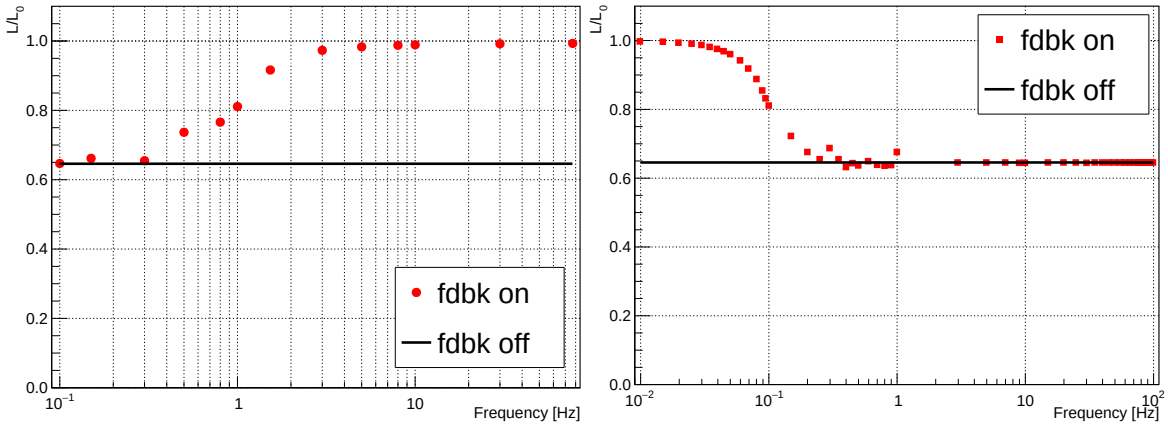


**Figure 4.43:** Left: Performance of the dithering feedback system as a function of the correction frequency when a sine wave with amplitude of $2 \times \sigma_x$ at 0.1 Hz is used as beam-beam offset to be corrected; Right: Performance of the dithering feedback system for sinusoidal beam-beam offsets as a function of the frequency when correcting at 1 Hz.

sufficient for beam orbit correction and stabilization in the horizontal plane at SuperKEKB. This will be confirmed in the next section using an explicit ground motion spectrum.

### 4.5.3 Feedback simulation with realistic GM spectrum

The measured PSD spectrum described in Section 4.5.1 was combined with an *ad hoc* extension down to 0.01 Hz, where the RMS integrated amplitude of GM is about 30 $\mu m$ [131], for usage as input to an inverse Fast Fourier Transform, to generate a set of statistically independent GM data sequences in time domain and to represent the successive random beam-beam offsets in the dithering feedback simulation. Figure 4.44 shows the feedback simulation results for the Phase-3 optics, assuming train integrated luminosity measurements at 1 kHz with a relative precision of 1%. In the plot, the luminosity with and without feedback, the train integrated luminosity signal provided by the diamond detectors and the beam-beam offsets with and without feedback are shown over a period of 3600 s. As it can be seen, the feedback system is able to recover the luminosity in the presence of such typical GM effects expected in the horizontal plane at SuperKEKB by maintaining the RMS value of the beam-beam offsets within 1.25 $\mu m$.

Without feedback correction, the luminosity loss would be larger than 60% from such GM induced horizontal beam-beam offsets, which have a RMS value of 30 $\mu m$ at 0.01 Hz. With the feedback corrections, the luminosity loss is only about 0.5% including the part caused by the dithering itself. Figure 4.45 shows the comparison of the beam-beam residual offsets with (red) and without (black) feedback. It is clear that good performance was obtained for a correction frequency at 1 Hz due to the small magnitude of the GM

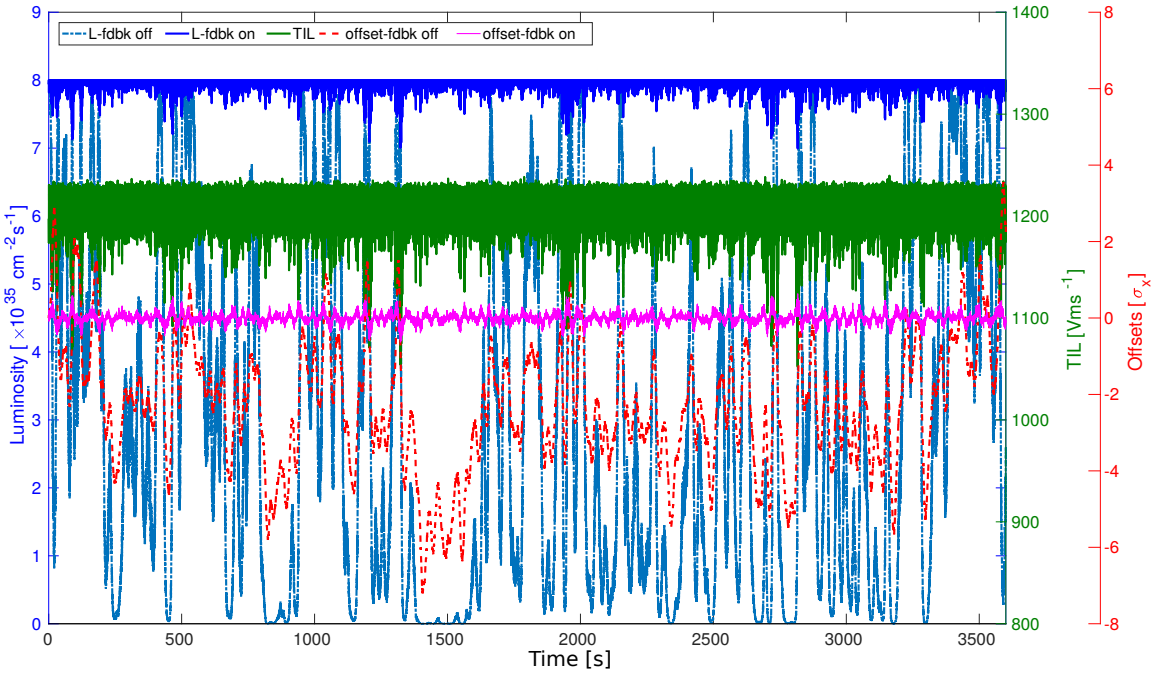


**Figure 4.44:** Luminosity, train integrated luminosity signal provided by diamond detector and the beam-beam offset with and without feedback for Phase-3 optics over a period of 3600 s.

induced horizontal vibrations relative to the horizontal beam size at frequencies above 0.05 Hz. A relative precision of 1% at 1 kHz for train integrated luminosity signals at nominal luminosity was assumed, and with the change of the luminosity due to beam-beam offset, the relative precision was scaled according to $1/\sqrt{N_{Bha}}$.

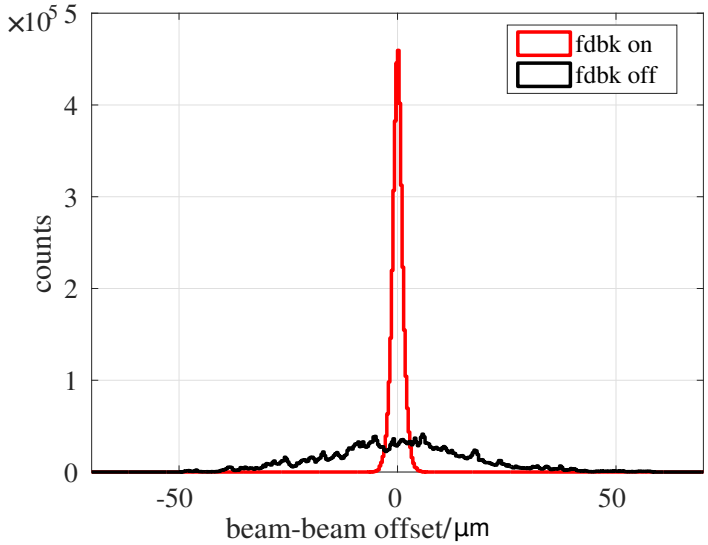


**Figure 4.45:** RMS beam-beam offset due to GM with (about 1.25 $\mu m$) and without feedback (about 15 $\mu m$).

Obviously, the relative precision of the luminosity monitoring signal needs to be good enough to accurately compute the size and sign of the beam-beam offsets in the lock-in amplifier model. If the relative precision is too bad, if it for instance covers the signal change due to the orbit dithering, the correct sign information will become more difficult to obtain, resulting in a potentially compromised corrections. Confusion from poor precision can in principle be mitigated by increasing the amplitude of dithering, however that will also reduce the average luminosity. To investigate the impact of the luminosity signal's relative precision, signals with different relative precision were used as input to the simulation model, all other conditions being the same. The results are shown in Figure 4.46. It is obvious that the residual beam-beam offsets are smaller (corresponding to a better luminosity under the same condition) with a better relative precision in the presence of the same GM induced vibration when the dithering feedback system is activated.

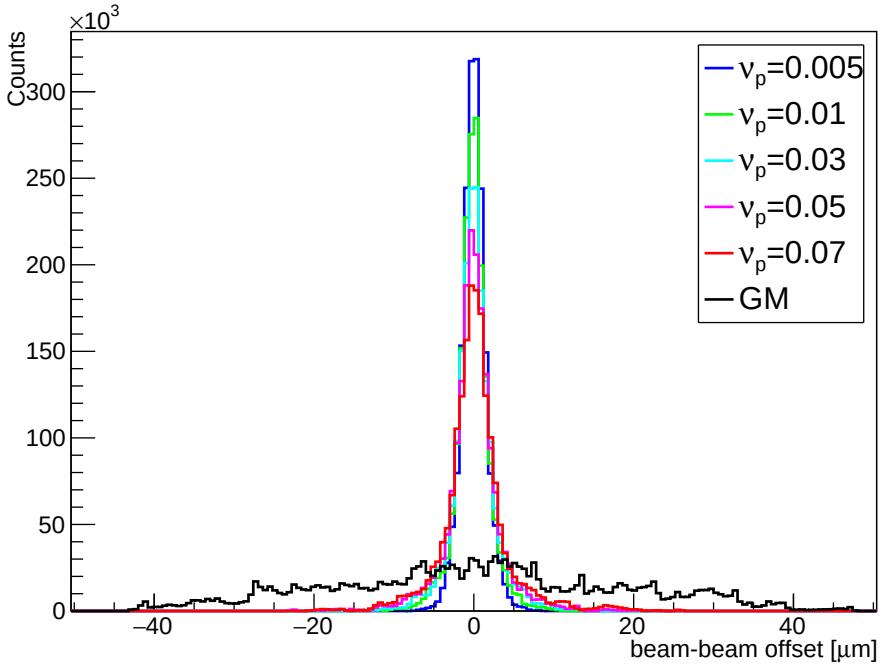


**Figure 4.46:** Residual beam-beam offset with feedback for different values of the relative luminosity precision: $\nu_p$.

Figure 4.47 shows the RMS values of the residual beam-beam offsets on left and the luminosity ratio with feedback to the ideal case on right as a function of the relative precision of the train integrated luminosity signals. The results show that the performances are almost proportional to the luminosity signal's relative precision. For example, with a relative precision of 5% at 1 kHz, the RMS offset can be kept as small as 2.5 $\mu m$, which corresponds to a luminosity loss of 1.5%, and for a relative precision of 1% at 1 kHz, the RMS offset and luminosity loss are 1.25 $\mu m$ and 0.5%, respectively.

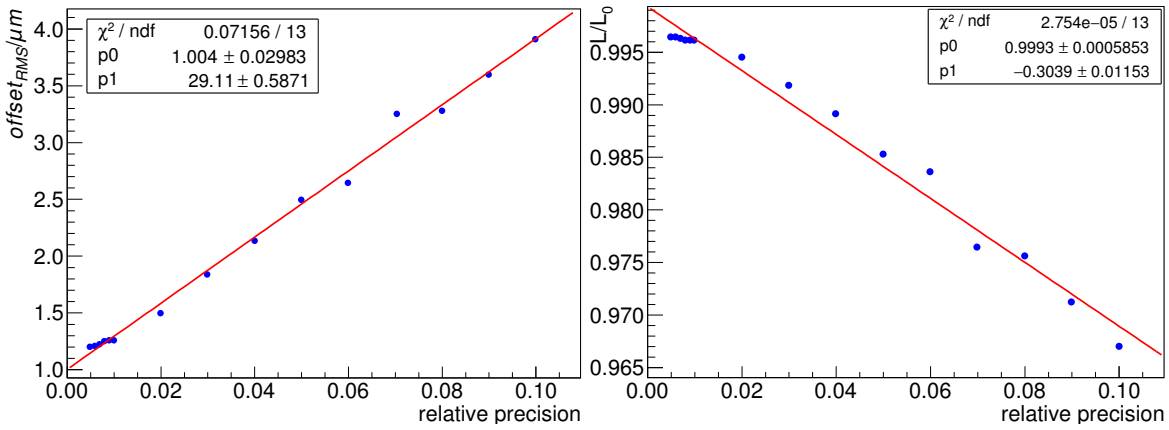


**Figure 4.47:** Residual RMS offset (left) and the ratio of luminosity with feedback with respect to the ideal luminosity (right) as a function of the train integrated luminosity signal's relative precision at 1 kHz.

During the Phase-2 of SuperKEKB, the $\beta_{x,y}$ were significantly larger than the nominal values in both horizontal and vertical planes, so the luminosity was much less sensitive to beam-beam offsets induced by GM. The feedback algorithm was also simulated for the Phase-2 optics, with relative precision of 1% at 1 kHz for the train integrated luminosity signals, and $\beta_{x,y}$ 8 times larger than the nominal parameters. The luminosity dependence of the beam-beam offset is provided in [57] using realistic numerical simulation. The results are shown in Figure 4.48 and Figure 4.49. The luminosity loss due to uncorrected GM induced horizontal beam-beam offsets is only about 0.7%, which can almost be ignored. It is reduced to less than 0.1% with the feedback system, and the residual RMS offset is then close to 6.5 $\mu m$, which indicates that the feedback algorithm still works well and can be tested in Phase 2 by deliberately introducing some horizontal beam-beam offsets.

As a conclusion, the simulation study of the horizontal IP dithering orbit feedback system based on luminosity monitoring has been done and the results show that the horizontal orbit stabilization can be achieved to recover and maintain the beams in collision. Due to the slow correction frequency, it does not work well for fast ground motion. However, the ground motion at high frequency is very small compared to the beam size in the horizontal plane, and so can basically be ignored. The relative precision of the luminosity signals was also studied, showing that the feedback system can maintain the residual RMS beam-beam offsets within about 1.25 $\mu m$ when the relative precision of the train integrated luminosity signal is about 1% at 1 kHz for the nominal machine parameters, corresponding to a luminosity loss less than 0.5%, which is good enough. In addition, considering the radiation damage issue of the diamond detector (see Section 4.4.2), 1% is preferable as relative precision for the train integrated luminosity signals at 1 kHz.

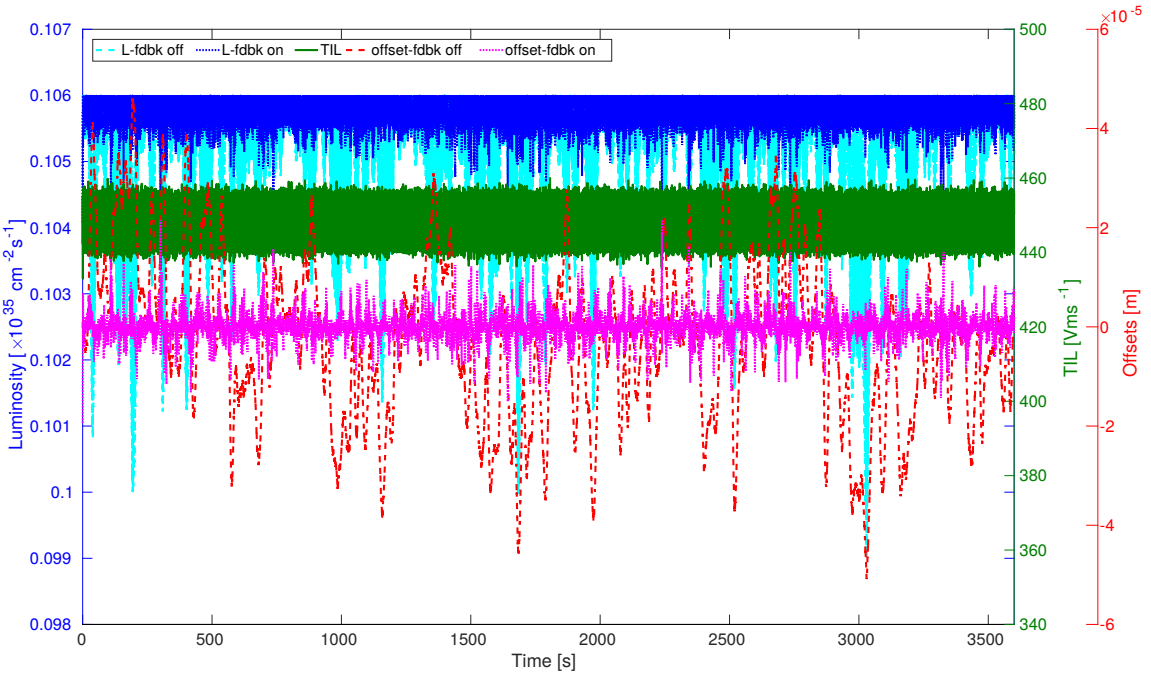


**Figure 4.48:** Luminosity, train integrated luminosity signal provided by diamond detector and the beam-beam offset with and without feedback for Phase-2 optics over a period of 3600 s.

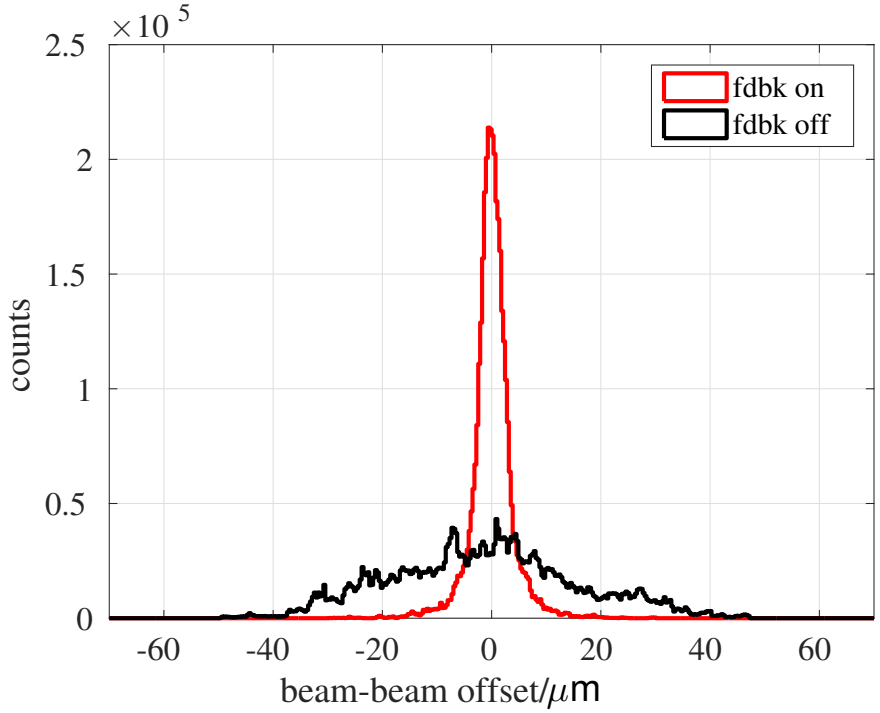


**Figure 4.49:** Comparison of residual beam-beam offset induced by the GM with and without feedback for Phase-2 optics (with $\beta_{x,y}$ 8 times larger than the nominal values).

# Chapter 5

# Experimental results during Phase-2 commissioning of SuperKEKB

During the Phase 2 commissioning of SuperKEKB which took place in the first half of 2018, the fast luminosity monitoring system based on diamond detectors was tested extensively including single beam loss measurements during single beam commissioning and luminosity measurements during beam collision commissioning. Its performance was established in different ways. Some studies were performed correlating our train integrated luminosity signals at 1 Hz with different machine parameters. The bunch integrated luminosity signals were also studied comparing with the bunch currents in both the HER and LER. During the machine optics tuning, the luminosity signals were also used to determine the vertical beam sizes at the IP based on vertical beam-beam scans, which are quite important in the process of $\beta_y^*$ squeezing. The 1 kHz train integrated luminosity signals were also used as input to the lock-in amplifier to test the dithering orbit feedback system after being converted to analog signal with a DAC. Moreover, the material activation of the 45° window shaped beam pipe was also studied and compared with simulation results.

## 5.1 SuperKEKB Phase-2 commissioning

After installation of the QCS superconductive final focusing magnets and Belle II detector, excluding the vertex detector, SuperKEKB Phase 2 commissioning was performed in several sub-phases, with corresponding machine parameters listed in Figure B.1 in the Appendix B. It aimed to verify the "nano beam collision scheme" by confirming the luminosity increase when squeezing $\beta_y^*$, in particular to values smaller than the bunch length $\sigma_z$, and tried to achieve the specific and instantaneous luminosities of $2 \times 10^{31}\ cm^{-2}s^{-1}mA^{-2}$ and $1 \times 10^{34}\ cm^{-2}s^{-1}$,

respectively. Besides, better understanding was expected of the Belle II detector's background from Coulomb, Beam-gas and Touschek single beam processes, from additional beam loss during injection, etc., and then to find the optimum way to control such beam backgrounds through collimation. In addition, the stability of the machine for a long period operation will also be established, especially for preventing the QCS quench and maintaining stable beam collision.

Figure 5.1 shows the history of SuperKEKB Phase 2 commissioning [132]. It started with single beam commissioning to perform the vacuum scrubbing, with a target of beam dose of about 100 Ah before the official physics running, and with closed orbit and general beam optics tuning. The beam collision tuning started from the second half of April, with the first collisions achieved on the 26th of April. Then the luminosity tuning was performed and the luminosity increased following to a large extent the progress of $\beta_y^*$ squeezing at the IP.

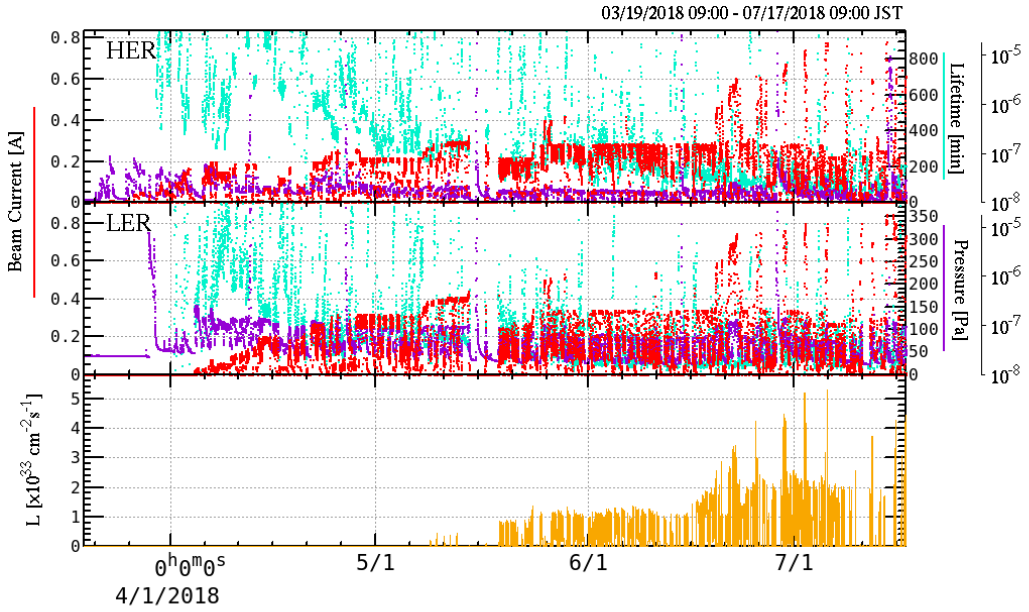


**Figure 5.1:** History of SuperKEKB operation in Phase 2 [132].

Figure 5.2 shows the comparison of $\beta_y^*$ at the IP between SuperKEKB and other machines (past and planned), on the left, as well as an illustration of the $\beta_y^*$ squeezing progress during Phase 2 commissioning, on the right [133]. As the first circular collider trying to push the $\beta_y^*$ from the *mm* world to the $\mu m$ world, only the optics settings and corrections for $\beta_y^* = 3$ *mm* in both the LER and HER have been achieved so far in Phase 2 and with relatively small beam currents. Due to limitations of a HER vacuum leak caused by the synchrotron radiation from the QCS and a LER bunch instability in the longitudinal direction, the beam current could not be increased to the target beam currents [132]. Therefore, the target peak luminosity of $10^{34}$ $cm^{-2}s^{-1}$ with beam currents equal to 1 A in the LER was not realized

in Phase 2. The maximum luminosity achieved in Phase 2 was $5.55 \times 10^{33}\ cm^{-2}s^{-1}$ for $\beta_y^* = 3\ mm$ at the IP with beam currents of 800 mA in the LER and 780 mA in the HER using 1576 bunches per train. However, in high bunch current trials with fewer bunches per train (394 bunches), in which case the vacuum leakage issue caused by the synchrotron radiation from the QCS downstream of the IP in the HER and the coupled bunch instability in the longitudinal direction in the LER could be avoided, a peak luminosity of $2.29 \times 10^{33}\ cm^{-2}s^{-1}$ was achieved with beam currents of 270 mA in the LER and 225 mA in the HER [132]. If we scale this to beam currents equal 1.08 A in the LER, the luminosity would reach $9.1 \times 10^{33}\ cm^{-2}s^{-1}$, very close to the target luminosity. Therefore, a conclusion was drawn that the SuperKEKB accelerator has made significant progress during the Phase 2 running time. Moreover, one can argue that the "nano-beam scheme" was demonstrated successfully since an increase in luminosity was observed when the vertical beam size $\sigma_y$ was reduced below the bunch length $\sigma_z$.

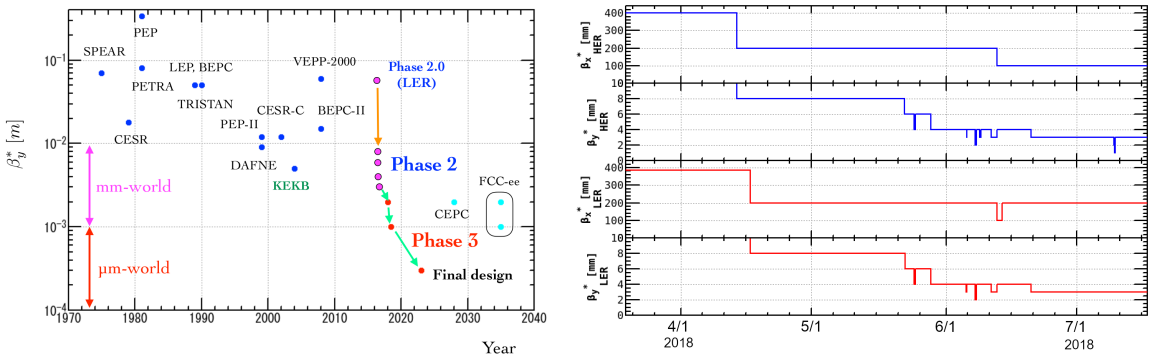


**Figure 5.2:** Illustration of SuperKEKB $\beta_y^*$ squeezing strategy compared with the other machines in the world (left) and the history of $\beta_{x,y}^*$ squeezing during Phase-2 commissioning in both LER and HER (right) [133].

During the whole commissioning period of Phase 2, our fast luminosity monitor based on diamond detectors was always operating, providing single beam loss information during the single beam commissioning and luminosity information during the beam collision commissioning, especially during the beam-beam collision searching and local optics tuning at the IP region, see the details in 5.5.2.

## 5.2 Experimental set-up at SuperKEKB

To perform the online luminosity monitoring, a new experimental set-up was prepared and installed in both the HER and LER at SuperKEKB, including a beam pipe modification, mechanical supports, detectors and the new DAQ system.

Figure 5.3 shows the general architecture of the fast luminosity monitoring based on diamond detectors at SuperKEKB. The diamond detectors were installed in both the LER and HER rings downstream of the IP at carefully studied positions, inside of the SuperKEKB tunnel. Half inch Heliax coaxial cables with length of 62 m for the LER and 86 m for the HER were used to bring the signals of six diamond detectors to the Belle II E-Hut. Limited by the number of channels of the ADC, four out of these six diamond signals could be selected to be connected to the back-plane of the electronics crate of the DAQ located in the Belle II E-Hut, depending on the needs and situation (relative location can be found in Figure A.3 in Appendix A). The processed signals by the DAQ system were then sent to the EPICS network , to share our information with the rest of the Belle II and SuperKEKB communities, and all the data were archived along with relevant machine parameters and saved in the 16 TB NAS (Network Attached Storage) located in B2. In addition, remote control of the DAQ system from a work space made available in the B2 floor of Tsukuba Hall (thanks to our colleague and collaborator at KEK [134]) was often used to avoid long periods of work in the noisy environment of the E-Hut.

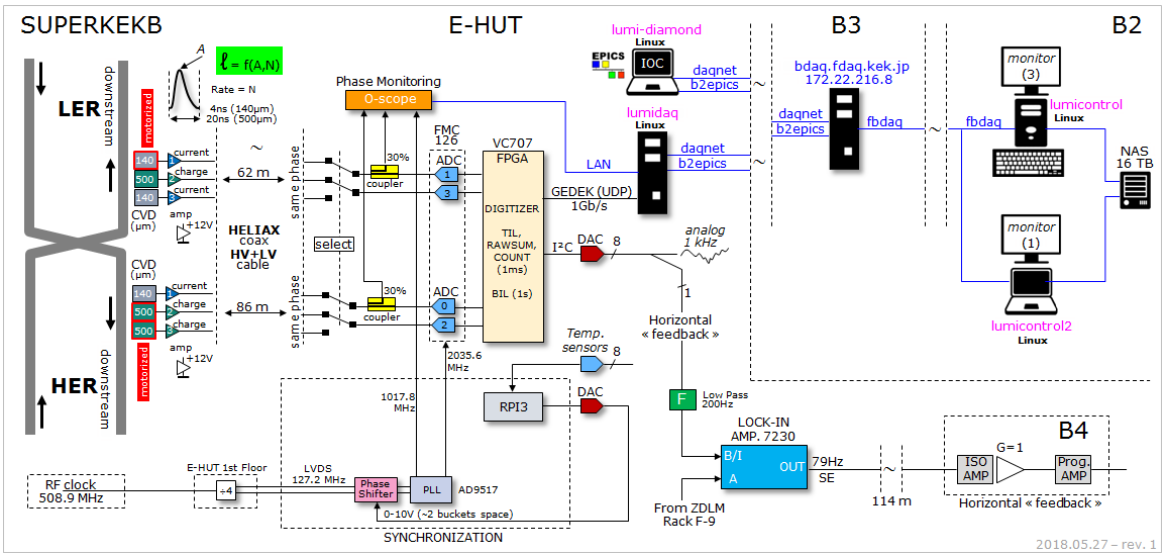


**Figure 5.3:** General architecture of LumiBelle2 project: fast luminosity monitoring based on diamond detectors at SuperKEKB (courtesy of D. Jehanno).

### 5.2.1 Beam pipe and mechanical supports

In order to achieve high relative precision for our luminosity monitoring, a 6 mm thick 45° window shaped beam pipe with a 15 mm depression was designed and installed to replace the regular cylindrical beam pipe, just after the QKBLP quadrupole magnet in the LER,

which allowed to concentrate at the window location the Bhabha scattered positrons that were previously lost over several meters of the cylindrical beam pipe. Figure 5.4 shows several views of this window shaped beam pipe, as well as the Tungsten radiator used to boost the electromagnetic showers.

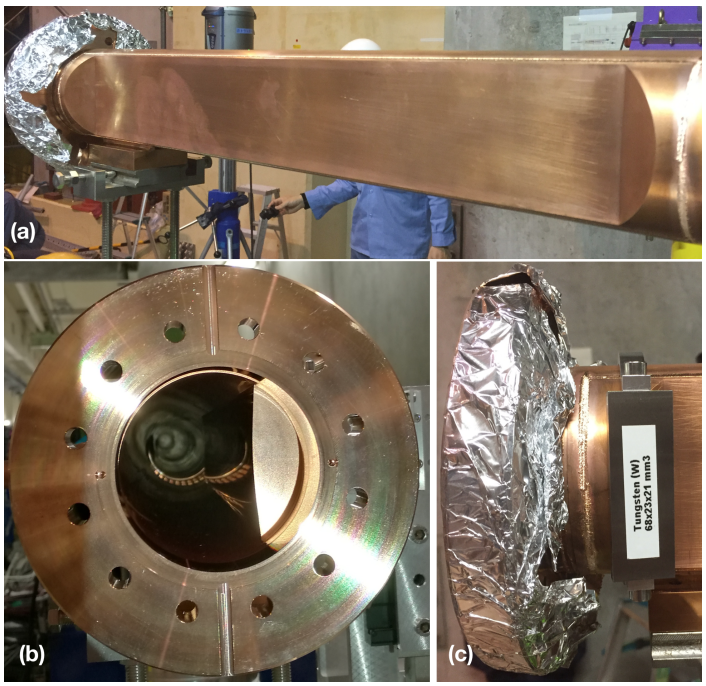


**Figure 5.4:** 45° window shaped beam pipe installed in the LER: (a) flat appearance (b) sectional view (c) Tungsten radiator.

The pillars and the movable plates installed in the LER and HER during Phase 1 were kept since the position for the diamond detectors were unchanged. However, due to the new window shaped beam pipe in the LER and a more careful study of the exit points of Bhabha scattered photons on the HER beam pipe, the mechanical supports used to hold the diamond detectors and amplifiers were also re-designed, see Figure 5.5. There are three holders in each ring, and they can be adjusted manually in the longitudinal direction according to the needs in the different situations. A stepping motor was also include to enable remote control of the mechanical supports horizontally, in order to scan the detectors in the horizontal plane, in a range of 25 mm.

### 5.2.2 Diamond detectors and DAQ system

During Phase 2 commissioning, six diamond detectors coupled with six amplifiers were prepared: two diamond detectors with thickness of 140 $\mu m$ coupled with broadband fast current amplifiers and one diamond detector with thickness of 500 $\mu m$ coupled with a fast

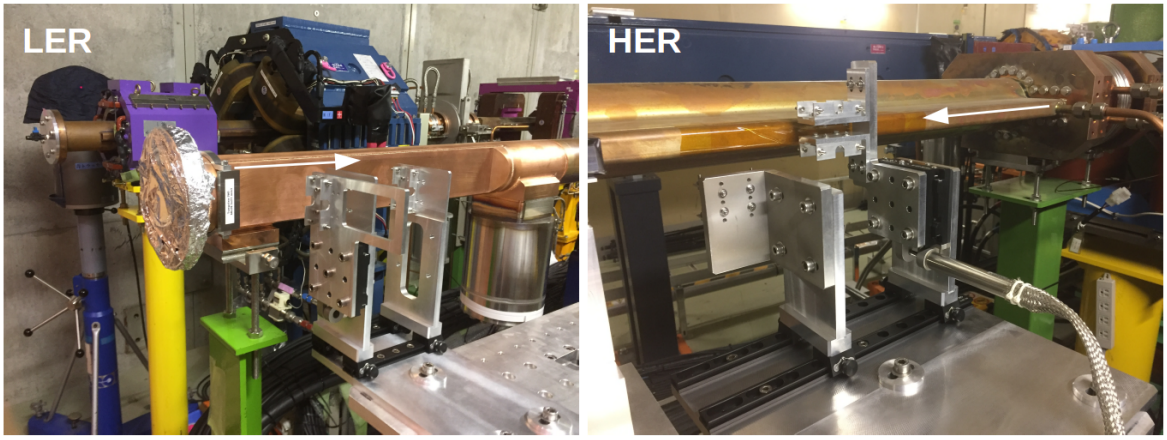


**Figure 5.5:** New mechanical supports in the LER and HER.

charge amplifier were installed in the LER, as shown in the left of Figure 5.6. The thicker detector was installed in the middle: position B. Since the target luminosity in Phase 2 was expected to be $10^{34}\ cm^{-2}s^{-1}$, which is relatively low compared to the nominal luminosity, the diamond detector at position A associated with the motor was installed as close as possible to the Tungsten radiator and beam pipe. The detectors at position B and C were also installed as close as possible with the limitation of the mechanical supports. The distance was 6 cm

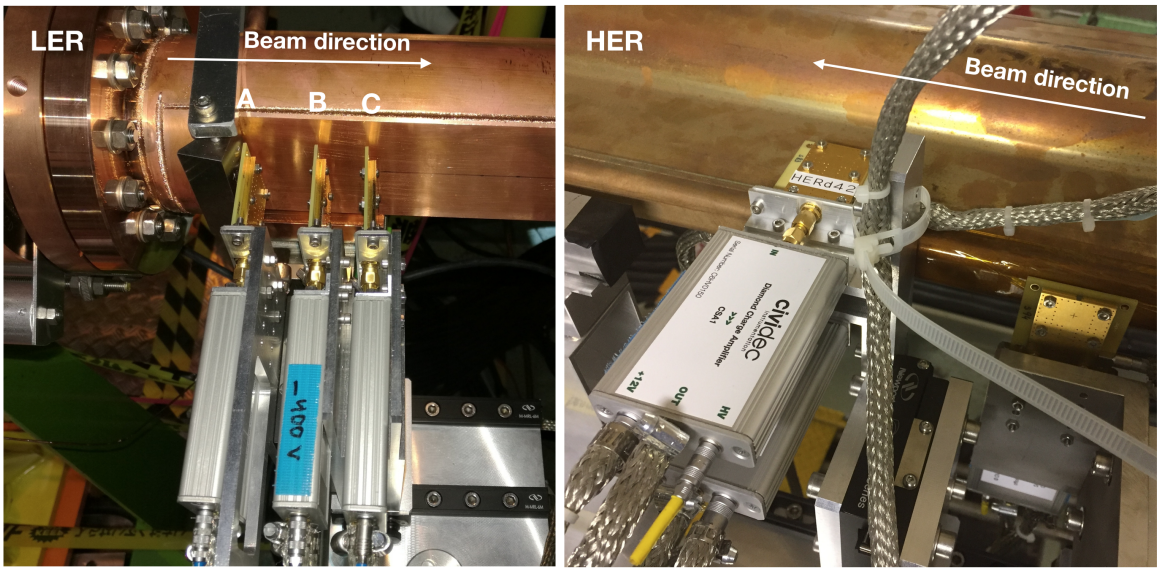


**Figure 5.6:** Diamond detectors installed in the LER and HER.

between A and B and 2.5 cm between B and C. A gap of 1 mm between the beam pipe surface and the edge of the detector's PCB board was kept as safety margin. On the other hand, since we aim to detect Bhabha scattered photons in the HER, two diamond detectors with thickness of 500 $\mu m$ coupled with a fast charge amplifiers and one detector with thickness of

140 $\mu m$ coupled with broadband current amplifier were installed, as shown in the right of Figure 5.6. Due to the special geometry of the ante-chamber beam pipe, two thicker diamond detectors were installed horizontally as close as possible to the top and bottom surfaces of the ante-chamber's wing, and a motor was installed to scan those two detectors in the horizontal plane, within a range of 25 mm. The thinner diamond detector was installed vertically very close the edge of the ante-chamber.

The power supplies for the diamond detectors and amplifiers were controlled from the E-Hut, with the high voltage for the diamond detectors set to achieve 0.8 $V/\mu m$, and the low voltage for the amplifiers at 12 V.

The diamond detector signals were sent to the DAQ system located in the Belle II Electronics-Hut via half inch Heliax coaxial cables with which the signal attenuation and broadening can be neglected. The DAQ system was developed based on the principle described in Section 3.3.3 and included as well other electronics, all installed in the F-8 rack on the 2nd floor of the E-Hut. During Phase 2 commissioning, two channels from the LER (diamond detectors mounted at positions A and C) and two channels from the HER (diamond detectors mounted at the top and bottom surface of the antechamber) were used most of the time as input to the DAQ, while the others were sometimes also tested, by exchanging the cables on the back-plane of the rack. Figure 5.7 shows pictures and an illustration of the electronics installation in the rack. The data acquisition part was developed based on an ADC (4 channels, 1 GSPS), an FPGA (for luminosity processing at 1 kHz) and a DAC (to convert the digital signal to analog as input to the lock-in amplifier used for the horizontal dithering feedback), and was installed at the top of the rack with a fan for cooling. The synchronization part generates a clock at $2 \times f_{RF}$ based on the $f_{RF}/4$ available from the RF clock of the SuperKEKB machine by an internal PLL to synchronize the signals and the beam bunches. It is installed below the acquisition part with a fan. A Phase shifter (JSPHS-150+ 100-150 MHz) was also integrated to find the optimum phase for sampling at the signal peak positions, in order to get their amplitudes. The time shift as a function of the input voltage can be found in Figure A.2 in Appendix A for this phase shifter, one cycle corresponds to a time shift of about 5 ns. The inner view of the acquisition and synchronization crates are also shown in left of Figure 5.7.

A 10 bit Keysight oscilloscope (2.5 GHz and up to 20 GSPS sampling) is installed below the synchronization crate for development purposes and to acquire raw data signal sequences for off line analysis. A Linux PC working as DAQ server controls the DAQ board with the FPGA and manages the luminosity data. A laptop PC manages the EPICS IOC and data archiving, both are installed below the oscilloscope and are connected to the daqnet and b2epics networks, which enables us to both broadcast the luminosity data via EPICS to share

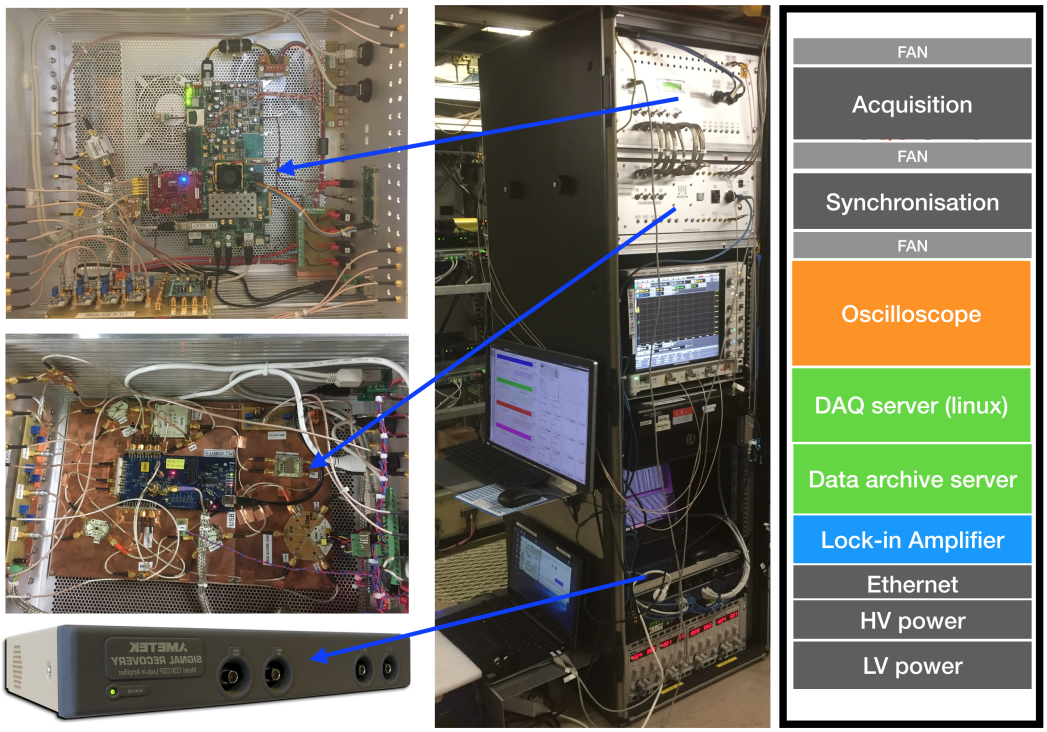


**Figure 5.7:** LumiBelle2 electronics in the F-8 rack on the 2nd floor of the E-Hut.

with the Belle II and SuperKEKB communities and to control those two computers remotely from the B2 work space that was arranged for our group in Tsukuba hall. In the bottom of the rack, the Lock-in amplifier (AMTEK 7230), Ethernet, high and low voltage power supplies are installed.

Several types of luminosity signals are provided by our system. The Train Integrated Luminosity (TIL), which integrates signal amplitudes, RAWSUM, which sums all samples above a pre-defined threshold, and COUNT, which counts the number of successive signals, all at 1 kHz, can be used for the dithering orbit feedback system. They are also provided at 1 Hz for general machine tuning and study. The Bunch Integrated Luminosity (BIL), which integrates the signal amplitudes separately for each bunch is also provided at 1 Hz. All those data are broadcasted via the EPICS network.

For convenience of the DAQ control and long term operation of the LumiBelle2 project, a small control desk was kindly made available to our group in B2, where the computers can control the DAQ server and data archive server in the E-Hut via the bdaq network. All the luminosity data including the train integrated luminosity signals at 1 kHz and 1 Hz, bunch integrated luminosity signal at 1 Hz for all the buckets, together with a number of related machine parameters, were saved as ROOT n-Tuples in a 16 TB NAS located in B2. The remote control and display interface is shown in Figure 5.8.

**Figure 5.8:** LumiBelle2 remote control desk located in B2 in Tsukuba hall.

As already mentioned in Section 3.2.2, in addition to the diamond detectors used for our fast luminosity monitoring, another system based on scintillator and Cherenkov detector, ZDLM is also installed in the immediate vicinity. It provides an important complementary fast luminosity measurements, based mainly on analog electronics [80].

## 5.3 Background signals from single beam losses

Detailed simulations of the background signals in the diamond detector have been described in Section 4.3.2, which shows that the Bremsstrahlung process dominates the background signals in Phase 2 due the large vacuum pressures near the IP region, which arises through the much narrower beam pipes in the Belle II detector, and absence of local vacuum pumping. During the single beam commissioning, our diamond detectors acted as beam loss monitors. As requested by the BEAST II group, specific background studies were performed to systematically study the beam-gas and Touschek sources not associated with the beam collisions. In addition, the huge particle losses observed during beam injections were also observed by the diamond detectors.

### 5.3.1 Typical background signals during single beam commissioning

One typical plot of the single beam loss signals from the diamond detectors in both the HER and LER in shown in Figure 5.9. During this period, the two beams were mismatched in

the longitudinal direction, so there was no beam collision at the IP. The big difference in the vacuum pressure between HER and LER can be explained by the usage of old and new vacuum beam pipes, as described in Chapter 2: 93% of the LER vacuum beam pipes are newly manufactured ones, while this fraction is only 18% for the HER, thus much more gas desorption could be expected in the LER. It is clear that the LER and HER signals depend on the beam current and vacuum pressure in each ring. The LER signal comes from the diamond detector with thickness of 140 $\mu m$ coupled with a C2 broadband current amplifier, mounted at the optimum position, based on the TIL computation in the FPGA. Meanwhile, the HER signal is the sum of the RAWSUM from the two diamond detectors with thickness of 500 $\mu m$ coupled with C6 fast charge amplifiers mounted on top and below the antechamber. Due to the window shaped beam pipe and Tungsten radiator in the LER, the LER signal rate is much larger than that from the HER, which explains the different levels of fluctuations.

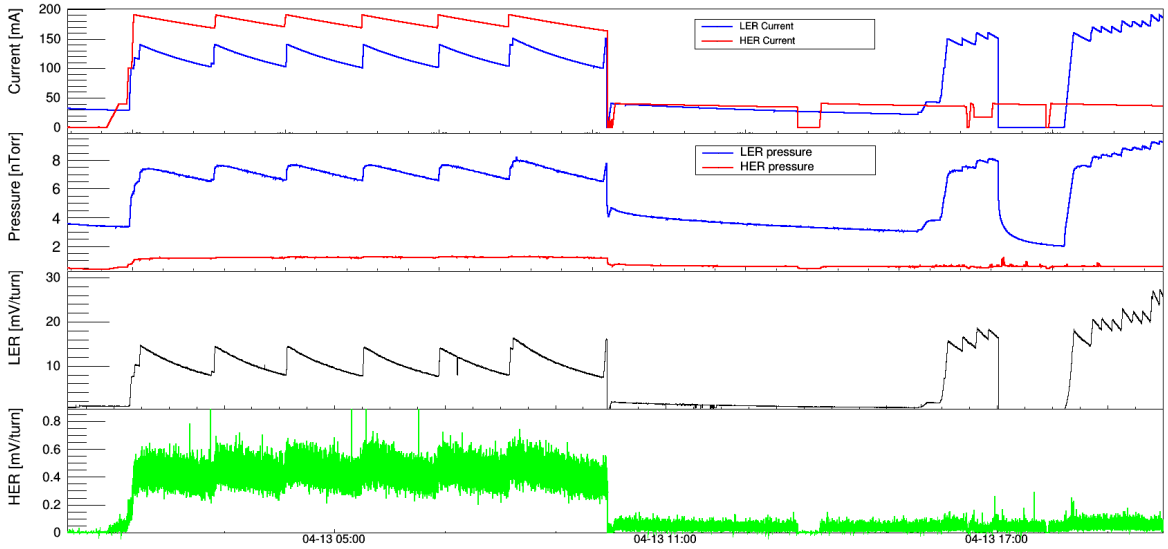


**Figure 5.9:** Example of diamond detector signal in the LER and HER during the single beam commissioning together with beam currents and vacuum pressures.

### Case of the LER

Before correlating the diamond detector signals with variations of different machine parameters, internal checks between channels and between RAWSUM and TIL estimates of the luminosity for the same channel were performed. In the case of the LER A and C channels, the only difference is their distance to the Tungsten radiator. Figure 5.10 shows an example of signal comparison during the single beam commissioning. The results show very good linearity between the two channels in the LER both for RAWSUM and TIL. The ratios between channel A and C are about 10 to 15, which is compatible with the prediction of the

simulation of 10 described in Section 4.1.4. The broad distribution is mainly caused by the signals from channel C, which has lower statistics.

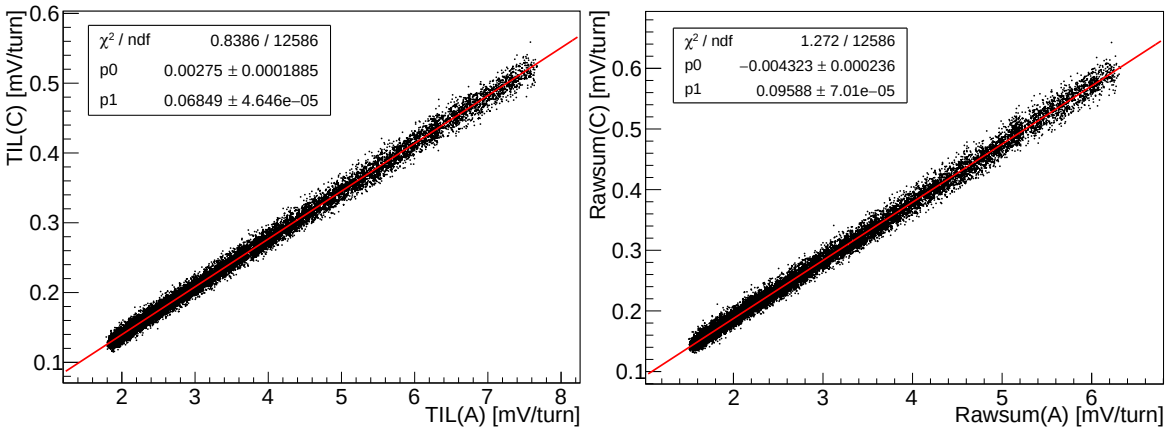


**Figure 5.10:** Signals comparison between the two channels (A and C) in the LER.

Another internal check is the comparison between the RAWSUM and TIL estimation of the luminosity for the same channel. Figure 5.11 shows an example of the correlation between the RAWSUM and TIL both for channels A and C. It is quite clear that the correlation

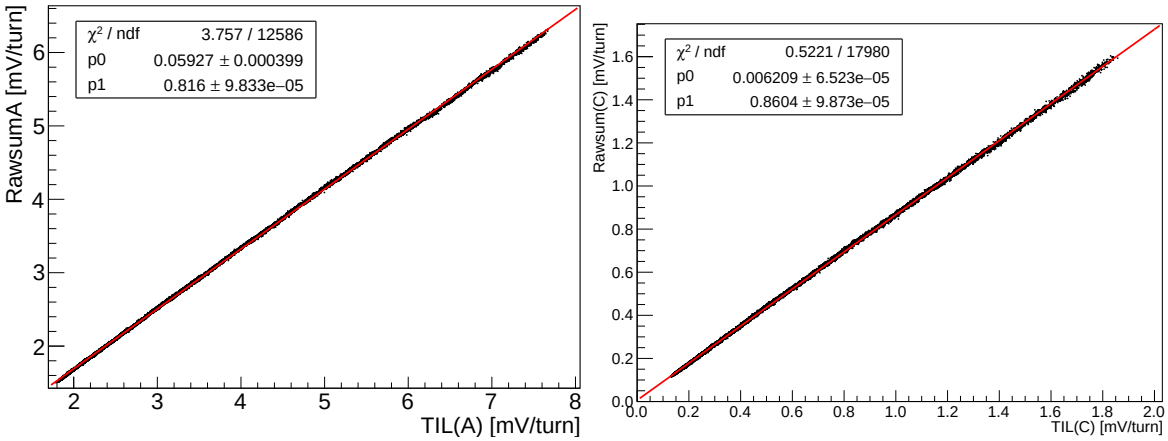


**Figure 5.11:** Comparison of the RAWSUM vs TIL for the same channels in the LER, left for channel A and right for channel C.

between the two calculations is very good, which gives us confidence that reliable signals from the thicker 500 $\mu m$ diamonds coupled with the C6 fast charge amplifier, for which the TIL calculation is not currently foreseen with the present DAQ system, will be obtained. The comparison between the RAWSUM signal from a thicker diamond detector and the TIL signal from a thinner diamond will be described later.

After the internal check between channels and signal algorithms, the signal dependence on the machine parameters was also studied. We can clearly see that the signals follow the

beam current in the ring from Figure 5.9. Looking more closely, we can see in Figure 5.12 that the variation of the TIL signal from the diamond detector at position A in the LER with respect to beam current and vacuum pressure measured about 15 m upstream of the IP includes a quadratic contribution to the dependence. This quadratic dependence may be caused by a contribution from the Touschek process or by a beam gas desorption induced vacuum pressure increase, since the Bremsstrahlung loss is proportional to both the beam current and vacuum pressure. More details will be explained below.

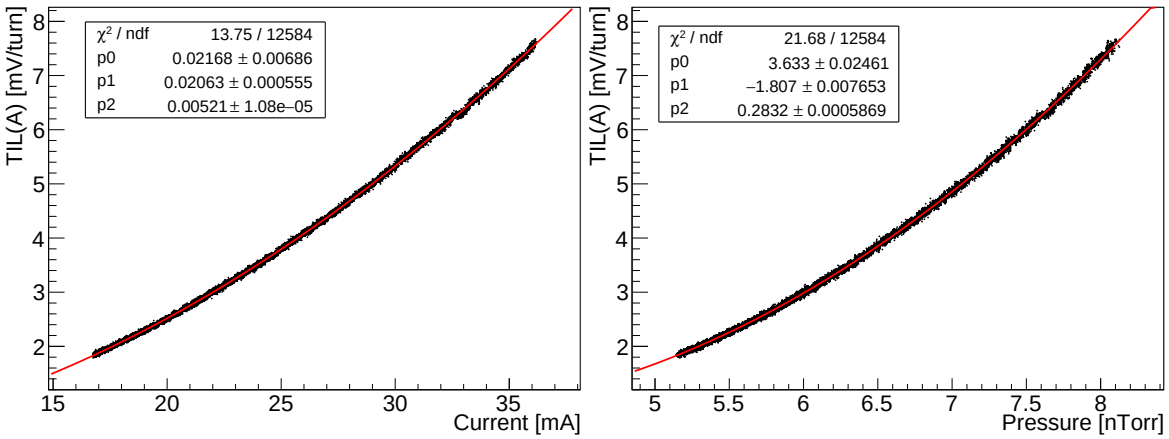


**Figure 5.12:** The TIL signal from the diamond detector at position A in the LER as a function of beam current (left) and pressure (right).

The beam pipe contains a significant number of gas molecules that are absorbed during manufacturing. When the beam circulates inside the beam pipe, some of those molecules are released from the walls, a phenomenon that is known as gas desorption. At SuperKEKB, the main process causing the desorption is synchrotron radiation, with the number of photons proportional to the beam current [135]. Those photons hit the beam pipe inner wall, causing gas molecule emission and thus increasing the vacuum pressure inside the vacuum pipe. Figure 5.13 shows the behavior of the pressure measured 15 m upstream of the IP as a function of beam current in the LER. The vacuum pressure is proportional to the beam current in the present condition because the gas desorption process is still going on.

Since the Bremsstrahlung process is proportional to the product of the beam current and vacuum pressure, the linear relationship between the pressure and the current explains the quadratic behavior of the background signals against the beam current and vacuum pressure. The background signals are on the other hand indeed found to be linearly dependent on the product of the beam current and pressure, see Figure 5.14, as expected for the Bremsstrahlung process.

It is quite clear that the background signals are proportional to the product of the beam current and vacuum pressure in the present condition, both for the RAWSUM and TIL

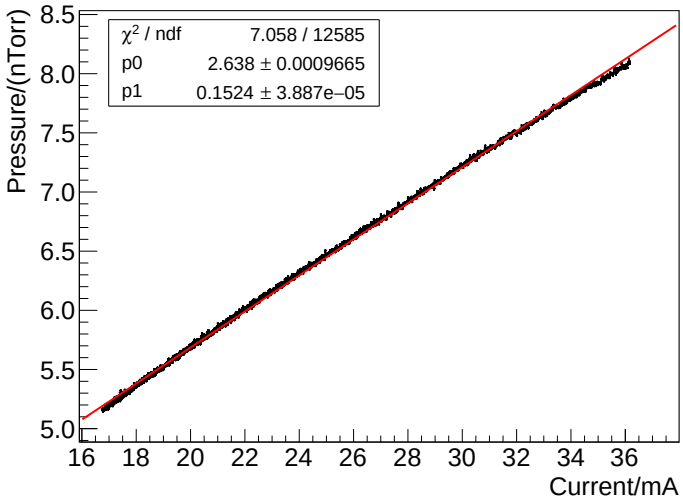


**Figure 5.13:** Vacuum pressure measured 15 m upstream of the IP as a function of beam current in the LER.

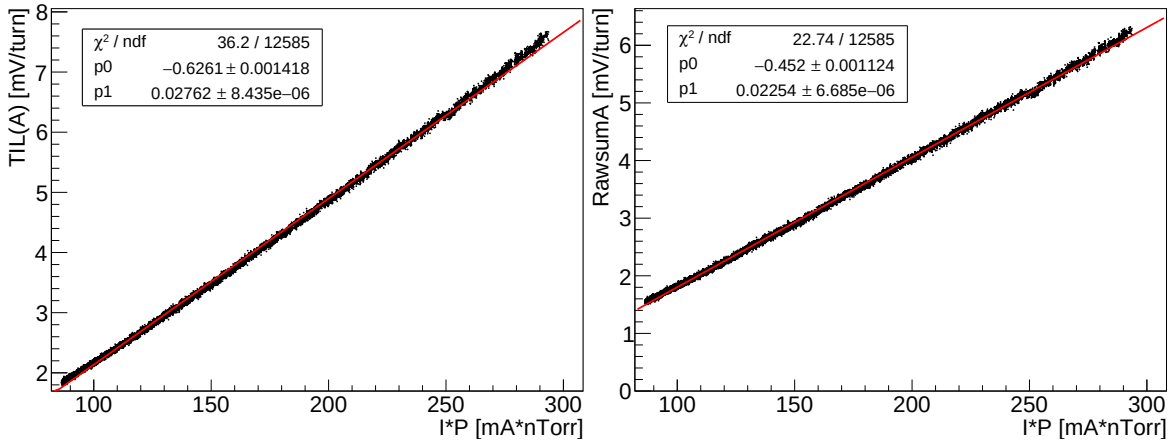


**Figure 5.14:** TIL (left) and RAWSUM (right) signals from the diamond detector at the position A in the LER as a function of the product of beam current and vacuum pressure.

signals, which indicates that the Bremsstrahlung process dominates the losses measured in our diamond detectors.

### Case of the HER

Meanwhile, similar studies were also performed for the HER side. Due to the much poorer statistics in the HER signals during Phase 2, the sum of two diamond detectors with a thickness of 500 $\mu m$ coupled with C6 fast charge amplifiers was used for the background study. Figure 5.15 shows an example of HER signals as a function of beam currents on the left and vacuum pressure on the right. Even though the statistics of the HER sum signal is

still not very good, the quadratic behavior is still obvious with respect to the beam current and vacuum pressure.

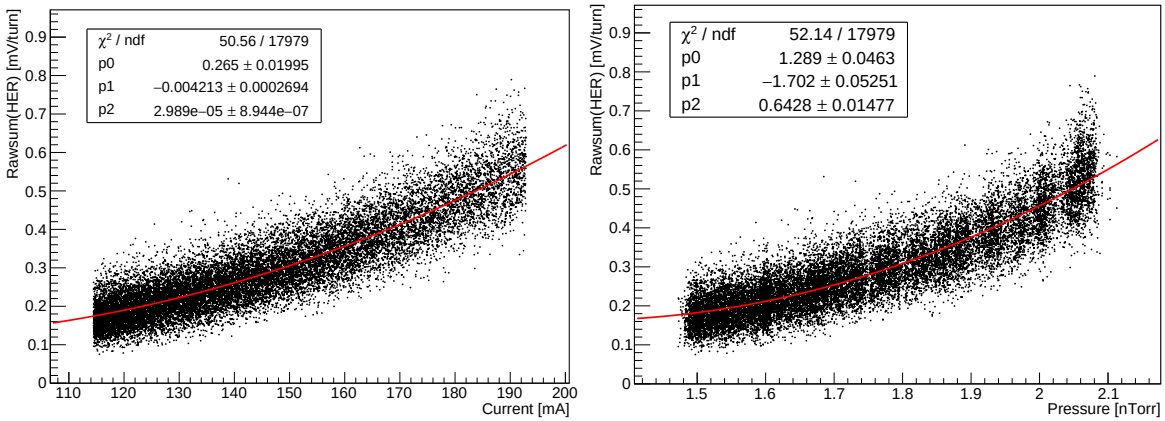


**Figure 5.15:** Example of HER signals as a function of machine parameters: beam current (left) and vacuum pressure (right).

Different from the LER, most of the beam pipe is reused in the HER from KEKB, where significant vacuum scrubbing has already taken place, therefore much less gas molecular emission was observed in the HER compared to the LER. As shown in Figure 5.16 on the left, the pressure is still proportional to the beam current, but the slope is much smaller than that from the LER. Similar to the LER, if we correlate the HER signals with the product of beam current and vacuum pressure, as shown in the right of Figure 5.16, good linearity can also be found. We can conclude from the above that there was a good qualitative agreement between the experiment results and our expectation in both the LER and HER.

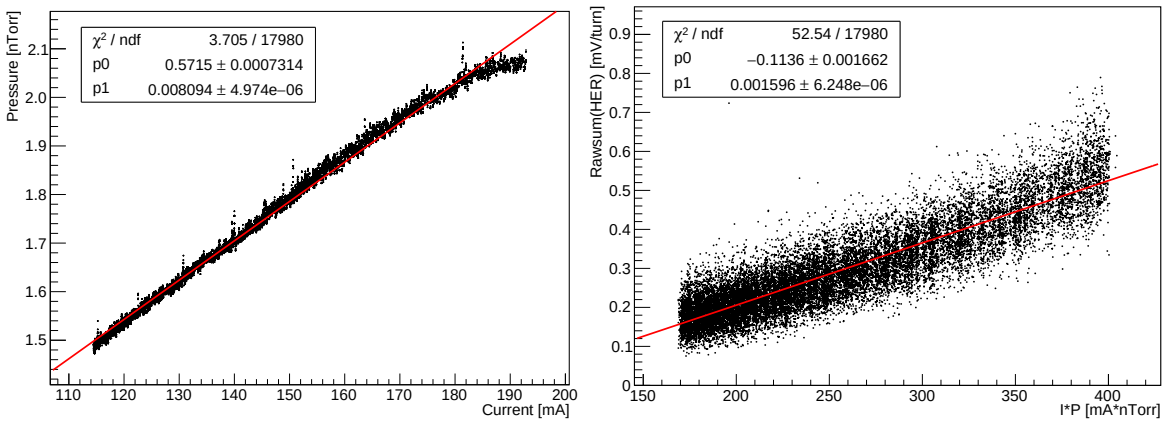


**Figure 5.16:** Vacuum pressure as a function of the beam current in the HER on the left and the HER signal as a function of the product of beam current and vacuum pressure on the right.

### 5.3.2 Bremsstrahlung and Touschek losses in the luminosity monitor diamond detectors

To study and understand the single beam losses from Bremsstrahlung and Touschek processes quantitatively, the beam currents and vertical beam size were changed in deliberate steps.

Firstly, the beam currents were increased from 0 mA to a certain level while keeping the other machine parameters constant to check the performance of the detector's response. For example, the beam current in the LER was increased from 0 mA to 110 mA in three steps during the single beam commissioning at the beginning of Phase 2, as shown in Figure 5.17. A clear corresponding change in the monitor's signal could be observed: the signal

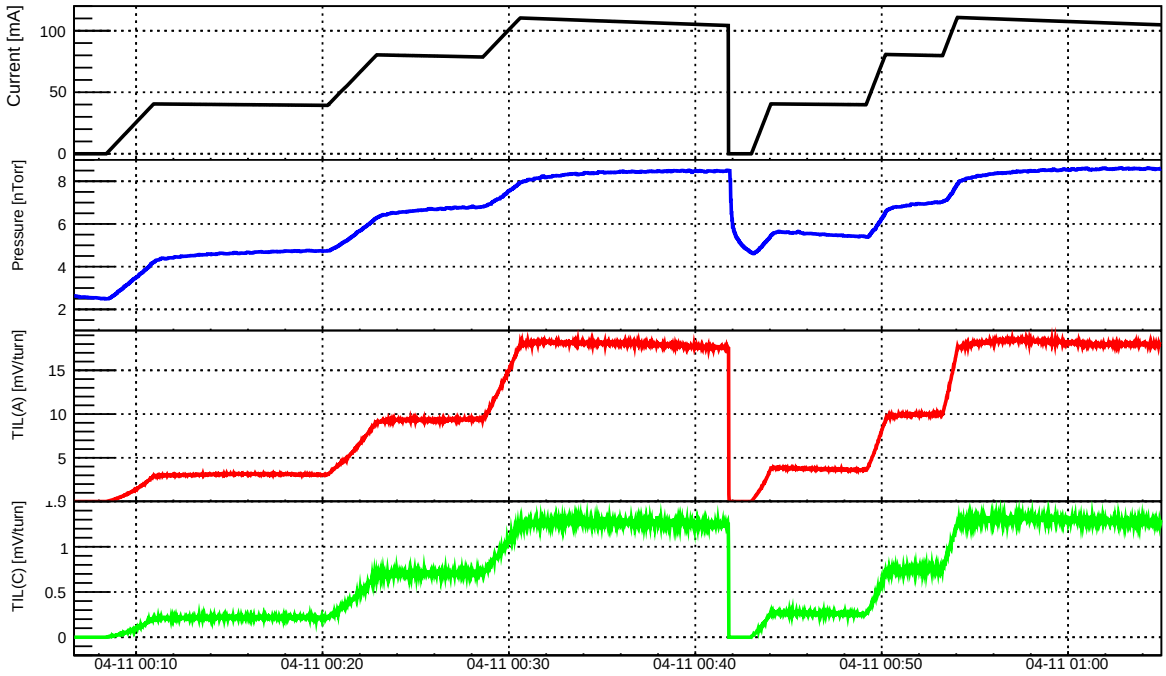


**Figure 5.17:** Example of background signal (TIL(A) in red for channel A and TIL(C) in green for channel C) study in the LER, the beam current was increased from 0 to 110 mA with three steps.

from Channel A in the LER was increasing from 0.04 mV/turn to 18.3 mV/turn with three steps, similar for channel C, as well as for the vacuum pressure caused by the gas desorption, which increased from 2.6 nTorr to 8.3 nTorr.

After re-scaling of the simulation results according to the real beam currents and measured vacuum pressure, the comparison between the experimental data and the simulation results can be performed to check the reliability of the simulation, which is important for the future SNR estimation for the luminosity measurements. The simulated signals and experimental data as a function of the product of beam current and vacuum pressure are shown in Figure 5.18 (left for LER and right for HER). The simulated results are about 11% in LER and 20%

in HER higher than the measurement, which is not unreasonable considering the uncertainties in the simulation. The difference between the simulated vacuum profile and the real vacuum pressure distribution around the IP region, where there is a large increase of more than one order of magnitude and from where most of the Bremsstrahlung scattered particles reaching our detectors originate, as well as the actual effective atomic number to be taken into account for the residual gas inside the vacuum pipe are likely the main biases that can explain this discrepancy.

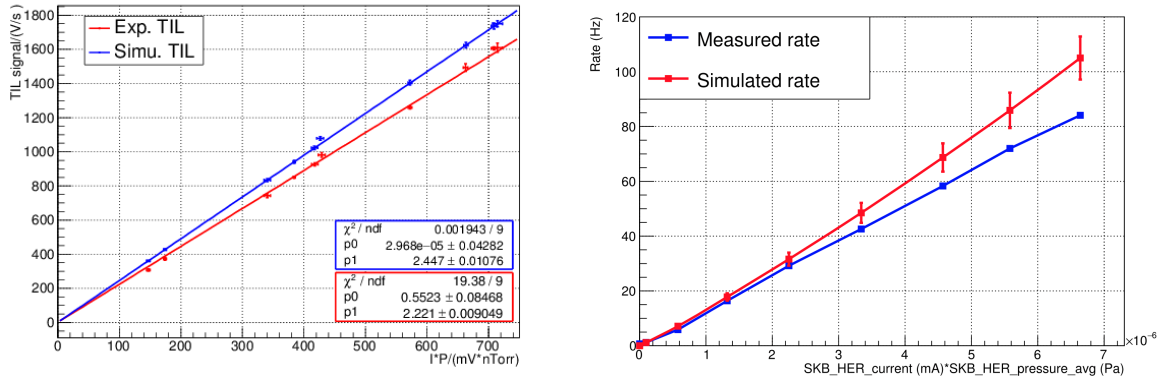


**Figure 5.18:** Comparison between simulated background signals and experimental data in the LER (left) and HER (right) [62, 93].

A "Touschek study" based on vertical beam size scanning was performed at the end of Phase-2 commissioning (with $\beta_x^* = 200\ mm$ and $\beta_y^* = 3\ mm$ in the LER) by changing the vertical emittance knob, which generates anomalous vertical dispersion all around the ring [136]. As it will be explained, the Touschek component can be extracted from the background signals by analyzing their variation in such a study. Figure 5.19 shows diamond detector signals and the beam current, vacuum pressure and vertical beam size during the "Touschek study". In this study, three vertical sizes $\sigma_{y@xray} = 45, 70, 130\ \mu m$ were set, the beam currents were set as 310 mA , and then were let to decay through beam loss around the ring down to 100 mA. In terms of qualitative observation of the diamond detector signals, they are still following the change of the beam currents and vacuum pressure, and it is not easy to see a difference when the vertical beam sizes were changed. This somehow supports our simulation results that the Bremsstrahlung process dominates the background signals of the diamond detectors during Phase 2. Besides, we can also observe that there was a sudden increase in the diamond detector signals during the beam injection (during which period, the beam currents were increasing), this is caused by the injection loss, more details will be described in Section 5.3.3.

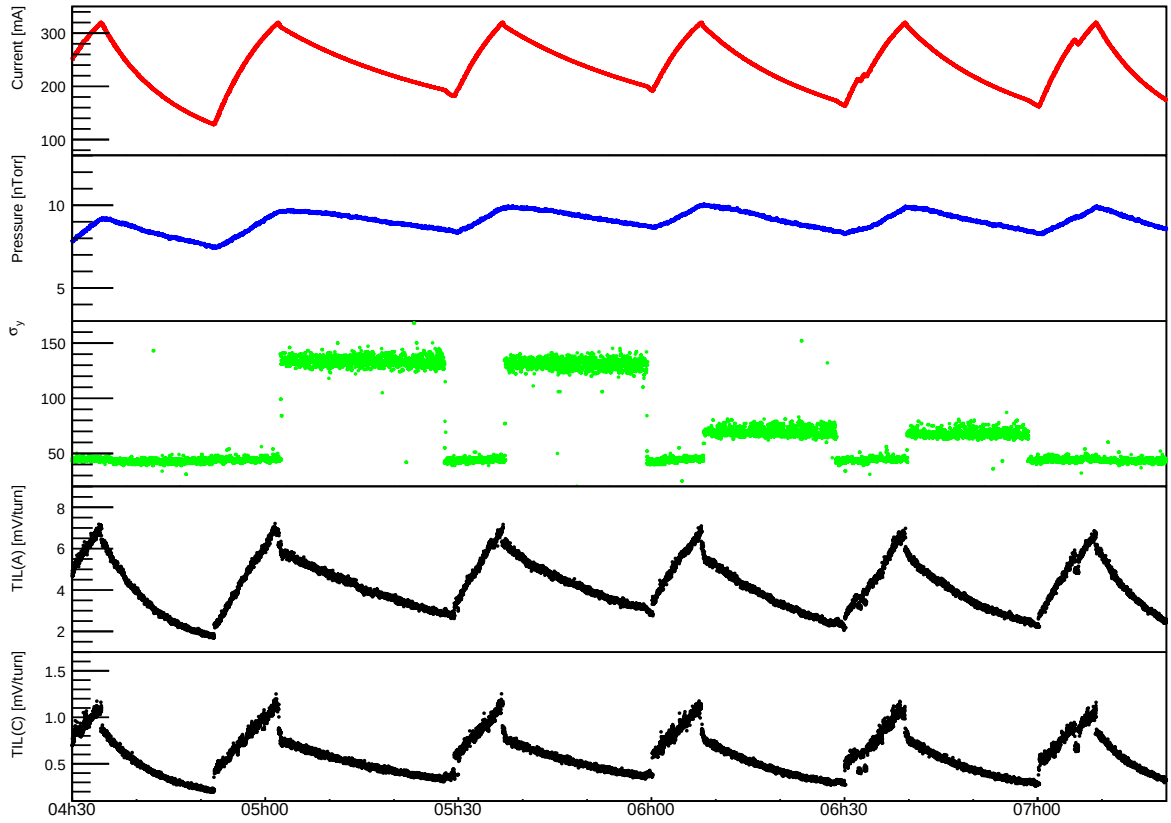


**Figure 5.19:** Diamond detector signals (TIL(A) for channel A and TIL(C) for channel C) and beam parameters during the "Touschek study" in the LER. The vertical beam size $\sigma_y$ is measured at a location in the ring where an X-ray monitor is used [137].

In order to disentangle the Bremsstrahlung and Touschek background signals, a simplified parameterization of those two background processes was used based on their expected behavior with respect to the accelerator and beam conditions. According to the characteristics of the Bremsstrahlung and Touschek processes, the background signals can be expressed as

$$S_{bkgd} = S_{bg} * IP_eZ_e^2 + S_T * \frac{I^2}{\sigma_y} \tag{5.1}$$

where $S_{bkgd}$ is the diamond detector signal. The first part on the right of the equation corresponds to the Bremsstrahlung process, which is proportional to the product of beam current and effective vacuum pressure, and the square of the effective atomic number of the residual gas molecules inside the vacuum pipe. $S_{bg}$ is a constant of proportionality of Bremsstrahlung sensitivity, $I$ is the beam current, $P_e$ is the effective pressure, which is about three times of $P_{CCG}$ measured by the cold cathode gauge (CCG), because the vacuum pressure at the center of the beam pipe is about three times higher than the one measured by the vacuum gauges [49], and $Z_e$ is the effective atomic number, characterizing the gas

composition. The second part on the right of the equation corresponds to the Touschek process, which is proportional to the square of the bunch current and the inverse of the vertical beam size (also the beam size in the other plane, while here we are going to study the Touschek process by only changing the vertical beam size). Touschek scattering also depends on the beam energy and number of bunches in the train, however in practice these do not change during routine operation. $S_T$ is the Touschek sensitivity, $\sigma_y$ is the vertical beam size at the scattering position, which is proportional to the beam size measured by the X-ray monitor [137]: $\sigma_y = \sqrt{\beta_y/\beta_{xray}}\sigma_{y,xray}$. $S_{bg}$ and $S_T$ should be constant for the same lattice.

For visualization purposes, it is more convenient to rewrite Equation 5.1 as Equation 5.2 and plot the $\frac{S_{bkgd}}{IP_eZ_e^2}$ as a function of $\frac{I}{P_eZ_e^2\sigma_y}$. With such a plot, the data should fall on a line with an offset indicating the Bremsstrahlung sensitivity $S_{bg}$ and the slope corresponds to the Touschek sensitivity $S_T$.

$$\frac{S_{bkgd}}{IP_eZ_e^2} = S_{bg} + S_T * \frac{I}{P_eZ_e^2\sigma_y} \tag{5.2}$$

If we study the signals with Equation 5.2, as shown in Figure 5.20, the approximate overall linearity of the distribution despite variations in current, pressure and horizontal beam size validates the hypothesis that the background signal mainly consists of Bremsstrahlung and Touschek processes. The offset of the fit line on the Y-axis contains the Bremsstrahlung contribution, and the slope indicates the change in the Touschek contribution as the vertical beam size is varied. From the fitted data, $S_{bg}$ is about 24.45 and $S_T$ is about 9.10. For the nominal case of this "Touschek study" with the measured vertical beam size, $\sigma_{y,xray} = 45\ \mu m$ by the X-Ray monitor [137], the $S_{bkgd}/(IP_eZ_e^2)$ term on the left of Equation 5.2 amounts to about 28 $mVnTorr^{-1}mA^{-1}$, and the contribution from Bremsstrahlung on the right amounts to 24.45 $mVnTorr^{-1}mA^{-1}$, and therefore the contribution from the Touschek process amounts to 3.55 $mVnTorr^{-1}mA^{-1}$. That means that the Bremsstrahlung process contributes about 87% and the Touschek process about 13% to the backgrounds in our system. Those fractions are consistent with the simulation which predicts fractions of 89% and 11% for the Bremsstrahlung and Touschek in Phase 2, respectively.

### 5.3.3 Injection noise signals

At SuperKEKB with nominal parameters, due to the extremely small beam sizes at the IP, the beam lifetime is only about 6 minutes, dominated by the Touschek process. An injection scheme known as top-up injection (continuous injection) is therefore vital for SuperKEKB to maintain the high luminosity. One important background source results however from this, referred to as the injection noise [138]. Due to the imperfection of the kicker magnet used

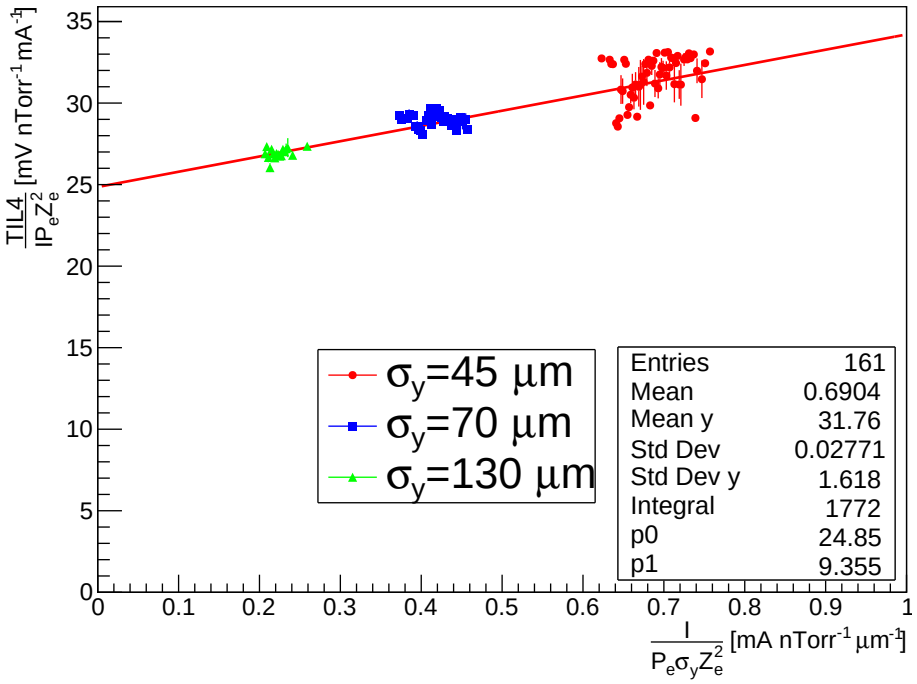


**Figure 5.20:** An example of fitting of Equation 5.2 using experimental data with different LER beam size sweeps. The offset of the fit line contains the Bremsstrahlung contribution and the slope indicates the change in the Touschek contribution as the beam size is varied. The beam size is measured by the X-Ray monitor.

for beam injection, injected particles are not exactly on the nominal orbit and oscillate with an amplitude larger than that of the stored particles. Once such a particle goes beyond the dynamic aperture, it will be lost after 10 to 1000 turns at some point in the ring. During Phase 2, especially in the LER, where we have the 45° window shape beam pipe, the injection noise was detected by our diamond detectors, representing a very large signal since many injected particles could be lost at once on the window. Figure 5.21 shows a screen shot of the oscilloscope during injection in the LER: the cyan negative pulse on top is the injection sign signal, and is used as trigger, red-violet is the signal from the diamond detector located at position A, closest to the Tungsten radiator, and yellow is for the diamond detector located at position C, about 8 cm away from the Tungsten radiator longitudinally. For position A, the average signal amplitude for one lost positrons detected by the diamond is about 16 mV from the simulation, while the first large signal has an amplitude about 430 mV, which means that there were more than 25 positron detected by the diamond detector at once due to the injection noise for the first large signal in the diamond detector. This injection noise is very important since it could be very large and cause a significant dead time in the data acquisition system of the Belle II detectors, by making electronic channels saturated and creating some large event sizes. It is under studying by the MDI group of Belle II.

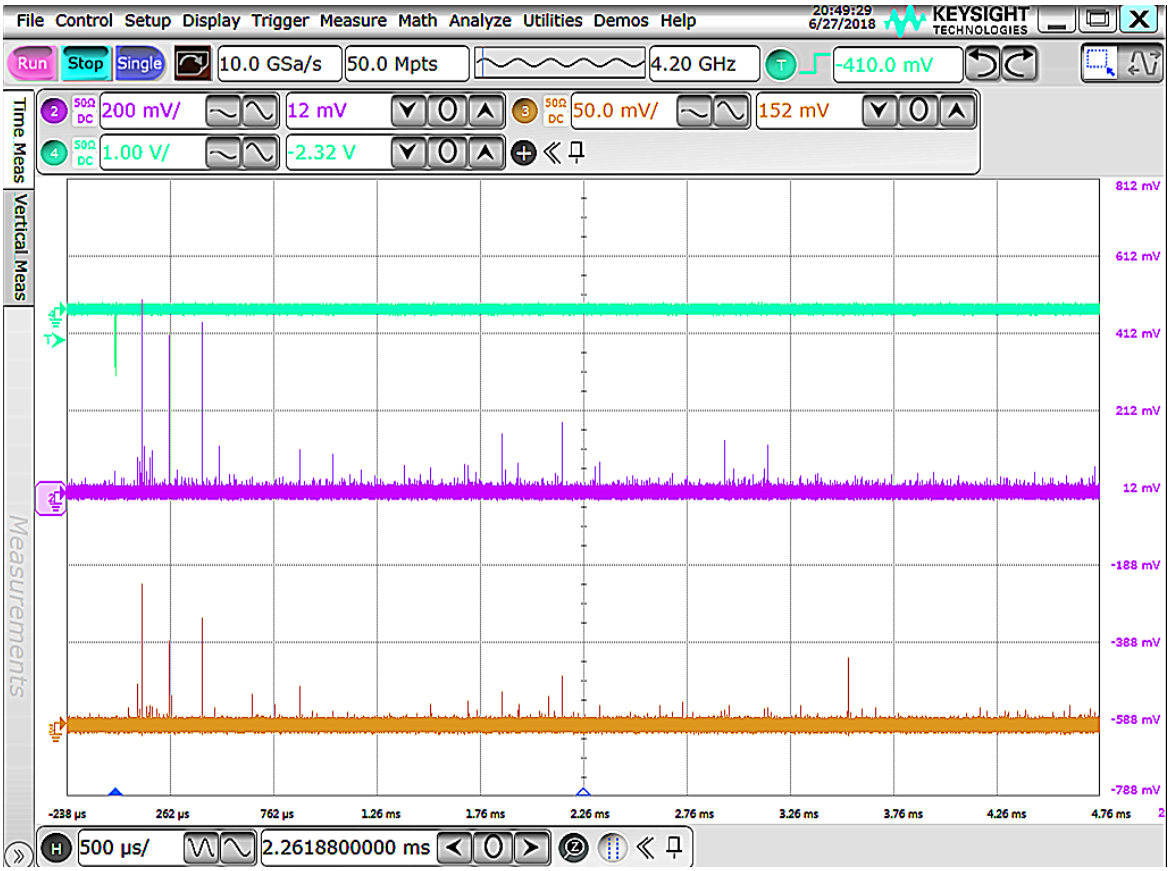


**Figure 5.21:** Screen shot of oscilloscope during the injection in LER: cyan is the injection signal, used as the trigger, red-violet is the signal from the diamond detector located at position A, closest to the Tungsten radiator and yellow is the signal from the diamond detector located about 8 cm from the Tungsten radiator longitudinally.

## 5.4 Luminosity measurement during collisions

During commissioning of colliding beams, a sensitive luminosity monitor is of great importance to provide luminosity information, not only during data taking but also for collision tuning, including searching for the collision at the very beginning and for optimization of collision parameters.

When searching for the beam collision at the IP during the Phase 2 period, beam-beam scans vertically and longitudinally were performed by applying local beam orbit bumps (vertical) and by adjusting the RF phase (longitudinal). Figure 5.22 shows the luminosity monitor signals recorded along with the beam currents and vacuum pressure in both the LER and HER. As can be clearly seen, those quasi Gaussian shaped signals from the luminosity monitors between 18:00 and 21:00 correspond to those scans. The sensitivity of the HER signal was not so good due to the very low luminosity (the geometric luminosity was at

the level of $10^{31}$ $cm^{-2}s^{-1}$ based on a calculation with beam currents and beam sizes) and resulting poor statistics. Afterwards, the first physics running started from 22:30. The luminosity monitors were then used for machine tuning and luminosity optimization during the entire Phase 2 commissioning.

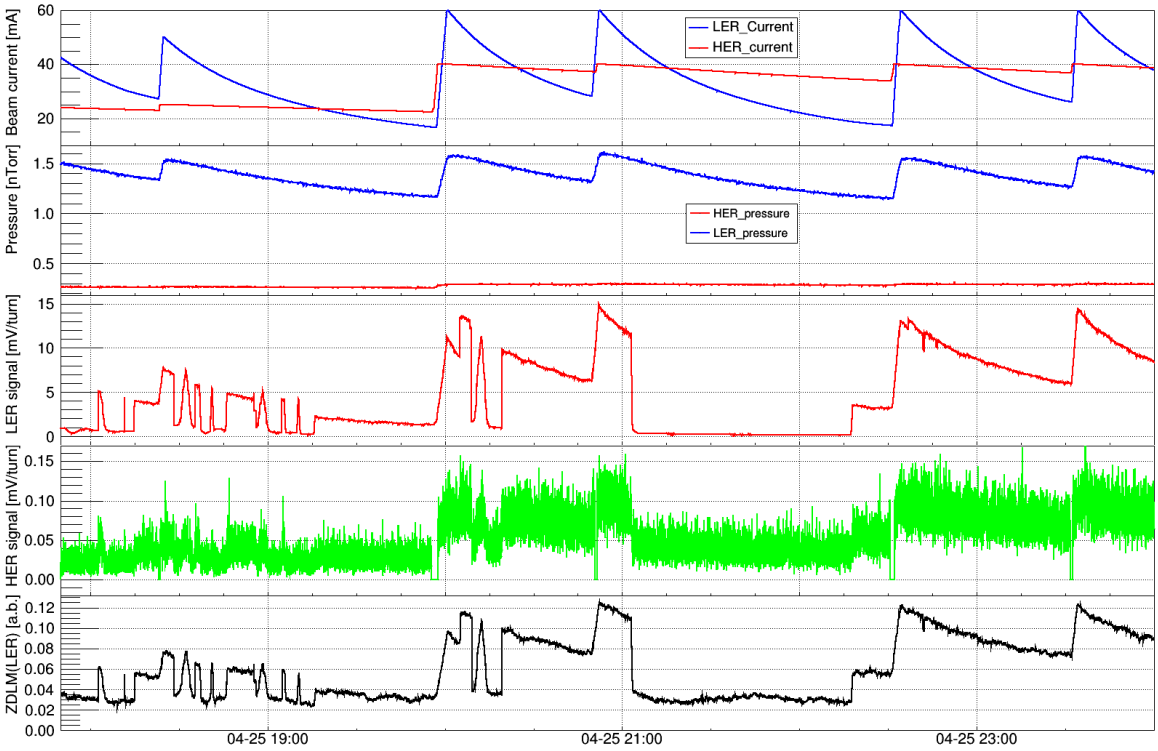


**Figure 5.22:** Signals from the luminosity monitors in both the LER and HER when searching for the beam collision with vertical and room phase scanning on April 25th.

### 5.4.1 Train Integrated Luminosity signals

Figure 5.23 gives another example of the luminosity signals at 1 Hz provided by our luminosity monitors for a whole day during the regular Phase 2 commissioning. In general, the luminosity signals from both the LER and HER follow the change of the product of beam currents in both rings. The maximum luminosity during this day was about $2.2 \times 10^{33}$ $cm^{-2}s^{-1}$, which is much higher than the luminosity during the searching for collision (mentioned above), therefore, the correlation of the HER signals with the product of the beam currents was much clearer. During the continuous injection period (17:00-22:00), the luminosity signals change more than the beam currents product because of varying offsets between the two colliding beams caused by vibrations of mechanical supports, driven essentially by ground motion, especially in the vertical plane.

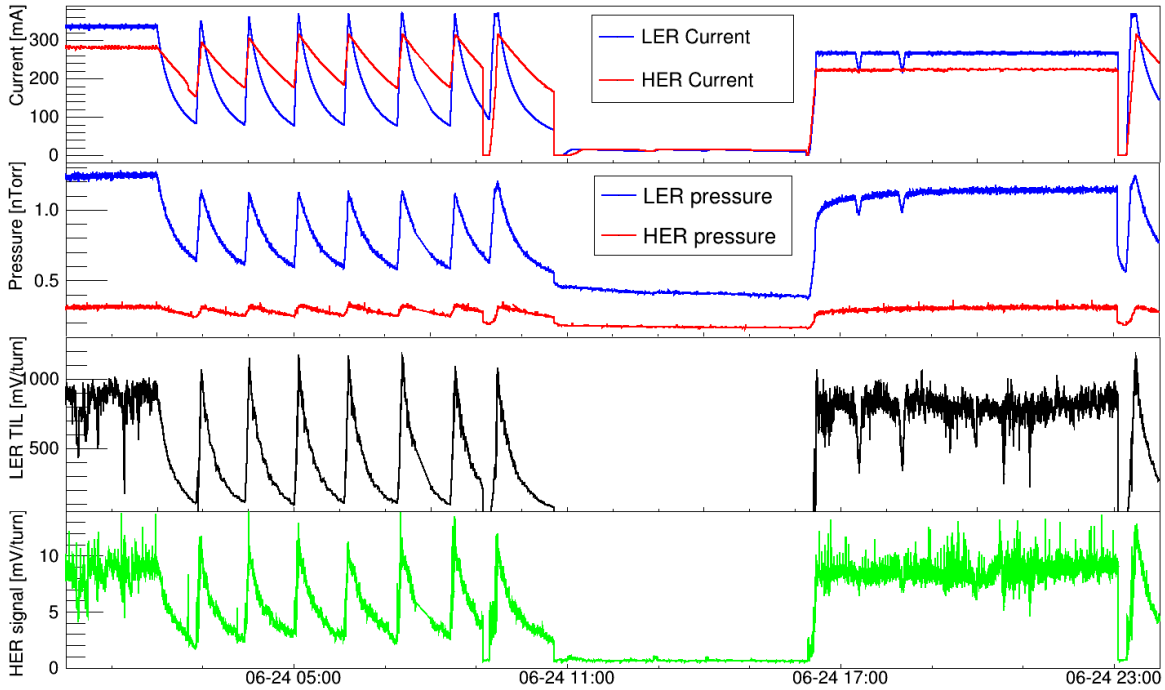


**Figure 5.23:** Example of the measured luminosity signals together with the beam currents and vacuum pressures in both the LER and HER, sampled every 1s over a day.

During the collision commissioning, the phase of our sampling needed careful consideration, especially for the TIL signals from the diamond detectors with thickness of 140 $\mu m$ coupled with a C2 broadband current amplifier, for which the full width of signal is very narrow (within 4 ns). A phase shifter was integrated into the DAQ system to treat this problem, as described in Section 5.2. Figure 5.24 shows an example of the TIL signal response to a sampling phase scan for the diamond detector with thickness of 140 $\mu m$ coupled with a C2 broadband current amplifier located at position A in the LER. Two cycles were performed (0-10 V and 10-0 V), and the TIL accumulated the effective difference for every bucket, thus there are 2 peaks during the phase scanning (A and B correspond to 1 scan cycle, C and D for another one). The optimum Phase was recorded and set after the phase scan. For the RAWSUM signal, especially for diamond detectors with thickness of 500 $\mu m$ coupled with a C6 charge amplifier, the result of the integration is not sensitive to the phase because all samples above the predefined threshold are accumulated and the pulses are much wider (about 14 ns FWHM or 30 ns full duration). During operation, the phase for the TIL signal was regularly checked (about once per week) to maintain the optimum sampling. Since the collision occurred in a very small region at the IP and the distance between the IP and our detectors doesn't change, the optimum phase should not change if the RF clock keeps the same. Our experience obtained in Phase 2 commissioning proves this argument.

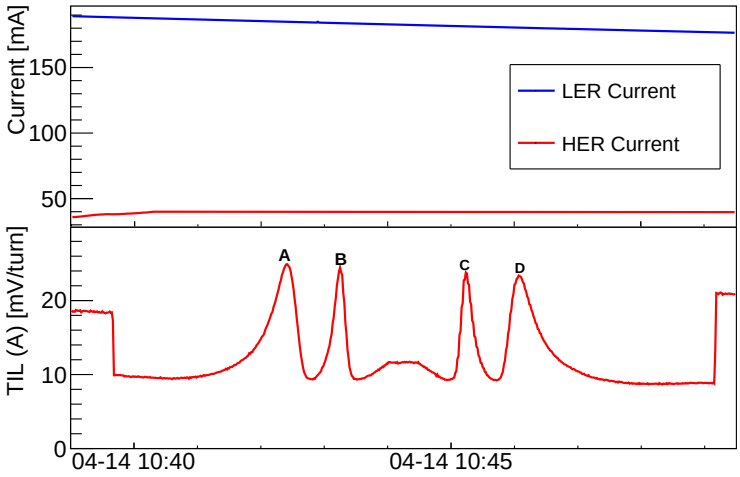


**Figure 5.24:** TIL signal response during the sampling phase scan with the phase shifter for the diamond detector with thickness of 140 $\mu m$ coupled with a C2 broadband current amplifier, located at position A in the LER.

In addition to the phase shifter, the diamond detector's response when scanning in the horizontal plane with the remotely controlled motor in the LER was also studied. To simplify the comparison between the simulation and experiment results, the signal degradation factor normalized to the signal when the diamond detector was not moved out are compared, the results are shown in Figure 5.25. Good agreement between the simulation and measurements can be found both for detectors at position A and C. For the position A case, the largest

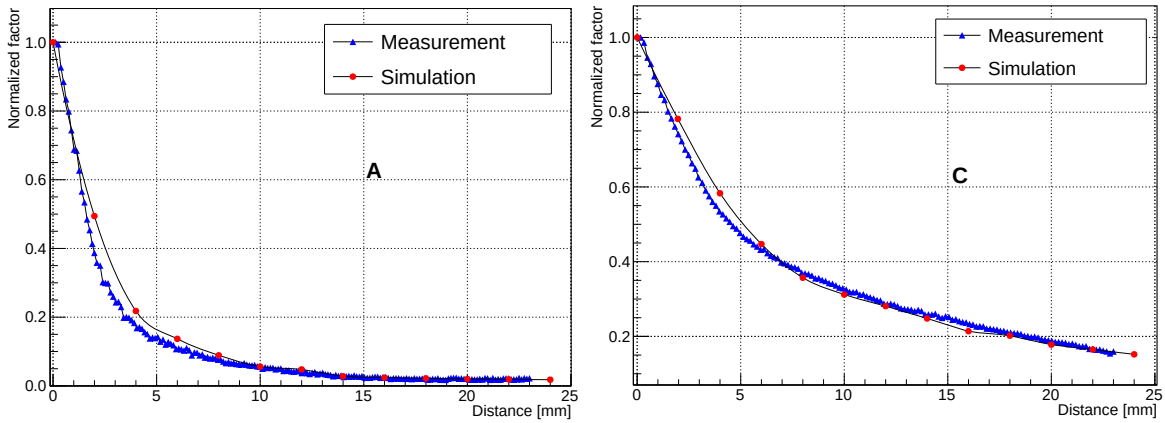


**Figure 5.25:** Signals degradation during diamond detector horizontal scans with the remotely controlled motors at position A (left) and C (right).

difference is when the detector was moved out from 2 to 5 mm, the simulation is about 20% higher than the measurement. In general, the maximum degradation factor of the signal for detector at position A is about 20 when it is fully pulled out (23 mm), and it is about a factor of 6 for position C.

#### 5.4.1.1 Internal correlations between different channels

As already mentioned before, we have mounted six diamond detectors as luminosity monitors, three for each ring, while we only have four DAQ channels. We therefore selected four out the six diamonds as input to the DAQ system, two for each ring. Since their signals mainly come from the radiative Bhabha scattering, the rate of which is proportional to the luminosity, all the signals from these channels should be proportional to one another. Of course, this needed to be checked. For the HER, due to its poor statistics, the sum of signals from both channels was used. For the LER, signals from each of the channels A, B and C (see Figure 5.6) were used for this study.

Figure 5.26 shows the correlations between the signals from channel A and channel B with that of the channel C in the LER. The good linearity is expected since they are detecting the charged secondary particles in the showers induced by the same lost Bhabha positrons. For the ratio between the signals from channel A and channel C we found 12.27, which is a little bit different from the same ratio with only the background (where it was about 14.5), but still very close to the prediction. Besides, during the Phase 2 commissioning, we also found

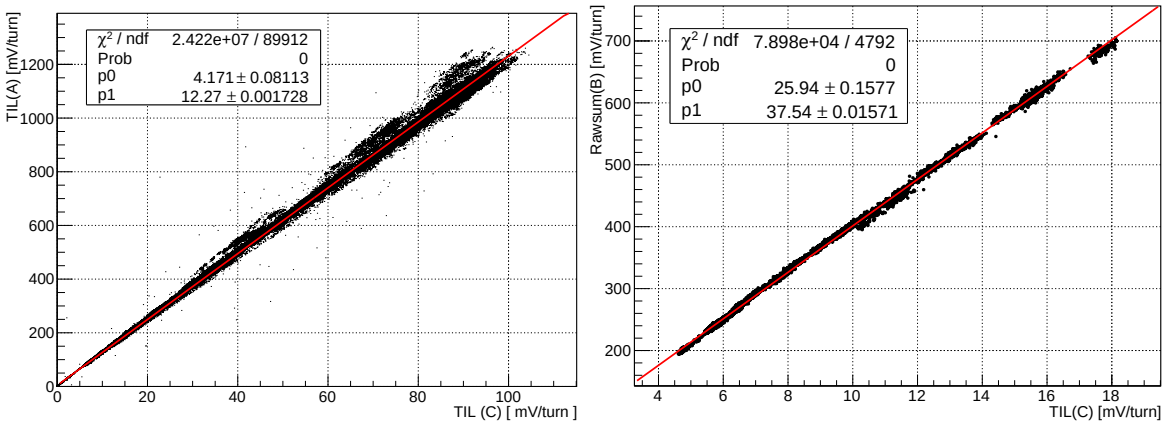


**Figure 5.26:** Examples of TIL signal from channel A with respect to channel C on the left and RAWSUM signal from channel B with respect to TIL signal from channel C on the right. All signals are from the LER.

that the signals from the channel A was sensitive to the beam vertical angle at the IP, while channel C was not. This is because our diamond detectors are very small ($4.5 \times 4.5\ mm^2$), and the divergence of the charged secondary particles in the showers in the vertical plane is very small just after the Tungsten radiator, while it spreads out much wider after about 10 cm where the diamond is placed corresponding to channel C. Considering that our diamond detectors were mounted about 10 m downstream of the IP, even a small change of beam vertical angle at the IP could affect the signals in channel A while effects are much reduced for channel C.

Even though the HER signal had very poor statistics during Phase 2 since the luminosity was relative low, the proportionality with respect to the LER signals is obvious, as shown in Figure 5.27.

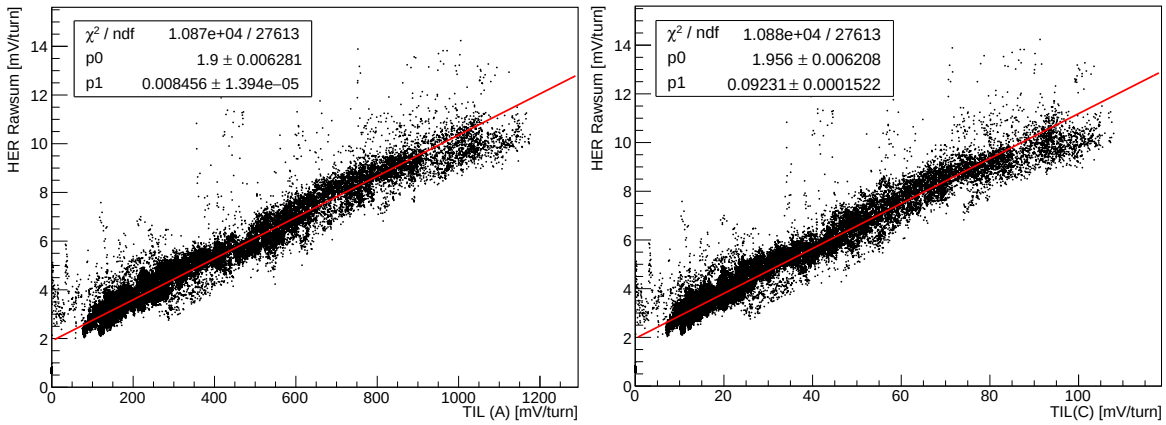


**Figure 5.27:** Example of HER sum signal with respect to the TIL signals in the LER.

Overall, good correlations were found between signals from different channels of our system, thus they can serve as backup for each other. The different sensitivities of the different channels also enable us to choose the proper channel based on specific requirements in different situations, e.g. existence of pickup noise appearing sometimes, or just the magnitude of the luminosity.

### 5.4.1.2 Comparison with other luminosity monitors

In addition to our fast luminosity monitor based on diamond detectors, there are also two more systems that provide luminosity information: the ZDLM based on scintillator and Cherenkov detectors, and the ECL, a sub-detector of the Belle II detector. As already mentioned in Section 3.2.2, the ZDLM, a complementary system to our luminosity monitor, is installed in the immediate vicinity of our diamond detectors. As mentioned in Section 2.3, the ECL, the Belle II electromagnetic calorimeter, measures the luminosity by recording the coincidence rates in the opposite sectors of its backward and forward end-caps for Bhabha events at finite scattering angles. It provides the absolute value of the luminosity after proper internal calibration.

Figure 5.28 shows an example of the luminosity signals from our diamond detectors in the LER (left) and HER (right) with respect to the luminosity information provided by the ZDLM scintillator mounted in the LER. As we expected, there are good linear relationships among these signals, although the HER signal from our diamond detector has poor statistics.

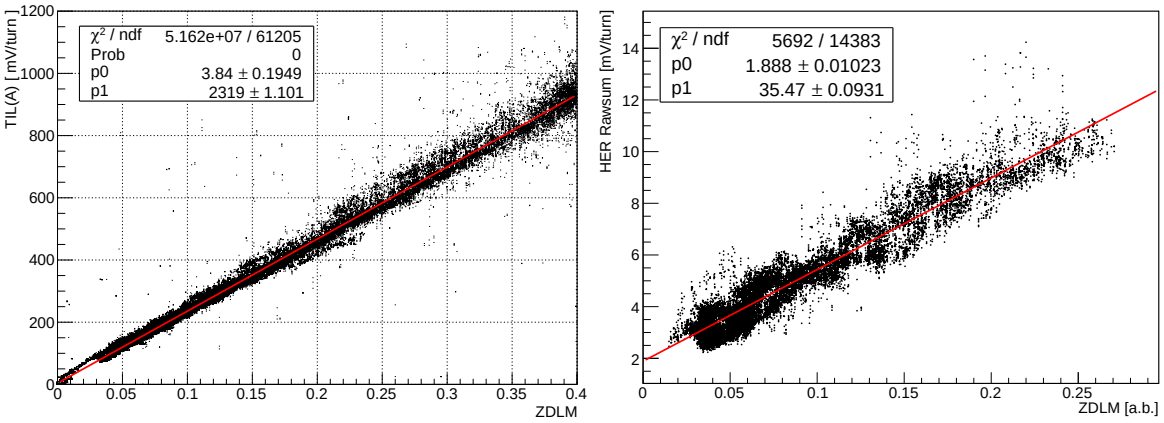


**Figure 5.28:** Example of our luminosity signals from the LER (left) and HER (right) with respect to the luminosity signals provided by the ZDLM using the scintillator mounted in the LER.

Different from the ZDLM and from our luminosity monitoring system based diamond detectors, which both provide only relative luminosity information, the ECL provides the absolute value. It is mainly used for Belle II physics studies, but can also serve as observable in the SuperKEKB machine tuning. To evaluate the performance of our relative luminosity monitors, the correlation between signals from our diamond detector and that provided by

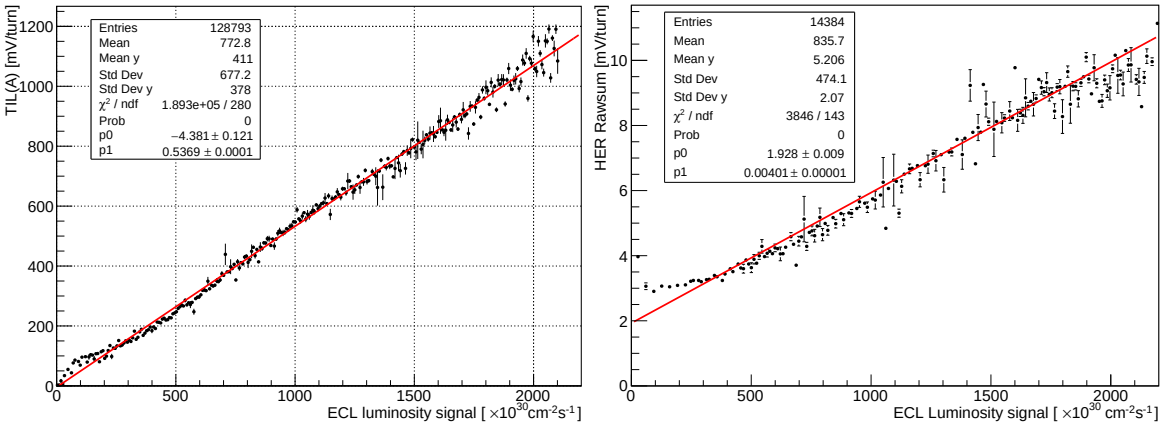


**Figure 5.29:** Example of our luminosity signals from the LER (left) and HER (right) with respect the luminosity signals provided by the ECL.

the ECL was checked. An example of the comparison is shown in Figure 5.29. As expected, our luminosity signals, by measuring the Bhabha events at vanishing scattering angle, are proportional to the absolute luminosity signals provided by the ECL. These good results confirm the reliability of our measurement and the possibility of using them as input to the dithering orbit feedback system to maintain the optimum geometric overlap between the two colliding beams in the horizontal plane, as well as to provide an effective diagnostic tool for local optics tuning in the IP region with extremely low beam currents.

#### 5.4.1.3 Relative precision estimation for TIL at 1 kHz

In addition to the Train Integrated Luminosity signal at 1 Hz, we also provide the TIL signal at 1 kHz as input to the lock-in amplifier serving for the dithering orbit feedback system. One of the most important parameters of the TIL signal at 1 kHz is the relative precision which represents the statistical fluctuation of luminosity signals that may make it harder to probe the luminosity modulation induced by the beam orbit dithering. According to the dithering orbit feedback simulation described in Section 4.5, the relative precision of the TIL signal at 1 kHz should be 1% to maintain the luminosity loss caused by horizontal vibrations within 0.5%, for the case of SuperKEKB operating with nominal parameters. Even though the luminosity degradation from the mechanical vibrations was almost negligible with the beam parameters in Phase 2, because the beam sizes at the IP were still quite large, it was meaningful to investigate the relative precision of the TIL signals at 1 kHz with the more limited luminosity and extrapolate it to the case of higher luminosities, such as $1.00 \times 10^{34}\ cm^{-2}s^{-1}$ or even $8.00 \times 10^{35}\ cm^{-2}s^{-1}$.

It is not really easy to maintain the luminosity at a quite stable level in the presence of mechanical vibrations (especially in vertical plane), beam current changes, even beam-beam effects, etc... However, if we only pick our TIL data within a time interval of a few seconds when the luminosity provided by ECL was stable, then we can at least provide a conservative estimate of the relative precision [33]. Figure 5.30 shows a sequence of our 1 kHz TIL signals from channel A in the LER. At that time, the ECL was measuring a luminosity of $(1.85 \pm 0.05) \times 10^{33}\ cm^{-2}s^{-1}$.

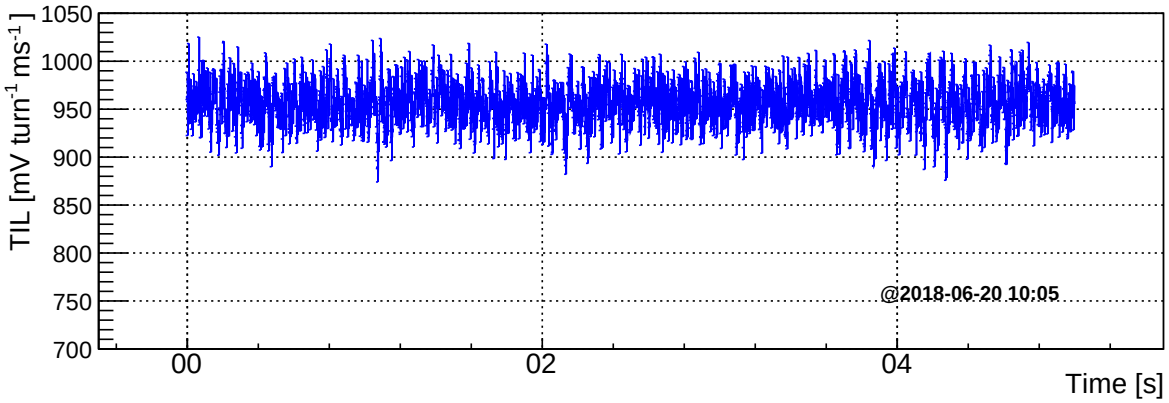


**Figure 5.30:** An example of Train Integrated Luminosity signal at 1 kHz from the channel A in the LER when the luminosity was about $(1.85 \pm 0.05) \times 10^{33}\ cm^{-2}s^{-1}$.

Based on this data sequence, we could get the histogram of the 1 kHz TIL, as shown in Figure 5.31, with an obvious Gaussian distribution.The mean value of the TIL is 956.2 mV/turn, and the Sigma is 21.7, which means a relative precision of 2.27%. The statistical

fluctuation from the simulation for this luminosity leads to a relative precision of 1.96%, which is reasonably compatible with the measurement. The difference between the simulation and experiment can be explained by the fact that the thresholds used for the real and simulated data were not fully calibrated, by imperfect signals peak sampling, and moreover the actual luminosity could also have varied slightly during the selected time interval. The relative precision for channel C was 7.63%, consistent with the signal ratio of about 10 compared to channel A. For the HER, the relative precision in 1 ms for the two Channels were not as good as for LER, about 61.95% and 75.5% for the top and bottom detectors, respectively.

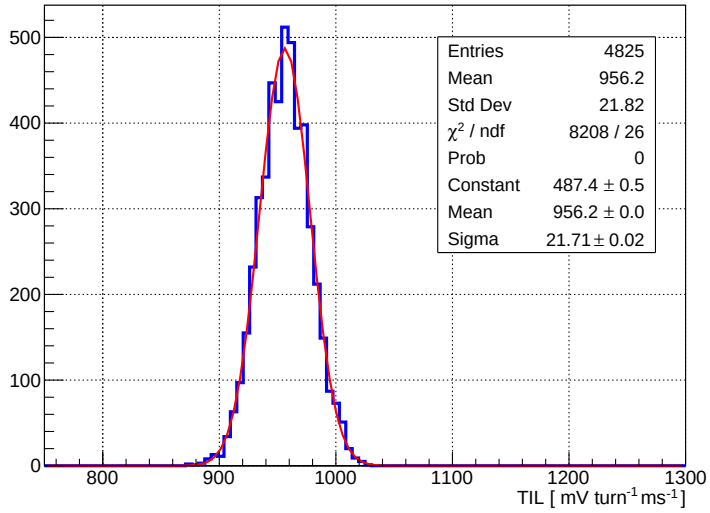


**Figure 5.31:** Histogram of the 1 kHz TIL data from Channel A in the LER when the luminosity is about $(1.85 \pm 0.05) \times 10^{33}\ cm^{-2}s^{-1}$.

If we assume that the fluctuation of our luminosity signals mainly comes from the statistical fluctuation of detected Bhabha events, it means that the relative precision of our luminosity signal is proportional to the inverse square root of the luminosity, as shown in Equation 5.3.

$$v_p \propto \frac{1}{\sqrt{N_{Bhabha}}} \propto \frac{1}{\sqrt{L}} \tag{5.3}$$

To verify our hypothesis on the relationship between the relative precision and the luminosity, we studied the relative precision as a function of the luminosity based on 1 kHz data during Phase 2. Similar to the above, five seconds data sequences were used when the luminosity information provided by the ECL was quite stable. Results are shown in Figure 5.32. It is quite clear that the relative precision improves when the luminosity is higher, and from the fit we can know that the relative precision is proportional to the inverse of the square root of the luminosity.

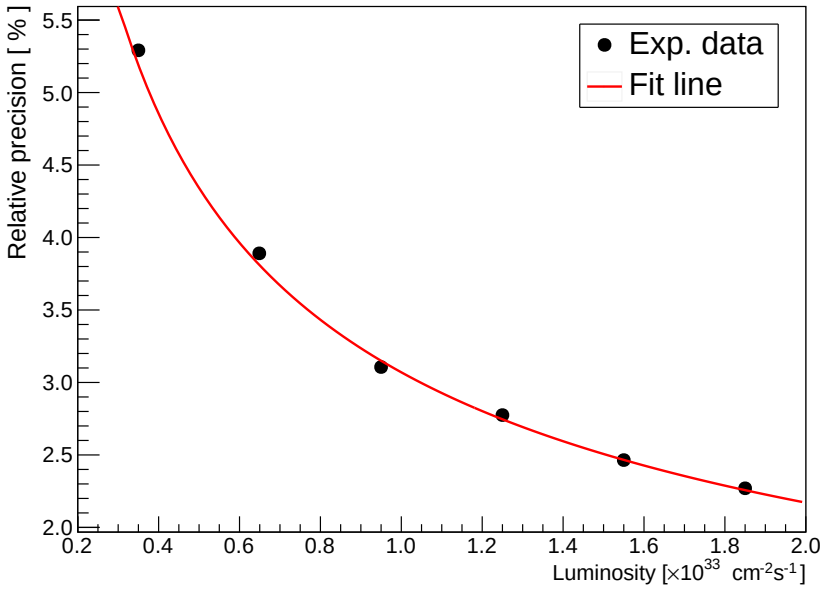


**Figure 5.32:** Relative precision of measured 1 kHz TIL signals as a function of luminosity during Phase 2 commissioning.

The good agreement between simulation and measurement gives us more confidence in our simulation and enables us to extrapolate the relative precision behavior to higher luminosities. Table 5.1 shows the comparison of the relative precision of 1 kHz train integrated luminosity signals from different channels in both the LER and HER for different luminosities based on the measurements during Phase 2, and with a reasonable extrapolation for higher luminosities cases.

| | | Relative precision ($\nu_p$) for 1 kHz signals | | | |
|---|---|---|---|---|---|
| | Luminosity $[cm^{-2}s^{-1}]$ | LER-A | LER-C | HER-1 | HER-2 |
| Exp. Data | $(1.85 \pm 0.05) \times 10^{33}$ | 2.27% | 7.63% | 75.5% | 61.95% |
| | $(1.25 \pm 0.06) \times 10^{33}$ | 2.76% | 9.28% | 91.85% | 75.31% |
| | $(0.65 \pm 0.08) \times 10^{33}$ | 3.83% | 12.87% | 127.4% | 104.43% |
| Extrapolation | $1.00 \times 10^{34}$ | 0.98% | 3.28% | 32.47% | 26.64% |
| | $1.00 \times 10^{35}$ | 0.31% | 1.04% | 10.27% | 8.44% |
| | $8.00 \times 10^{35}$ | 0.11% | 0.37% | 3.63% | 2.98% |

**Table 5.1:** Relative precision of 1 kHz luminosity signals from our system based on measurement in Phase 2 and reasonable extrapolation for Phase 3 luminosities with the present measurement set-up.

For channel A in the LER, once the luminosity reaches $1.00 \times 10^{34}\ cm^{-2}s^{-1}$, the relative precision can be expected to be better than 1%, which is the requirement to serve as input to dithering orbit feedback system (details are described in Section 4.5), and eventually 0.1%

can be achieved for the nominal luminosity of SuperKEKB if we keep this measurement set-up. Meanwhile, channel C can also provide the input signal to the lock-in amplifier with a relative precision of 1% once the luminosity reaches $1.00 \times 10^{35}\ cm^{-2}s^{-1}$. On the other hand, the relative precision of the HER signals were quite poor in Phase 2, and even for the nominal luminosity, the relative precision is at the 3% level with the present set-up. Fortunately, based on careful simulation, a new position was found to mount our diamond detector where the Bhabha event rate is expected to be about 10 times higher, which should enable a 1% relative precision to be reached at the nominal luminosity. A new set-up at this new location is being tested during the Phase 3 commissioning period.

In conclusion, with our luminosity monitor, which consists of six channels located both in the LER and HER, coupled with remotely controlled motors to scan in the horizontal plane, we can provide the train integrated luminosity signals at 1 kHz with a relative precision of 1% for a large luminosity dynamic range, from $10^{34}\ cm^{-2}s^{-1}$ to $8 \times 10^{35}\ cm^{-2}s^{-1}$, about two orders of magnitude. In addition, we can extrapolate our relative precision results for 1 kHz signals to 1 Hz signals. For instance, for channel A in LER, if we accumulate the signals every 1 second when luminosity is $1.00 \times 10^{31}\ cm^{-2}s^{-1}$, we can also obtain the luminosity signals at 1 Hz with a relative precision of 1%. This is very useful for machine optics tuning with beam collisions at the IP, especially in the extremely low beam current case to avoid beam-beam blow up and get the geometrical luminosity, more details will be described in Section 5.5.2.

### 5.4.2 Bunch Integrated Luminosity signals

There will be 2500 bunches circulating in the ring in the nominal case of SuperKEKB. With such a large number of bunches populating the ring, variations in the bunch transverse positions and beam sizes are in principle possible through a variety of effects, causing systematic reduction in luminosity for some of the bunches. This should be monitored just like the individual bunch currents.

After getting the BIL sums for the 5120 buckets, and comparing with the fill pattern used at the given time in SuperKEKB, the Bunch Integrated Luminosity signals can be provided. Figure 5.33 gives an example of display from channel A in the LER for the beam conditions at the end of Phase-2 commissioning, when the instantaneous luminosity was about $1.6 \times 10^{33}\ cm^{-2}s^{-1}$, with 395 bunches circulating in each ring, separated by 24 ns. Obvious differences in the luminosities between bunches can be observed, while it is not easy to evaluate the individual bunch behaviors from this plot. On the other hand, coupled with the individual bunch currents, we can do some preliminary analysis of the bunch integrated luminosities.

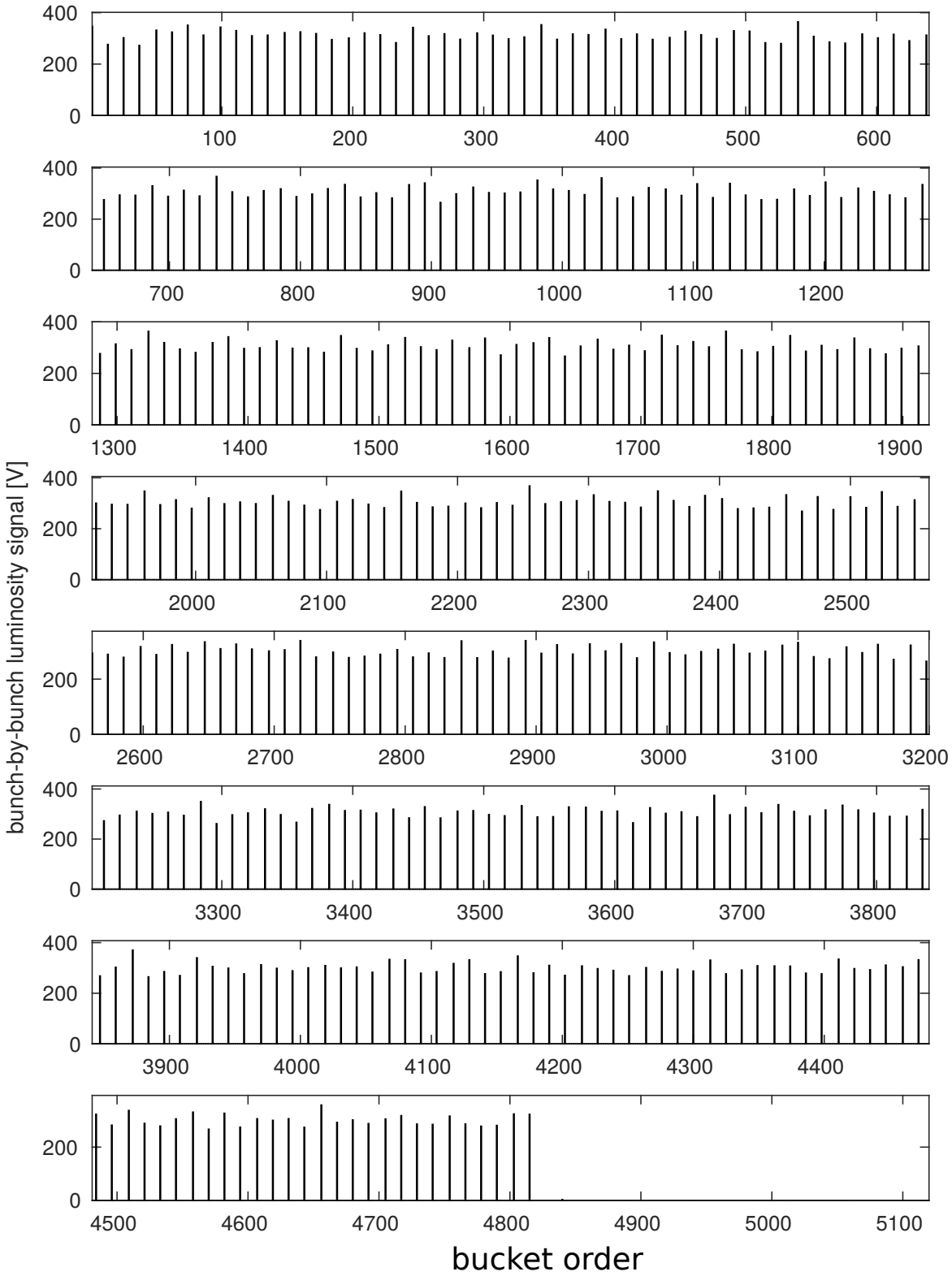


**Figure 5.33:** An example of Bunch Integrated Luminosity signals provided by channel A in the LER. 395 bunches were filled when this plot was recording, and the instantaneous integrated luminosity was $1.6 \times 10^{33}\ cm^{-2}s^{-1}$.

Figure 5.34 shows the histogram of the Bunch Integrated Luminosity signals displayed in Figure 5.33 on the left and the product of beam bunch currents on the right, the spread in bunch integrated luminosity signals was about 8.13% at that moment, dominated by the measured spread of the products of bunch currents, which was found to be about 7.25% using the bunch-by-bunch current monitor [139]. As a comparison, the relative precision for the 1 kHz TIL signals was about 2.55%, from which the average relative precision of BIL signals at 1 Hz could be estimated at the level of 1.6% by a simple scaling in the assumption of uniform bunch currents and perfect alignment of the bunches along the trains in both rings.

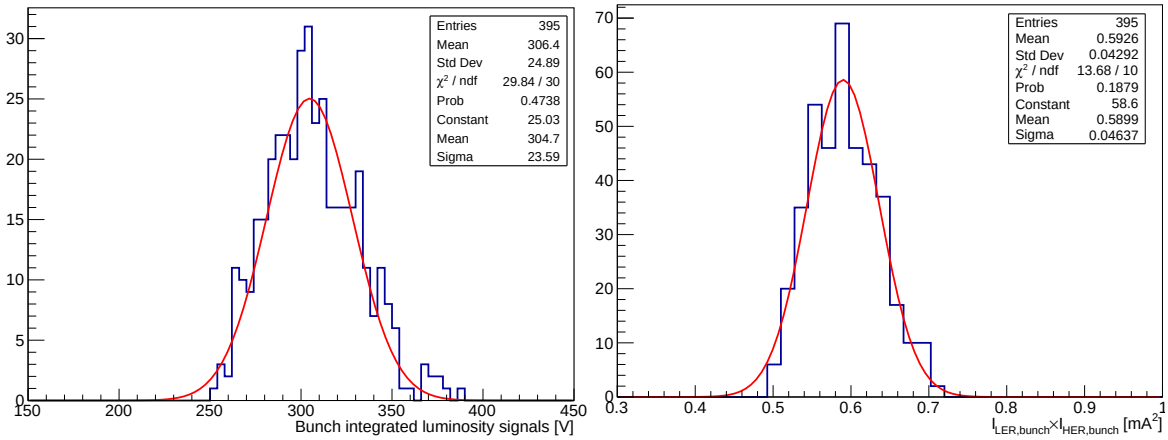


**Figure 5.34:** Histogram of the Bunch Integrated Luminosity signals displayed in Figure 5.33 in the left and the product of the LER and HER bunch currents in the right.

In Phase 2, due to the longitudinal instability between bunches when increasing the beam current for a large number of bunches populating in the rings (1576 bunches), vacuum leakage in the HER and other limitations [132], the machine was commissioned with either low bunch current and large number of bunches or high bunch currents and small number of bunches. Other than the bunch integrated luminosity signal variations induced by beam current variations in both rings, there was no other observation of the luminosity changing due to other effects, such as imperfect alignment, different amounts of bunch beam size blow up and so on. It will nonetheless be important to check for differences between bunches for the high beam currents and bunch charges expected when SuperKEKB nominal parameters will be reached.

## 5.5 Applications of our luminosity monitor

There are three main important applications of our luminosity monitor based on diamond detectors:

1. Train integrated luminosity signals at 1 kHz with relative precision of 1% used as input to the lock-in amplifier part of the dithering orbit feedback system to maintain the optimum geometrical overlap between the two colliding beams in the horizontal plane;

2. As a sensitive luminosity monitor to provide luminosity information at 1 Hz, which is very useful for beam collision and machine optics tuning through vertical beam-beam scans, especially with very low beam currents;

3. Bunch integrated luminosity signals at 1 Hz, which can be used to study the machine performance along the bunch train.

During Phase 2 commissioning, the dithering orbit feedback system based on the 1 kHz train integrated luminosity signals was tested, and the 1 Hz signal was commonly used when performing the vertical beam-beam scans during collisions for the purpose of the IP local optics tuning and optimization of the collision parameters.

### 5.5.1 Dithering orbit feedback system test

Because the beam sizes during Phase 2 commissioning of SuperKEKB were not as small as specified in the nominal parameters, the luminosity was not very sensitive to the horizontal vibration of mechanical supports caused by ground motion. The dithering orbit feedback system was therefore not used continuously during the operation, only tested at a basic level to check if it worked or not.

During the test, the LER positron beam was dithered sinusoidally at a frequency of 79 Hz, with an amplitude of 40 $\mu m$, by a set of dithering magnets according to the dither driven reference provided by the lock-in amplifier [140]. Figure 5.35 shows the Fast Fourier Transform spectrum of the fast luminosity signals when the dithering magnets were active. The peaks at the first (79 Hz) and second (158 Hz) harmonics of the dithering frequency can be observed, and also the AC power frequency at 50 Hz. The dithering orbit feedback system, described in Section 3.2, is designed to optimize the luminosity by minimizing the magnitude of the peak at the fundamental frequency, therefore only the first harmonic is needed.

The 1 kHz TIL signal from channel A in the LER was used as input to the lock-in amplifier (Ametek 7230 [141]) after being converted from digital to analog via the DAC integrated in our DAQ system. The lock-in amplifier will mix the luminosity signal with the dithering reference used to drive the dithering coils, before applying a low pass filter to provide an output voltage proportional to the luminosity and to the offset between the two colliding beams (for offsets near $x_0 = 0$) and a phase which represents the sign of the offset. The output voltage becomes zero when the beams are perfectly centered and the luminosity

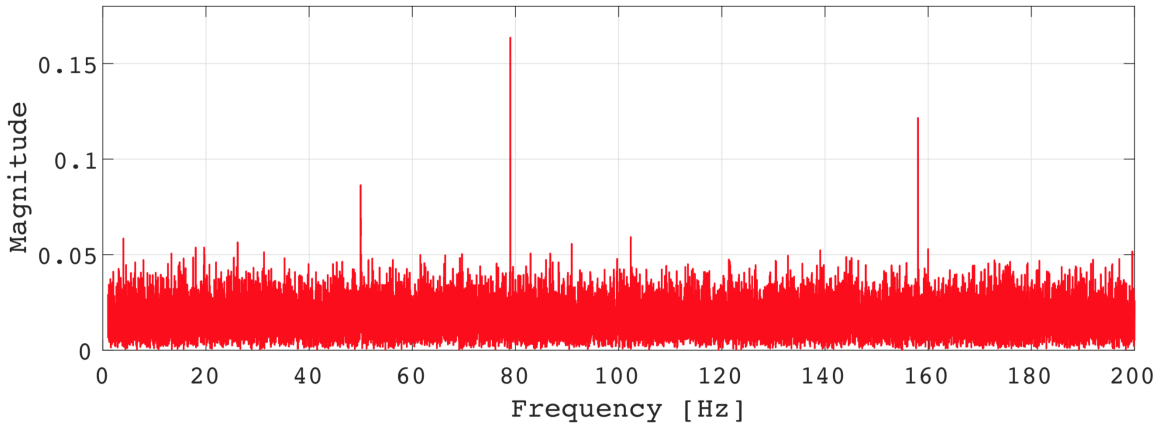


**Figure 5.35:** FFT spectrum of the train integrated luminosity signals at 1 kHz when the LER positron beam was dithered at 79 Hz with an amplitude of 40 $\mu m$.

is maximized. The Phase will also change polarity when the beam goes across the peak. In this way, the HER beam can be kicked in the correct direction to recover the luminosity. The information from successive offsets is exploited using the Newton method to search for zero in the dithering orbit feedback control algorithm.

#### 5.5.1.1 First test with $\beta_y^*$=8 mm

The first dithering orbit feedback test was performed with $\beta_{x\pm}^* = 200$ mm and $\beta_{y\pm}^* = 8$ mm, which is much larger than the nominal values. In this case, the luminosity should not be very sensitive with respect to the horizontal beam-beam offsets.

Before the feedback test, the response of the lock-in amplifier with respect to horizontal beam-beam offsets was first studied. Horizontal beam-beam offsets were introduced deliberately with several steps on both side of the peak luminosity position, the outputs of the lock-in amplifier, including the magnitude and phase of the first harmonic in the frequency domain, were obtained for each step both when using 1 kHz luminosity signal from LumiBelle2 and ZDLM as input, see Figure 5.36 [142, 143]. It is clear that the magnitude follows the "V" shape as predicted in the simulation (see left of Figure 3.4), even though the luminosity modulation due to the dithering was not so sensitive because of the large beam sizes, which results in some fluctuation in the results. The opposite polarity of the phase for LumiBelle2 and ZDLM is because the connection for LumiBelle2 was inverted on the lock-in amplifier [141].

As already explained, the sign ambiguity resulting from the evenness of the luminosity dependence with the beam-beam offset described in Equation 4.12 was resolved by comparing the phase of the dither driven reference signals with that of the resulting luminosity signal

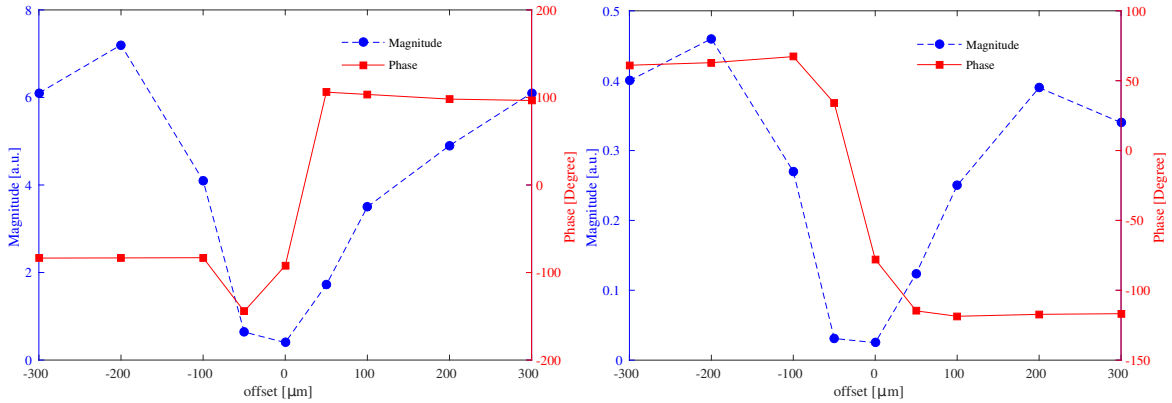


**Figure 5.36:** Output of the lock-in amplifier, with the magnitude of the 79 Hz Fourier component in blue and the phase in red as a function of the horizontal offsets between the two colliding beams by using LumiBelle2 (left) and ZDLM (right) signals from the LER as input.

modulation, through the mixing operation in the lock-in amplifier mentioned above. The magnitude of the first harmonic reached a minimum when the offset was zero, which is also the place where the phase changed the sign, consistent with our expectation based on the luminosity behavior. In addition, it is also quite clear that when the offset between the two colliding beams is small, the relationship between the output of the lock-in amplifier and the beam offset is approximately linear.

To investigate the performance of the dithering orbit feedback system for the horizontal beam orbit stabilization based on Newton's method and using a PI (Proportional Integrator) control algorithm, several horizontal offsets were introduced deliberately and then the dithering orbit feedback system was activated. The feedback algorithm determines the proper

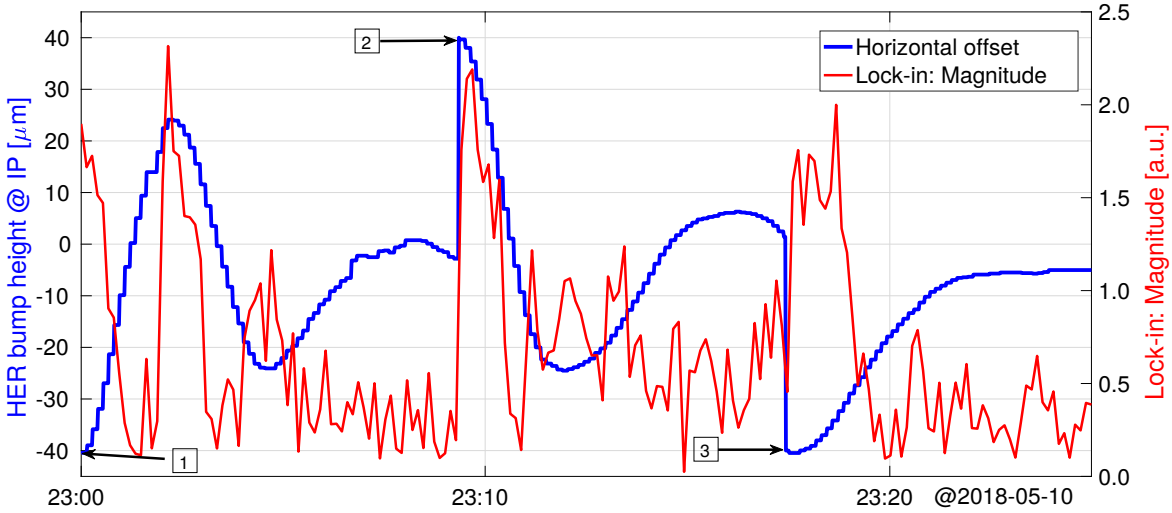


**Figure 5.37:** Dithering feedback system test with deliberately introduced horizontal offsets by using the LumiBelle2 signal as input to the lock-in amplifier.

size and direction of the offset correction needed at the IP. The information is then sent to the magnet control system via EPICS to create a local correction bump in the HER beam to compensate the offset between the two colliding beams. The results including the bump height at the IP and the magnitude of the lock-in amplifier are shown in Figure 5.37. Tests were done with three different magnitudes for the horizontal local bump at the IP of (1) -40 $\mu m$, (2) 40 $\mu m$ and (3) -40 $\mu m$ again by using LumiBelle2 signals as input to the lock-in amplifier.

It is clear that the dithering orbit feedback system can correct the beam orbit by steering the HER beam toward the LER beam. For the first two tests, due to inappropriate parameters in the PI controller, some overshooting were observed in the beam orbit correction. After optimizing the PI control parameters, the feedback converged smoothly to an optimum value without any overshoot (test 3) and the lock-in amplifier output magnitude, representing the 79 Hz Fourier component, was brought very close to zero.

#### 5.5.1.2 The second test with $\beta_y^*$=3 mm

At the end of the Phase 2 commissioning, with the progress of the $\beta_{y\pm}^*$ squeezing, the $\beta_{y\pm}^*$ reached 3 mm in both rings and $\beta_x^*$ was 100 mm in the HER and 200 mm in the LER. Another dithering orbit feedback test was performed with these much smaller beam sizes, even if they are still far away from the nominal ones. Comparing to the first test with $\beta_y^*$ equals 8 mm, the beam size was smaller and the luminosity was higher.

As for the first test described in Section 5.5.1.1, the response of the lock-in amplifier was studied through scans in the horizontal plane. Four scanned data sets were taken using LumiBelle2 and ZDLM alternatively as input to the lock-in amplifier, with varying HER horizontal local bumps at the IP, see Table 5.2 [144]. During this test, the signal from the channel located at position A in the LER was used for LumiBelle2, and the same channel as in the first test described above for ZDLM. Here we will discuss the results from Scan 1 and Scan 3.

| | Input | Scan range ($\mu m$) [1] |
|---|---|---|
| Scan 1 | LumiBelle2 | -250∼+250 |
| Scan 2 | LumiBelle2 | +250∼-250 |
| Scan 3 | ZDLM | -150∼+150 |
| Scan 4 | ZDLM | +150∼-150 |

**Table 5.2:** Four luminosity scans in the horizontal plane performed at the end of the Phase 2 commissioning to study the response of the lock-in amplifier.

For Scan 1, the HER horizontal bump was scanned from -250 $\mu m$ to 250 $\mu m$, and the LumiBelle2 signal was used as input to the lock-in amplifier. The normalized luminosity information both from LumiBelle2 and ZDLM with respect to the horizontal beam-beam offset are shown in the left of Figure 5.38, fitted with Gaussian functions.

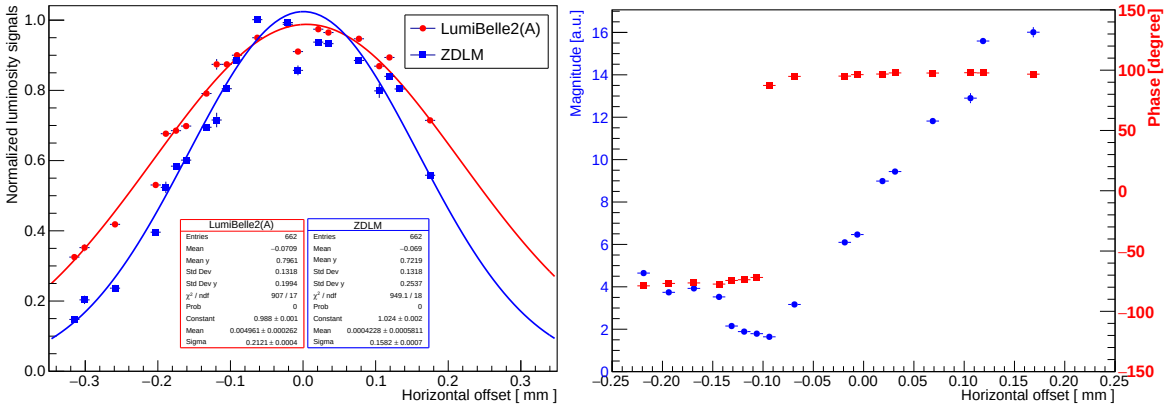


**Figure 5.38:** The luminosity information from LumiBelle2 and ZDLM normalized to that when there is no offset (left) and output of the lock-in amplifier, with the magnitude of the 79 Hz Fourier component and the phase (right, shown with plain squares and circles, respectively) using LumiBelle2(A) as input, as a function of the horizontal offsets between the two colliding beams.

Both luminosity monitors reached the maximum when the horizontal beam-beam offset was zero. However, the magnitude of the lock-in amplifier output reached the minimum when the beam-beam offset was -0.1 mm, where the phase also changed its polarity. In addition, the magnitude is supposed to be symmetrical on both sides of the peak luminosity position, which was not the case.

For Scan 3, the ZDLM signal from the LER was used as input to the lock-in amplifier and the HER horizontal bump was scanned from -150 $\mu m$ to 150 $\mu m$. The same plots as for Scan 1 are shown in Figure 5.39. The luminosity also peaked when the horizontal beam-beam offset was zero for both luminosity monitors, consistent with the results of Scan 1. On the other hand, the outputs of the lock-in amplifier, including the magnitude and phase, agreed with our expectation that the magnitude should reach a minimum and the phase should change its sign when the horizontal beam-beam offset goes through zero. Moreover, the magnitudes are symmetrical with respect to the horizontal beam-beam offset on both sides of the peak luminosity position. The results are consistent with the first test described in Section 5.5.1.1 and with the simulation prediction (see Figure 3.4).

In comparison with Scan 3 (which used ZDLM signal as input), for Scan 1 (for which LumiBelle2(A) signal was used), we found that the position where the magnitude reached a minimum and the phase changed its sign did not match the peak luminosity position: there was a difference of 0.1 mm between them. The dependence of the magnitude of the 79

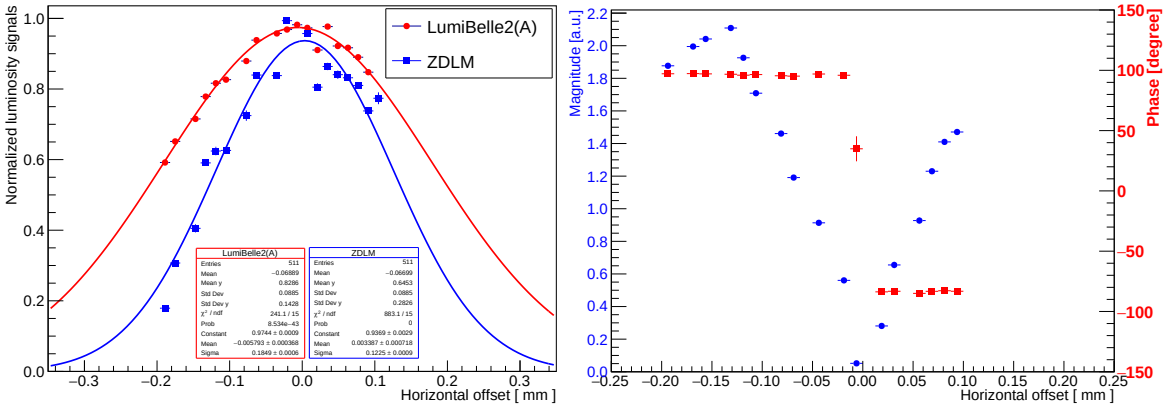


**Figure 5.39:** The luminosity information normalized to that when there is no offset (left) and output of the lock-in amplifier, with the magnitude of the 79 Hz Fourier component and the phase (right, shown with plain squares and circles, respectively) using ZDLM as input, as a function of the horizontal offsets between the two colliding beams.

Hz Fourier component of the luminosity signal is also not symmetrical with respect to the horizontal beam-beam offset, which is not the case of Scan 3. It is clear that something was wrong that we did not understand with the channel A of LumiBelle2 during this dithering orbit feedback test.

Fortunately, we have another channel which was installed 8 cm further down of the Tungsten radiator, channel C (see the left plot. of Figure 5.6), and all the 1 kHz data were saved during the whole period of Phase 2 commissioning, just like the 1 Hz data. Figure 5.40 shows the normalized luminosity information of channel A and C from LumiBelle2 and ZDLM during Scan 1 and 3 as a function of the horizontal beam-beam offsets. We observed that the spare signal from channel C behaved as the other two, with the luminosity peaking when the offset between the two colliding beams was zero.

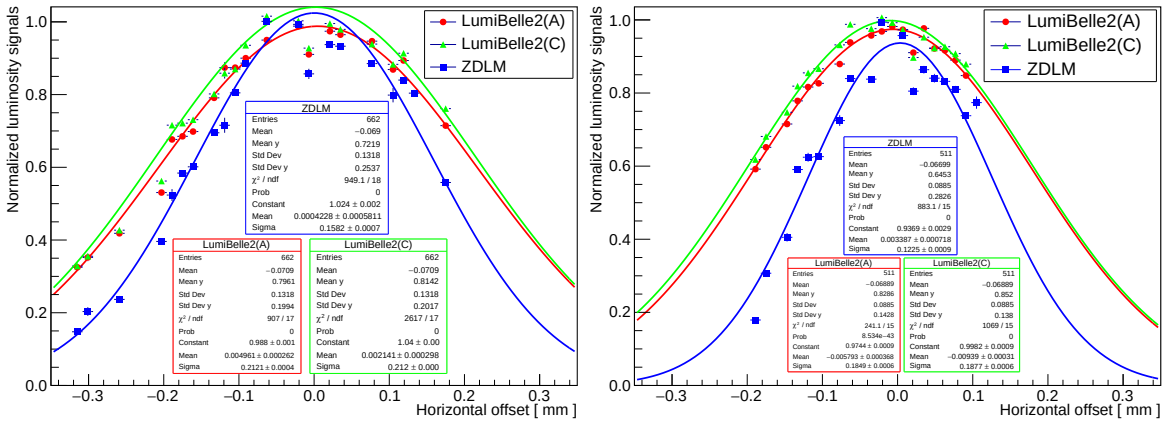


**Figure 5.40:** The luminosity information normalized to that when there is no offset for Scan 1 (left) and Scan 3 (right) as a function of the horizontal offsets between the two colliding beams.

Fast Fourier Transforms using the archived 1 kHz data were performed to extract the magnitude and phase information of the dithering frequency component in a way equivalent to what is done in the lock-in amplifier. The same sample lengths of two seconds were used when performing the FFT analysis as in the dithering feedback test. The results for channel C are shown in Figure 5.41, left for Scan 1 and right for Scan 3.

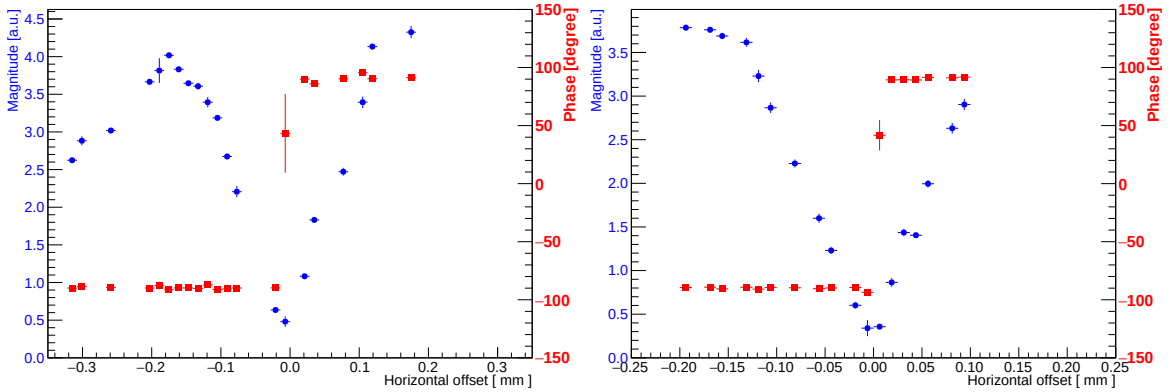


**Figure 5.41:** Magnitude of the 79 Hz Fourier component in blue and phase in red as q function of the horizontal offsets between the two colliding beams based on off-line FFT analysis with the 1 kHz data from LumiBelle2 channel C, for Scan 1 (left) and Scan 3 (right).

Different from the test which used channel A as input to the lock-in amplifier, the results from the off-line FFT analysis with the 1 kHz data from channel C show that the magnitude reached a minimum at zero offset, that the phase changed its polarity, and the magnitude curves were also symmetrical with respect to the horizontal beam-beam offsets, consistent with our expectations and with the results from ZDLM.

In addition, to verify the reliability of the FFT analysis, the same off-line analysis was performed with the archived 1 kHz data from channel A, see Figure 5.42. The FFT analysis indeed reproduced the results from the lock-in amplifier, for both the magnitude and the phase: for both Scan 1 and 3, the magnitude reached a minimum when the beam-beam offsets were -0.1 mm, where the phase also changed its sign, with the magnitude clearly unsymmetrical with respect to the horizontal beam-beam offsets. All those characteristics are consistent with the actual experimental results (see the right of Figure 5.38).

The good agreement between the on-line dithering tests and off-line analysis results for channel A proves that our off-line analysis based on a FFT using the archived 1 kHz data is reliable. In addition, the good consistency of the off-line analysis results for channel C with the online test results using ZDLM as input for Scan 3 and the internal consistency between Scan 1 and 3 for channel C indicate that channel C was working well and agreed with our expectation.

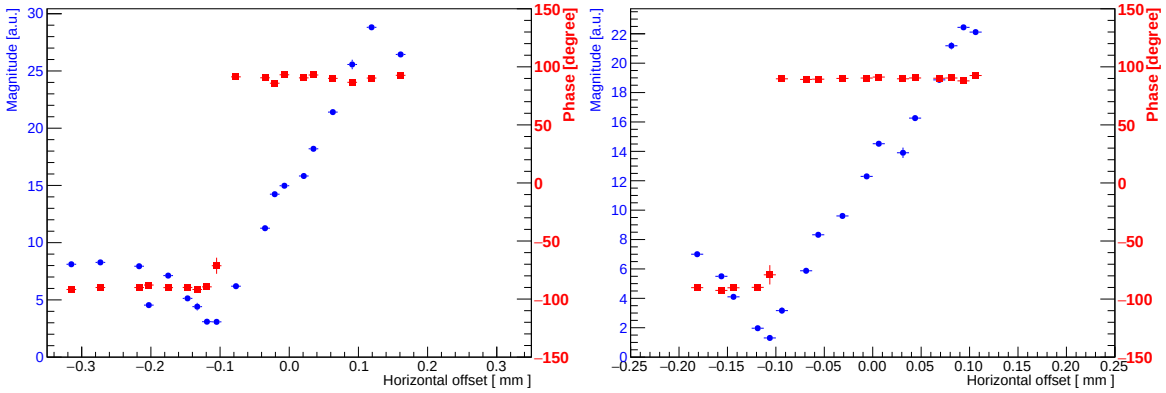


**Figure 5.42:** Magnitude of the 79 Hz Fourier component in blue and the phase in red as a function of the horizontal offsets between the two colliding beams based on off-line FFT analysis with the 1 kHz data from LumiBelle2 channel A, for Scan 1 (left) and Scan 3 (right).

On the other hand, the differences between channel A and channel C show that something was wrong with channel A. At a later stage, during early Phase-3 commissioning in 2019 when further tests of the dithering feedback system were performed, we actually found such an abnormal behavior again, this time both when using LumiBelle2 and ZDLM as inputs to the lock-in amplifier. This is described in detail below, along with a plausible explanation for the misbehavior.

#### 5.5.1.3 X-Y coupling in dithering coils and an explanation for the misbehavior of channel A during the second test in the 2018 Phase 2 commissioning

Two dithering IP orbit feedback system tests were also performed in the first half of 2019. X-Y coupling was found in the horizontal dithering coils in LER, which means part of the horizontal dithering was leaked to the vertical plane, and due to the imperfection of the fast IP orbit feedback system in the vertical plane, vertical beam-beam offsets existed during these two dithering tests. The minimum magnitude position shifted from the peak luminosity position, and the magnitude was asymmetry with respect to the horizontal beam-beam offset, both LumiBelle2 and ZDLM were used as input to the lock-in amplifier, see Figure 5.43 and 5.44. To better understand the effect of the X-Y coupling on the horizontal dithering IP orbit feedback system, a detailed simulation study was carried out.

**Simulation study on X-Y coupling in the dithering coils**

In the presence of some X-Y coupling of the dithering coils, the LER beam is not only dithered in the horizontal plane, but also the vertical plane. Since the vertical beam size is much smaller than the horizontal one, even a very small amount of coupling can induce a

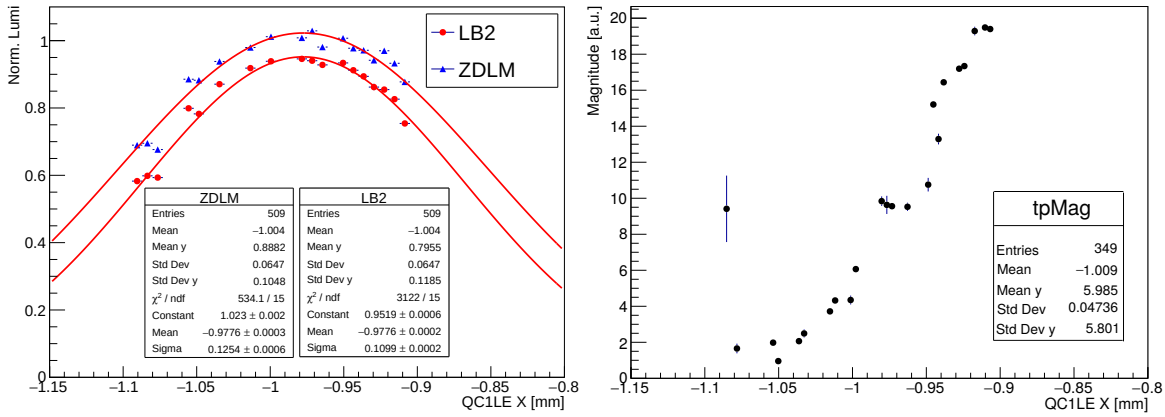


**Figure 5.43:** The luminosity information normalized to that when there is no offset (left) and output of the lock-in amplifier, with the magnitude of the 79 Hz Fourier component (right) using LumiBelle2 (channel C) as input, as a function of the horizontal measurement provided by QC1LE BPM.

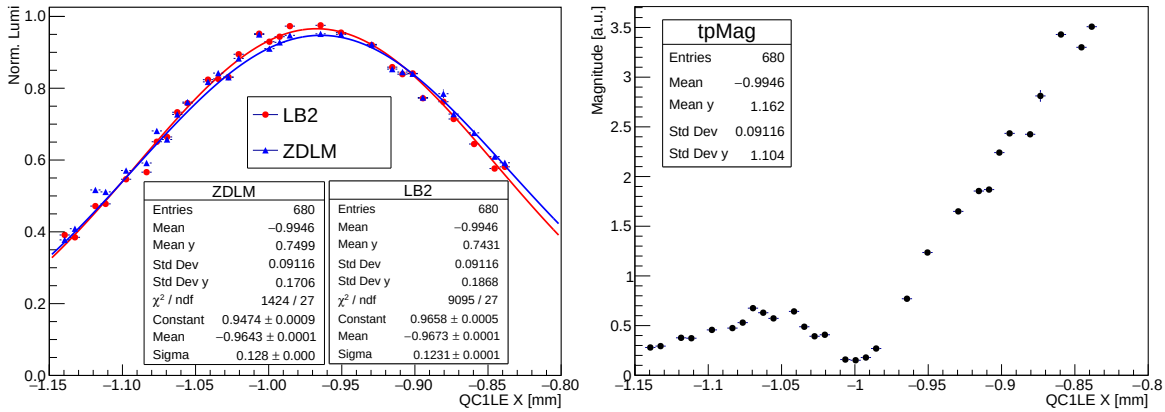


**Figure 5.44:** The luminosity information normalized to that when there is no offset (left) and output of the lock-in amplifier, with the magnitude of the 79 Hz Fourier component (right) using ZDLM as input, as a function of the horizontal measurement provided by QC1LE BPM.

large luminosity modulation. In this case, the luminosity will be described as Equation 5.4 instead of Equation 4.12,

$$L = L_0 \times exp\left[-\frac{[x_0 + \Delta x sin(2\pi f t)]^2}{2\Sigma_x^2}\right] exp\left[-\frac{[\Delta y + k\Delta x sin(2\pi f t)]^2}{2\Sigma_y^2}\right] \tag{5.4}$$

where the $L$ is the luminosity, $L_0$ is the nominal luminosity without dithering and beam-beam offset, $x_0$ is the horizontal beam-beam offset, $\Delta x$ is the horizontal dithering amplitude, $\Delta y$ is the residual vertical offset, $k$ is the coupling factor of the dithering, and $\Sigma_y = \sqrt{2}\sigma_y$, $\sigma_y$ is the vertical beam size at the IP.

Since the dithering orbit feedback system is based on minimizing the magnitude at the dithering frequency in the frequency domain to optimize the luminosity, as described in

Section 3.2.1, if the beams at the IP are well aligned in the vertical plane ($\Delta y$=0), then the magnitude of the Fourier component in the presence of the simultaneous vertical dithering induced by the X-Y coupling will remain at its minimum, and there will be no effect on the horizontal dithering orbit feedback system. For instance, when $k = 0.01$, the normalized luminosity and simulated magnitude at the dithering frequency as a function of the horizontal beam-beam offset are shown in Figure 5.45. It is clear that the magnitude reaches a minimum where the luminosity is maximum, the magnitude itself is symmetrical with respect to the horizontal beam-beam offset, consistent with the results without the X-Y coupling of the dithering coils (see Section 3.1.2).

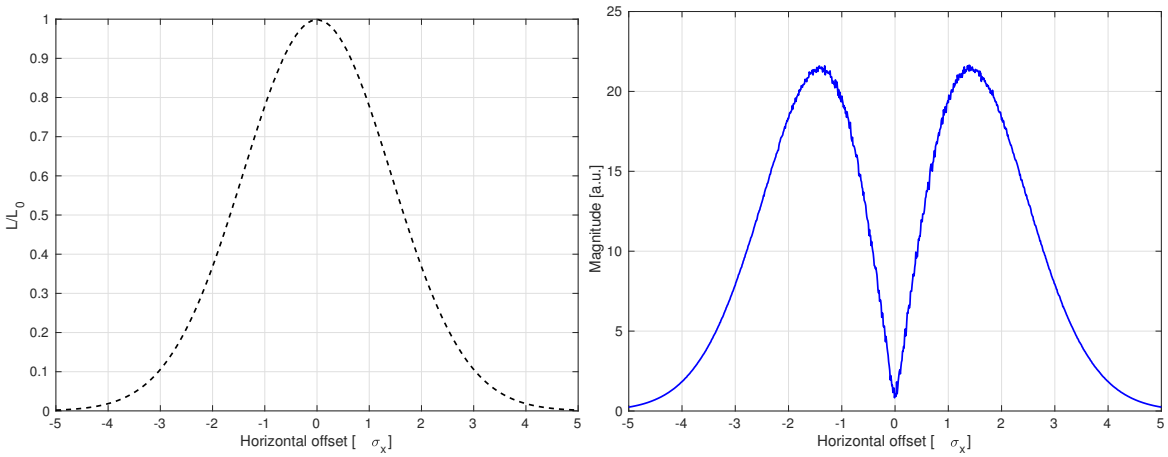


**Figure 5.45:** Normalized luminosity (left) and magnitude (right) at the dithering frequency with respect to the horizontal beam-beam offset in the presence of the vertical beam dithering due to the X-Y coupling of the dithering coils ($k$=0.01), and the vertical offset at the IP is zero ($\Delta y = 0$).

However, if there is a vertical offset ($\Delta y$) between the two beams at the IP due to the mechanical vibrations and imperfect vertical IP orbit feedback system,especially in the case of a vertical beam offset larger than the vertical dithering amplitude ($\Delta y > k\Delta x$), which means the LER beam is dithered on one side of the luminosity curve in the vertical plane, then the magnitude at the dithering frequency from the vertical dithering will not be at its minimum and that will impact the lock-in amplifier's response with respect to the horizontal beam-beam offset. For instance, when a non-zero vertical offset ($\Delta y = 0.6\sigma_y^*$) is added to the case of Figure 5.45, as shown in Figure 5.46, we find that the minimum magnitude position at the dithering frequency shifts from the peak luminosity position in the horizontal plane, and the magnitude itself is not symmetrical anymore with respect to the horizontal beam-beam offset.

In addition, if there is no X-Y coupling, the vertical beam-beam offset will only lead to luminosity degradation, and no effect to the horizontal dithering beam orbit feedback system.

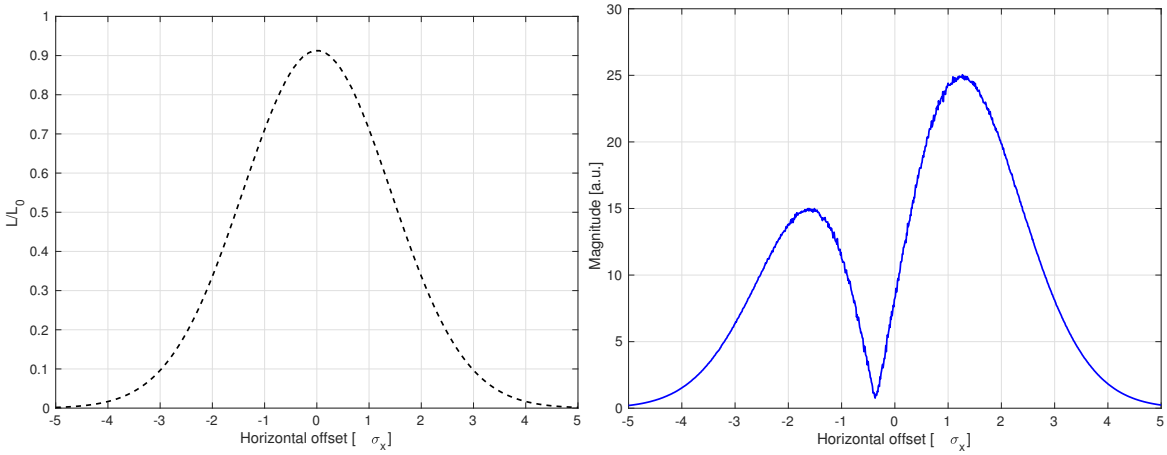


**Figure 5.46:** Normalized luminosity (left) and magnitude (right) at the dithering frequency with respect to the horizontal beam-beam offset in the presence of the vertical beam dithering due to the X-Y coupling of the dithering coils ($k$=0.01), and non-zero vertical offset at the IP ($\Delta y = 0.6\sigma_y^*$).

Therefore, we can draw a conclusion that only when there is both residual X-Y coupling and vertical beam offset will the lock-in amplifier not work well and the dithering orbit feedback system can not correct the horizontal beam-beam offset to optimize the luminosity and maintain it.

Furthermore, the asymmetry of the magnitude at the dithering frequency will become worse with a large coupling factor and vertical beam-beam offset, as shown in Figure 5.47 and 5.48, e.g., the shift size is proportional to the coupling factors when the vertical beam

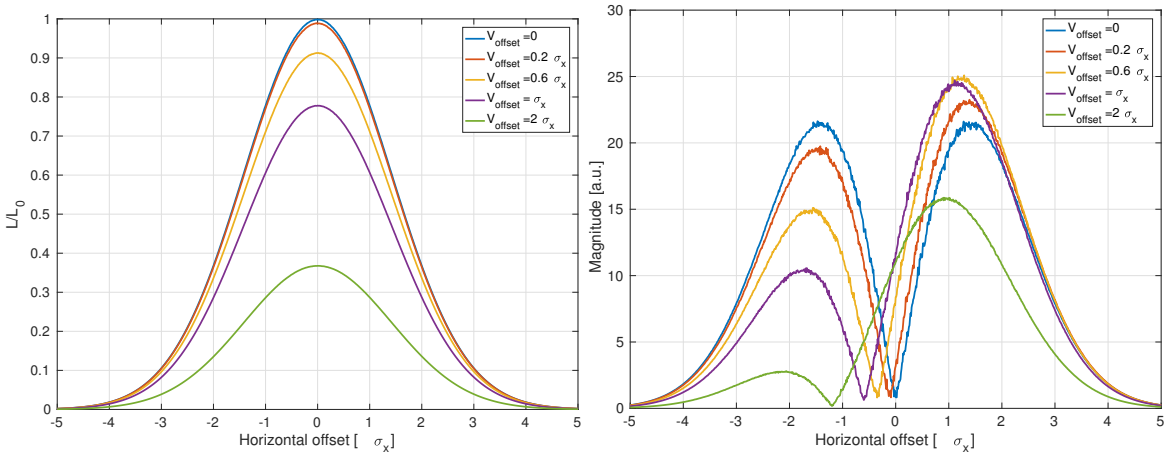


**Figure 5.47:** Normalized luminosity (left) and magnitude (right) at the dithering frequency with respect to the horizontal beam-beam offset in the presence of the vertical beam dithering due to the X-Y coupling of the dithering coils ($k = 0.01$), and different vertical offsets at the IP.

offset is at a fixed level, and the same for vertical beam offset with a fixed coupling factors.

The shift (asymmetry) direction is determined by the sign of the coupling and the vertical offset.

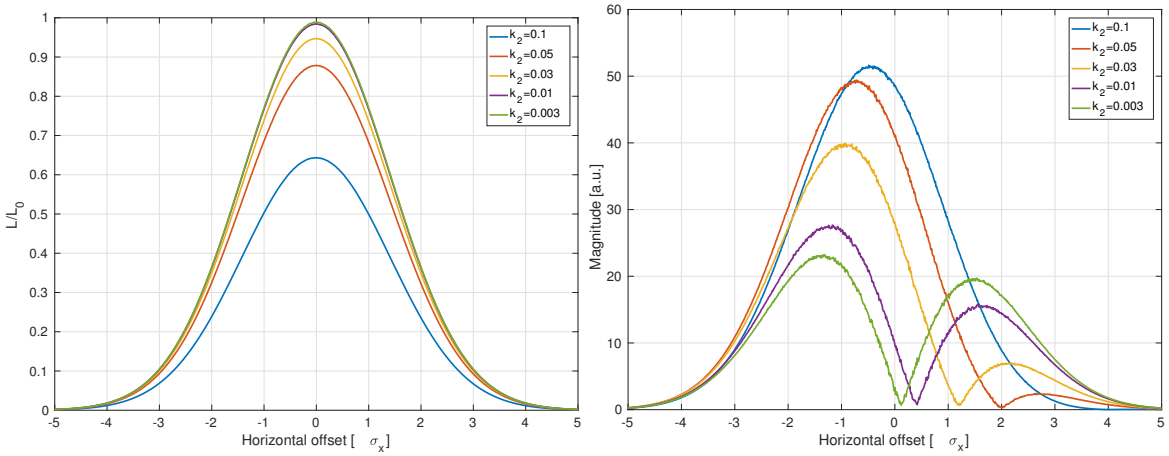


**Figure 5.48:** Normalized luminosity (left) and magnitude (right) at the dithering frequency with respect to the horizontal beam-beam offset in the presence of the vertical beam dithering due to the X-Y coupling of the dithering coils (with varies of coupling factors $k$), and non-zero vertical offset at the IP ($\Delta y = -0.2\sigma_y^*$).

If the luminosity change only comes from the beam-beam offset, in horizontal or vertical planes, which means the other machine parameters are kept as constant, the shift size of the minimum magnitude position from the peak luminosity is determined by the size of coupling level and vertical offset. As shown in Figure 5.49,

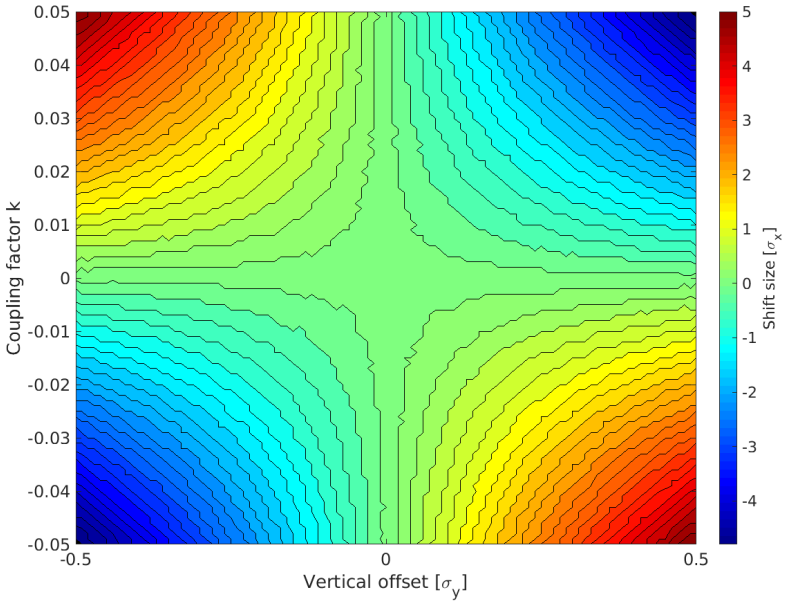


**Figure 5.49:** Shift size of the minimum magnitude position from the peak luminosity with respect to the different X-Y coupling factors and residual vertical beam-beam offsets.

As a conclusion, the dithering coils are needed to be checked carefully before the operation, especially the possible X-Y coupling, from which the horizontal dithering may leak to the vertical plane, and induce the unexpected vertical beam dithering. On the other hand, since vertical beam size is much smaller than the horizontal plane (at the level of tens of nm), the luminosity degradation will be more sensitive than the horizontal plane, and considering that the presence of the vertical beam-beam offset will also induce some unexpected effect (such as what explained above), it is very important to employ an effective and fast vertical IP orbit feedback system.

**An explanation for the misbehavior of channel A during the second test in the 2018 Phase 2 commissioning**

In the presence of X-Y coupling in the dithering coils and vertical beam-beam offsets at the IP, both LumiBelle2 and ZDLM will have the same behavior, with shifts and asymmetries observed in the magnitude of the lock-in amplifier at the dithering frequency. However, during the second dithering test in the Phase 2 commissioning in 2018, only when channel A from LumiBelle2 was used as input to the lock-in amplifier was the abnormal behavior of the magnitude at the dithering frequency observed, while it was fine when using both channel C of LumiBelle2 and ZDLM.

We noticed that in the presence of the X-Y coupling of the dithering coils, a small vertical beam-beam offset could also be created sinusoidally at 79 Hz. Due to the beam-beam deflection in the vertical plane at the IP due to the beam-beam interaction (as described in Equation 3.1), the vertical position of Bhabha scattered positron at the Tungsten radiator will also move up and down sinusoidally at 79 Hz, as shown in the schematic in Figure 5.50. For instance, with the beam parameters during the second test, if the maximum beam-beam

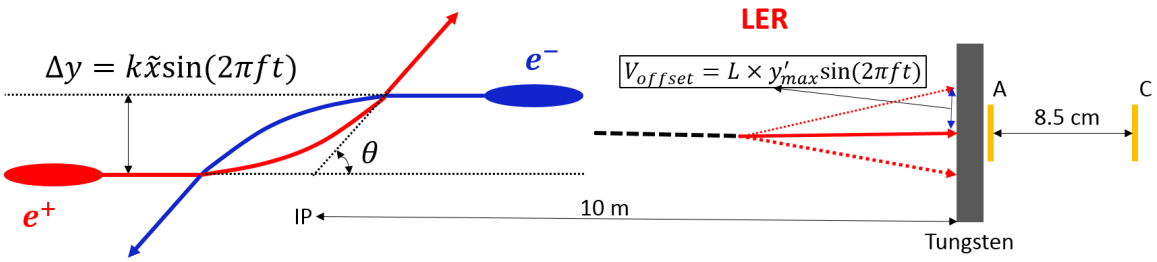


**Figure 5.50:** Schematic of the beam-beam deflection and Bhabha positrons movement in the vertical plane at the Tungsten radiator in the LER.

offset induced by the X-Y coupling reached 10% of the vertical beam size, then the Bhabha positrons that will be lost on the Tungsten radiator will be modulated sinusoidally with

an amplitude about 0.5 mm, based on the beam-beam deflection calculation described in Equation 3.1.

According to the GEANT4 simulation, the electromagnetic showers induced by the lost Bhabha positron have Gaussian distributions in the vertical plane both for position A and C, and the distribution in A (with an RMS $\approx$ 3 mm) is much narrower than that in C (with an RMS $\approx$ 20 mm), because it is much closer to the Tungsten radiator, as shown in Figure 5.51.

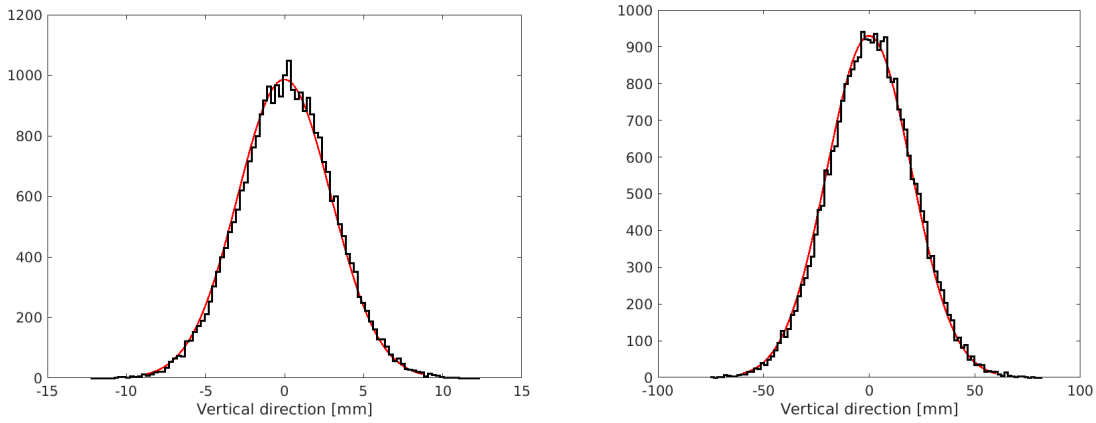


**Figure 5.51:** Vertical distribution of the secondary showers induced by the lost Bhabha positrons at the position A (left) and C (right) just after the Tungsten radiator in the LER.

In this case, especially for the diamond detector at position A, if there is any misalignment between the mechanically installed diamond sensor and the actual beam trajectory in the interaction region, then there could be offset (e.g. at the level of a mm) between the center of the diamond detector and Bhabha positrons induced secondary shower, resulting in the signal provided by the diamond detector not being at its maximum (see Figure 5.52).

Therefore, the modulation of the lost Bhabha positrons at the Tungsten radiator due to the beam-beam deflection at the IP is equivalent to the LER beam dithering for the diamond detector at position A (see Figure 5.53). In the case of no offset, the diamond signals are modulated around the peak at twice of the dithering frequency, and the magnitude at the dithering frequency is at the minimum, so there will be no effect to the horizontal dithering IP orbit feedback system. On the other hand, if the offset is not zero, especially when the offset is larger than the Bhabha positrons modulation, then the diamond signals will be modulated at the dithering frequency, and magnitude at the dithering frequency will be shifted due the contribution of the vertical dithering from X-Y coupling, even if there is no vertical beam-beam offset at the IP. However, for the diamond detector at position C, because it is further downstream of the Tungsten radiator, the vertical distribution of secondary showers is much broader, and thus even if there is an offset at the level of a mm, the modulation of the

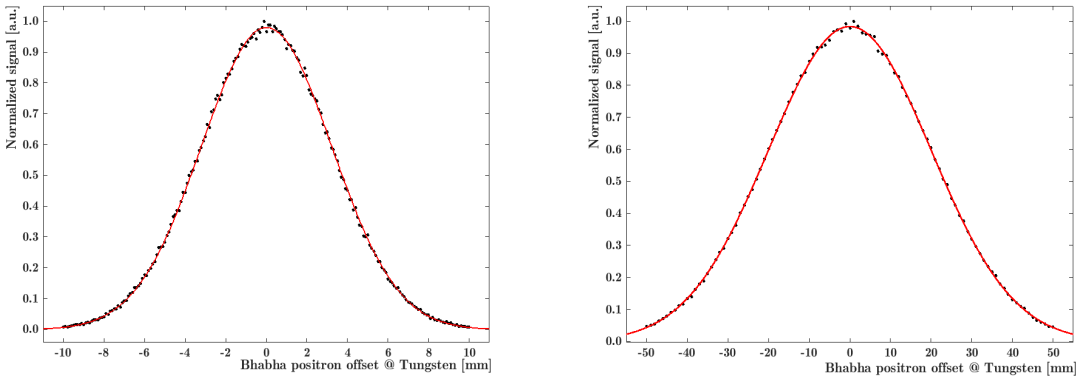


**Figure 5.52:** Normalized signal detected by the diamond detectors as a function of the offset between the center of the secondary showers and the diamond detector in the vertical plane, left for channel A and right for channel C.

diamond detector signal will still be near the peak. The same holds for the ZDLM detector, which is even further behind and has a larger size. This is why channel A did not work well while both channel C of LumiBelle2 and ZDLM did during the second dithering IP orbit feedback test.

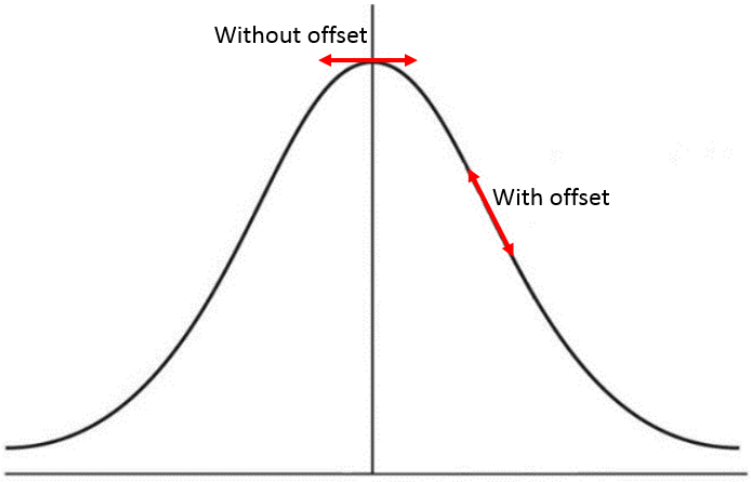


**Figure 5.53:** Schematic of the luminosity signals provided by the diamond detector at position A w/o an offset between the center of the secondary showers and the diamond detector in the vertical plane in the presence of the Bhabha positrons modulation up and down due to the beam-beam deflection induced by the vertical dithering from X-Y coupling.

It is worth mentioning that the positions of channels A and C were swapped in early June of 2018, which was between these two dithering tests during the Phase 2 commissioning of SuperKEKB. This means that channel C worked well for both of the described dithering orbit feedback tests, while it was placed at different locations. In addition, the positions of channel

A and C were swapped again in 2019 during early Phase 3 commissioning, channel A worked well during the dithering test after the optimization of the vertical beam-beam offset at the IP when it was placed at the position C. Besides, the shift of the minimum magnitude position from the peak luminosity position were always the same, which supports the argument of the X-Y coupling in the dithering coils in the presence of the offset between the center of the secondary showers and the diamond detector in the vertical plane. This supports all our explanations described above.

According to all the results from these tests, in short, the dithering orbit feedback system was successfully tested and it worked well, as we expected. However, X-Y coupling was found in the dithering coils, and it will significantly affect the horizontal dithering IP orbit feedback system in the presence of the vertical beam-beam offsets with the imperfect vertical IP orbit feedback system. Therefore, the X-Y coupling in the dithering coils needs to be checked carefully in the future, and the vertical IP feedback will need to operate with better performance. Besides, only a few tests were performed on this system due to the limited commissioning time and plenty of other tasks during the Phase 2 and early Phase 3 commissioning periods. More tests are expected in the next period commissioning, to make it ready for the future continuous operation. It is also clear that optimization of the PI control parameters was needed, to avoid overshooting, in order to correct the beam orbit as efficiently as possible.

### 5.5.2 Vertical beam size determination at the IP

SuperKEKB, as the first collider based on the "nano beam scheme", requires careful tuning of the local optics at the IP. For this purpose, a method to estimate the beam size directly at the IP, and not based on extrapolation from e.g. the beam size measured by the X-Ray monitor, is quite essential, since beam size estimates at other places than the IP are not sensitive to a number of small optics distortions which can affect the beam size at the IP. The only way is then by observing the luminosity changes with respect to the vertical beam-beam offsets, based on vertical beam offset scans. In addition, beam-beam blow-up was also observed during the scans when the beam current was high, which significantly influences the luminosity change, causing the beam size to be underestimated [145]. When the beam current is very small ($\sim$ 0.1 mA/bunch), the beam blow-up can be neglected [133]. Therefore, the vertical beam offset scans were performed at very small beam current for the optics tuning during Phase-2. For this purpose, since our luminosity monitor had very good sensitivity, it was used to directly estimate the vertical beam size at the IP.

By steering the electron beam and observing the signal changes in the luminosity monitor with extremely low beam current, the optimum position in the vertical plane and the vertical

beam size at the IP can be estimated [2]. At the first beginning of collision tuning in Phase-2, this was used to search for the beam-beam collision and the optimum vertical position.

With the assumption that the vertical spatial distributions of the electron and positron beams are Gaussian and that the luminosity signal is proportional to the number of colliding electrons and positrons, the luminosity can be expressed as the convolution of the two beam Gaussian distributions in the vertical plane:

$$\begin{aligned} L &\sim Ae^{-(x-a)^2/2\sigma^2_{y,e^-}} \otimes Be^{-(x-b)^2/2\sigma^2_{y,e^+}} = Ce^{\frac{-(x-c)^2}{2\Sigma^2_y}}, \\ C &= AB\sqrt{2\pi}\sigma_{y,e^-}\sigma_{y,e^+}/\sqrt{\sigma^2_{y,e^-}+\sigma^2_{y,e^+}} \end{aligned} \tag{5.5}$$

where $L$ is the relative luminosity signal provided by our luminosity monitor, $c = a+b$ represents the peak luminosity position in the vertical plane, and $\Sigma^2_y$ is the quadratic sum of the two vertical beam sizes at the IP: $\Sigma^2_y = \sigma^2_{y,e^-} + \sigma^2_{y,e^+}$. Assuming that the vertical beam sizes of the two beams are equal to $\sigma_y$, we have: $\sigma_y = \Sigma_y/\sqrt{2}$, and $\Sigma_y$ can be obtained from the fit of the luminosity signal against the beam vertical offset, and then the vertical beam size $\sigma_y$ can be calculated.

Since our monitor provides both the train integrated luminosity and bunch integrated luminosity signals at 1 Hz, we can extract both the averaged vertical beam size over the entire train and the bunch-by-bunch vertical beam sizes.

#### 5.5.2.1 Average vertical beam size

Figure 5.54 shows an example of the train integrated luminosity signals from Channel A in the LER when the vertical beam offset scan was performed at the end of the Phase 2 commissioning. The $\beta^*_y$ was 3 mm for both the LER and HER during this scan. To avoid the beam-beam blow-up effects and get the geometrical luminosity from the scan, extremely low beam currents were set: $I_b \approx 0.05\ mA$. The HER beam was steered to scan from $-5\ \mu m$ to $5\ \mu m$ with steps of 1 or 0.5 $\mu m$ in the vertical plane. It is clear that when the two beams were overlapped we could observe clear luminosity signals and when they were totally separated the signals represented the backgrounds.

Based on the change in train integrated luminosity signal during the scan, the average vertical beam size was estimated. Figure 5.55 shows a Gaussian fit of the luminosity signals

[2]Due to the large crossing angle of the two beams in the horizontal plane, the projection of the bunch length in the horizontal plane should be considered as the effective horizontal beam size, which is much larger than the real horizontal beam size, and out of the range of the local bumps at the IP that the steering magnets can produce, therefore, the horizontal beam offset scan was not performed and unnecessary.

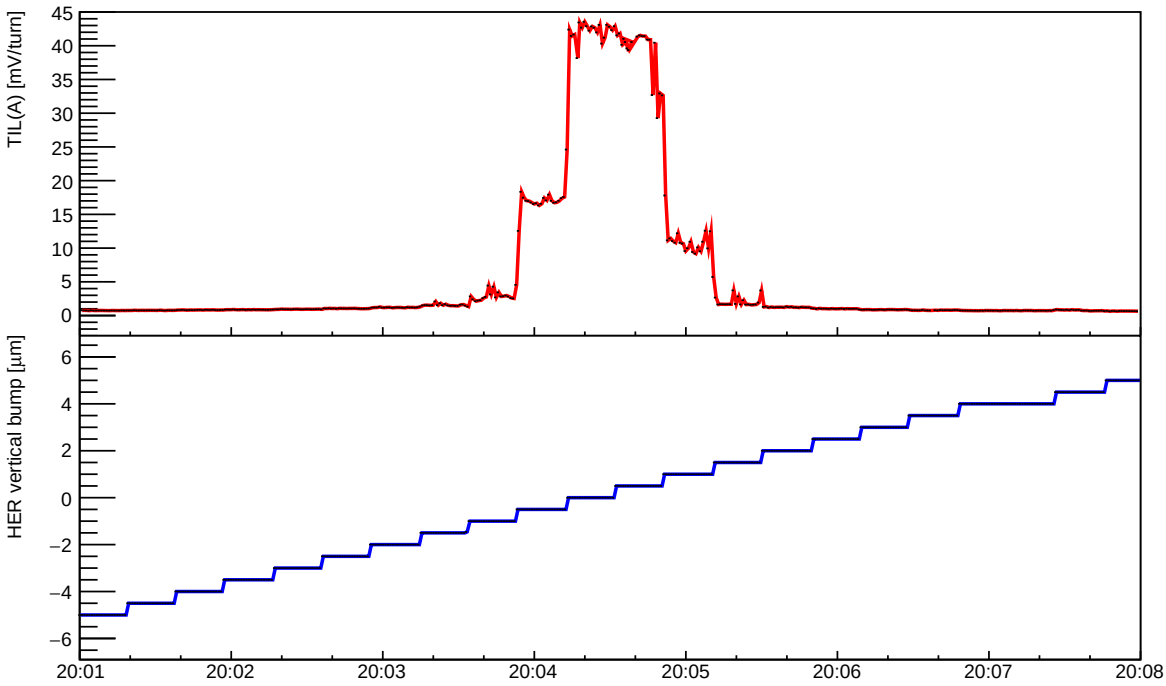


**Figure 5.54:** Example of train integrated luminosity signal from Channel A in the LER (upper plot) and magnitude of the HER vertical bump applied at the IP (lower plot).

with respect to the HER vertical bump, giving a mean value of $0.1851 \pm 0.012\ \mu m$ and $\Sigma$ of $0.5063 \pm 0.0112\ \mu m$.

According to Equation 5.5, the mean value from the fit corresponds to the optimum position for the HER beam at the IP to maximize the luminosity, and the standard deviation $\Sigma$ is equal to the quadratic sum of the vertical beam sizes of the two colliding beams, assumed to be equal:

$$\sigma_y = \Sigma_y/\sqrt{2} = 0.3581 \pm 0.0079\ \mu m \tag{5.6}$$

Therefore, from the vertical beam offset scan, we can obtain two important pieces of information:

- The optimum position of the HER beam where we can achieve maximum luminosity, which is very useful for the beam collision initialization for the regular beam collision commissioning. During the SuperKEKB Phase-2 commissioning, this technique was used many times to search for collisions and to initialize the collision parameters in the vertical plane. It is foreseeable that this will continue to be used in the future operation.

- Effective vertical beam sizes at the IP, which are quite important to verify the process of $\beta_y^*$ squeezing, as a diagnostic tool directly at the IP, since the extrapolation based on the

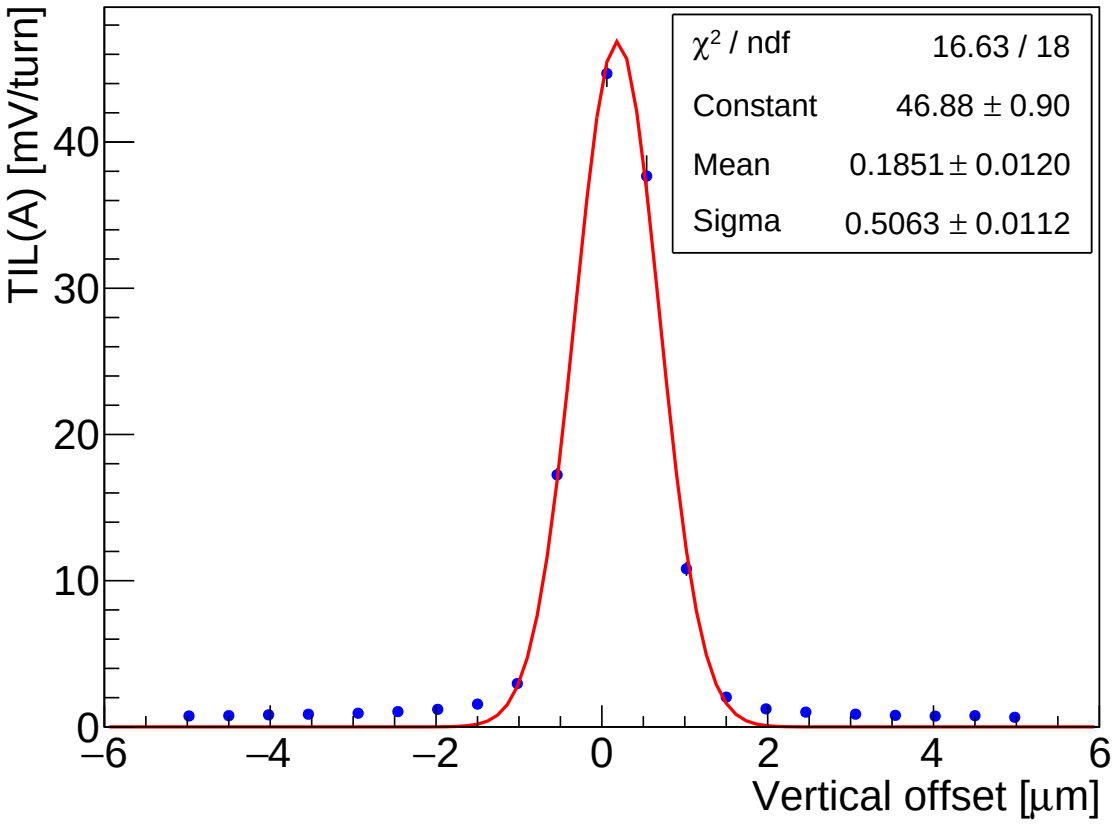


**Figure 5.55:** Example of train integrated luminosity signal from Channel A in LER with respect to the HER vertical bump, fitted by a Gaussian.

X-Ray monitor is not reliable for the purpose of minimizing optical distortions at the IP. Figure 5.56 shows the preliminary results of such vertical beam size determinations, during Phase 2 with different optics. It is clear that with the squeezing of the $\beta_y^*$, the vertical beam sizes were decreasing. It is worth mentioning that when the $\beta_y^*$ was squeezed from 6 mm to 4 mm, the vertical beam size based on vertical beam scans did not decrease as expected, and the specific luminosity did not increase, either. However, the extrapolation from the measured beam size by the X-Ray monitor ($\sigma_y = \sqrt{\beta_y/\beta_{xray}}\sigma_{xray}$) did decrease, in the same proportion as expected from the ratio of $\beta_y^*$. It turned out that this behavior was due to an X-Y coupling term (R2), thought to arise from the QC1 skew quadrupole [133]. After adjustment of the R2 X-Y coupling, the beam sizes based on the vertical offset scans decreased as expected and the specific luminosity was also increased. On the other hand, the extrapolation from the X-Ray monitor did not change after the adjustment. This supports the argument that an effective/sensitive luminosity monitor is quite important for the machine tuning, especially for the optics tuning during the $\beta_y^*$ squeezing.

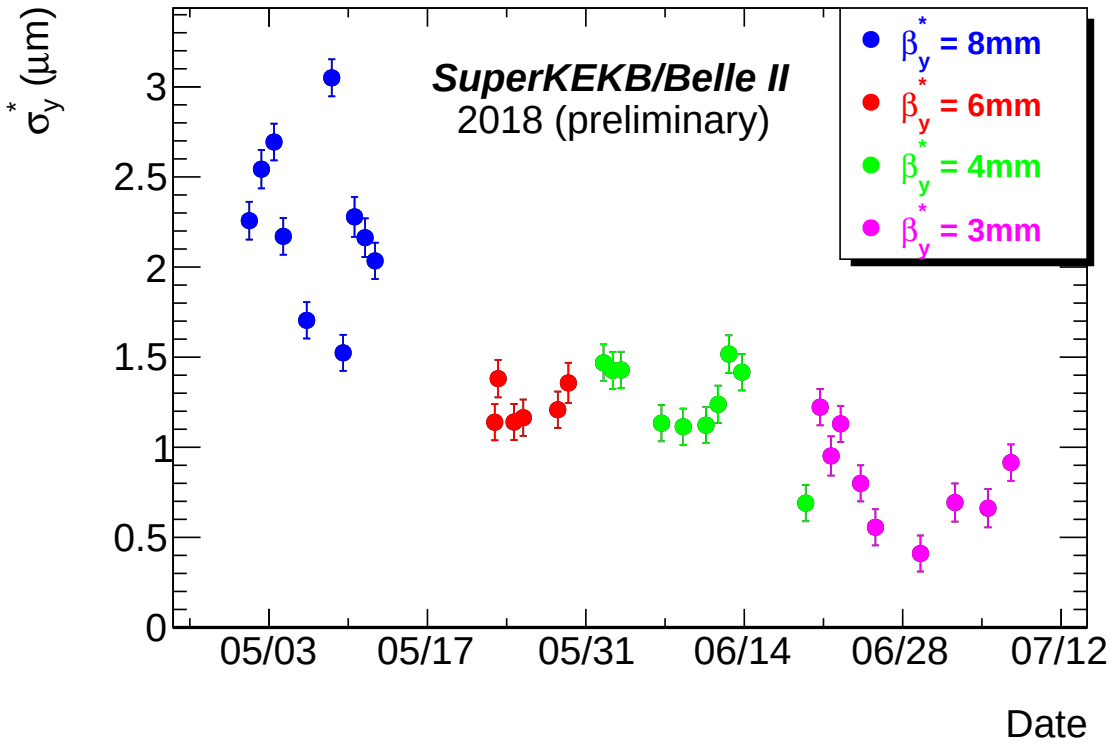


**Figure 5.56:** Vertical beam sizes based on beam offset scans during Phase 2 commissioning (courtesy of S. Di Carlo).

Other than the vertical beam size determination and HER beam position optimization, the signal-to-noise ratio (SNR) could also be estimated, as the ratio of luminosity signal at peak position and when the two beams were completely separated. During the scan shown in Figure 5.54, the maximum luminosity provided by the ECL was $1.3\times\ 10^{32}\ cm^{-2}s^{-1}$, and the SNR for Channel A in LER was about 65. This is not as high as we would like, but it is because the luminosity was very low for this scan. According to the simulation, when the luminosity will reach $10^{34}\ cm^{-2}s^{-1}$, through further $\beta_y^*$ squeezing and increases of beam currents, an SNR for this channel larger than 100 can be expected, even if there will be more background from Touschek scattering.

#### 5.5.2.2 Bunch-by-bunch vertical beam size

Apart from the averaged vertical beam size determination based on train integrated luminosity signals during the vertical beam offset scans, vertical beam sizes for individual bunches can also be estimated based on the bunch integrated luminosity signals during vertical scans, including as well the peak luminosity positions for each bunch of the HER beam. The same method is used as for the average vertical beam size estimation. Figure 5.57 shows the four first individual bunch integrated luminosity signals as a function of the HER electron beam

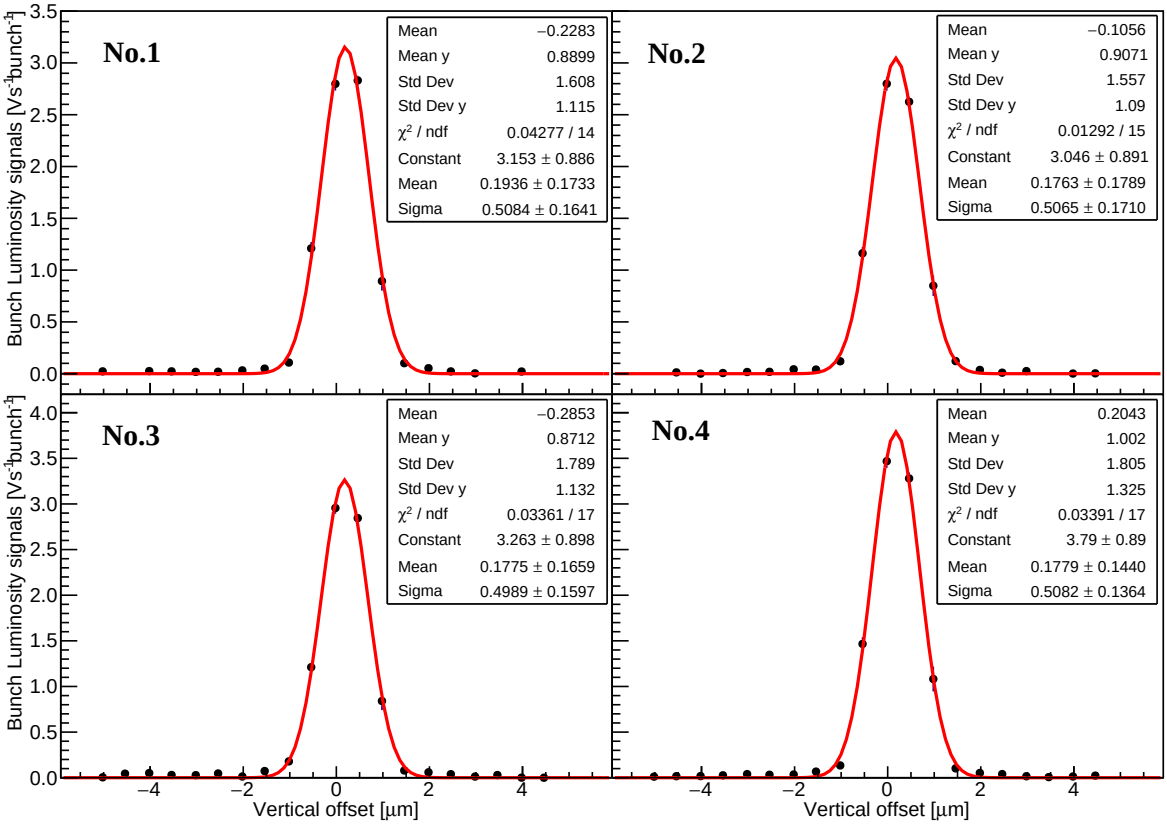


**Figure 5.57:** Example of the relative bunch integrated luminosity signals as a function of the HER vertical bumps: No.1-4→1st-4th bunch.

vertical offset, fitted with Gaussians. Similar to the average vertical beam size calculation described in 5.5, vertical beam sizes calculated for these four bunches are listed below:

$$\begin{aligned}
\sigma_{y1} &= \Sigma_{y1}/\sqrt{2} = 0.3595 \pm 0.1160\ \mu m \\
\sigma_{y2} &= \Sigma_{y2}/\sqrt{2} = 0.3582 \pm 0.1209\ \mu m \\
\sigma_{y3} &= \Sigma_{y3}/\sqrt{2} = 0.3528 \pm 0.1129\ \mu m \\
\sigma_{y4} &= \Sigma_{y4}/\sqrt{2} = 0.3594 \pm 0.0965\ \mu m
\end{aligned} \tag{5.7}$$

In addition to the vertical beam size determinations for the individual bunches, the optimum vertical position of the electron beam for every single bunch were also obtained. Figure 5.58 shows the set of the HER electron beam vertical bumps achieving maximum luminosity for each bunch and the corresponding vertical beam sizes: red dots represent the peak position and the error bars correspond to the vertical beam sizes. It is clear that although there are some variations in the optimum positions, the bunch train was aligned reasonably well.

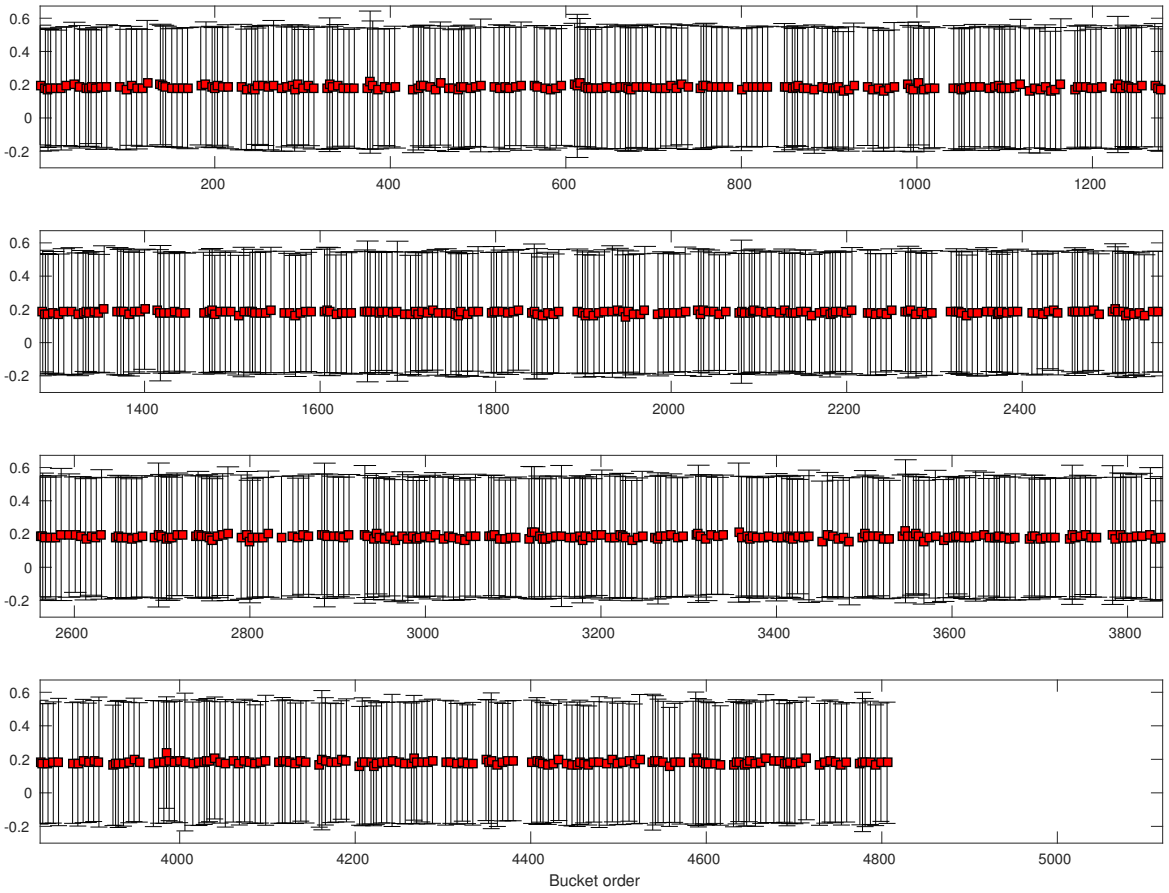


**Figure 5.58:** Example of optimum positions for the HER vertical bump with corresponding individual bunch sizes along the train: red dots represent the optimum positions and the error bars represent to the vertical beam sizes.

For the 754 colliding bunches during this vertical offset scan, the distribution of measured bunch vertical beam sizes is shown in the left of Figure 5.59. As can be seen, it is a Gaussian centered at 0.3645 $\mu m$ with a standard deviation of 0.007 $\mu m$. As a comparison, the average vertical beam size was 0.3581 $\mu m$ during this scan, which is quite consistent. The spread of the vertical beam sizes along the train is less than 2%. A small non-Gaussian tail can however be observed, with some bunches having somewhat larger sizes.

The alignment of the bunches along the train is also an important quantity to evaluate machine performance. As shown in the right of Figure 5.59, the distribution of individual optimum positions for each bunch is also a Gaussian centered at 0.1826 $\mu m$ with a standard deviation of 0.0081 $\mu m$. This spread in alignment along the train is only about 2.3% of the average vertical beam size: $\sigma_y$=0.3581 $\mu m$, which is very small. It indicates the maximum level of the fluctuations/coherent oscillations of the bunches around their average trajectory. Besides, the optimum position in the vertical plane fitted from the train integrated luminosity

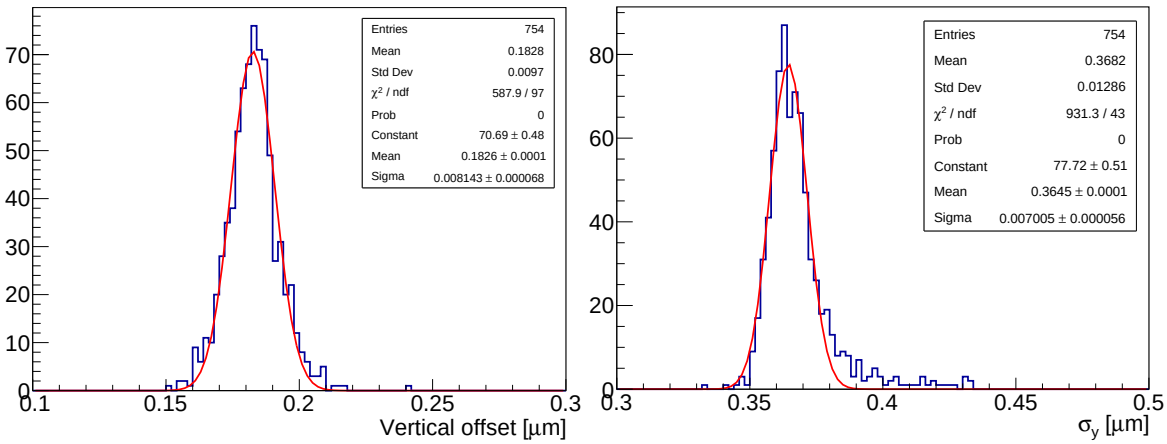


**Figure 5.59:** Histogram of the optimum bunch positions(left) and corresponding vertical beam sizes (right) for the data displayed in Figure 5.58.

signals was 0.1851±0.0120 $\mu m$, which is reasonably compatible with the optimum position of the individual bunches. Based on this distribution, individual bunches were aligned with respect to their average position with a relative precision of 4.43%. Taking into account relevant machine parameters, studies of interactions between bunches, especially for high bunch currents and much smaller size beams, can be pursued, for example for beams with parameters closer to the nominal ones expected during the Phase-3 commissioning period.

## 5.6 Material activation issue in the LER

Thanks to the insertion of the 45° inclined window shaped beam pipe with a depression of 15 mm and integration of the Tungsten radiator in the LER, the multiplicity of the secondary particles in the showers generated by positrons exiting the beam pipe at this location, and thereby the diamond detector's detection efficiency for Bhabha events, have improved significantly. This makes our diamond detector an extremely sensitive luminosity monitor, even for very low luminosities. On the other hand, these huge number of Bhabha positrons lost on the window may also induce significant beam pipe and radiator material activation, thereby becoming a hot spot which may bring some difficulties for the maintenance of the machine after a long period of high luminosity operation.

To evaluate this situation, the activation of the relevant beam pipe sections was measured during the Phase 2 commissioning to benchmark simulations based on FLUKA, and then the simulation was used with nominal machine parameters to predict future activation levels. Figure 5.60 shows the positions near the beam pipe where dose measurements were performed in the LER during Phase-2 commissioning. A is the closest position to the Tungsten radiator,

just above the diamond detector, B is closest to the third diamond detector and centered in the vertical plane, about 10 cm away from the Tungsten radiator, C is at the center of the window shaped beam pipe section, and D is on top of the ZDLM detectors.

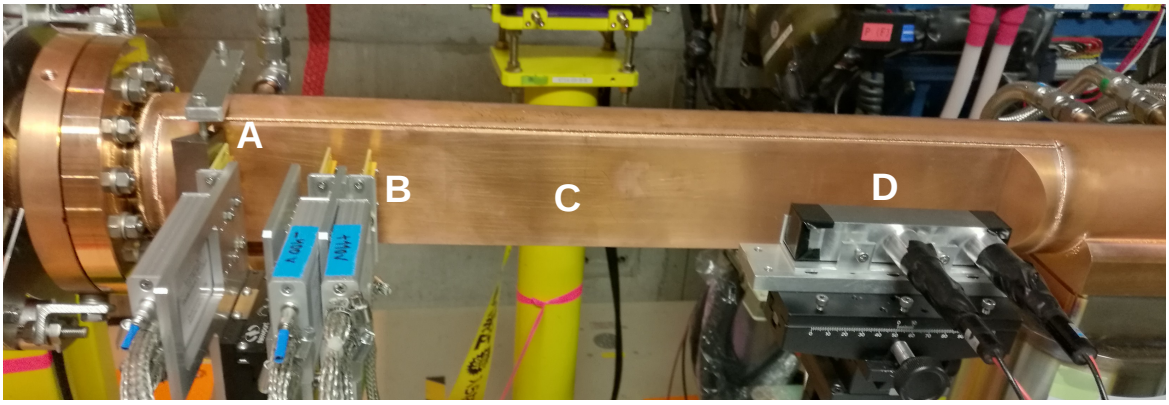


**Figure 5.60:** Activation induced dose measurement points near the LER window shaped beam pipe section.

The loss rate of Bhabha positrons incident on the inclined window was estimated based on the luminosity, and their energy and loss position profiles were obtained using the SAD tracking simulation (see Section 4.1.2). The activation-induced dose measurement was performed on the $14^{th}$ of June, on a maintenance day, about one hour after stopping the beam operation. The simulated irradiation profile was based on the Bhabha positrons lost on the window in the last 24 hours. Figure 5.61 shows the luminosity profile and Bhabha positron loss rate on the window shape beam pipe that were used to simulate the material activation. To simplify the simulation, the average loss rate every half hour was implemented as the irradiation profile, and the activation-induced dose rate map was recorded.

According to the measurement on the $14^{th}$ of June, after one hour of cooling, the dose rate for points A and B were about 3.2 $\mu Sv/h$ and 3.3 $\mu Sv/h$, respectively. As a comparison, the simulation gave about 4.2 and 6.1 $\mu Sv/h$ for points A and B, respectively, see Figure 5.62, which illustrates the simulated dose rate map induced by material activation in the horizontal and vertical planes after one hour of cooling. The uncertainties resulting from the geometry and irradiation profile used in the simulation are quite large and may explain that the difference between the measurement and simulation is almost a factor of two. On the other hand, the relative distribution seems consistent in the sense that position B has the highest dose rate, A somewhat less, and D the lowest one (see Table 5.3).

A second independent measurement was also performed during the Phase-2 commissioning, on June 28, with a different luminosity profile, along with a corresponding simulation. Table 5.3 summaries the comparison of the activation-induced dose from these two measure-

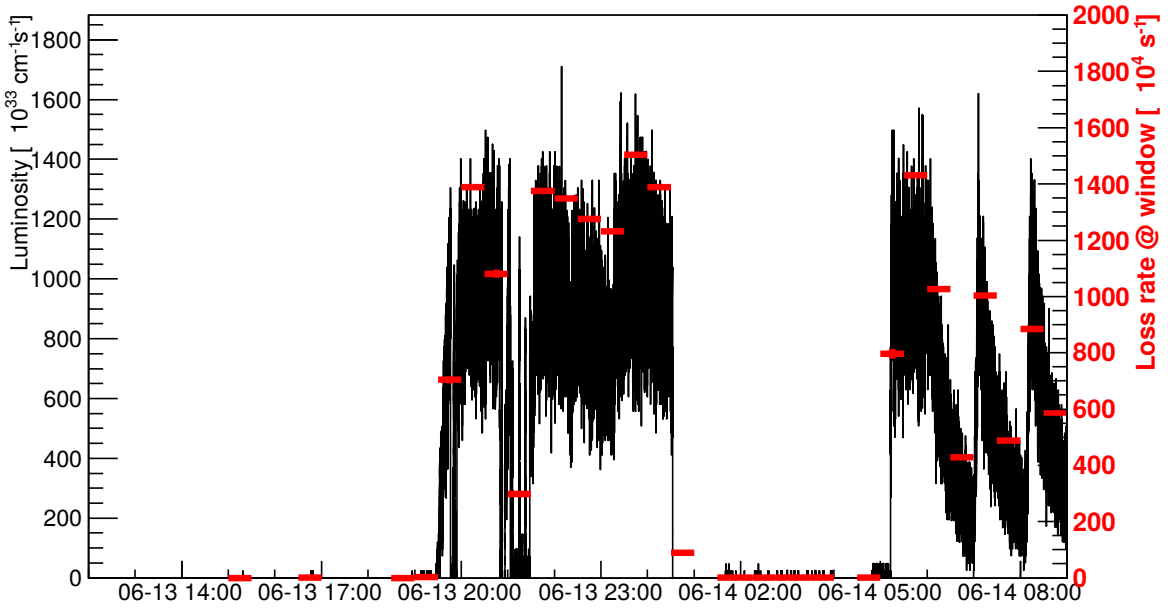


**Figure 5.61:** The luminosity profile and Bhabha positron loss rate on the window shape beam pipe that used to simulate the materials' activation.

ments and simulations. It is clear that the dose rate from the simulation is always higher than that from the measurements, but the order of magnitude is correct and the relative rates for different positions near the beam pipe are reproduced. This permits us to roughly predict the material activation for higher luminosity cases, especially the nominal beam parameters.

| | Measurement / Simulation $[\mu Sv/h]$ | | | |
|---|---|---|---|---|
| Date | A | B | C | D |
| 2018-06-14 | 3.156 / 4.213 | 3.333 / 6.136 | 2.193 / 3.131 | 1.403 / 1.512 |
| 2018-06-28 | 3.433 / 5.835 | 4.557 / 11.732 | 3.018 / 4.385 | 2.015 / 2.732 |

**Table 5.3:** Comparison of dose rates induced by material activation from measurements and simulation.

To investigate the beam pipe and radiator material activation during operation with nominal luminosity, a simulation was performed with a luminosity of $8 \times 10^{35}\ cm^{-2}s^{-1}$ continuously during 100 hours. The material activation induced dose map after one hour of cooling is shown in Figure 5.63. It is clear that the dose rate is much higher than that during Phase 2 with more than 100 times higher luminosity. For the diamond detector region, the dose rate can reach 1 mSv/h, which greatly exceeds the control level. Even 10 cm away from the Tungsten radiator in the horizontal direction, the dose rate is still at the level of a few hundred $\mu Sv/h$. This will be a hot spot of the radiation which may be an issue for

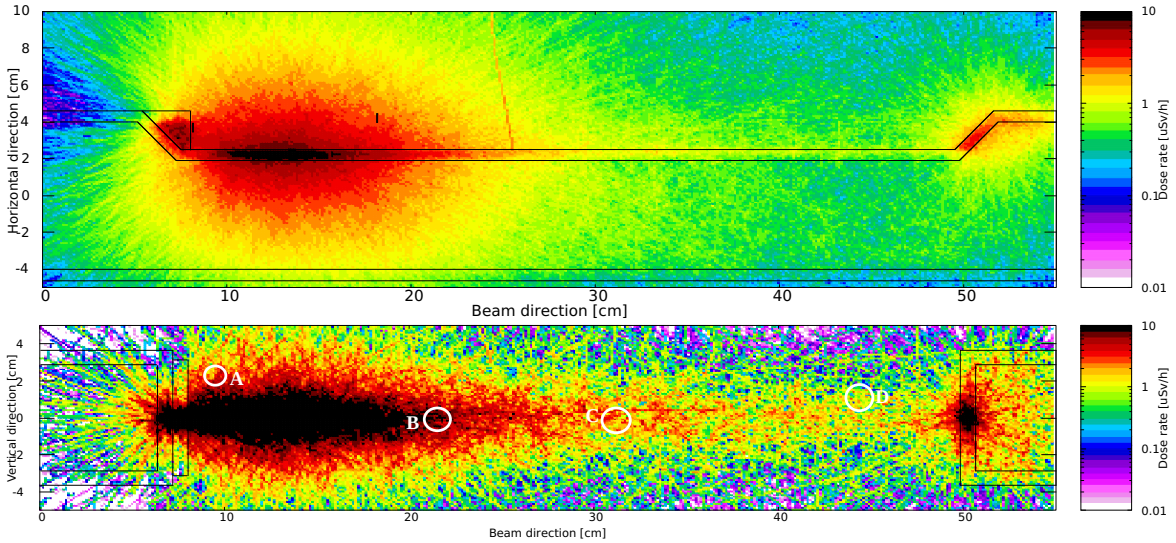


**Figure 5.62:** Simulated activation induced dose rate map in horizontal plane centered in vertical (top) and vertical plane just outside of the flat part of the beam pipe (bottom) after one hour of cooling.

radiation workers who need to get close to perform necessary maintenance in this area. Some protection or shielding will need to be implemented to avoid direct exposure to this activation-induced radiation by getting too close to this hot spot.

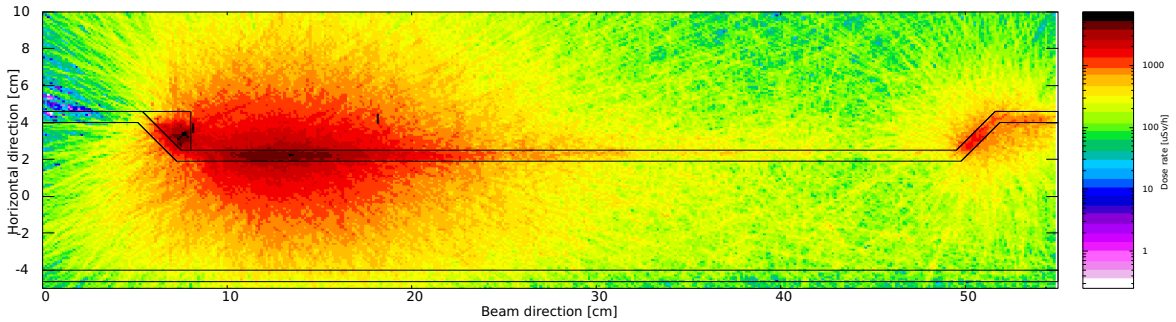


**Figure 5.63:** Simulated activation induced dose map for the SuperKEKB nominal luminosity of $8 \times 10^{35}\ cm^{-2}s^{-1}$, after 100 hours of continuous operation, and one hour of cooling.

A leaded glass box was proposed as shielding just outside of this window shaped beam pipe section, including the space where the detectors and amplifiers are mounted, to prevent radiation workers from getting close to the high dose rate area near the Tungsten radiator and beam pipe by accident, while at the same time reducing the dose rate outside of the leaded glass box, see Figure 5.64. The box with leaded glass also has the advantage that our setup with diamond detectors and other components remains visible from outside. A rectangle box with a thickness of 2 cm made up of typical leaded glass with a density of 4 $g/cm^3$ was added to the simulation, see Figure 5.64.

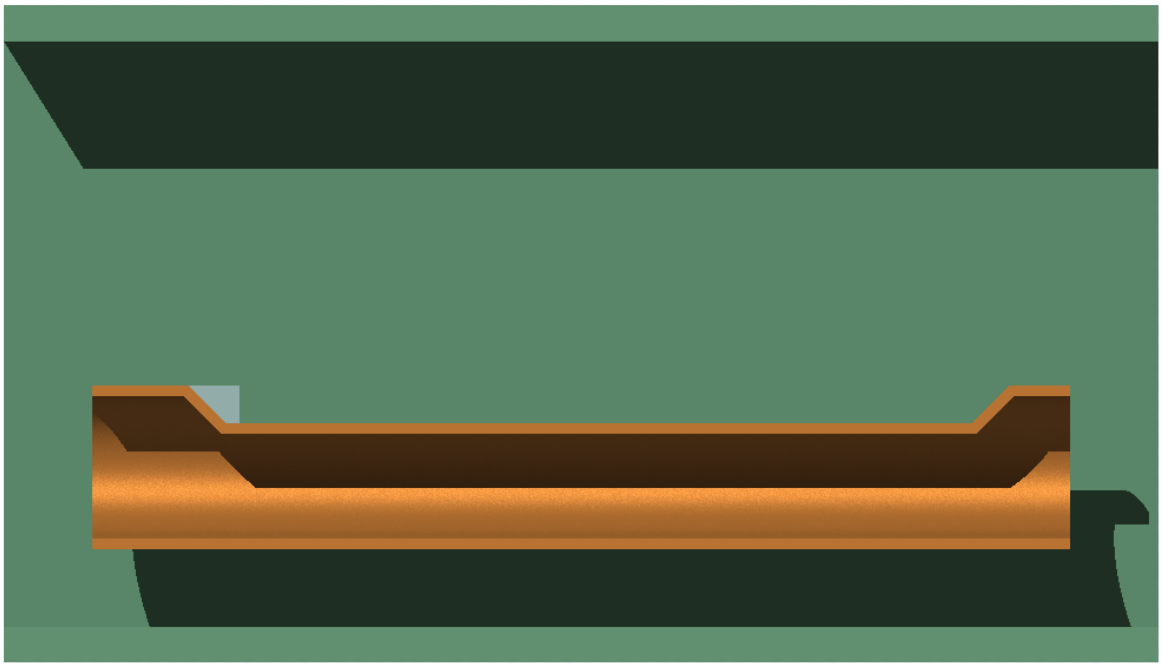

**Figure 5.64:** Geometry of the inclined window shaped beam pipe with a local leaded glass shielding box surrounding it.

The result of the simulation of the activation-induced dose rate map after one hour of cooling with the same irradiation profile as in Figure 5.63 (100 hours with luminosity of $8 \times 10^{35}\ cm^{-2}s^{-1}$) is shown in Figure 5.65. The dose rates close to the Tungsten radiator and beam pipe are more than 1 $mSv/h$, still exceeding the radiation control limits. However, the dose rate is less than 100 $\mu Sv/h$ just outside of the leaded glass box in the positive horizontal direction where people can access, about 50% of the radiation control level at KEK. This means that with this leaded glass box, the activation-induced dose rate close to our system after one hour of cooling can be well controlled, while the high sensitivity for extremely low luminosity can be kept. In Phase-2 and early Phase-3 commissioning, the luminosity is not expected to be very high, such that the activation-induced radiation will not be a serious problem. This leaded glass box will therefore not be installed at this point. In the future, with the foreseeable increase of luminosity, this leaded glass box could however be one of the options to mitigate the activation-induced dose rate while keeping a high sensitivity for our luminosity monitors. This is important, since the machine tuning, especially optics tuning at the IP, will be needed throughout the life of the SuperKEKB project.

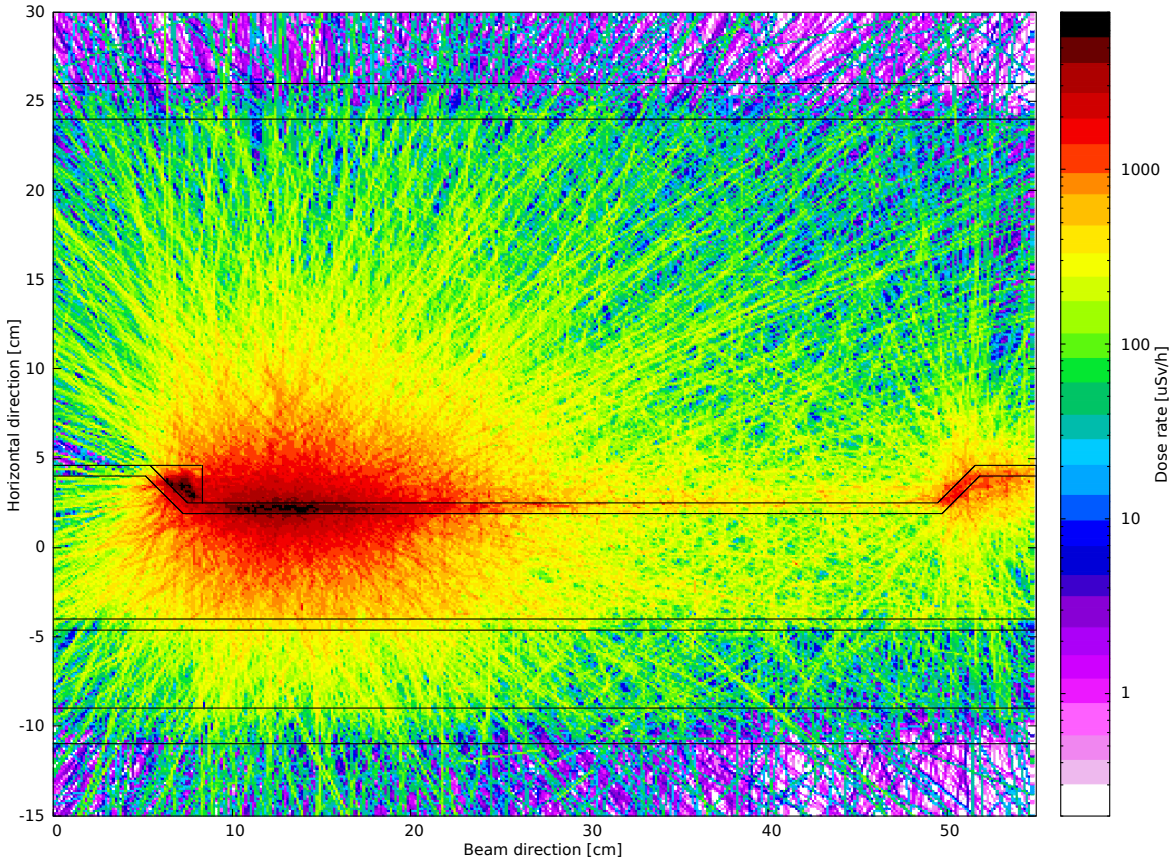


**Figure 5.65:** Simulated activation induced dose rate map for the SuperKEKB nominal luminosity: $8 \times 10^{35}\ cm^{-2}s^{-1}$ with a leaded glass local shielding box, after 100 hours of continuous operation, and one hour of cooling.

# Chapter 6

# Conclusions and prospects

SuperKEKB, being at the foremost frontier of high luminosity particle colliders, by involving extremely tiny beams at the IP based on the "nano-beam scheme", requires excellent control of its beam orbit at the IP to ensure optimum geometrical overlap between the colliding beams, and thereby maximize the luminosity. In the presence of mechanical vibrations caused by the ground motion, the induced offset between the two colliding beams at the IP can be large compared to the beam size, thereby significantly degrading the luminosity. Even for offsets smaller than the beam size, the luminosity degradation can become large due to additional sensitivity through the hourglass and beam-beam blow-up effects. To maintain very high luminosity in the presence of ground motion, beam orbit feedback systems are needed. However, the large crossing angle at the IP in the horizontal plane results in very weak beam-beam deflections in that plane. Limited by the resolution that BPMs can achieve at present, the beam-beam deflection method is not viable to stabilize the horizontal beam orbit at the IP. Therefore, a dithering orbit feedback system was adopted and tested which requires precise and fast luminosity signals as input.

Moreover, being the first collider in the world to operate with such tiny beam sizes at the IP, it is foreseeable that the machine tuning of SuperKEKB towards the nominal beam parameters will be a long and rather difficult process, which will put specific requirements on the luminosity measurements. One first example is the measurement of the vertical beam size at the IP during the $\beta_y^*$ squeezing, which can be inferred from the luminosity changes during vertical beam-beam offset scans. To avoid the influence from the beam-beam interaction, which could lead to beam blow-up and confuse the results of the $\beta_y^*$ squeezing, it must be done at very low bunch current ($\sim$0.1 mA/bunch from the simulation in the SuperKEKB case), which results in very low luminosity. This leads to specific requirements on the sensitivity of the luminosity monitoring. The second example is the possible interactions between bunches along the train, which can induce variations in their beam size and relative

alignment. Such effects can be studied using the bunch-by-bunch luminosity signals in association with the relevant machine parameters (e.g. beam bunch currents). Therefore, it is important to have a system providing the bunch-by-bunch luminosity information with sufficient precision. Overall, fast luminosity monitoring with very high sensitivity is quite important in the presence of dynamical imperfections, for feedback and optimization.

The aim of this thesis was to develop a sensitive instrument to provide the fast train and bunch-by-bunch integrated luminosity signals at SuperKEKB, based on sCVD diamond detectors read out by a DAQ system based on an ADC and FPGA. This system enabled studies of the dithering orbit feedback in the horizontal plane, the local optics tuning at the IP based on IP vertical beam size determination through vertical offset scans and the possible variations in the bunch beam size and alignment along the bunch train. According to the results and our experience from the whole period of the SuperKEKB Phase 2 commissioning performed in 2018 and first part of the Phase 3 commissioning in 2019, our project is successful, and a lot of meaningful results were obtained, although there were also some problems, and confusion still exists for some aspects.

## 6.1 Summary of main results

Overall, a significant amount of the effort was put into implementing fast luminosity monitoring based on the sCVD diamond detectors at SuperKEKB. The preparation work included in particular:

- **Diamond signal characterization.** In the clean room at LAL, sCVD diamond detectors of different thicknesses coupled with two different kinds of amplifiers were tested using a Sr-90 $\beta$ source. The timing characteristics and signal amplification were studied, especially for the sCVD diamond detector with a thickness of 140 $\mu m$ coupled with the broadband current amplifier. Those studies provided very important information for the design of the DAQ system based on a 1 GHz sampling ADC and a FPGA, as well as for the understanding of the train and bunch-by-bunch integrated luminosity signals through a realistic start-to-end simulation.

- **Data acquisition system development.** Based on the ADC and FPGA, the DAQ system was built by the electronics engineer in our group at LAL to provide relative train and bunch-by-bunch integrated luminosity signals simultaneously for the sCVD diamond detector with a thickness of 140 $\mu m$ coupled with the broadband current amplifier. In this case, signal triggering was not needed, and after careful synchronization, continuous monitoring could be achieved. Moreover, an alternative calculation

of the integrated train luminosity was also implemented, based on a sum of all the sampling points above a predefined threshold, which does not require any specific synchronization, was therefore more robust in that respect, and could also be used for the sCVD diamond detector with a thickness of 500 $\mu m$ coupled with a fast charge amplifier.

- **Signal estimation in the LER.** A custom made beam pipe with 45° inclined window was built and installed to enable very high signal rates in the LER, and thereby excellent statistical precision for our fast luminosity monitoring. Detailed simulations including the particle generation, optics tracking and signal estimation in the diamond detector were performed both for luminosity signals from Bhabha scattering events at vanishing angle and for background signals, which mainly come from Bremsstrahlung and Touschek scattering. The results was used as basic input information in the dithering orbit feedback simulation. It also helped us to better understand both the luminosity and background signals from the experiments.

- **Simulation on the dithering orbit feedback system.** Based on all the previous work, a detailed simulation of the dithering orbit feedback system was performed, which gives us a clue of how precise our 1 kHz relative luminosity signals should be and how fast the beam orbit should be corrected.

- **Diamond detector radiation damage estimation in LER at SuperKEKB.** Based on the NIEL hypothesis and previous experimental results of diamond detector radiation damage, the expected diamond detector CCD degradation was estimated in the LER case. The results provide a prediction for the diamond detector lifetime at SuperKEKB, which is very important to make future plans for our project.

During the Phase-2 and early Phase-3 commissioning periods of SuperKEKB, our luminosity monitor based on sCVD diamond detectors was installed and operated successfully. The main achievements and results of this thesis are summarized below:

- In the single beam commissioning period, during which the monitor acted as a beam loss monitor, the background signals were measured and analyzed, with results showing good consistency with the detailed simulation. The Bremsstrahlung process dominated the backgrounds in the Phase-2 and early Phase-3, with a fraction typically of about 87% in the LER, while the Touschek process accounted for most of the remaining losses, about 13%. The rather good qualitative and quantitative agreement between the measurements and simulation enabled us to estimate the background level and the

SNR for the subsequent commissioning periods with colliding beams: an SNR larger than 100 can be expected when the instantaneous luminosity will reach $10^{34}\ cm^{-2}s^{-1}$, which is rather good to provide the precise fast luminosity signal.

- After the first collisions were achieved, the diamond luminosity monitor played an important role in the machine tuning during the luminosity optimization process. It provided several luminosity related observables: Relative train integrated luminosity signals at 1 Hz, giving direct feedback on the instantaneous luminosity to the SuperKEKB control system via EPICS for the machine tuning and study; Train integrated luminosity at 1 kHz, which was used as one of the inputs, along with the ZDLM signal, for the first tests of the dithering orbit feedback system to maintain an optimal horizontal offset between the two colliding beams; Bunch integrated luminosity signals at 1 Hz, which provide the relative luminosity information for each individual bunch. As a cross check, the luminosity signals from our monitor were compared with ZDLM and ECL. Good linearity between them proves that the luminosity monitor works well. Thanks to the 45° window and Tungsten radiator in the LER, the relative precision of the relative train-integrated-luminosity signal at 1 kHz is about 2.2% for a luminosity of $(1.85\pm0.05)\times10^{33}\ cm^{-2}s^{-1}$. 1% precision can be expected when luminosity reaches $10^{34}\ cm^{-2}s^{-1}$, which was shown in simulation to be good enough to serve as input to the dithering feedback system.

- During the past SuperKEKB commissioning periods, the beam sizes at the IP were still quite large thus the luminosity was not yet sensitive to the typical beam-beam offsets induced by ground motion in the horizontal plane. The dithering orbit feedback system was therefore not really used although it was carefully tested with deliberately introduced offsets created by the magnets. The results show that the dithering orbit feedback system using our precise 1 kHz luminosity signal as input can correct the beam orbit to maintain an optimum geometrical overlap between the two beams, and thereby maximize the luminosity.

- With the vertical offset scan technique, the beam size at the IP can be evaluated and the optimum position in the vertical plane can be found, which is very important during collision tuning at the IP. In addition, the bunch integrated luminosity signals during the scans can also provide information on the vertical beam size and alignment for each individual bunch, which is quite useful for studying potential variations along the bunch trains.

## 6.2 Prospects for luminosity monitoring at SuperKEKB

Based on all the results and experience obtained during the past SuperKEKB commissioning, we have also found some remaining issues, which we summarize below, along with possible mitigation actions. Some of the described improvements and further studies will be needed in view of the expected increases in luminosity and evolution of the machine in future years.

- Optimizing the combination and positions of detectors and amplifiers to ensure sufficient relative precision over the full range of expected luminosities from the lowest values during optical tuning with very low bunch currents to the nominal value, which corresponds to more than three orders of magnitude, while at the same time minimizing the radiation dose accumulating on the diamond detectors, to avoid potential deterioration in their performance.

- Shielding to mitigate risks from activation of the beam pipe and radiator on the LER side, which is expected to become relatively large at nominal luminosity.

- The radiation tolerance performance of the diamond detector was estimated based on the simulation, while its long-term performance should be monitored in future years after being irradiated more.

- Equipping a new station for scattered Bhabha photon measurements on the HER side was implemented at the start of the Phase-3 commissioning in 2019, where higher rates are predicted.The experimental results from the detectors at this new location need to be checked.

- Upgrading and maintaining the DAQ for long-term operation, including remote capabilities for control and monitoring of performances.

As the first $e^+e^-$ circular collider with nano-meter scale beam size at the IP and the highest instantaneous luminosity in the world until now, SuperKEKB could provide a lot of useful experience for the future high luminosity $e^+e^-$ circular colliders using the "nano-beam scheme", such as for instance CEPC and FCCee at the high energy frontier, or the super Tau-charm factories currently under discussion at the intensity frontier. Based on the results and experience of our project, some implications for future circular colliders may need to be considered with respect to fast luminosity monitoring, in particular for the beam orbit stabilization at the IP, the possible interaction between the bunches, and the local optics tuning at the IP with vertical offset scans based on precise luminosity signals at very low luminosity, to avoid the beam-beam interaction effects. These three applications mainly

depend on the availability of fast, precise integrated and bunch-by-bunch luminosity signals. Therefore, for the future high luminosity $e^+e^-$ circular colliders, requirements of the fast and precise luminosity monitoring will certainly need to be considered, and the work done for the SuperKEKB described in this thesis could serve as an example for such future colliders.

# References


[1] P. F. Dahl, "Rolf Wideroe: Progenitor of Particle Accelerators," 1992.

[2] R. Wideröe, "Some Memories and Dreams from the Childhood of Particle Accelerators," *Europhysics News*, vol. 15, pp. 9–11, 1984.

[3] P. J. Bryant, "A Brief history and review of accelerators," in *CAS-CERN Accelerator School: 5th general accelerator physics course, Jyvaskyla, Finland, 7-18 Sep 1992: Proceedings. 2 vol.*, pp. 1–16, 1992.

[4] Wikipedia contributors, "Rolf widerøe — Wikipedia, the free encyclopedia," 2018. [Online; accessed 19-October-2018].

[5] O. S. Brüning, P. Collier, P. Lebrun, S. Myers, R. Ostojic, J. Poole, and P. Proudlock, *LHC Design Report*. CERN Yellow Reports: Monographs, Geneva: CERN, 2004.

[6] G. Aad, T. Abajyan, B. Abbott, *et al.*, "Observation of a new particle in the search for the standard model higgs boson with the atlas detector at the lhc," *Physics Letters B*, vol. 716, no. 1, pp. 1 – 29, 2012.

[7] S. Chatrchyan, V. Khachatryan, A. Sirunyan, *et al.*, "Observation of a new boson at a mass of 125 gev with the cms experiment at the lhc," *Physics Letters B*, vol. 716, no. 1, pp. 30 – 61, 2012.

[8] R. Hammond, *The Unknown Universe: The Origin of the Universe, Quantum Gravity, Wormholes, and Other Things Science Still Can't Explain*. New Page Books, 2008.

[9] Y. Grossman, Y. Nir, and R. Rattazzi, "CP violation beyond the standard model," *Adv. Ser. Direct. High Energy Phys.*, vol. 15, pp. 755–794, 1998.

[10] Z. F, "HL-LHC: parameter space, constraints, and possible options," in *Proceedings, LHC Performance Workshop (Chamonix 2011): Chamonix, France, January 24-28,*, 2011.

[11] P. Lebrun, L. Linssen, A. Lucaci-Timoce, D. Schulte, F. Simon, S. Stapnes, N. Toge, H. Weerts, and J. Wells, "The CLIC Programme: Towards a Staged e+e- Linear Collider Exploring the Terascale : CLIC Conceptual Design Report," *Technical report*, 2012.

[12] L. Evans and S. Michizono, "The International Linear Collider Machine Staging Report 2017," *Technical report*, 2017.

[13] B. Barish and J. E. Brau, "The International Linear Collider," *Int. J. Mod. Phys.*, vol. A28, no. 27, p. 1330039, 2013.

[14] A. Blondel and F. Zimmermann, "A High Luminosity $e^+e^-$ Collider in the LHC tunnel to study the Higgs Boson," *Technical report*, 2011.

[15] M. Benedikt, A. Blondel, O. Brunner, M. Capeans Garrido, F. Cerutti, J. Gutleber, P. Janot, J. M. Jimenez, V. Mertens, A. Milanese, K. Oide, J. A. Osborne, T. Otto, Y. Papaphilippou, J. Poole, L. J. Tavian, and F. Zimmermann, "Future Circular Collider," Tech. Rep. CERN-ACC-2018-0057, CERN, Geneva, Dec 2018. Submitted for publication to Eur. Phys. J. ST.

[16] CEPC-Study-Group, "CEPC Conceptual Design Report," *Technical report*, 2018.

[17] T. Abe *et al.*, "Belle II Technical Design Report," *Technical report*, 2010.

[18] Y. Ohnishi, T. Abe, *et al.*, "Accelerator design at SuperKEKB," *Progress of Theoretical and Experimental Physics*, vol. 2013, no. 3, p. 03A011, 2013.

[19] V. Schlott, M. Böge, B. Keil, P. Pollet, and T. Schilcher, "Fast orbit feedback and beam stability at the swiss light source," *AIP Conference Proceedings*, vol. 732, no. 1, pp. 174–181, 2004.

[20] S. Gayadeen and S. R. Duncan, "Design of an electron beam stabilisation controller for a synchrotron," *Control Engineering Practice*, vol. 26, pp. 201 – 210, 2014.

[21] J. Lee, C. Kim, J. Kim, K. Kim, E. Lee, J. Lee, T. Lee, C. Park, S. Shin, J. Yoon, W. Cho, G. Park, and S. Kim, "Fast global orbit feedback system in pls-ii," *Journal of Instrumentation*, vol. 11, no. 12, p. T12003, 2016.

[22] A. S. Fisher, S. Ecklund, R. C. Field, S. Gierman, P. Grossberg, K. Krauter, E. Miller, M. Petree, K. G. Sonnad, N. Spencer, M. K. Sullivan, K. K. Underwood, and U. Wienands, "Commissioning the fast luminosity dither for pep-ii," in *2007 IEEE Particle Accelerator Conference (PAC)*, pp. 4165–4167, June 2007.

[23] Y. Funakoshi, M. Masuzawa, K. Oide, J. Flanagan, M. Tawada, T. Ieiri, M. Tejima, M. Tobiyama, K. Ohmi, and H. Koiso, "Orbit feedback system for maintaining an optimum beam collision," *Phys. Rev. ST Accel. Beams*, vol. 10, p. 101001, Oct 2007.

[24] Y. Funakoshi *et al.*, "Interaction Point Orbit Feedback System at SuperKEKB," in *Proceedings, 6th International Particle Accelerator Conference (IPAC 2015): Richmond, Virginia, USA, May 3-8, 2015*, p. MOPHA054, 2015.

[25] M. Masuzawa, J. W. Flanagan, Y. Funakoshi, and K. Oide, "IP orbital feedback for collision tuning at KEKB," in *Particle accelerator. Proceedings, 7th European Conference, EPAC 2000, Vienna, Austria, June 26-30, 2000. Vol. 1-3*, pp. 1211–1213, 2000.

[26] L. HENDRICKSON, T. Gromme, P. Grossberg, *et al.*, "SLOW FEEDBACK SYSTEMS FOR PEP-II," in *7th European Particle Accelerator Conference (EPAC),Vienna, Austria*, pp. 1897–1899, 2000.

[27] L. Hendrickson *et al.*, "Slow feedback systems for PEP-II," in *Particle accelerator. Proceedings, 7th European Conference, EPAC 2000, Vienna, Austria, June 26-30, 2000. Vol. 1-3*, pp. 1897–1899, 2000.

[28] W. Herr and B. Muratori, "Concept of luminosity," in *Intermediate accelerator physics. Proceedings, CERN Accelerator School, Zeuthen, Germany, September 15-26, 2003*, pp. 361–377, 2003.

[29] S. Robins, *A Study of Bhabha scattering at LEP*. PhD thesis, Queen Mary, University of London, 1992.

[30] B. G. Cheon *et al.*, "Electromagnetic calorimeter trigger at Belle," *Nucl. Instrum. Meth.*, vol. A494, pp. 548–554, 2002.

[31] Belle-ECL, V. Aulchenko, A. Bobrov, A. Bondar, B. G. Cheon, S. Eidelman, D. Epifanov, Y. Garmash, Y. M. Goh, S. H. Kim, P. Krokovny, A. Kuzmin, I. S. Lee, D. Matvienko, K. Miyabayashi, I. Nakamura, V. Shebalin, B. Shwartz, Y. Unno, Y. Usov, A. Vinokurova, V. Vorobjev, V. Zhilich, and V. Zhulanov, "Electromagnetic calorimeter for Belle II," *Journal of Physics: Conference Series*, vol. 587, no. 1, p. 012045, 2015.

[32] T. Hirai, S. Uehara, and Y. Watanabe, "Real-time luminosity monitor for a B-factory experiment," *Nuclear Instruments and Methods in Physics Research A*, vol. 458, pp. 670–676, Feb. 2001.

[33] C. G. Pang, P. Bambade, S. D. Carlo, Y. Funakoshi, D. Jehanno, V. Kubytskyi, M. Masuzawa, Y. Peinaud, C. Rimbault, and S. Uehara, "A fast luminosity monitor based on diamond detectors for the superkekb collider," *Nuclear Instruments and Methods in Physics Research Section A: Accelerators, Spectrometers, Detectors and Associated Equipment*, vol. 931, pp. 225 – 235, 2019.

[34] T. Abe, K. Akai, N. Akasaka, *et al.*, "Achievements of KEKB," *Progress of Theoretical and Experimental Physics*, vol. 2013, no. 3, p. 03A001, 2013.

[35] M. Kobayashi and T. Maskawa, "CP-Violation in the Renormalizable Theory of Weak Interaction," *Progress of Theoretical Physics*, vol. 49, no. 2, pp. 652–657, 1973.

[36] S. Emery-Schrenk, "Recent results on CP violation at B factories," *Hyperfine Interact.*, vol. 239, no. 1, p. 36, 2018.

[37] G. Marchiori, "Search for CP violation and new physics in rare B decays at the B factories," in *Proceedings, 10th Conference on Flavor Physics and CP Violation (FPCP 2012): Hefei, Anhui, China, May 21-25, 2012*, 2012.

[38] N. Soni, "CP-violation in b —> s penguin decays at BaBar," in *SUSY 2007 Proceedings, 15th International Conference on Supersymmetry and Unification of Fundamental Interactions, July 26 - August 1, 2007, Karlsruhe, Germany*, pp. 740–743, 2007.

[39] A. Abdesselam *et al.*, "First Observation of CP Violation in $\overline{B}^0 \to D_{\rm CP}^{(*)} h^0$ Decays by a Combined Time-Dependent Analysis of BABAR and Belle Data," *Phys. Rev. Lett.*, vol. 115, no. 12, p. 121604, 2015.

[40] M. Bona *et al.*, "SuperB: A High-Luminosity Asymmetric e+ e- Super Flavor Factory. Conceptual Design Report," *SLAC-R-856, INFN-AE-07-02, LAL-07-15, INFN-AE-07-2*, 2007.

[41] K. Akai, K. Furukawa, and H. Koiso, "SuperKEKB Collider," *Nucl. Instrum. Meth.*, vol. A907, pp. 188–199, 2018.

[42] N. Ohuchi *et al.*, "Design of the Superconducting Magnet System for the SuperKEKB Interaction Region," in *1st North American Particle Accelerator Conference (NAPAC2013) Pasadena, CA, USA, September 29-October 4*, 2013.

[43] K. Shibata *et al.*, "Commissioning status of SuperKEKB vacuum system," in *Proceedings, eeFACT 2018: Hongkong, September 24-27*, 2018.

[44] K. Akai, "Progress in Super B-factories," in *Proceedings, 4th International Particle Accelerator Conference (IPAC 2013): Shanghai, China, May 12-17, 2013*, p. TUYB101, 2013.

[45] H. Koiso, "Commissioning Status of High Luminosity Collider Rings for SuperKEKB," in *Proceedings, 8th International Particle Accelerator Conference (IPAC 2017): Copenhagen, Denmark, May 14-19, 2017*, p. TUZB2, 2017.

[46] K. ichi Kanazawa, "Status of superkekb construction," *Nuclear and Particle Physics Proceedings*, vol. 273-275, pp. 204 – 209, 2016. 37th International Conference on High Energy Physics (ICHEP).

[47] Y. Funakoshi, "Commissioning of SuperKEKB," in *Proceedings, 58th ICFA Advanced Beam Dynamics Workshop on High Luminosity Circular $e^+e^-$ Colliders (eeFACT2016): Daresbury, United Kingdom, October 24-27, 2016*, p. MOOTH2, 2017.

[48] Y. Funakoshi and Y. Ohnishi, "Highlights from SuperKEKB Commissioning Phase 1 and Plan for Phase 2," *ICFA Beam Dyn. Newslett.*, vol. 72, pp. 11–19, 2017.

[49] Y. Suetsugu, K. Shibata, T. Ishibashi, K. Kanazawa, M. Shirai, S. Terui, and H. Hisamatsu, "First commissioning of the superkekb vacuum system," *Phys. Rev. Accel. Beams*, vol. 19, p. 121001, Dec 2016.

[50] H. Fukuma *et al.*, "Study of vertical beam blowup in KEKB low energy ring," in *Proceedings, 18th International Conference on High-Energy Accelerators, HEACC 2001: Tsukuba, Japan, March 26-30, 2001*, p. P1hlf10, 2001.

[51] K. Ohmi and F. Zimmermann, "Head - tail instability caused by electron cloud in positron storage rings," *Phys. Rev. Lett.*, vol. 85, pp. 3821–3824, 2000.

[52] H. Fukuma, K. Ohmi, Y. Suetsugu, and M. Tobiyama, "Electron Cloud at SuperKEKB," in *Proceedings, 58th ICFA Advanced Beam Dynamics Workshop on High Luminosity Circular $e^+e^-$ Colliders (eeFACT2016): Daresbury, United Kingdom, October 24-27, 2016*, p. TUT3AH6, 2017.

[53] Y. Suetsugu, H. Fukuma, K. Ohmi, M. Tobiyama, J. Flanagan, H. Ikeda, E. Mulyani, K. Shibata, T. Ishibashi, M. Shirai, S. Terui, K. Kanazawa, and H. Hisamatsu, "Mitigating the electron cloud effect in the superkekb positron ring," *Phys. Rev. Accel. Beams*, vol. 22, p. 023201, Feb 2019.

[54] Y. Ohnishi, "Report on SuperKEKB Phase 2 Commissioning," in *Proceedings, 9th International Particle Accelerator Conference (IPAC 2018): Vancouver, BC Canada*, p. MOXGB1, 2018.

[55] P. Lewis, I. Jaegle, H. Nakayama, *et al.*, "First measurements of beam backgrounds at SuperKEKB," *Nuclear Instruments and Methods in Physics Research Section A: Accelerators, Spectrometers, Detectors and Associated Equipment*, 2018.

[56] H. Yamaoka, Y. Arimoto, K.-i. Kanazawa, M. Masuzawa, Y. Ohsawa, N. Ohuchi, K. Tsuchiya, and Z. Zong, "The Mechanical and Vibration Studies of the Final Focus Magnet-cryostat for SuperKEKB," in *Proceedings, 5th International Particle Accelerator Conference (IPAC 2014): Dresden, Germany, June 15-20, 2014*, p. THPRI005, 2014.

[57] K. Ohmi. Personal communication.

[58] M. Tobiyama, "IP feedback system for SuperKEKB," in *INFN seminar, https://agenda.infn.it/conferenceDisplay.py?confId=3522*, p. 1, 2011.

[59] C. G. Pang, P. Bambade, Y. Funakoshi, and S. Uehara, "Simulation study on luminosity feedback for horizontal beam stabilization at SuperKEKB," *Journal of Physics: Conference Series*, vol. 1067, no. 7, p. 072023, 2018.

[60] Y. Funakoshi *et al.*, "Recent Progress of Dithering System at SuperKEKB," in *Proceedings, 8th International Particle Accelerator Conference (IPAC 2017): Copenhagen, Denmark, May 14-19, 2017*, p. TUPIK059, 2017.

[61] C. G. Pang *et al.*, "LumiBelle2 and ZDLM Luminosity Measurements," in *30th B2GM, KEK, Tsukuba, Japan, June 18-22*, 2018.

[62] C. G. Pang, P. Bambade, S. Di Carlo, Y. Funakoshi, D. Jehanno, V. Kubytskyi, Y. Peinaud, C. Rimbault, and S. Uehara, "First Tests of SuperKEKB Fast Luminosity Monitors During 2018 Phase-2 Commissioning," in *9th International Particle Accelerator Conference*, (Vancouver, Canada), p. WEPAL038, Apr. 2018.

[63] C. G. Pang, P. Bambade, D. El Khechen, D. Jehanno, V. Kubytskyi, Y. Peinaud, and C. Rimbault, "Preparation of CVD Diamond Detector for fast Luminosity Monitoring of SuperKEKB," in *8th International Particle Accelerator Conference*, (Copenhagen, Denmark), p. MOPAB027, May 2017.

[64] D. El Khechen, *Fast Luminosity Monitoring Using Diamond Sensors for SuperKEKB*. Theses, Université Paris-Saclay, Dec. 2016.

[65] M. Gabrysch, "Electronic properties of diamond," *Uppsala University, Electricity*, no. 305-08L, p. 56, 2008.

[66] D. Kania, M. Landstrass, M. Plano, L. Pan, and S. Han, "Diamond radiation detectors," *Diamond and Related Materials*, vol. 2, no. 5, pp. 1012 – 1019, 1993. Diamond 1992.

[67] A. Brambilla, D. Tromson, N. Aboud, C. Mer, P. Bergonzo, and F. Foulon, "Cvd diamond gamma dose rate monitor for harsh environment," *Nuclear Instruments and Methods in Physics Research Section A: Accelerators, Spectrometers, Detectors and Associated Equipment*, vol. 458, no. 1, pp. 220 – 226, 2001. Proc. 11th Inbt. Workshop on Room Temperature Semiconductor X- and Gamma-Ray Detectors and Associated Electronics.

[68] L. Wang, J. Liu, R. Xu, H. Peng, W. Shi, and Y. Xia, "A nanocrystalline cvd diamond film as an x-ray radiation detector," *Semiconductor Science and Technology*, vol. 22, no. 2, p. 128, 2007.

[69] Y. Sato, T. Shimaoka, J. H. Kaneko, H. Murakami, M. Isobe, M. Osakabe, M. Tsubota, K. Ochiai, A. Chayahara, H. Umezawa, and S. Shikata, "Radiation hardness of a single crystal cvd diamond detector for mev energy protons," *Nuclear Instruments and Methods in Physics Research Section A: Accelerators, Spectrometers, Detectors and Associated Equipment*, vol. 784, pp. 147 – 150, 2015. Symposium on Radiation Measurements and Applications 2014 (SORMA XV).

[70] F. Schirru, B. S. N. Singh, *et al.*, "Development of large area polycrystalline diamond detectors for fast timing application of high-energy heavy-ion beams," *Journal of Instrumentation*, vol. 7, no. 05, p. P05005, 2012.

[71] CIVIDEC, *https://cividec.at/.*

[72] K. Kobashi, "Chapter 2 - diamond – structure and cvd growth," in *Diamond Films* (K. Kobashi, ed.), pp. 9 – 13, Oxford: Elsevier Science Ltd, 2005.

[73] Peschel, Gina, "Carbon-carbon bonds: hybridization,"

[74] R. Nor, S. Bakar, T. Thandavan, and M. Mahmood, *Diamond: Synthesis, characterisation and applications*, pp. 195–217. Advanced Structured Materials, 12 2011.

[75] G. F. Knoll, *Radiation detection and measurement; 4th ed.* New York, NY: Wiley, 2010.

[76] M. Tanabashi, K. Hagiwara, K. Hikasa, K. Nakamura, *et al.*, "Review of particle physics," *Phys. Rev. D*, vol. 98, p. 030001, Aug 2018.

[77] S. Agostinelli, J. Allison, K. Amako, J. Apostolakis, *et al.*, "Geant4—a simulation toolkit," *Nuclear Instruments and Methods in Physics Research Section A: Accelerators, Spectrometers, Detectors and Associated Equipment*, vol. 506, no. 3, pp. 250 – 303, 2003.

[78] S. Ramo, "Currents induced by electron motion," *Proceedings of the IRE*, vol. 27, pp. 584–585, Sep. 1939.

[79] Z. He, "Review of the shockley–ramo theorem and its application in semiconductor gamma-ray detectors," *Nuclear Instruments and Methods in Physics Research Section A: Accelerators, Spectrometers, Detectors and Associated Equipment*, vol. 463, no. 1, pp. 250 – 267, 2001.

[80] C. G. Pang, P. Bambade, *et al.*, "Fast Luminosity Monitoring for the SuperKEKB Collider (LumiBelle2 Project)," in *7th International Beam Instrument Conference*, (Shanghai, China), p. MOPA13, 2018.

[81] D. Jehanno. Group cooperation and personal communication.

[82] C. Rimbault, P. Bambade, *et al.*, "Guinea-pig++: an upgraded version of the linear collider beam-beam interaction simulation code guinea-pig.," in *2007 IEEE Particle Accelerator Conference (PAC)*, pp. 2728–2730, June 2007.

[83] C. Rimbault *et al.*, "Guinea-pig++ manual." http://flc.web.lal.in2p3.fr/mdi/BBSIM/guineaPigHtml/userman.htm.

[84] G. L. Meur *et al.*, "Guinea-pig++ project." https://trac.lal.in2p3.fr/GuineaPig.

[85] Y. Ohnish. privite communication.

[86] K. Hirata, "An Introduction to SAD," in *2nd Advanced ICFA Beam Dyanmics Workshop, Lugano, Switzerland, 11-16 Apr 1988: Proceedings*, pp. 62–65, 1988.

[87] http://acc-physics.kek.jp/SAD/.

[88] https://geant4.web.cern.ch/.

[89] A. Ferrari, P. R. Sala, A. Fassò, and J. Ranft, *FLUKA: A multi-particle transport code (program version 2005)*. CERN Yellow Reports: Monographs, Geneva: CERN, 2005.

[90] http://www.fluka.org/fluka.php.

[91] http://www-superkekb.kek.jp/documents.html.

[92] S. D. Carlo. Personal communication.

[93] S. D. Carlo, P. Bambade, D. Jehanno, V. Kubytskyi, C. Pang, Y. Peinaud, and C. Rimbault, "Early phase 2 results of LumiBelle2 for the SuperKEKB electron ring," *Journal of Physics: Conference Series*, vol. 1067, p. 072025, sep 2018.

[94] https://www.mathworks.com/products/matlab.html.

[95] H. Nakayama, Y. Funakoshi, T. Ishibashi, K.-i. Kanazawa, and Y. Ohnishi, "SuperKEKB Background Simulations, Including Issues for Detector Shielding," in *Proceedings, 55th ICFA Advanced Beam Dynamics Workshop on High Luminosity Circular e+e- Colliders – Higgs Factory (HF2014): Beijing, China, October 9-12, 2014*, p. FRT3A1, 2015.

[96] K. Kanazawa, Y. Ohnishi, H. Nakayama, C. Kiesling, S. Koblitz, A. Moll, M. Ritter, H. Nakano, and H. Yamamoto, "Beam Background Simulation for SuperKEKB/Belle-II," *Conf. Proc.*, vol. C110904, pp. 3700–3702, 2011.

[97] H. Nakano and H. Yamamoto, *A simulation study of beam backgrounds at the KEKB and Super KEKB colliders*. PhD thesis, Tohoku, Tohoku University, Tohoku, 2011. Presented on 03 02 2011.

[98] H. Wiedemann, *Particle accelerator physics I*. Berlin, Germany: Springer, 1999.

[99] R. Barlow, W. Kozanecki, P. Roudeau, A. Stocchi, T. Fieguth, and S. Majewski, "Simulation of PEP-II Accelerator Backgrounds Using Turtle," in *Proceedings of the 2005 Particle Accelerator Conference*, pp. 1835–1837, May 2005.

[100] M. Boscolo, O. R. Blanco-García, H. Burkhardt, F. Collamati, R. Kersevan, and M. Lueckhof, "Beam-gas background characterization in the fcc-ee ir," *Journal of Physics: Conference Series*, vol. 1067, no. 2, p. 022012, 2018.

[101] A. F. Wrulich, "Single-beam lifetime," 1994.

[102] V. A. Yerokhin and A. Surzhykov, "Electron-atom bremsstrahlung: Double-differential cross section and polarization correlations," *Phys. Rev. A*, vol. 82, p. 062702, Dec 2010.

[103] A. Piwinski, "The Touschek effect in strong focusing storage rings," 1998.

[104] J. Le Duff, "SINGLE AND MULTIPLE TOUSCHEK EFFECTS," in *CERN Accelerator School: Advanced Accelerator Physics Berlin, Germany, September 14-25, 1987*, pp. 114–130, 1988.

[105] https://www.lnf.infn.it/conference/lnfss/touschek.htm.

[106] E. Amaldi, *The Bruno Touschek legacy: Vienna 1921 - Innsbruck 1978*. CERN Yellow Reports: Monographs, Geneva: CERN, 1981.

[107] L. Bonolis and G. Pancheri, "Bruno Touschek and AdA: from Frascati to Orsay.," 2018.

[108] Y. Ohnishi. Single beam loss tracking with SAD, Personal communication.

[109] M. Ady, R. Kersevan, and R. Leonid, *"Monte Carlo simulations of ultra high vacuum and synchrotron radiation for particle accelerators"*. PhD thesis, Ecole Polytechnique Férérale de Lausanne (EPFL), May, 2016.

[110] N. Venturi, A. Alexopoulos, *et al.*, "Results on radiation tolerance of diamond detectors," *Nuclear Instruments and Methods in Physics Research Section A: Accelerators, Spectrometers, Detectors and Associated Equipment*, 2018.

[111] W. Adam, "Radiation hard diamond sensors for future tracking applications," *Nucl. Instrum. Methods Phys. Res., A*, vol. 565, pp. 278–283, 2006.

[112] W. Adam, E. Berdermann, P. Bergonzo, W. de Boer, *et al.*, "The development of diamond tracking detectors for the LHC," *Nucl. Instrum. Methods Phys. Res., A*, vol. 514, pp. 79–86, 2003.

[113] W. Adam, E. Berdermann, P. Bergonzo, *et al.*, "Radiation tolerance of CVD diamond detectors for pions and protons," *Nucl. Instrum. Methods Phys. Res., A*, vol. 476, no. 3, pp. 686–693. 8 p, 2002.

[114] S. Seidel, "Recent results on diamond radiation tolerance," *JINST*, vol. 9, no. 01, p. C01013, 2014.

[115] A. Vasilescu, "The niel scaling hypothesis for fluence normalisation in radiation damage testing of silicon detectors for collider experiments (ifin-hh-ar–1997)," *Badescu, Elisabeta (Ed.). Romania*, 1998.

[116] M. Guthoff, *Radiation Damage to the diamond-based Beam Condition Monitor of the CMS Detector at the LHC*. PhD thesis, KIT, Karlsruhe, 2014.

[117] J. Lindhard, V. Nielsen, M. Scharff, and P. Thomsen, "Integral equations governing radiation effects. (notes on atomic collisions, iii)," *Kgl. Danske Videnskab., Selskab. Mat. Fys. Medd.*

[118] M. Guthoff, W. de Boer, and S. Müller, "Simulation of beam induced lattice defects of diamond detectors using fluka," *Nuclear Instruments and Methods in Physics Research Section A: Accelerators, Spectrometers, Detectors and Associated Equipment*, vol. 735, pp. 223 – 228, 2014.

[119] W. Trischuk, "Recent Advances in Diamond Detectors," in *Proceedings, 34th International Conference on High Energy Physics (ICHEP 2008): Philadelphia, Pennsylvania, July 30-August 5, 2008*, 2008.

[120] M. Cristinziani, "Diamond Prototypes for the ATLAS SLHC Pixel Detector," *Nucl. Instrum. Meth.*, vol. A623, pp. 174–176, 2010.

[121] J. W. Tsung, M. Havranek, and ohters, "Signal and noise of diamond pixel detectors at high radiation fluences," *Journal of Instrumentation*, vol. 7, no. 09, p. P09009, 2012.

[122] F. Kassel, M. Guthoff, A. Dabrowski, and W. de Boer, "Severe signal loss in diamond beam loss monitors in high particle rate environments by charge trapping in radiation-induced defects," *physica status solidi (a)*, vol. 213, no. 10, pp. 2641–2649, 2016.

[123] F. Bachmair, "Diamond sensors for future high energy experiments," *Nuclear Instruments and Methods in Physics Research Section A: Accelerators, Spectrometers, Detectors and Associated Equipment*, vol. 831, pp. 370 – 377, 2016. Proceedings of the 10th International "Hiroshima" Symposium on the Development and Application of Semiconductor Tracking Detectors.

[124] C. Tuvé, "Development of CVD diamond tracking detectors for experiments at high-luminosity colliders," *Nuovo Cim.*, vol. C34, no. 6, pp. 184–188, 2011.

[125] F. R. Kassel, *The rate dependent radiation induced signal degradation of diamond detectors*. PhD thesis, KIT, Karlsruhe, 2017-06-23.

[126] H. O. S. Kagan and W. T. Trischuk, "Development of Diamond Tracking Detectors for High Luminosity Experiments at the LHC, HL-LHC and Beyond," Tech. Rep. CERN-LHCC-2018-015. LHCC-SR-005, CERN, Geneva, May 2018.

[127] A. FASSO, A. FERRARI, G. SMIRNOV, F. SOMMERER, and V. VLACHOUDIS, "FLUKA Realistic Modeling of Radiation Induced Damage," *Prog. Nucl. Sci. Tech.*, vol. 2, pp. 769–775, 2011.

[128] G. Battistoni *et al.*, "FLUKA Capabilities and CERN Applications for the Study of Radiation Damage to Electronics at High-Energy Hadron Accelerators," *Prog. Nucl. Sci. Tech.*, vol. 2, pp. 948–954, 2011.

[129] M. Masuzawa, Y. Ohsawa, R. Sugahara, and H. Yamaoka, "Vibration measurements in the KEKB tunnel," in *Proceedings, 8th International Workshop on Accelerator Alignment (IWAA 2004): Geneva, Switzerland, October 4-7, 2004*, vol. C04100411, p. 042, 2004.

[130] M. Masuzawa *et al.*, "Vibration issues for SuperKEKB," in *11th IWAA, DESY, September*, pp. 11–17, 2010.

[131] A. Seryi, "Ground motion models for future linear colliders," in *Particle accelerator. Proceedings, 7th European Conference, EPAC 2000, Vienna, Austria, June 26-30, 2000. Vol. 1-3*, pp. 501–503, 2000.

[132] Y. Funakoshi *et al.*, "Operation of SuperKEKB in Phase 2," in *Proceedings, eeFACT 2018: Hongkong, September 24-27*, 2018.

[133] Y. Ohnishi *et al.*, "Highlights from SuperKEKB Phase 2 commissioning," in *Proceedings, eeFACT 2018: Hongkong, September 24-27*, p. MOXAA02, 2018.

[134] S. Uehara. Group collaboration and personal communication.

[135] Y. Suetsugu, K.-i. Kanazawa, K. Shibata, T. Ishibashi, H. Hisamatsu, M. Shirai, and S. Terui, "Design and construction of the superkekb vacuum system," *Journal of Vacuum Science & Technology A*, vol. 30, no. 3, p. 031602, 2012.

[136] Y. Funakoshi *et al.*, "COMMISSIONING OF SuperKEKB," in *Proceedings, eeFACT 2016: Daresbury, UK, October 24-27*, 2016.

[137] E. Mulyani and J. Flanagan, "Calibration of X-ray Monitor during the Phase I of SuperKEKB commissioning," in *Proceedings, 5th International Beam Instrumentation Conference (IBIC 2016): Barcelona, Spain, September 11-15, 2016*, p. TUPG72, 2017.

[138] Y. Funakoshi *et al.*, "Superkekb project," in *Institute for Advanced Study, Hongkong, January, 23*, 2017.

[139] M. Tobiyama *et al.*, "Beam Commissioning of SuperKEKB Rings at Phase 1," in *Proceedings, 5th International Beam Instrumentation Conference (IBIC 2016): Barcelona, Spain, September 11-15, 2016*, p. MOAL03, 2017.

[140] U. Wienands, S. Anderson, Y. Funakoshi, S. Gierman, M. Kosovsky, M. Masuzawa, C. Spencer, and M. K. Sullivan, "Dither Coils for the SuperKEKB Fast Collision Feedback System," in *Proceedings, 6th International Particle Accelerator Conference (IPAC 2015): Richmond, Virginia, USA, May 3-8, 2015*, p. WEPWI006, 2015.

[141] "AMETEK DSP Lock-Amplifier Model 7230." https://www.ameteksi.com/-/media/ameteksi/download_links/documentations/7230/198004-a-mnl-b.pdf.

[142] C. G. Pang *et al.*, "Fast Luminosity Monitoring System at SuperKEKB," in *Proceedings, International workshop on the CEPC: Beijing, China, November 12-14*, 2018.

[143] C. G. Pang *et al.*, "Fast luminosity monitoring and background measurements at SuperKEKB," in *Joint workshop of 10th TYL/FJPPL-FKPPL, Nara, Japan, May 09-11*, 2018.

[144] M. Masuzawa *et al.*, "Early Commissioning of the Luminosity Dither System for SuperKEKB)," in *Proceedings, 7th International Beam Instrument Conference (IBIC 2018): Shanghai, China, September*, p. TUPC13, 2018.

[145] S. D. Carlo *et al.*, "Vertical beam size determination at the interaction point of superkekb using offset scans," *submitted to Physical Review Accelerators and Beams*, 2019.

# Appendix A

# Practical information for LumiBelle2

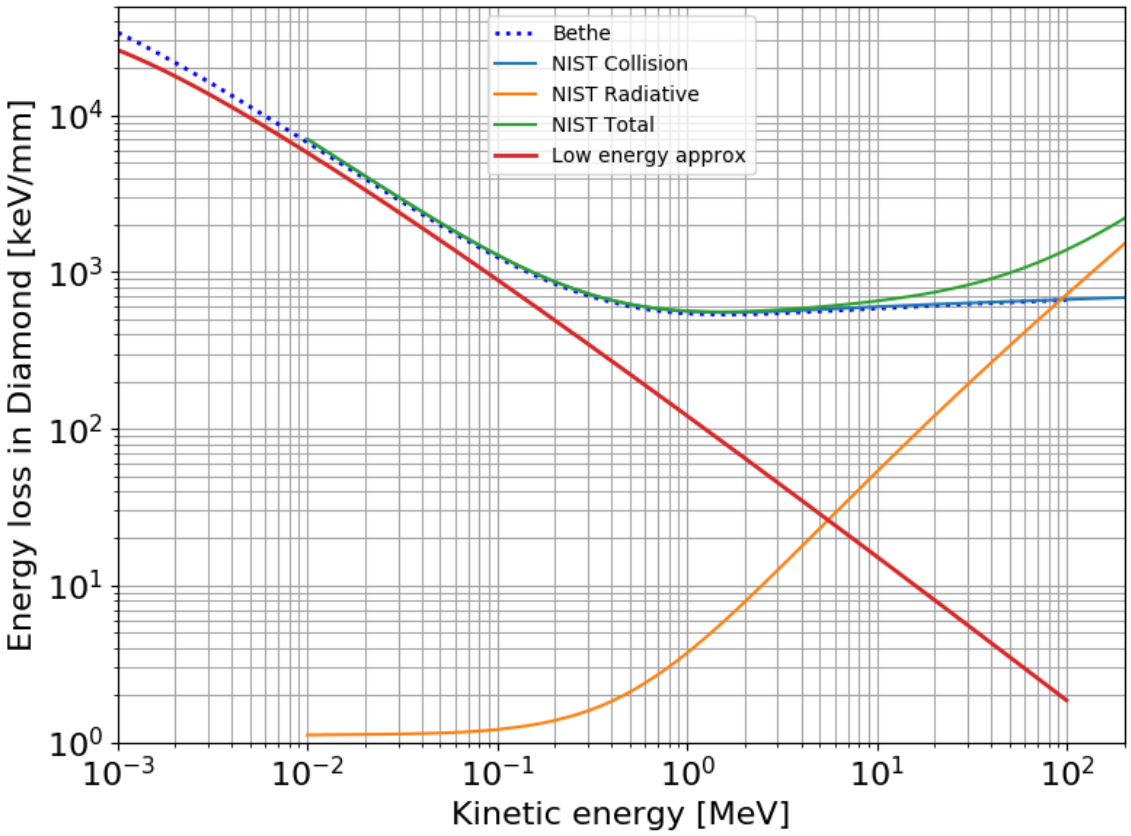


**Figure A.1:** Energy deposited in the diamond detector against the incident electron's energy.

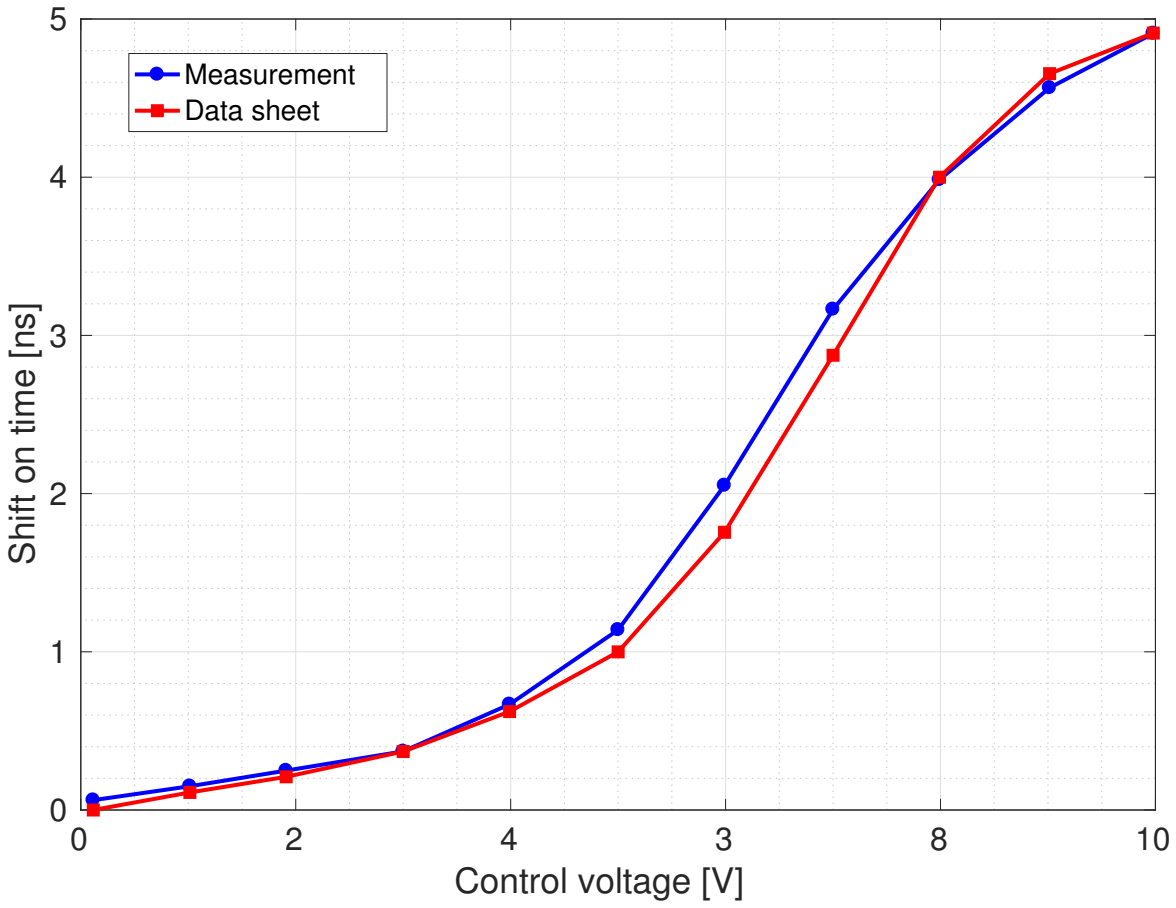


**Figure A.2:** The response function of the Phase shift against the control voltage.

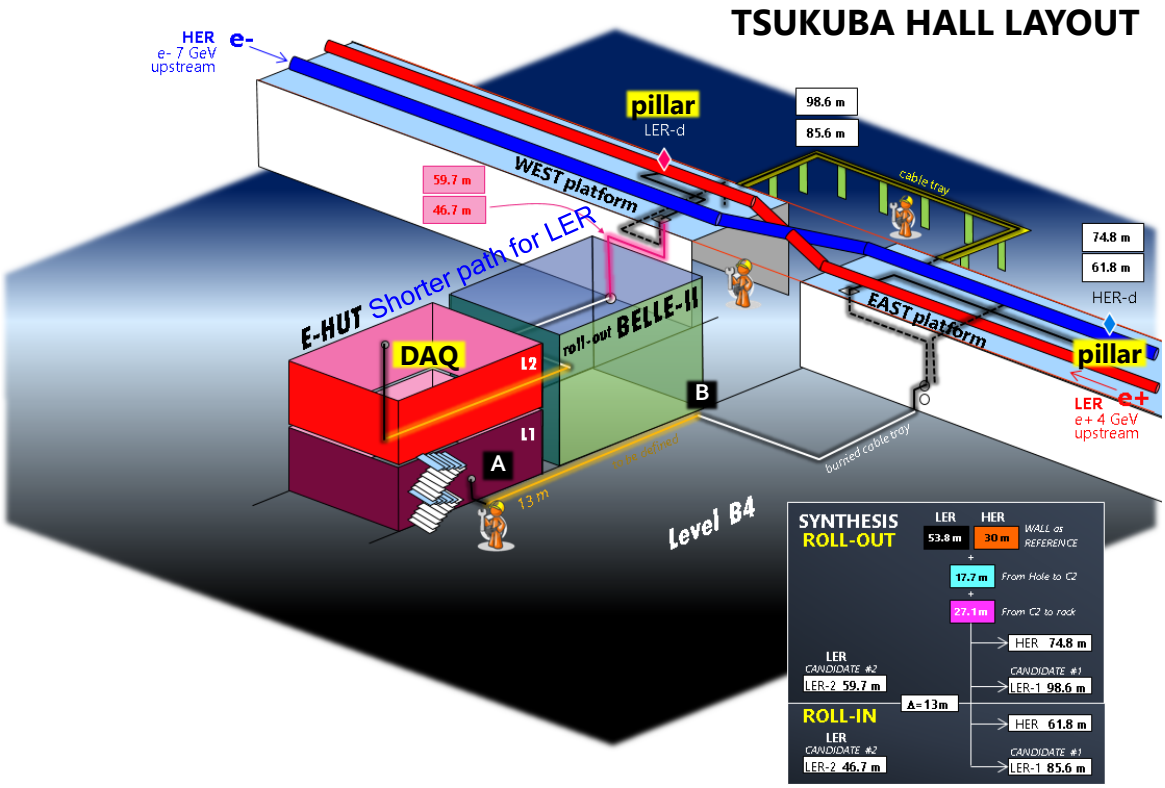


**Figure A.3:** The layout of the Tsukuba hall showing the Belle II detector with its Electronics-Hut and the cabling path for the diamond detectors in LER and HER.

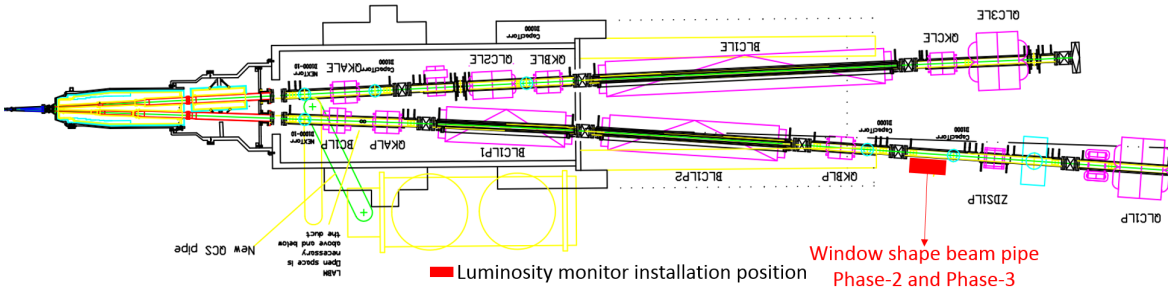


**Figure A.4:** The installation position of our luminosity monitor in the LER, about 10 m downstream of the IP.

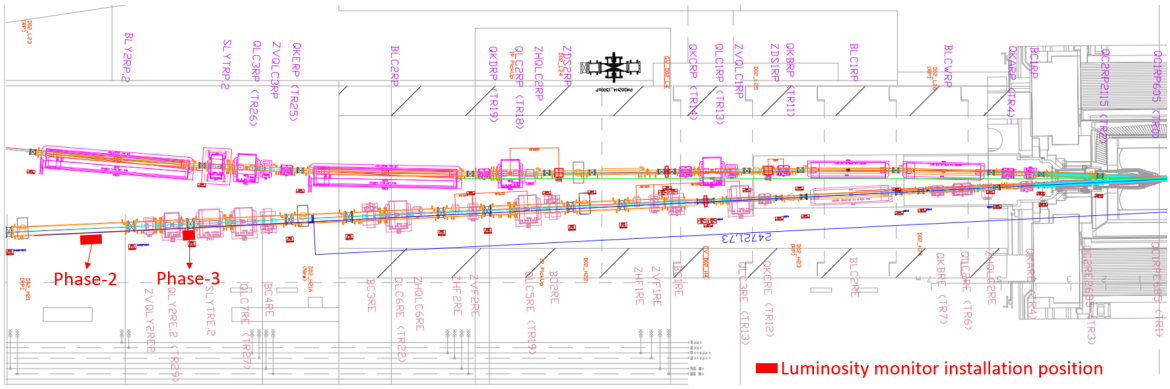


**Figure A.5:** The installation position of our luminosity monitor in the HER, different in Phase-2 and Phase-3. At the new location, the signal rates are expected to be 10 times more than the old position in Phase-2.

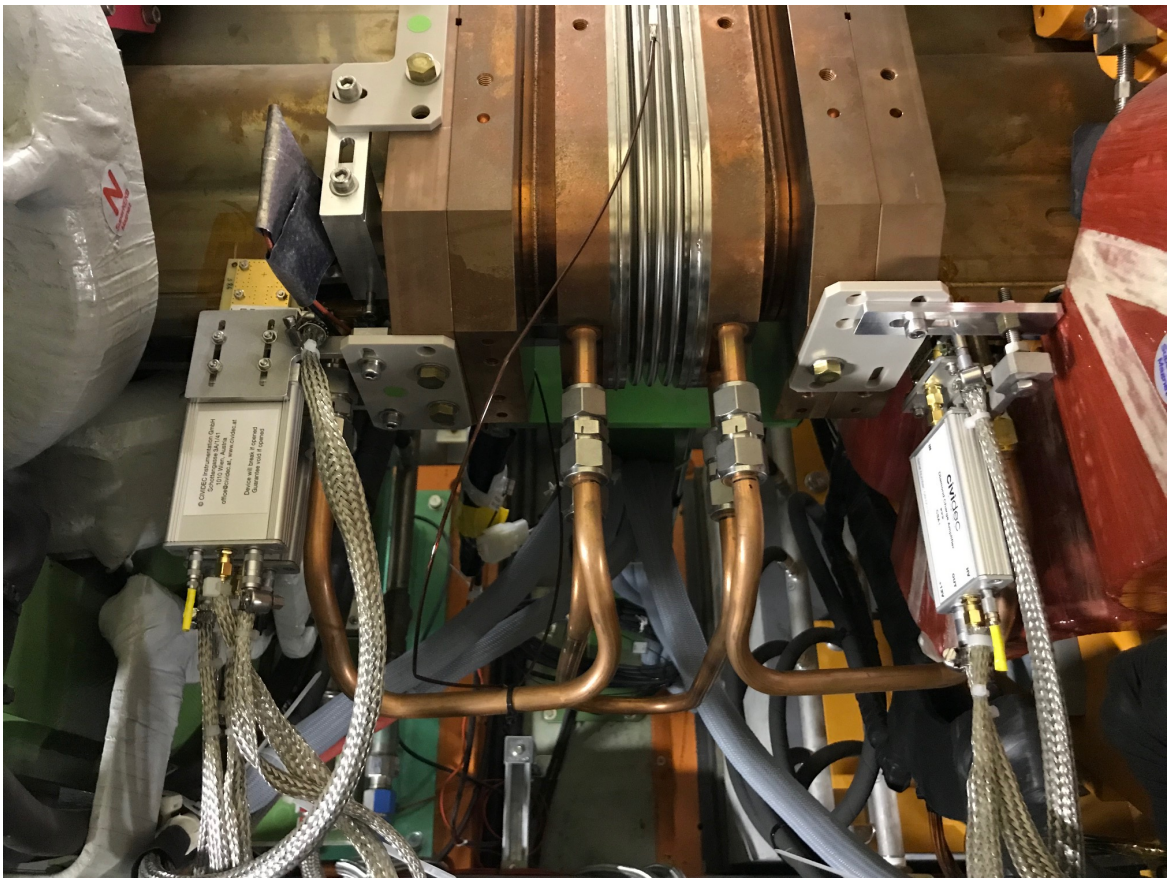

**Figure A.6:** Installation layout of the diamond detectors at the new position in HER since Phase-3.

**Figure A.7:** Schematic of the Tungsten radiators (parallel above and trapezoid bottom) coupled with the 45° window shape beam pipe.

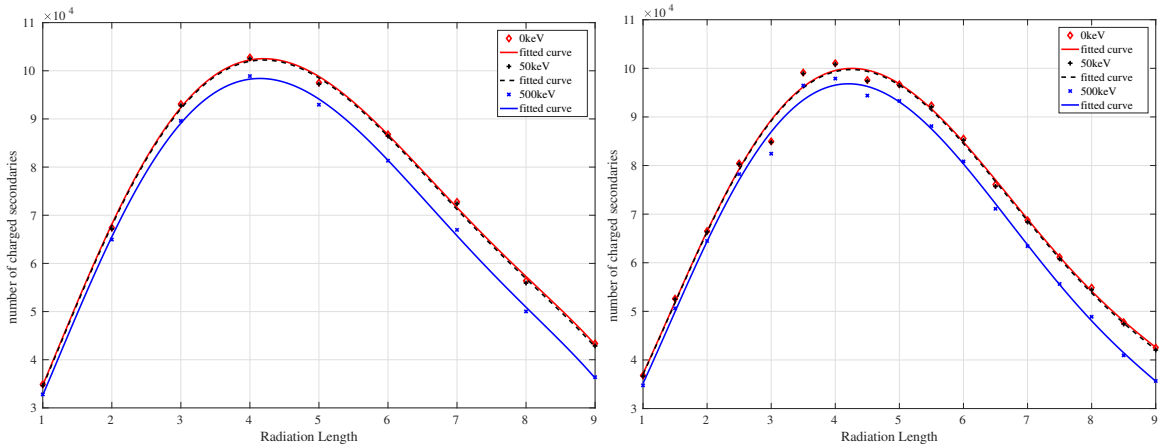


**Figure A.8:** Number of charged particles across the diamond detector as function of the effective thickness of the Tungsten radiator: parallel on the left and trapezoid on the right.

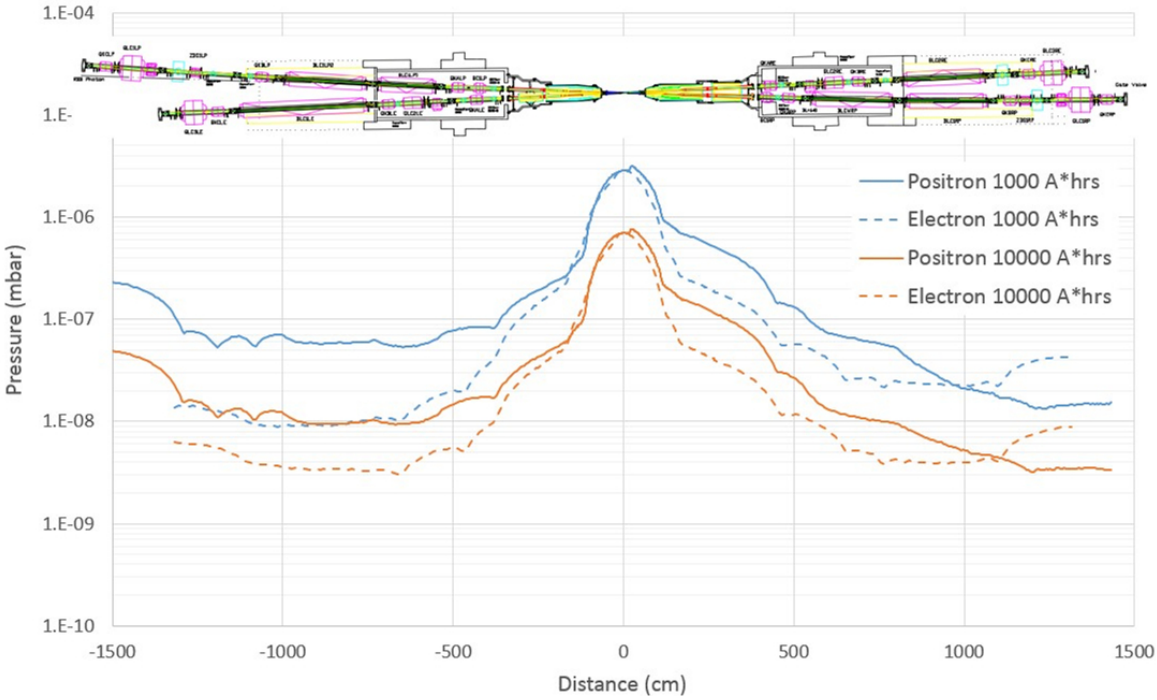


**Figure A.9:** Simulated vacuum profile distribution of the IP region at SuperKEKB [109]

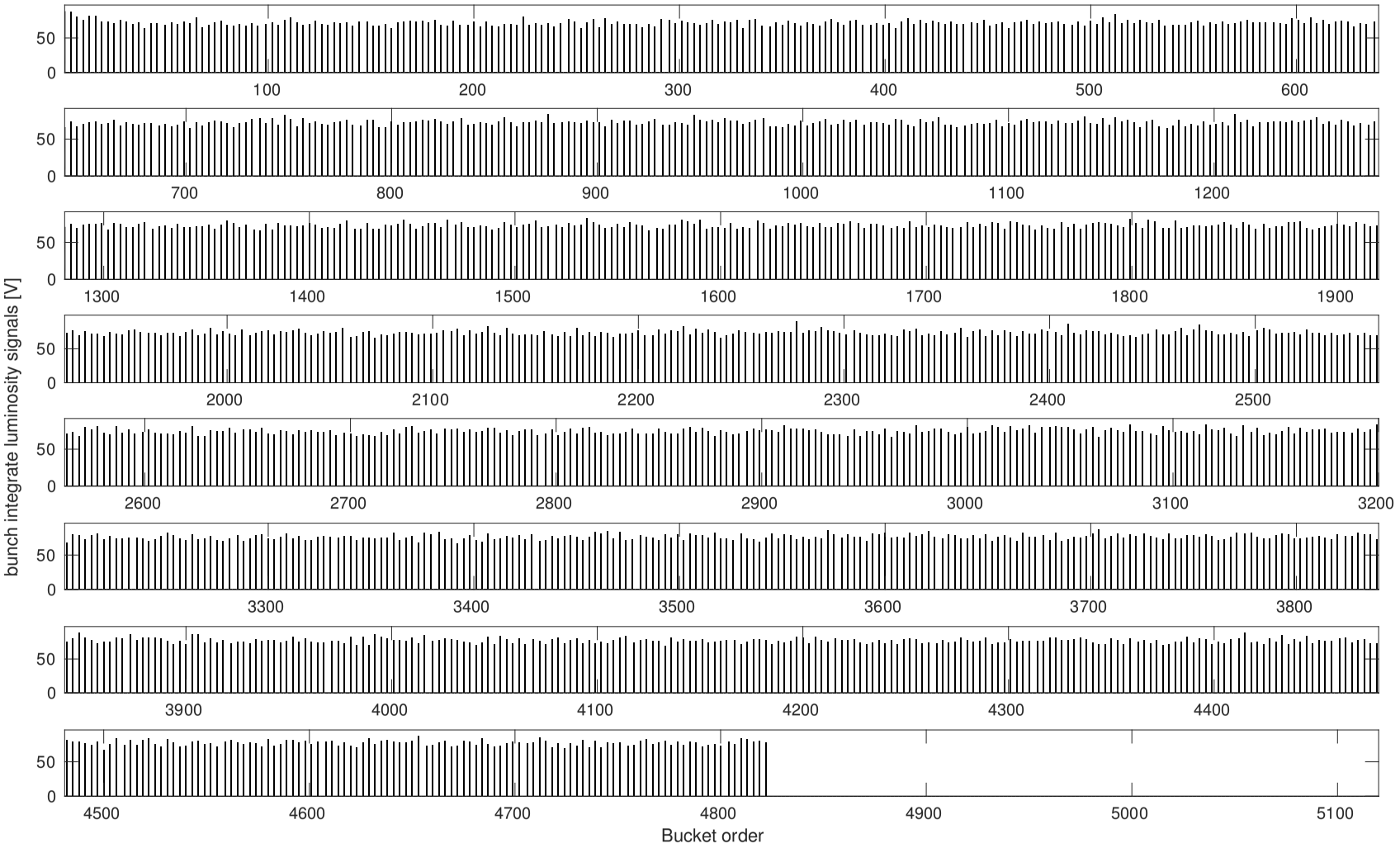


**Figure A.10:** An example of Bunch Integrated Luminosity signals provided by channel C in the LER.

# Appendix B

# Practical information for SuperKEKB

| *Parameter LER / HER* | *KEKB (2006)* | *Phase 2.2* | *Phase 2.3* | *Phase 2.4* | *Phase 3 (final)* |
|---|---|---|---|---|---|
| $\beta_x^*$ [mm] | 590 / 560 | 256 / 200 | 128 / 100 | 128 / 100 | 32 / 25 |
| $\beta_y^*$ [mm] | 6.5 / 5.0 | 2.16 / 2.40 | 2.16 / 2.40 | 1.08 / 1.20 | 0.27 / 0.3 |
| $\varepsilon_x$ [nm] | 18 / 24 | 2.1 / 4.6 | 2.1 / 4.6 | 2.1 / 4.6 | 3.2 / 4.6 |
| $\varepsilon_y/\varepsilon_x$ [%] | 3 / 2.5 | 5.0 | 1.4 | 0.7 | 0.27 / 0.28 |
| $\sigma_x^*$ [μm] | 103 / 116 | 23.2 / 30.3 | 16.4 / 21.4 | 16.4 / 21.4 | 10.1 / 10.7 |
| $\sigma_y^*$ [nm] | 1900 / 1900 | 476 / 743 | 252 / 393 | 126 / 197 | 48 / 62 |
| $\sigma_z$ [mm] | 7 / 7 | 6 / 5 | 6 /5 | 6 / 5 | 6 / 5 |
| $\phi_x$ [mrad] | 11 | 41.5 | 41.5 | 41.5 | 41.5 |
| Φ (Piwinski) | 0.75 / 0.66 | 10.7 / 8.2 | 15.2 / 9.7 | 15.2 / 9.7 | 24.7 / 19.4 |
| I [A] ($n_b$) | 1.66 / 1.34 (1388) | 1.0 / 0.8 (1576) | 1.0 / 0.8 (1576) | 1.0 / 0.8 (1576) | 3.6 / 2.6 (2500) |
| $\xi_x$ | 0.117 / 0.070 | 0.005 / 0.002 | 0.005 / 0.002 | 0.005/ 0.002 | 0.0028 / 0.0012 |
| $\xi_x$ | 0.105 / 0.056 | 0.026 / 0.026 | 0.048 / 0.050 | 0.050 / 0.050 | 0.0881 / 0.0807 |
| $L_{sp}$ [$cm^{-2}s^{-1}/mA^2$] | $1.06 \times 10^{31}$ | $1.97 \times 10^{31}$ | $3.94 \times 10^{31}$ | $7.88 \times 10^{31}$ | $2.14 \times 10^{32}$ |
| L [$cm^{-2}s^{-1}$] | $1.71 \times 10^{34}$ | $10^{34}$ | $2 \times 10^{34}$ | $4 \times 10^{34}$ | $8 \times 10^{35}$ |

**Figure B.1:** Machine parameters of SuperKEKB for different Phases, compared with KEKB. The left column is for LER and those of HER in the right. The parameters for Phase 3 corresponds to the final design of SuperKEKB. the unit of specific luminosity and luminosity are $cm^{-2}s^{-1}mA^{-2}$ and $cm^{-2}s^{-1}$, respectively.

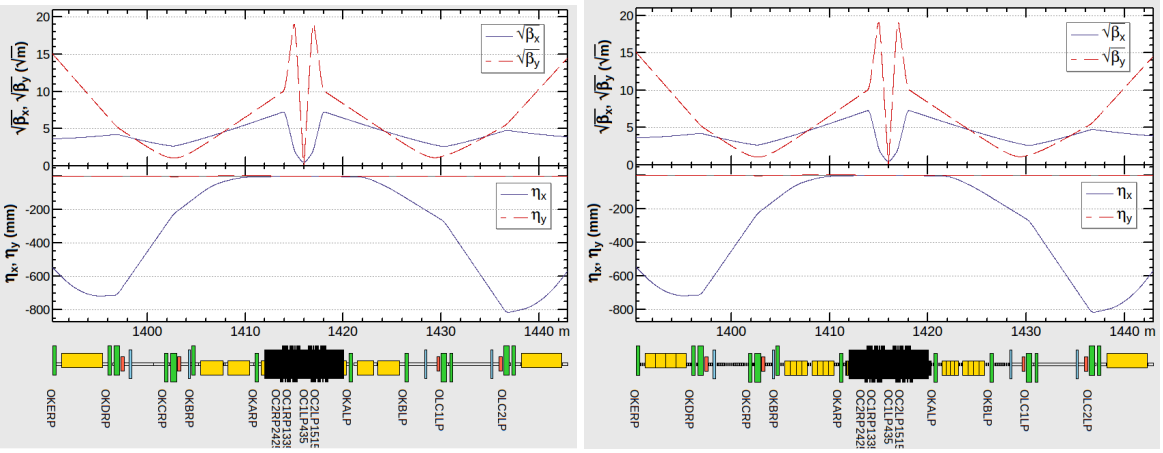


**Figure B.2:** Optics function in the IP region: regular on the left and sliced on the right for Phase 2.2

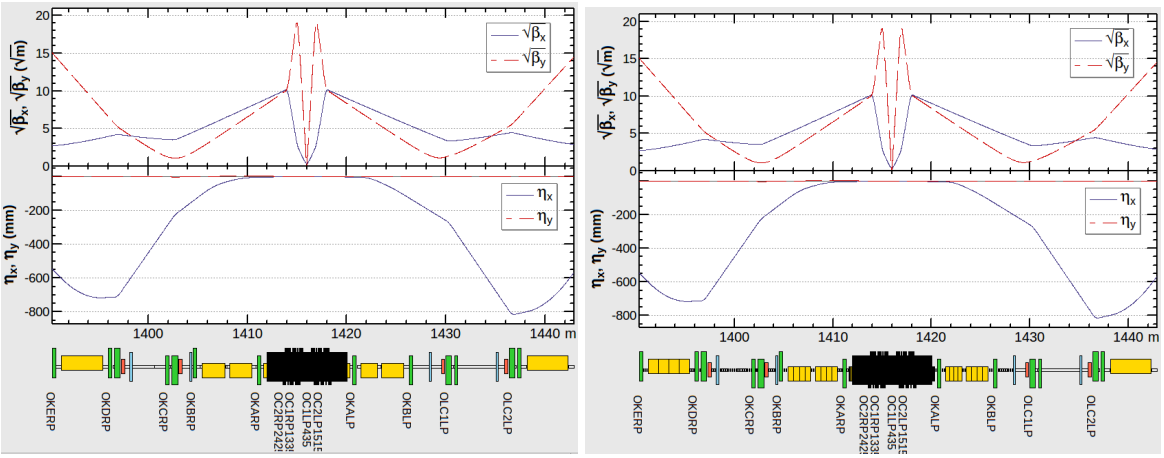


**Figure B.3:** Optics function in the IP region: regular on the left and sliced on the right for Phase 2.3

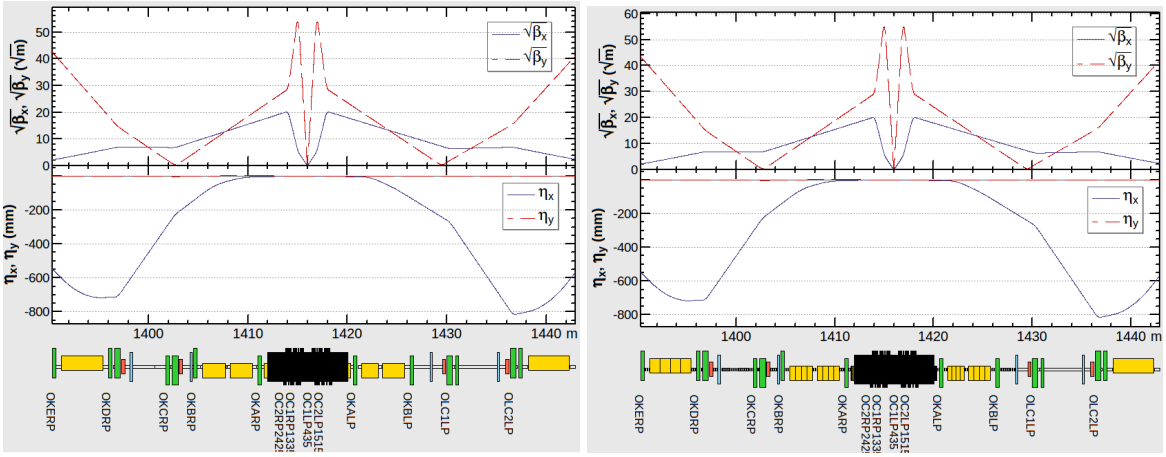


**Figure B.4:** Optics function in the IP region: regular on the left and sliced on the right for Phase 3

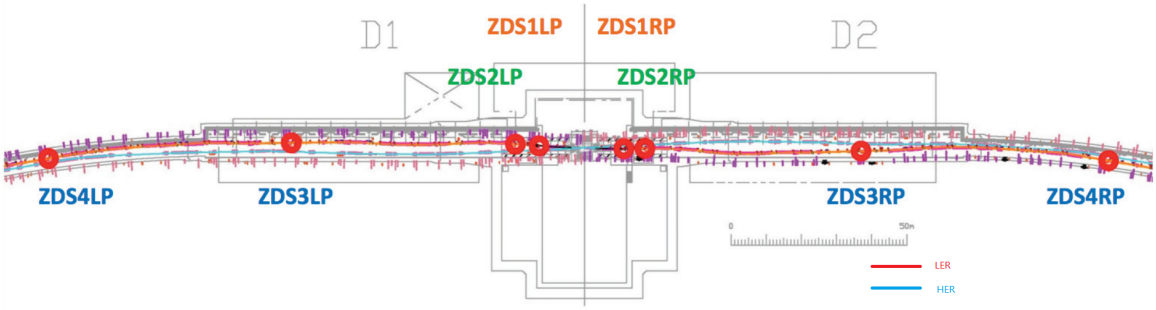


**Figure B.5:** Locations of the dithering coils installed at SuperKEKB.

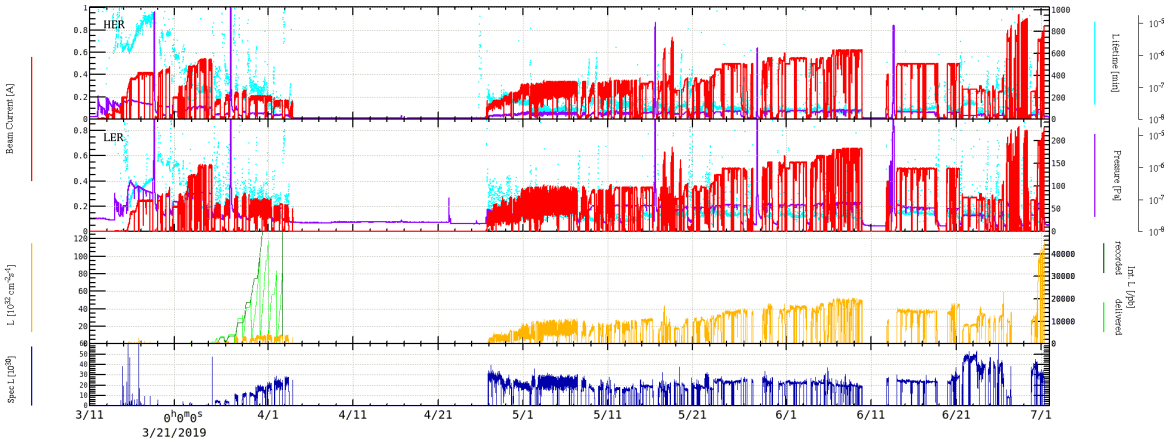


**Figure B.6:** History of SuperKEKB early Phase-3 commissioning in the first half of 2019.

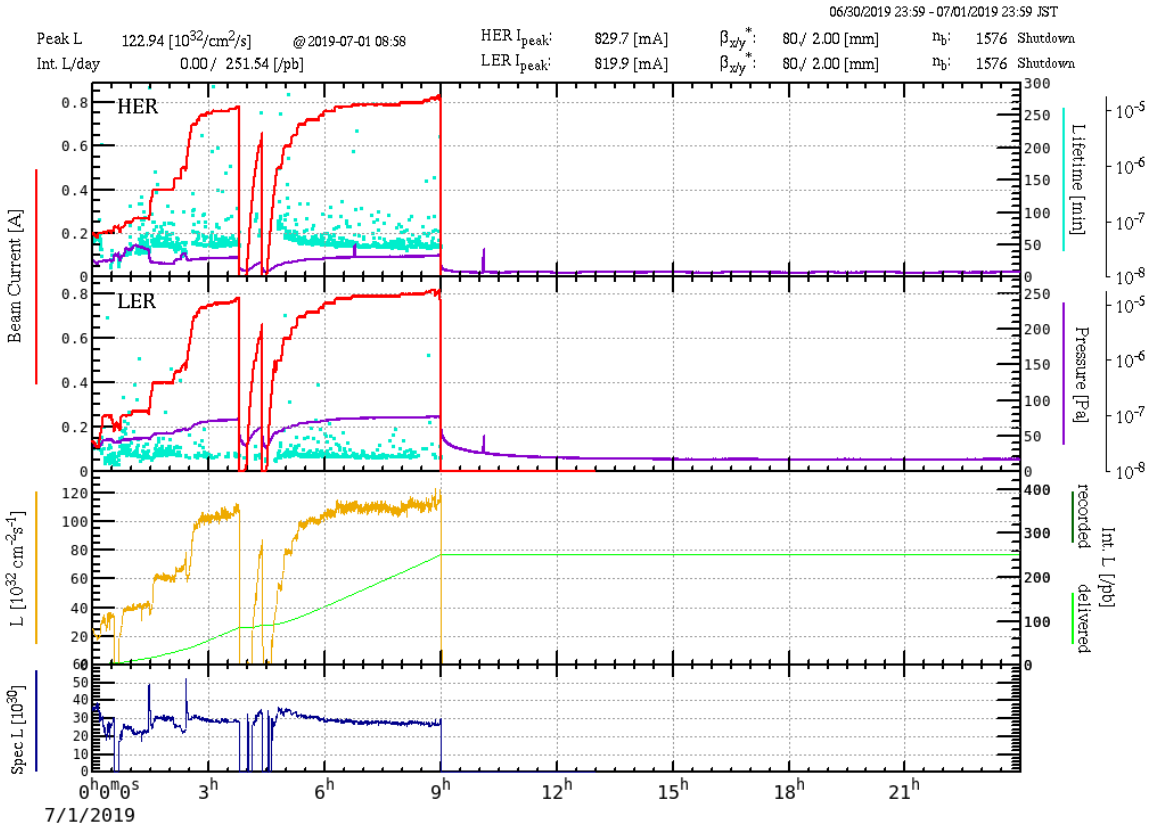


**Figure B.7:** Peak luminosity of about $1.23 \times 10^{34}\ cm^{-2}s^{-1}$ was achieved in the end of the SuperKEKB early Phase-3 commissioning period in the first half of 2019.

université PARIS-SACLAY | ÉCOLE DOCTORALE PHENIICS

**Titre :** Monitorage rapide et asservissement de la luminosité du collisionneur électron-positron japonais SuperKEKB avec des capteurs diamant CVD monocristallins

**Mots clés :** monitorage rapide de la luminosité, détecteur diamant sCVD, diffusion Bhabha radiative, système d'asservissement de l'orbite par modulation et détection synchrone, SuperKEKB

**Résumé :** Le collisionneur SuperKEKB, dédié à l'expérience Belle II, prévoit une très haute luminosité, inégalée à ce jour. Son objectif est de fournir une luminosité instantanée de $8 \times 10^{35}\ cm^{-2}s^{-1}$ en mettant en collision des faisceaux minuscules au point d'interaction (IP) sur la base du schéma "nano-beam". Par conséquent, un excellent contrôle de l'orbite du faisceau à l'IP est nécessaire pour assurer un recouvrement géométrique optimal entre les deux faisceaux en collision, et ainsi maximiser la luminosité. Par ailleurs, des instruments efficaces pour diagnostiquer le comportement des faisceaux à l'IP ainsi que les interactions potentielles entre paquets successifs le long du train sont également essentiels pendant le processus long et plutôt difficile d'ajustement des paramètres des faisceaux pour atteindre les valeurs nominales.
Dans ce cadre, cette thèse présente le développement et l'implémentation d'un système de monitoring rapide de la luminosité de SuperKEKB basé sur des détecteurs en diamant sCVD qui fournit : (1) un signal de luminosité intégré toutes les 1 ms qui sera utilisé en tant qu'entrée pour l'asservissement de l'orbite du faisceau à l'IP, sa précision relative devant être meilleure que 1% lorsque la luminosité atteindra $10^{34}\ cm^{-2}s^{-1}$, (2), un signal de luminosité intégré toutes les 1 s, qui doit être sensible sur une grande dynamique de luminosité, et qui sera envoyé à la salle de contrôle de SuperKEKB comme observable pour permettre le réglage des paramètres des faisceaux en collision, et (3) des signaux de luminosité intégrés toutes les 1 s pour chaque paquet des trains, avec une précision relative suffisante pour surveiller les paramètres de chacun d'entre-eux individuellement.
Pour atteindre une précision relative aussi élevée et couvrir une gamme dynamique de luminosité élevée, le processus de diffusion Bhabha radiatif à très petit angle est utilisé, dont la section efficace d'interaction est très importante et relativement bien connue. Des détecteurs diamant sCVD, dont le signal est rapide et qui ont une bonne tolérance au rayonnement, sont utilisés pour détecter les particules chargées dans les gerbes électromagnétiques induites par l'interaction entre les particules Bhabha diffusées et perdues dans le tube à vide du faisceau, et dans les autres matériaux , en particulier un radiateur, à des emplacements choisis spécialement en aval de l'IP, dans les deux anneaux LER et HER.
Une simulation de bout en bout du système d'asservissement de l'orbite du faisceau à l'IP basé sur notre signal de luminosité rapide et précis a été réalisée, qui comprend : une estimation du signal du détecteur de diamant sCVD, basé sur des mesures de laboratoire à l'aide d'une source radioactive, la construction de séquences de signal représentatives de SuperKEKB comprenant les bruits de fond à un seul faisceau et les particules diffusées par le processus Bhabha, un traitement du signal de luminosité, et la simulation de l'asservissement de l'orbite. Il a été possible de vérifier la faisabilité de ce système pour maintenir la très haute luminosité de SuperKEKB en présence des mouvements du sol et déterminer la précision relative du signal de luminosité rapide qu'il est possible d'obtenir toutes les 1 ms. En outre, les dommages causés par le rayonnement au niveau des détecteurs diamant sCVD dans le LER ont également été estimés sur la base de la simulation FLUKA et de l'hypothèse NIEL.
Pendant la phase 2 de mise en service de SuperKEKB, ainsi qu'au début de la phase 3, notre moniteur de luminosité rapide basé sur des détecteurs en diamant sCVD a été installé et utilisé avec succès. Les processus de perte de faisceau, principalement ceux provenant des processus de Bremsstrahlung et de Touschek, ont été étudiés en détail et, par rapport à la simulation, un bon accord a été trouvé. Lors de la mise en service de la collision, des signaux de luminosité intégrés toutes les secondes étaient fournis en continu pour le réglage des paramètres des faisceaux à l'IP. Par exemple. les tailles de faisceau verticales ont été déterminées avec la technique de balayage du décalage vertical basée sur nos signaux de luminosité, tant pour la valeur moyenne sur tous les paquets que pour chaque paquet individuel, ce qui est très important et utile pour l'optimisation des collisions et pour le réglage de l'optique locale à l'IP. En outre, un signal de luminosité intégré toutes les 1 ms avec la précision relative attendue a également été fourni et utilisé comme entrée du système d'asservissement de l'orbite à l'IP, pour des premiers tests conduits avec succès avec des décalages de faisceau horizontaux introduits volontairement. Davantage de tests de ce système d'asservissement sont attendus pour assurer son bon fonctionnement en continu à l'avenir.

**Title :** Fast luminosity monitoring and feedback using monocrystalline CVD diamond detectors at the SuperKEKB electron-positron collider in Japan

**Keywords :** fast luminosity monitoring, sCVD diamond detectors, radiative Bhabha scattering, dithering orbit feedback system, SuperKEKB

**Abstract :** SuperKEKB is at the foremost frontier of high luminosity $e^+e^-$ colliders, dedicated to the Belle-II experiment. It aims to provide an instantaneous luminosity of $8 \times 10^{35}\ cm^{-2}s^{-1}$ by involving extremely tiny beams colliding at the Interaction Point (IP) based on the "nano-beam scheme". Therefore, excellent control of its beam orbit at the IP is required to ensure the optimum geometrical overlap between the two colliding beams, and thereby maximize the luminosity. Besides, effective instrumentation to diagnose the behavior of the beam at the IP and possible beam interactions between bunches along the trains are also quite essential during the long and rather difficult process of machine tuning towards the nominal beam parameters.

In this context, this thesis presents the development and implementation of a fast luminosity monitoring system based on sCVD diamond detectors at SuperKEKB, which provides : (1), train integrated luminosity signals every 1 ms which will be used as input to the dithering orbit feedback system, its relative precision is expected to be better than 1% when luminosity reaches $10^{34}\ cm^{-2}s^{-1}$, (2), sensitive train integrated luminosity signals over a large luminosity dynamic range every 1 s which will be sent to the SuperKEKB control room as immediate observable for machine collision tuning, and (3) bunch integrated luminosity signals every 1 s with sufficient relative precision to monitor the collision performance for each single bunch.

To achieve such high relative precision and to cover a large luminosity dynamic range, the radiative Bhabha process at vanishing scattering angle will be measured, whose interaction cross-section is quite large and reasonably well known. The sCVD diamond detectors, which have fast signal formation and good radiation tolerance, are used to detect the charged particles in the secondary showers induced by the interaction between the lost Bhabha scattered particles and the beam pipe and specific radiator materials, at carefully chosen locations downstream of the IP, in both the LER and HER.

A start-to-end simulation was performed for the dithering orbit feedback system using our fast and precise luminosity signal as input, based on : sCVD diamond detector signal estimation based on laboratory measurements with a radioactive source, signal sequence construction at SuperKEKB including single beam backgrounds and Bhabha scattered particles, luminosity signal procession, dithering orbit feedback simulation. It enabled verifying the feasibility of this system to maintain very high luminosity in the presence of ground motion, in particular it determined the needed precision for the provided luminosity signals. Besides, the radiation damage of the sCVD diamond detectors in the LER was also estimated based on a FLUKA simulation and applying the NIEL hypothesis.

During the Phase-2 and early Phase-3 commissioning periods of SuperKEKB, our fast luminosity monitor based on sCVD diamond detectors was installed and operated successfully. Single beam loss processes, mainly Bremsstrahlung and Touschek, were studied in detail and compared with the simulation, showing good agreement. During the collision commissioning, train and bunch integrated luminosity signals every 1 s were provided for machine tuning, and the vertical beam sizes could be determined with the vertical offset scan technique based on our luminosity signals, both the average and for the individual bunches, which is very important and useful for the collision and IP local optics tuning during the long and rather difficult process of SuperKEKB machine tuning towards the nominal beam parameters. Besides, a train integrated luminosity signal every 1 ms with the expected relative precision was also provided as input to the dithering orbit feedback system for its first successful tests with deliberately introduced horizontal beam-beam offsets. More tests of the dithering orbit feedback system are expected to establish its future continuous operation.

**Université Paris-Saclay**
Espace Technologique / Immeuble Discovery
Route de l'Orme aux Merisiers RD 128 / 91190 Saint-Aubin, France